Dipolar Quantum Gases of Erbium

DISSERTATION

by

Albert Frisch, Mag.

submitted to the Faculty of Mathematics, Computer Science,
and Physics of the University of Innsbruck

in partial fulfillment of the requirements
for the degree of Doctor of Philosophy (PhD)

advisors:
Univ.-Prof. Dr. Francesca Ferlaino,
Institute for Experimental Physics, University of Innsbruck
Institute for Quantum Optics and Quantum Information of the
Austrian Academy of Sciences

Univ.-Prof. Dr. Rudolf Grimm,
Institute for Experimental Physics, University of Innsbruck
Institute for Quantum Optics and Quantum Information of the
Austrian Academy of Sciences

Innsbruck, October 2014

Summary

Since the preparation of the first Bose-Einstein condensate about two decades ago and the first degenerate Fermi gas following four years later a plethora of fascinating quantum phenomena have been explored. The vast majority of experiments focused on quantum degenerate atomic gases with short-range contact interaction between particles.

Atomic species with large magnetic dipole moments, such as chromium, dysprosium, and erbium, offer unique possibilities to investigate phenomena arising from dipolar interaction. This kind of interaction is not only long-range but also anisotropic in character and imprints qualitatively novel features on the system. Prominent examples are the d-wave collapse of a dipolar Bose-Einstein condensate of chromium atoms realized by the group in Stuttgart, the spin magnetization and demagnetization dynamics observed by groups in Stuttgart, Paris, and Stanford, and the deformation of the Fermi surface observed by our group in Innsbruck.

This thesis reports on the creation and study of the first Bose-Einstein condensate and degenerate Fermi gas of erbium atoms. Erbium belongs to the lanthanide group of elements and has a large magnetic moment of seven Bohr magneton. In particular, this thesis describes the experimental apparatus and the sequence for producing a dipolar quantum gas. There is an emphasis on the production of the narrow-line magneto-optical trap of erbium since this represents a very efficient and robust laser-cooling scheme that greatly simplifies the experimental procedure.

After describing the experimental setup this thesis focuses on several fundamental questions related to the dipolar character of erbium and to its lanthanide nature. A first set of studies centers on the scattering properties of ultracold erbium atoms, including the elastic and the inelastic cross section and the spectrum of Feshbach resonances. Specifically, we observe that identical dipolar fermions do collide and rethermalize even at low temperatures. The corresponding elastic cross section predicted by the theory of universal dipolar scattering scales only with the particle's mass and its magnetic moment and is temperature independent. This represents a dramatic difference compared to non-dipolar fermions, which exhibit a rapidly vanishing elastic cross section at lower temperatures.

Another distinctive feature of erbium is its spectrum of Feshbach resonances. Using bosonic erbium we observed an enormous density of resonances exceeding that of alkali metals by at least a factor of ten. We statistically analyzed the spectrum in terms of the random matrix theory and demonstrated that the resonances bare a strong correlation to each other. We identify the origin of this correlation in the highly anisotropic van der Waals interaction potential of erbium. This is a phenomenon not previously encountered in ultracold quantum gases.

At the many-body level we observed the d-wave collapse of the Bose-Einstein condensate as previously observed in the chromium experiment in Stuttgart. With the dipolar Fermi gas we demonstrated that the Fermi surface deforms into an ellipsoid induced by the action of the dipole-dipole interaction in momentum space.

Zusammenfassung

Die Erzeugung des ersten Bose-Einstein-Kondensats vor ungefähr zwei Jahrzehnten sowie des ersten entarteten Fermigases vier Jahre später, öffnete die Tür zur Erkundung einer Vielzahl faszinierender Quantenphänomene. Der Großteil dieser Experimente konzentrierte sich dabei auf quantenentartete atomare Gase mit kurzreichweitiger Kontaktwechselwirkung zwischen den Teilchen.

Atome mit großem magnetischen Dipolmoment, wie zum Beispiel Chrom, Dysprosium und Erbium, bieten einmalige Möglichkeiten, durch die Dipolwechselwirkung hervorgerufene Phänomene zu erforschen. Der Charakter dieser Wechselwirkung ist nicht nur langreichweitig sondern auch richtungsabhängig und prägt dem System qualitativ neue Eigenschaften auf. Herausragende Beispiele hierfür sind der d-Wellen-Kollaps eines dipolaren Bose-Einstein-Kondensats aus Chromatomen, realisiert von der Gruppe in Stuttgart, die Spin-Magnetisierungs- und Demagnetisierungsdynamik, beobachtet von Gruppen in Stuttgart, Paris und Stanford sowie eine Deformation der Fermifläche, welche von unserer Gruppe beobachtet werden konnte.

Die vorliegende Dissertation behandelt die Erzeugung und Untersuchung des ersten Bose-Einstein-Kondensats und des ersten entarteten Fermigases von Erbiumatomen. Erbium gehört zur Gruppe der Lanthanoide und besitzt ein großes magnetisches Moment von sieben Bohr Magnetonen. Diese Arbeit beschreibt im Besonderen die experimentelle Apparatur und den Ablauf, welcher zur Erzeugung eines dipolaren Quantengases notwendig ist. Das Hauptaugenmerk liegt dabei auf der Produktion der schmalbandigen magneto-optischen Falle für Erbium, die eine sehr effiziente und robuste Art der Laserkühlung darstellt und das experimentelle Herstellungsverfahren maßgeblich vereinfacht.

Nach der Beschreibung des experimentellen Aufbaus werden in der Arbeit einige fundamentale Fragen bezüglich des dipolaren Charakters von Erbium und seiner Natur als Element der Lanthanoiden behandelt. Erste Untersuchungen konzentrieren sich dabei auf die Streueigenschaften bei ultrakalten Temperaturen, welche den elastischen und inelastischen Streuquerschnitt sowie das Spektrum von Feshbach-Resonanzen einschließen. Im Speziellen beobachten wir, dass identische dipolare Fermionen kollidieren und rethermalisieren können, und dies sogar im tiefen Temperaturbereich. Der damit verbundene elastische Streuquerschnitt, welcher im Rahmen der Theorie der universellen dipolaren Streuung berechnet werden kann, hängt nur von der Masse des Teilchens und seinem magnetischen Moment ab und ist temperaturunabhängig. Dies stellt einen entscheidenden Unterschied im Vergleich zu nicht dipolaren Fermionen dar, welche einen mit der Temperatur schnell abklingenden elastischen Streuquerschnitt aufweisen.

Eine weitere markante Eigenschaft von Erbium ist dessen Spektrum von Feshbach-Resonanzen. Unter der Verwendung von bosonischem Erbium beobachteten wir eine enorme Dichte von Resonanzen, welche die bei Alkalimetallen vorhandene Resonanzdichte um mehr als das Zehnfache übersteigt. Wir führten eine statistische Analyse der Verteilung von Feshbach-Resonanzen im Sinne der Theorie der Zufallsmatrizen durch und zeigten, dass die Resonanzen eine starke Korrelation aufweisen. Wir identifizierten den Urprung dieser Korrelation in dem

hochgradig richtungsabhängigen van der Waals Potential von Erbium, wie es erstmals in ultrakalten Quantengasen beobachtet werden konnte.

In Bezug auf Mehrkörperwechselwirkungen konnten wir den d-Wellen-Kollaps des Bose-Einstein-Kondensates beobachten, ähnlich wie im Chrom-Experiment in Stuttgart. Mithilfe des dipolaren Fermigases demonstrierten wir darüberhinaus die Deformation der Fermifläche in ein Ellipsoid, welche durch Auswirkungen der Dipolwechselwirkung im Impulsraum zu erklären ist.

Contents

1

Introduction

1.1. Motivation

About 90 years ago Satyendranath Bose and Albert Einstein predicted a novel quantum state of matter, called Bose-Einstein condensate (BEC). This state of matter is formed by the macroscopic occupation of a single quantum state with bosonic particles. It took 70 years and major technological advances to produce the first BEC in experiment, see Refs. [And95, Dav95]. A key development was the advent of laser cooling and atom trapping, see Ref. [Chu85]. For atomic systems, cooling to ultralow temperatures is necessary to achieve the BEC, since it requires the thermal de Broglie wavelength to be larger than the mean distance between particles.

From then on the field of atomic physics experienced an enormous boost in the number of research groups working on ultracold gases. Some of the early ground-breaking studies on ultracold atomic systems include the verification of matter-wave interferences, the creation of vortices in the superfluid, and the realization of an atomic laser, see Ref. [Blo08] for a summary. Nowadays, the condensation of particles into a BEC is demonstrated not to be limited to ultracold atomic gases only but is also possible with other bosonic systems like photons or solid-state quasi-particles as magnons or exciton-polaritons, for which condensation happens even at room temperature, see Ref. [Den10].

Parallel to the research with bosons, experimental efforts focused on the production of a degenerate Fermi gas (DFG) to access the other fundamental class of particles. The interest in fermions is great because they are often found in nature, e. g. within the electron gas of metals, as neutrons of heavy stars, or as quarks in plasmas as constituent elements of composite particles. The production of a DFG has been achieved in the late 1990s, see Refs. [DeM99b], and it challenged experimentalists for a simple reason: identical alkali fermions do not collide at ultralow temperatures. This stringent property is derived from the Pauli exclusion principle and the Wigner threshold law. However, experimentalists have found an elegant way to overcome this fundamental limitation by introducing a second spin state, another species, or a different isotope, making particle collisions and cooling possible. Beautiful experiments with fermions include the study of the famous BEC-BCS crossover, the production of fermionic mixtures with unequal densities, and the measurement of fundamental

properties of the superfluid in a strongly interacting Fermi gas, see Ref. [Gio08, Ket08] for an overview.

Several tools exist for ultracold gases to manipulate the interaction between particles and confine them in various geometries. Tuning the interactions between particles via a Feshbach resonance (FR) is one of the most prominent example. Dependent on an external magnetic field, the scattering length can be changed from zero (non interacting) to very large values (strongly interacting) across a resonance. FRs are further used to associate two ultracold particles to weakly-bound molecules, which in the next step can be optically transferred into their rovibrational ground state. A second commonly-used tool are optical lattices, periodic structures of light mimicking solid-state crystal-like structures. They offer full control over lattice parameters, e.g. the tunneling rate, and are free of lattice dynamics induced by the environment.

A trend has developed in atomic physics within the last ten years from exploring degenerate matter towards the realization of interesting theoretical models like the well-known Bose-Hubbard model in lattices [Jak98], the superfluid to Mott-insulator transition [Gre02], or Anderson localization using disorder [Bil08]. It is precisely this trend which marked a turning point from the mere awareness and observation of quantum effects in ultracold gases to the possibility of engineering quantum mechanical systems with an unprecedented large degree of control and flexibility.

Dramatic advances in laser technology and more sophisticated cooling techniques made it possible to condense elements other than alkali metals. Figure 1.1 shows a periodic table of elements with those elements, which have been brought to degeneracy to this day, highlighted. Today, a total of 13 elements are available in ultracold quantum gas experiments, three of which allow for the study of dipolar systems.

In contrast to conventional atomic gases, dipolar systems add an interaction between particles, the so-called *dipole-dipole interaction* (DDI), which is anisotropic and long-range. As reviewed in Ref. [Bar02a] it is possible to study fundamentally different phenomena in dipolar systems compared to experiments with alkali metals. Dipolar systems had been proposed for accessing exotic quantum phases already in the late 1990s. Nowadays, at least three dipolar systems are experimentally accessible, namely atoms with a large magnetic dipole moment in the ground state, heteronuclear molecules with an electric dipole moment, and atoms in highly excited Rydberg states.

Chromium was the first dipolar element to be Bose-Einstein condensed by the group of T. Pfau in Stuttgart (Germany) about a decade ago, see Ref. [Gri05]. It has a magnetic moment of $6 \mu_B$ and a total quantum number of three. Several interesting phenomena, which are purely caused by the DDI, had been realized with chromium, such as the principle of demagnetization cooling [Fat06], the d-wave collapse of the BEC [Lah08], and the spin relaxation in an optical lattice [Pas11].

In the last several years, a new class of dipolar atoms from the lanthanide series have come into play, which posses an even larger magnetic moment than that of chromium. Elements like dysprosium or erbium have a magnetic moment of up to $10 \mu_B$ and a large total spin

Figure 1.1.: Periodic table showing Bose-Einstein-condensed elements up to 2014. Initially, only alkali atoms were brought to degeneracy, but in the last years the interest in alkaline-earth elements and elements with a large magnetic dipole moment (blue frame) increased significantly. List of references: Na [Dav95], Rb [And95], Li [Bra95], H [Fri98], He [Rob01], K [Mod01], Cs [Web03], Yb [Tak03], Cr [Gri05], Ca [Kra09], Sr [Ste09], Dy [Lu11], and Er [Aik12].

quantum number in the ground state, which makes them particularly interesting for ultracold gas experiments.

Early experimental work on trapping and laser cooling erbium was done by the group of J.J. McClelland at NIST (USA), see Refs. [McC06b, Ber08]. Different laser-cooling schemes and magnetic-trapping methods were successfully demonstrated but the atomic sample was never brought to degeneracy in these experiments. Laser cooling of dysprosium atoms was soon to follow by the group of B. Lev now in Stanford (USA), see Ref. [Lu10]. The same group produced the first dysprosium Bose-Einstein condensate [Lu11] and first degenerate Fermi gas [Lu12]. In our group in Innsbruck we have been able to laser cool erbium using a narrow-line transition and to create the first Bose-Einstein condensate and the first degenerate Fermi gas of erbium atoms. This forms a solid basis for future experiments on dipolar quantum gases. Moreover, thulium [Suk10] and holmium [Mia14] are two more elements from the lanthanide series, which have been successfully laser cooled. Nowadays, bosonic as well as fermionic systems (or even mixtures thereof) in combination with a large magnetic dipole moment are readily available for experimental studies. The success of lanthanides in ultracold atomic physics can be already observed, as several research groups around the globe are setting up new experiments on lanthanide atoms at the moment.

Alternatively to magnetic atoms, one can use ultracold diatomic, heteronuclear ground-state molecules to study dipolar effects. Such molecules can be associated from ultracold alkali-metal atoms and have a strong electric dipole moment. Commonly used molecules in current experiments are KRb [Ni08], LiCs [Dei08], or RbCs [Tak14]. Up to date, only gases of diatomic molecules composed of alkali-metal atoms are available at ultracold temperatures
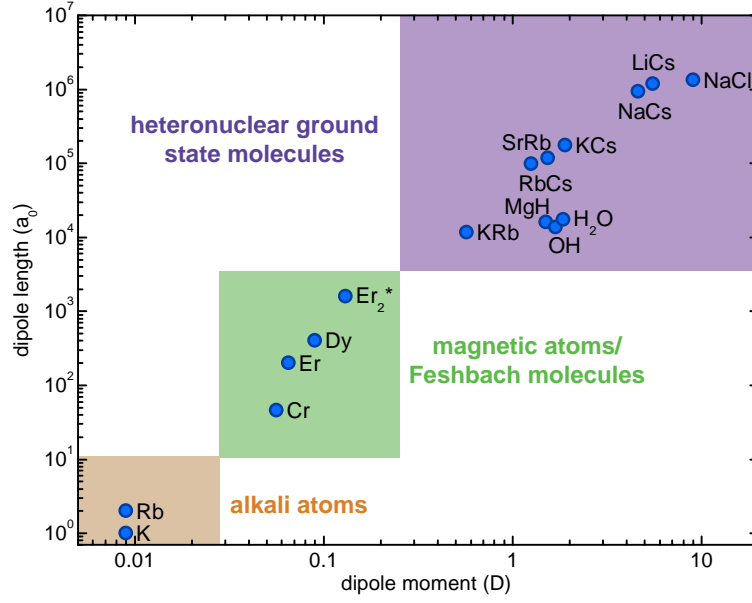
Figure 1.2.: Comparison of alkali atoms with magnetic atoms and heternuclear molecules. The dipole interaction length is plotted in units of the Bohr radius against the dipole moment given in Debye. Weakly-bound Feshbach molecules are marked with a star. Rydberg atoms have an extremely high dipole moment of several thousand Debye, which is out of scale for this figure.

but developments in slowing and trapping polyatomic molecules look very promising. Very recently a magneto-optical trap of SrF molecules has been shown in Ref. [Bar14], which might have future applications for testing the standard model of particle physics [Hun12] or for searching for variations of fundamental constants [Chi09].

A relevant quantity to compare the dipolar character of particles with, is the so-called *dipole length*, a_d. It is defined for magnetic atoms by

$$a_d = \frac{m\mu_0\mu^2}{4\pi\hbar^2} \; , \qquad\qquad 1.1$$

and depends on the magnetic moment μ and the mass of a single dipole m. Here, μ_0 is the magnetic constant and $\hbar$ the Planck constant divided by 2π. Figure 1.2 shows a plot of the dipole length as function of the dipole moment for several dipolar systems in comparision with alkali atoms. The plot includes magnetic atoms, Feshbach molecules from magnetic atoms, and heteronuclear molecules. Alkali atoms have the smallest dipole moment, whereas heteronuclear molecules have a very high dipole moment. Magnetic atoms lie in between these two cases and Feshbach molecules of magnetic atoms, such as weakly bound Er_2, have a dipole length, which is only one order of magnitude smaller than that of polar molecules. Note that Rydberg atoms have a much higher dipole moment than heteronuclear molecules and are not shown in Fig. 1.2.

The large magnetic moment of lanthanide atoms is caused by an unfilled $4f$ electron shell. The lanthanide electron configuration forms a so-called submerged-shell structure as the $4f$ shells are immersed in the outer-lying $6s$ shell, which is completely filled. This structure provides a rich atomic energy spectrum with transition linewidths ranging from broad to

ultra-narrow. Several atomic transitions turn out to be very convenient for implementing efficient laser-cooling techniques, which makes it surprisingly simple to prepare lanthanide atoms in ultracold gas experiments.

All these reasons make lanthanide systems to be very suitable candidates for exploring dipolar quantum phenomena.

1.2. Thesis overview

This thesis describes the production and study of a dipolar quantum gas of ultracold bosonic and fermionic erbium atoms. In particular, the thesis covers the following achievements: (I) production of the first Bose-Einstein condensate and (II) the first degenerate Fermi gas of erbium, (III) observation of Feshbach resonances and chaotic scattering, and (IV) observation of anisotropic dipolar scattering and the deformation of the Fermi surface.

On a personal note, I joined the erbium team in 2009, when the experiment was still in its conceptual phase. In the beginning, the design and setup of the vacuum apparatus was solely undertaken by me under the guidance of Francesca Ferlaino. Once the experiment approached the point of first measurements, the team quickly enlarged. I actively participated in the above mentioned achievements of the experiment. The scope of this thesis covers many of the technical challenges, so that it might serve as a reference for future PhD students.

The thesis is structured as follows:

Chapter 2 presents the relevant properties of atomic erbium for ultracold gas experiments. It contains detailed information on the electron configuration, the magnetic properties, and the atomic energy spectrum, including the laser-cooling transitions of erbium.

Chapter 3 describes the erbium experimental setup. It is structured in four sections including the vacuum apparatus, the preparation of a slow atom beam, the main coil system, and the laser light setup.

Chapter 4 offers an introduction to ultracold dipolar scattering. The aim is to highlight the difference arising in scattering physics between short- and long-range interactions and introduce the anisotropic van der Waals interaction. The chapter starts with a discussion on anisotropic interactions between atoms. Then the theory of universal dipolar scattering is presented. The last part of this chapter offers an overview of the emergence of Feshbach resonances in a dipolar quantum gas.

Chapter 5 is devoted to random matrix theory and quantum chaos. A very general introduction is given as many readers of this thesis might be unfamiliar with that topic. The second part of this chapter draws a connection between quantum chaos and atomic physics and presents an application of random matrix theory for calculating scattering properties of complex systems by means of the theory of ultracold resonant scattering.

The next five chapters present scientific results, which have been published within the scope of this thesis. Each of these chapters contains one publication. The publications are given in chronological order and every chapter follows the same structure, with experimental background information at the beginning, the actual publication in the middle, and further unpublished work at the end.

Chapter 6 contains our publication on the magneto-optical trap for erbium.
Narrow-line magneto-optical trap for erbium
Albert Frisch, Kiyotaka Aikawa, Michael Mark, Alexander Rietzler, Johannes Schindler, Eric Zupanič, Rudolf Grimm, and Francesca Ferlaino
Physical Review A *85*, 051401(R) (2012). DOI 10.1103/PhysRevA.85.051401
This publication shows the experimental realization of the narrow-line magneto-optical trap for erbium. Specifically, it addresses the Zeeman slowing process, the physical limitations of the narrow-line magneto-optical trap and the spin polarization of the atom cloud.

Chapter 7 presents our publication on the first Bose-Einstein condensate of erbium.
Bose-Einstein Condensation of Erbium
Kiyotaka Aikawa, Albert Frisch, Michael Mark, Simon Baier, Alexander Rietzler, Rudolf Grimm, and Francesca Ferlaino
Physical Review Letters *108*, 210401 (2012). DOI 10.1103/PhysRevLett.108.210401
Editor's suggestion and Viewpoint in physics.
It presents detailed information on evaporative cooling towards a degenerate Bose gas. Furthermore, this chapter contains a measurement of the scattering length for different isotopes of erbium.

Chapter 8 contains our publication on the hyperfine structure of erbium.
Hyperfine structure of laser-cooling transitions in fermionic erbium-167
Albert Frisch, Kiyotaka Aikawa, Michael Mark, Francesca Ferlaino, Ekaterina Berseneva, and Svetlana Kotochigova
Physical Review A *88*, 032508 (2013). DOI 10.1103/PhysRevA.88.032508
It shows a spectroscopic measurement of the hyperfine structure of fermionic erbium using a hollow cathode lamp.

Chapter 9 contains our publication on the first degenerate Fermi gas of erbium.
Reaching Fermi degeneracy via universal dipolar scattering
Kiyotaka Aikawa, Albert Frisch, Michael Mark, Simon Baier, Rudolf Grimm, and Francesca Ferlaino
Physical Review Letters *112*, 010404 (2014). DOI 10.1103/PhysRevLett.112.010404
Editor's suggestion.
The publication sets the path for producing a degenerate Fermi gas using a similar approach as for bosons. It turns out that evaporative cooling of a single, dipolar fermionic species can be employed with equal efficiency as in the bosonic case.

Chapter 10 presents our publication on signatures of quantum chaos in erbium.
Quantum chaos in ultracold collisions of gas-phase erbium atoms
Albert Frisch, Michael Mark, Kiyotaka Aikawa, Francesca Ferlaino, John L. Bohn, Constantinos Makrides, Alexander Petrov, and Svetlana Kotochigova
Nature *507*, 475–479 (2014). DOI 10.1038/nature13137
Nature News & Views associated article.
It provides a high-resolution Feshbach spectroscopy measurement revealing up to 200 Feshbach resonances at low magnetic fields. A statistical analysis of these resonances indicates quantum chaos in the collision of erbium atoms.

Chapter 11 contains our publication on the observation of the Fermi surface deformation.
Observation of Fermi surface deformation in a dipolar quantum gas
Kiyotaka Aikawa, Simon Baier, Albert Frisch, Michael Mark, Cornelis Ravensbergen, and Francesca Ferlaino
Science *345*, 1484 (2014). DOI 10.1126/science.1255259
It contains the first experimental realization and observation of the deformation of the Fermi surface induced by anisotropic interactions. The deformation is a quantum many-body effect and depends on the temperature of the gas.

Finally, I conclude the thesis in Chapter 12 with an outlook on possible future directions in the erbium experiment.

2

> The rare earth elements perplex us in our researches, baffle us in our speculations, and haunt us in our very dreams. They stretch like an unknown sea before us mocking, mystifying and murmuring strange revelations and possibilities.
>
> *(Sir William Crookes* 1887*)*

Erbium properties

Erbium (Er) is a rare-earth metal belonging to the lanthanide series of the periodic table of elements. It has an atomic number of $Z = 68$ and an atomic mass of $167.26\,\text{amu}$, with $1\,\text{amu} = 1.6605402 \times 10^{-27}\,\text{kg}$. Pure solid erbium is a silvery-white metal and needs to be artificially isolated as it naturally occurs only in chemical compounds on Earth mostly in oxides with trivalent bonds. As a solid it is a malleable and soft metal.

Erbium can be found in the Earth crust with a concentration of about $3.5\,\text{ppm}$ and thus belongs to the rare-earth metals, see Ref. [Lid10]. It is a very important element for many technological applications. For example, it is commonly used as dopant in the form of Er^{3+}-ions in silica-glass fibers for erbium-doped fiber amplifiers. Such laser light amplifiers are usually operated at wavelengths in ranges from $1525\,\text{nm}$ to $1565\,\text{nm}$ and $1570\,\text{nm}$ to $1610\,\text{nm}$ and are nowadays the core elements in optical telecommunication networks. The same erbium ion has a prominent transition at $2940\,\text{nm}$, which is highly absorbed by water and thus perfectly suitable for laser surgery and other medical applications. In a very recent publication the electrical detection of an optical excitation of Er^{3+} has been demonstrated in Ref. [Yin13]. This technique might lead to a novel interface between optical-based quantum computing and common silicon-based semiconductor technologies.

In the 1990s the price for erbium oxide, as well as for other rare-earth elements, dropped significantly due to the construction of large production facilities in China. Recently, prices were rising again as up to about $90\,\%$ of the worldwide production of rare-earth elements is now carried out in China. This lead to a global discussion about China's monopoly in the production of rare-earth metals and its strong influence on the high-tech industry.

2.1. The discovery of erbium

The erbium element was first mentioned by Carl Gustaf Mosander in 1843, see Ref. [Mos43]. From the mineral gadolinite he was able to separate three fractions of oxides that he called yttria, erbia, and terbia. Gadolinite was found in large amounts close to the village Ytterby near Stockholm, Sweden. Eventually also the elements ytterbium, terbium and yttrium were directly named after this place. Other elements, which were discovered at the same place

isotope	^{162}Er	^{164}Er	^{166}Er	^{167}**Er**	^{168}**Er**	^{170}Er
abundance	0.14 %	1.61 %	33.6 %	23.0 %	26.8 %	15.0 %
statistics	boson	boson	boson	fermion	boson	boson

Table 2.1.: Relative abundances and type of quantum mechanical statistics for all stable erbium isotopes. Isotopes commonly used in the work of this thesis are highlighted.

but later, were named gadolinium (after gadolinite), holmium (after the Latin name for Stockholm), and thulium (with thule an ancient word for Scandinavia). All together, nearly half of all elements from the lanthanide series were discovered in Ytterby for the first time. Many years later it turned out that the originally separated parts of gadolinite were actually a mixture of several oxides and pure erbium as a solid metal could be isolated by Wilhelm Klemm and Heinrich Bommer as late as in 1934.

2.2. Basic properties

As many other lanthanides, erbium has a high melting point at 1529 °C and boiling point at 2900 °C. It oxidizes and tarnishes slowly under air atmosphere but burns readily to form erbium(III)-oxide at high temperatures. Thin structures made out of erbium, like foils or powder, are easily flammable when brought from an inert atmosphere into air. It reacts with water and produces hydrogen gas. Erbium can be dissolved in dilute sulfuric acid, forming rose red hydration complexes containing Er^{3+} ions. Vacuum gettering properties of erbium in the form of evaporated films are studied in Ref. [Mül72].

Erbium has six stable isotopes, of which five (^{162}Er, ^{164}Er, ^{166}Er, ^{168}Er, and ^{170}Er) are bosons and one (^{167}Er) is a fermion, see Table 2.1 for a list of all stable erbium isotopes and their abundances. This thesis focuses mostly on the bosonic isotope ^{168}Er and on the fermionic isotope ^{167}Er, which both have natural abundances above 20 % as well as convenient scattering properties for efficient evaporative cooling.

Another basic property of erbium is its large magnetic moment of about $7\,\mu_\mathrm{B}$, with μ_B the Bohr magneton. Although a large magnetic moment is not common to all elements within the lanthanide series, some of them have the highest magnetic moment of all elements. This includes dysprosium and terbium, which both have the largest magnetic moment of $10\,\mu_\mathrm{B}$, and holmium with $9\,\mu_\mathrm{B}$. See Table 2.6 for a full list of all lanthanide elements.

2.2.1. Electron configuration

According to the Aufbau principle ground-state erbium has an electron configuration, which is often referred to as a *submerged-shell* configuration. Electrons are distributed among

electron orbitals[1] simply as

$$(1s^2\, 2s^2\, 2p^6\, 3s^2\, 3p^6\, 3d^{10}\, 4s^2\, 4p^6\, 4d^{10}\, 5s^2\, 5p^6)\, 4f^{12}\, 6s^2\ ,\qquad\qquad 2.1$$

Following the Madelung rule with increasing number of electrons, the $6s$ orbital is filled up before the $4f$ orbitals. Because of this, all orbitals except the $4f$ orbitals are completely filled in the electron configuration of erbium. The part of above electron configuration written in brackets equals the electron configuration of xenon and is often abbreviated as [Xe].

There are seven $4f$ orbitals available, which can in principle take up to 14 electrons in total. In case of erbium two electrons are missing in the $4f$ shells, having an angular momentum projection quantum number of $m_\ell = +2$ and $+3$. In both cases the spin projection quantum number of the missing electrons is $m_s = -1/2$, see Table 2.2. Furthermore, the $4f$ electron orbitals are highly anisotropic due to their large angular momentum quantum number of $\ell = 3$, whereas the $6s$ orbital is spherically symmetric with $\ell = 0$. See corresponding figures in Table 2.2. It has to be noted here, that these anisotropic orbitals result in a highly anisotropic van der Waals interaction potential between atoms, not yet observed in ultracold gas experiments so far, see Sec. 4.1.2.

In case of heavy elements the coupling of electrons is more complicated than for light elements. The reason for this is that the spin-orbit interaction gets comparable or even stronger than the Coulomb interaction for electrons in higher orbitals. The well-known and simple spin-orbit (LS) coupling scheme of electrons[2] is not applicable any more and the jj-coupling scheme has to be used. A special case of this is the $J_1 J_2$-coupling, which is important for most excited states of lanthanide elements, see Ref. [Wyb07]. In this scheme, all inner electrons, i. e. electrons in the [Xe] configuration including the $4f$ shells, as well as all outer electrons in the $6s$ shell couple independently in a LS-coupling scheme to states with angular momentum quantum numbers J_1 and J_2. They then sum up to the overall total angular momentum $\mathbf{J} = \mathbf{J_1} + \mathbf{J_2}$ with quantum number J, which is denoted as $(J_1, J_2)_J$.

Erbium in its ground state (g. s.) is in an H-state with an orbital angular momentum quantum number of $L = 5$ due to LS-coupling of all electrons[3]. This angular momentum is unusually large compared to alkali and alkaline-earth atoms, which have $L = 0$ in the ground state. Using S and J as the spin and total electronic angular momentum quantum numbers, respectively, the ground state of erbium is written as

$$\text{g. s. :}\quad {}^3\text{H}_6$$
$$L = 5,\quad S = 1,\quad J = 6\ .$$

We take the prominent 401-nm transition in erbium as an example for the electron coupling of an excited state. Its excited state (e. s.) results from the excitation of an electron from the $6s$ orbital into the $6p$ orbital. Following jj-coupling, first the $6s$ and $6p$ electrons couple

---

[1] Using the standard spectroscopic notation, $n\ell^e$, with n the principal quantum number, followed by the orbital quantum number, ℓ (denoted by $s = 0$, $p = 1$, $d = 2$, $f = 3$, ...), and the number of electrons, e, in each orbital as superscript.

[2] The LS-coupling is also known as Russel-Saunders coupling scheme.

[3] As shown in Sec. 2.4.2 small corrections on the order of $0.3\,\%$ have to be made compared to a pure LS-coupling scheme.
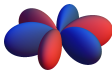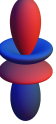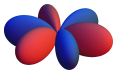
Table 2.2.: Electron configuration of erbium in the ground state for the $4f$ and $6s$ orbitals[4]. Electrons are filled into the $6s$ orbital before the $4f$ orbitals according to the Aufbau principle. Arrows denote occupied states with a spin quantum number of $m_s = +1/2$ and $-1/2$ by $|\uparrow\rangle$ and $|\downarrow\rangle$, respectively. The two vacancies in the $4f$ shells with $m_l = +2, +3$ give rise to the large magnetic moment and the strongly anisotropic van der Waals potential of erbium.

to a $^1P_1$ state and the rest of the inner electrons couple to $^3H_6$ by LS-coupling. Then, these two states couple to a $(J_1, J_2)_J$ state. The 401-nm excited state is thus written as

$$401\,\text{nm e.s.}: \quad [\text{Xe}]4f^{12}(^3H_6)6s6p(^1P_1)(6,1)_7$$
$$J_1 = 6, \quad J_2 = 1, \quad J = 7 \ .$$

All bosonic isotopes of erbium have a zero nuclear spin quantum number I. On the contrary, the fermionic isotope has $I = 7/2$, which leads to hyperfine structure as J couples with the nuclear spin to give the total angular momentum quantum number F.

$$^{164}\text{Er}, \ ^{166}\text{Er}, \ ^{168}\text{Er}, \ ^{170}\text{Er}: \quad I = 0$$
$$^{167}\text{Er}: \quad I = 7/2 \quad \text{g.s.}: \quad F = 19/2 \ .$$

It is interesting to point out that nuclei with an even number of protons and neutrons will always have zero nuclear spin, whereas odd-even or even-odd nuclei will have half-integer and odd-odd nuclei an integer nuclear spin, see Ref. [Wyb07]. More details about the hyperfine structure of fermionic erbium in the ground state is found in Sec. 2.3.2 and Chapter 8.

On the one hand, erbium's exceptional electron configuration gives rise to its large magnetic moment, as shown in Sec. 2.4 and on the other hand, it causes a strongly anisotropic van der Waals potential, see Sec. 4.1.2. In conclusion, the submerged-shell structure of erbium with two vacancies in the anisotropic $4f$ orbitals is at the foundations of its exotic scattering properties, which will be discussed in detail in Chapter 4.

---

4   The size of the $6s$ orbital is shown out of scale with respect to the $4f$ orbitals.
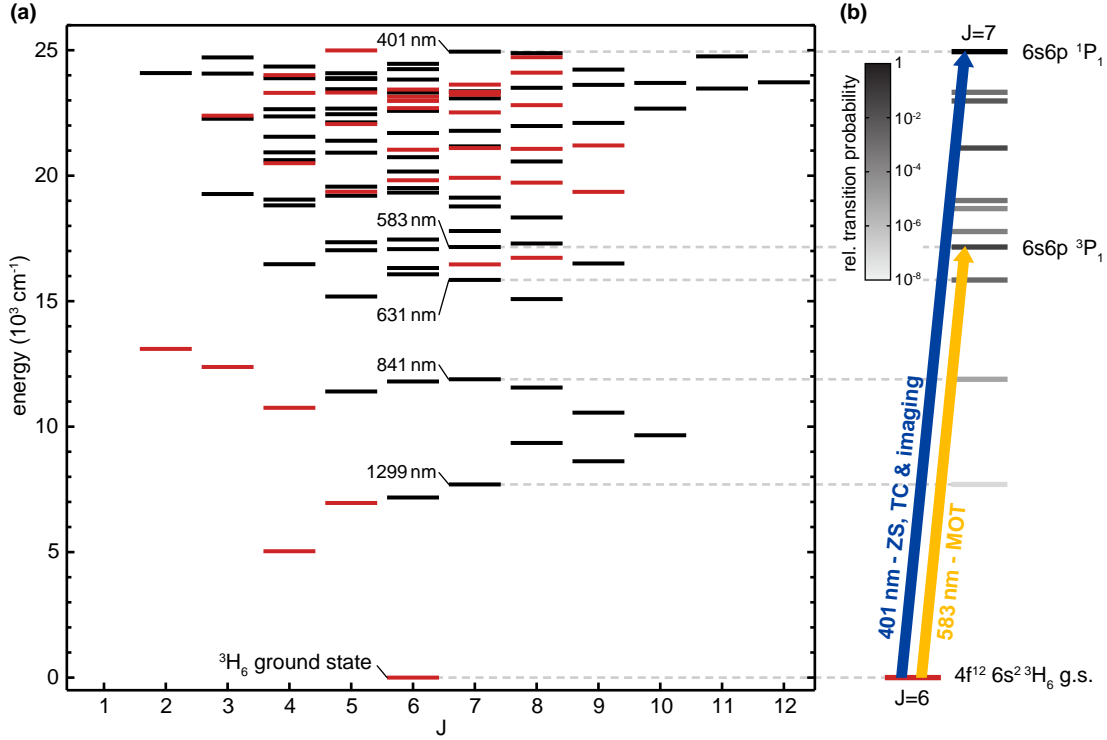
Figure 2.1.: Energy level scheme of erbium. (a) Levels up to an energy of a wavenumber of $25{,}000\,\mathrm{cm}^{-1}$. The full level scheme is presented in appendix E. States with even (odd) parity are shown in red (black). (b) Energy levels of transitions from the ground state to an excited state with $J \rightarrow J+1$. The two important transitions for the erbium experiment are at a wavelength of 401 nm (blue) and 583 nm (yellow). The blue transition is used for Zeeman slowing (ZS), transversal cooling (TC), and imaging, whereas the yellow transition is used for creating the magneto-optical trap (MOT).

2.3. Atomic energy spectrum

The submerged-shell electron configuration of erbium is the reason for its complicated energy level structure. Figure 2.1(a) shows part of the erbium level scheme up to a wavenumber of $25{,}000\,\mathrm{cm}^{-1}$. The full level scheme is presented in appendix E. A comprehensive set of spectroscopic data of all lanthanide elements can be found in Refs. [Ral11, Mar78]. For erbium a total of 312 states with odd parity[5] and 358 states with even parity are known up-to-date. Its ground state has even parity.

The natural linewidth of several excited states of erbium was initially determined by measuring the radiative lifetime after excitation by a pulsed laser. These measurements had been carried out in Ref. [Mar80]. More recent measurements on a slow atom beam of erbium include many more transition probabilities of excited states, see Refs. [Law10, Har10].

---

[5] The parity refers to the symmetry property of the electronic wave function. Let the parity operator $\hat{P}$ invert the wave function through the origin. If $\hat{P}\Psi(\vec{r}) = \Psi(-\vec{r})$ the wave function has even parity, if $\hat{P}\Psi(\vec{r}) = -\Psi(-\vec{r})$ it has odd parity.

energy $(\mathrm{cm^{-1}})$	wavelength in vacuum (nm)	natural linewidth	excited state el. conf.	jj-coupling
24943.272	400.91	29.7(6) MHz	$[\mathrm{Xe}]4f^{12}\ (^{3}\mathrm{H}_{6})$ - $6s6p\ (^{1}\mathrm{P}^{o}_{1})$	$(6,1)^{o}_{7}$
17157.307	582.84	186(10) kHz	$[\mathrm{Xe}]4f^{12}\ (^{3}\mathrm{H}_{6})$ - $6s6p\ (^{3}\mathrm{P}^{o}_{1})$	$(6,1)^{o}_{7}$
15846.549	631.04	28(7) kHz	$[\mathrm{Xe}]4f^{11}\ (^{4}\mathrm{I}^{o}_{13/2})$ $5d_{3/2}$ $6s^{2}$	$(13/2,3/2)^{o}_{7}$
11887.503	841.22	8.0(2) kHz	$[\mathrm{Xe}]4f^{11}\ (^{4}\mathrm{I}^{o}_{15/2})$ $5d_{5/2}$ $6s^{2}$	$(15/2,5/2)^{o}_{7}$
7696.956	1299.21	2.1(1.1) Hz	$[\mathrm{Xe}]4f^{11}\ (^{4}\mathrm{I}^{o}_{15/2})$ $5d_{3/2}$ $6s^{2}$	$(15/2,3/2)^{o}_{7}$

Table 2.3.: Laser-cooling transitions with $J \to J+1$ of erbium in the ground state. Note the decreasing natural linewidth of these transitions. The electron configuration (el. conf.) of the excited state is given. Electrons in the inner shells (up to the $4f$ shell) first couple via LS-coupling (shown in brackets) and then couple via jj-coupling with electrons in outer shells. Spectroscopic data is taken from Refs. [Ban05, Har10, Law10]. The natural linewidth of the 401-nm transition has been remeasured within the work of this thesis, see Appendix A.

Due to the large number of energy levels it is possible that an excited state decays with a large probability into a lower-lying state under the constriction of changing the parity of the electronic wave function. Dependent on the lifetime of the target state it decays further down and eventually reaches the ground state again. Intermediate states with much longer lifetimes compared to the lifetime of the initially excited state are also called metastable states and have to be considered in laser-cooling applications, see Ref. [McC06b]. In principle, a few metastable states can be actively depleted by using a repumper laser. To reduce large technical costs, a simple cooling strategy should avoid repumping many metastable states.

2.3.1. Laser-cooling transitions

Electric-dipole transitions are commonly used for laser cooling. In case of erbium, this restricts possible transitions from the ground state to an excited state with $J = 5$ or 7. A broad transition allows an efficient operation of the Zeeman slower (ZS), whereas a narrow transition is better suited for operating a magneto-optical trap (MOT) due to a lower achievable temperature of atoms, see Chapter 3 for the ZS and Chapter 6 for the MOT. To reduce the number of possible decay channels into metastable states, the excited state should not have a too high energy as the number of possible decay channels increases with increasing energy.

laser cooling parameter		transition	
		401 nm	583 nm
transition rate	Γ (s^{-1})	1.87×10^8	1.17×10^6
lifetime	τ (ns)	5.35	857
natural linewidth	$\Delta\nu$ (MHz)	29.7	0.19
saturation intensity	$I_{\rm S}$ (mW/cm^2)	60.3	0.13
Doppler temperature	$T_{\rm D}$ (μK)	714	4.6
Doppler velocity	$v_{\rm D}$ (mm/s)	267	21
recoil temperature	$T_{\rm r}$ (nK)	717	339
recoil velocity	$v_{\rm r}$ (mm/s)	6.0	4.1
	Refs.	[Har10] Appendix A	[Har10] [Law10]

Table 2.4.: Relevant laser-cooling parameters of the 401-nm and 583-nm transition in erbium used in the present work. See also Appendix A for a recent measurement of the natural linewidth of the 401-nm transition using a sample of cold atoms.

Early work on laser-cooling of erbium atoms have identified several suitable electric-dipole transitions from the ground state, with $J = 6$ and even parity, to an excited state, with $J = 7$ and odd parity, see Ref. [Ban05]. The linewidths of these transitions range from a large linewidth, of a few ten MHz, to a very small one, of only a few Hz. In Fig. 2.1(b) these laser-cooling transitions are highlighted and Table 2.3 gives a summary of their properties. For laser cooling in the current work only two transitions are relevant, which will be discussed in more detail below.

The first transition is at a wavelength of 401 nm (blue), where a $6s$ electron is excited into a $6p$ state and couples with the second $6s$ electron to the singlet state $^1{\rm P}_1$. This transition has a natural linewidth of 29.7 MHz and is comparable to the broad $|{\rm S}_{1/2}, F = 2\rangle \rightarrow |{\rm P}_{3/2}, F = 3\rangle$ transition of the D$_2$ line in alkali-metal atoms, which are commonly used in ultracold gas experiments. The large linewidth makes this transition very suitable for Zeeman slowing, transversal cooling, and imaging purposes. The second transition is at a wavelength of 583 nm (yellow), where the $6s$ and the excited $6p$ electron couple to the triplet state $^3{\rm P}_1$. It is an intercombination line and has a narrow linewidth of only 190 kHz, which implies several advantages for operating the MOT on this transition, see Chapter 6.

Table 2.4 gives many laser-cooling parameters of these two transitions. It consists of the transition rate Γ, the lifetime $\tau = \frac{1}{\Gamma}$, the natural linewidth $\Delta\nu = \frac{\Gamma}{2\pi}$, the saturation intensity $I_{\rm S} = \frac{\pi h c \Gamma}{3\lambda^3}$, the Doppler temperature $T_{\rm D} = \frac{\hbar\Gamma}{2k_{\rm B}}$, the Doppler velocity $v_{\rm D} = \sqrt{\frac{k_{\rm B}T_{\rm D}}{m}}$, the recoil temperature $T_{\rm r} = \frac{\hbar^2 k^2}{2mk_{\rm B}}$, and the recoil velocity $v_{\rm r} = \frac{\hbar k}{m}$. Here, h is Planck's constant with $\hbar = \frac{h}{2\pi}$, $k_{\rm B}$ the Boltzmann constant, m the atomic mass, and $k = \frac{2\pi}{\lambda}$ the wavenumber with λ the wavelength of the transition.
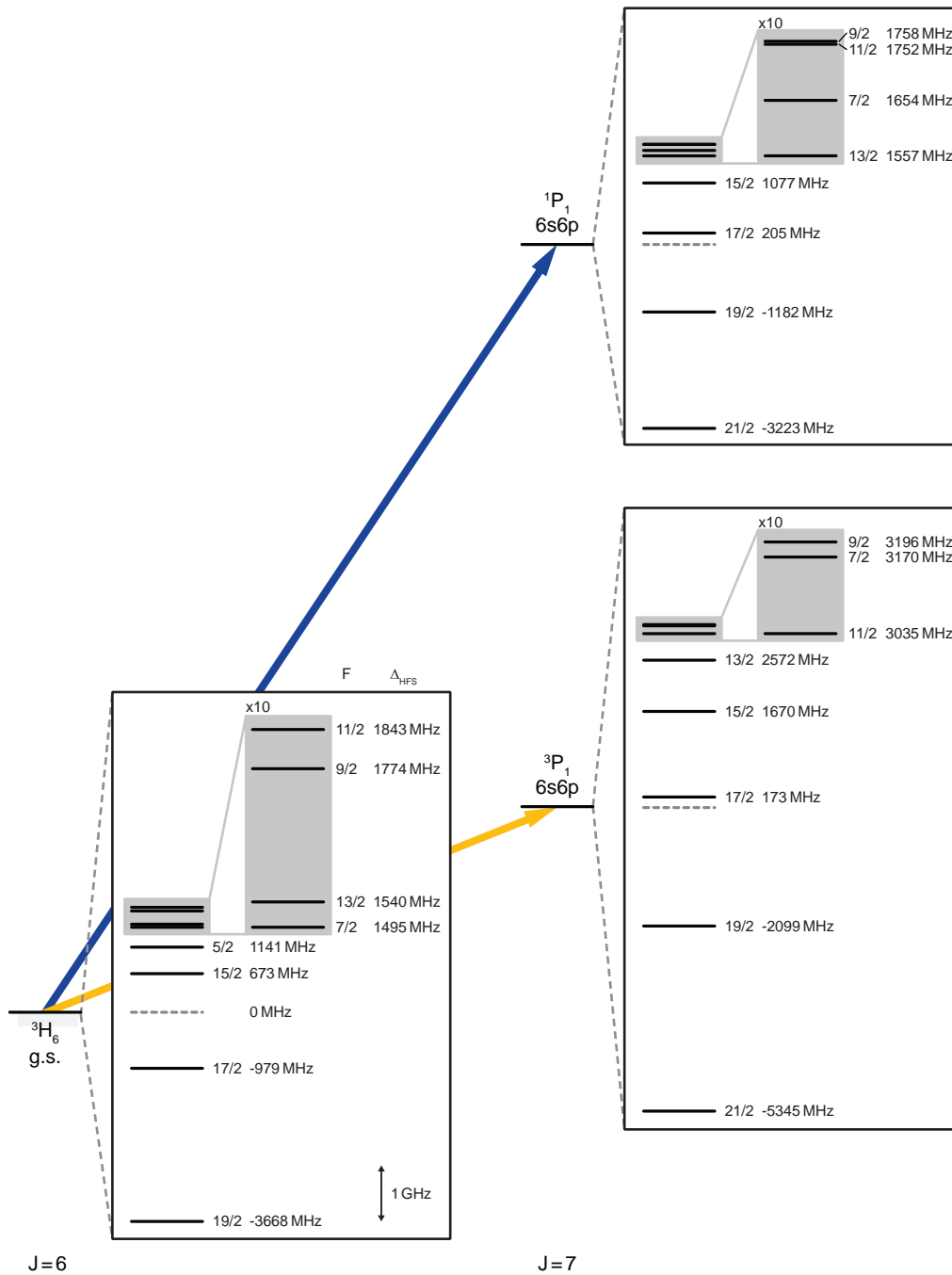
Figure 2.2.: Hyperfine structure of the ground state and two excited states. The frequency splitting, Δ_{HFS}, for each hyperfine state with total angular momentum quantum number F is given with respect to an assumed state with $I = 0$ depicted by a dashed line. Gray boxes indicate a magnification in frequency by a factor of ten.

level	A (MHz)	B (MHz)	Ref.
ground state	-120.487(1)	-4552.984(10)	[Chi83]
401 nm e.s.	-172.70(7)	-4457.2(29)	[Jin90]
583 nm e.s.	-100.1(3)	-3079(30)	Chap. 8

Table 2.5.: Magnetic dipole, A, and electric quadrupole, B, hyperfine constants in units of frequency for the ground state and two excited states (e.s.) used for laser cooling of the fermionic isotope ^{167}Er.

2.3.2. Hyperfine structure

Fermionic ^{167}Er has a rich hyperfine structure due to its nonzero nuclear spin of $I = 7/2$. This gives a total of eight hyperfine states with quantum numbers ranging from $F = J - 7/2$ to $J + 7/2$. The relevant A and B constants for the ground state and for the 401-nm and 583-nm excited states are presented in Table 2.5. Using these two coefficients the transition energy from the ground state to an excited state with hyperfine energies $E_g(F_g, J_g, I)$ and $E_e(F_e, J_e, I)$, respectively, can be calculated by

$$\hbar\omega_{F_e F_g} = \Delta_{167} + \hbar\omega_{166} + E_e(F_e, J_e, I) - E_g(F_g, J_g, I) \; , \qquad 2.2$$

with $\hbar\omega_{166}$ the transition energy of the most abundant isotope ^{166}Er. For ^{167}Er an isotope shift Δ_{167} with respect to ^{166}Er is specified by evaluating the 'center of gravity' of the full hyperfine structure, details are presented in Chapter 8. The hyperfine energies, E_i with $i = g, e$, are calculated via

$$E_i(F_i, J_i, I) = \frac{1}{2}A_i\,C_i + \frac{1}{2}B_i\frac{3C_i(C_i + 1) - 4I(I + 1)J_i(J_i + 1)}{2I(2I - 1)2J_i(2J_i - 1)} \qquad 2.3$$

$$C_i = F_i(F_i + 1) - J_i(J_i + 1) - I(I + 1) \; . \qquad 2.4$$

The resulting hyperfine structure of the ground state and the two excited states are shown in Fig. 2.2 for zero magnetic field.

2.3.3. Isotope shift

Due to a change in the charge distribution of the nucleus for different isotopes the transition energy changes linearly dependent on the atomic mass. This is known as isotope shift. The isotope shift between the two nearest bosonic erbium isotopes is about 820 MHz for the 401-nm transition and 980 MHz for the 583-nm transition, corresponding to a shift per atomic mass unit of 410 MHz and 490 MHz, respectively.

In Fig. 2.3 the isotope shift is shown for both transitions by plotting data taken from literature, see Refs. [Jin90, Con10]. The expected linear dependence of the isotope shift on the atomic mass can be observed for both transitions within the uncertainty of the reference values. Within the present work, the isotope shift was experimentally verified by using a hollow-cathode lamp as spectroscopy cell, see Chapter 8.
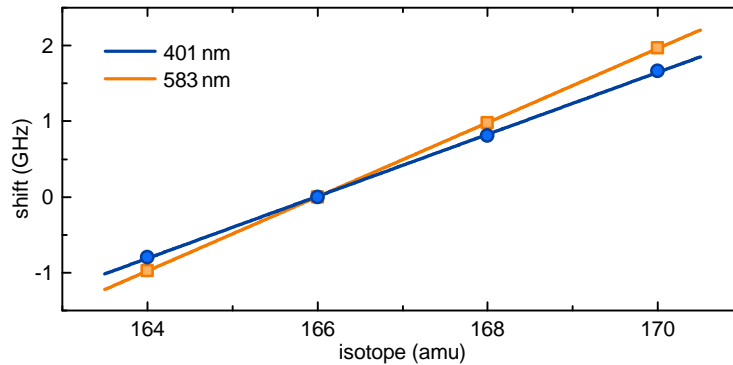
Figure 2.3.: Isotope shift for bosonic isotopes ^{164}Er, ^{168}Er, and ^{170}Er with respect to ^{166}Er. The isotope shift is plotted for the 401-nm transition in circles and for the 583-nm transition in squares. Lines are a linear fit to the data points. Data is taken from Refs. [Jin90, Con10].

2.4. Magnetic properties

Lanthanides are ferromagnetic metals but they have a Curie temperature, which is below room temperature. However, they easily form compounds with transition metals like iron, nickel or cobalt and are frequently used in alloys to create some of the strongest permanent magnets, known as rare-earth magnets[6]. Using these magnets it is possible to create permanent magnetic fields of up to 1.2 T. Rare-earth magnets can maintain such large magnetic fields because electrons in the $4f$ shells are strongly localized close to the atomic nucleus. This means that the $4f$ electrons tend to have no overlap with orbitals of neighboring atoms within the compound and lanthanide atoms form so-called *paramagnetic centers*. These paramagnetic centers prevent a reduction of the magnetic moment of the lanthanide atom, which would happen in case of overlapping orbitals[7]. This process explains the large magnetic field strength of rare-earth magnets, see Ref. [Jen91].

Several elements of the lanthanide series have a magnetic moment, which is amongst the largest magnetic moments of all elements. The coupling of electrons results in exceptionally large quantum numbers. Specifically, large values of the total orbital angular momentum L and total angular momentum J can be found, see Ref. [Mar78].

2.4.1. Magnetic moment

A full comparison of the atomic magnetic moment, μ, of all elements belonging to the lanthanide series is shown in Table 2.6. The magnetic moment is given in units of the Bohr magneton[8], μ_{B}. Elements with the largest magnetic moment are terbium and dysprosium with $\mu = 10\,\mu_{\mathrm{B}}$, followed by holmium with $8\,\mu_{\mathrm{B}}$, as well as europium and erbium with $7\,\mu_{\mathrm{B}}$.

---

[6]   Neodymium magnets and samarium-cobalt magnets are most commonly available.

[7]   A single hydrogen atom is paramagnetic, but in the form of molecular hydrogen as H_2 it has diamagnetic properties, because opposite electron spins pair up and the magnetic moment is lost.

[8]   The Bohr magneton is defined as $\mu_{\mathrm{B}} = \frac{e\hbar}{2m_e}$ with e the elementary charge and m_e the electron mass. It is convenient to use $\mu_{\mathrm{B}} \approx 1.39962$ MHz/G.

element	isotopes		ground	$4f^n$	$5d^m$			has many	is highly
symbol	bos.	ferm.	state	n	m	g_J	μ (μ_B)	isotopes	magnetic
La	1	0	$^2D_{3/2}$	0	1	0.80	1.20		
Ce	3	0	$^1G_4$	1	1	0.95	3.78		
Pr	1	0	$^4I_{9/2}$	3	0	0.73	3.29		
Nd	3	2	$^5I_4$	4	0	0.60	2.41	✓	
Pm	0	0	$^6H_{5/2}$	5	0	0.31	0.76		
Sa	4	0	$^7F_0$	6	0	0	0		
Eu	1	0	$^8S_{7/2}$	7	0	1.99	6.98		✓
Gd	3	2	$^9D_2$	7	1	2.65	5.30	✓	
Tb	1	0	$^6H_{15/2}$	9	0	1.33	9.94		✓
Dy	5	2	$^5I_8$	10	0	1.24	9.93	✓	✓
Ho	1	0	$^4I_{15/2}$	11	0	1.20	8.96		✓
Er	5	1	$^3H_6$	12	0	1.16	6.98	✓	✓
Tm	1	0	$^2F_{7/2}$	13	0	1.14	3.99		
Yb	5	2	$^1S_0$	14	0	0	0	✓	
Lu	1	0	$^2D_{3/2}$	14	1	0.80	1.20		

Table 2.6.: Number of different isotopes, ground-state electron configuration, and magnetic properties of all elements belonging to the group of lanthanides in comparison. The number of stable bosonic (bos.) and fermionic (ferm.) isotopes of each element is given. The electron configuration is written as the number of electrons in the $4f$ and $5d$ shells using the notation $[\text{Xe}]4f^n5d^m6s^2$. Two selection criteria are included as a guide for the reader. Having many isotopes requires that an element has more than three stable isotopes, of which at least one is fermionic. Being highly magnetic means that $\mu > 6\,\mu_B$. Elements of interest for novel laser-cooling experiments are written in bold. Data is taken from Ref. [Mar78].

This is in stark contrast to many other atomic species. Alkaline-earth metals and ytterbium are in a $^1S_0$ state and do not have any magnetic moment at all, whereas alkali-metal atoms have $\mu = 1\,\mu_B$ in the ground state due to their single electron in the s shell. Chromium, on the other hand, has a large magnetic moment of $6\,\mu_B$.

The component of the atomic magnetic moment along the direction of an external magnetic field[9] in z-direction can be calculated by

$$\mu = m_J g_J \mu_B \;, \qquad\qquad 2.5$$

with m_J the magnetic quantum number, i.e. the projection of the total angular momentum **J** along the direction of the magnetic field B. Values for m_J range from $-J$ to $+J$. Furthermore, g_J is the Landé g-factor, which is also known as the gyromagnetic ratio. It can be calculated and measured in the experiment by observing the Zeeman splitting of energy levels in presence of a magnetic field. The precise knowledge of g_J is very important for the experiment and its exact value for erbium will be derived in the following.

---

[9] The homogeneous magnetic field vector points in the vertical z-direction, unless otherwise noted, and gives the quantization axis of the system.

ground state	Landé value	LS correction	relativistic and diamagn. correction	calc. g_J	exp. g_J
$^3\mathrm{H}_6$	1.1670533	-0.0013345	-0.00192	1.1637985	1.163801(1)
Refs.	Eq. 2.6	[Con63]	[Jud61]	[Con63]	[Con63]

Table 2.7.: Landé value g_J for the ground state of bosonic erbium including corrections. The relative deviation between theoretical and experimental values is only 2×10^{-6}.

2.4.2. Landé g-factor

For the calculation of the Landé g-factor, g_J, two different cases have to be taken into account, which correspond to either LS-coupling or jj-coupling. In the case of simple LS-coupling, g_J can be calculated according to

$$g_J = 1 + (g_S - 1)\frac{J(J+1) - L(L+1) + S(S+1)}{2J(J+1)} \ . \qquad 2.6$$

with g_S the gyromagnetic ratio of the electron spin. It is given by

$$g_S = 2\left(1 + \frac{\alpha}{2\pi} + \dots\right) \approx 2.00232 \ , \qquad 2.7$$

with $\alpha \approx 1/137$ the fine-structure constant. In the case of lanthanides, several corrections have to be taken into account for an exact calculation of g_J. A theoretical derivation of all corrections is given in Ref. [Jud61]. The first correction is due to deviations from perfect LS-coupling. Second, a relativistic correction addresses the fact that high-orbit electrons of lanthanides posses a relativistic kinetic energy. The third correction is a diamagnetic correction and depends on the electron density at the core. All corrections and the experimental value for g_J of bosonic erbium in the ground state are summed up in Table 2.7, see also Refs. [Cab61, Con63]. The most precise experimental value for g_J of erbium is 1.163801(1) and thus the magnetic moment of bosonic erbium in the energetically lowest state with $m_J = -6$ is

$$\mu = m_J g_J \mu_{\mathrm{B}} = -6.982806(6)\,\mu_{\mathrm{B}} \approx -9.77\,\mathrm{MHz/G} \ . \qquad 2.8$$

In the case of jj-coupling, with a total electronic angular momentum quantum number J_1 and J_2 of the two coupled parts, the gyromagnetic ratio can be calculated by

$$
\begin{aligned}
g_J = {} & g_{J_1}\frac{J(J+1) + J_1(J_1+1) - J_2(J_2+1)}{2J(J+1)} \\
& + g_{J_2}\frac{J(J+1) + J_2(J_2+1) - J_1(J_1+1)}{2J(J+1)} \ .
\end{aligned}
\qquad 2.9
$$

Here, g_{J_1} and g_{J_2} are the Landé g-factors for each part according to Eq. 2.6. The excited states of the 401-nm and 583-nm transitions are $[\mathrm{Xe}]4f^{12}(^3\mathrm{H}_6)6s6p(^1\mathrm{P}_1)(6,1)_7$ and $[\mathrm{Xe}]4f^{12}(^3\mathrm{H}_6)6s6p(^3\mathrm{P}_1)(6,1)_7$, respectively. Including above mentioned corrections for LS-coupling for g_{J_1} and g_{J_2}, Eq. 2.9 gives a value of $g_J = 1.160$ for the excited state of the 401-nm transition and $g_J = 1.195$ for the excited state of the 583-nm transition, see Ref. [Mar78].
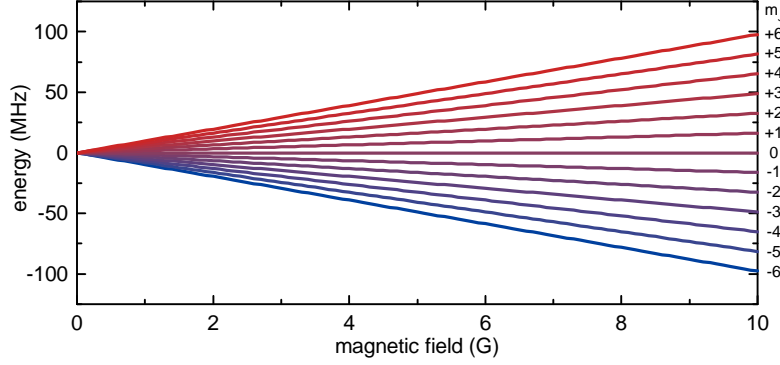
Figure 2.4.: Zeeman energy splitting of bosonic erbium in the ground state with $J = 6$ for all Zeeman substates. For this magnetic field range, the Zeeman splitting is linear (see text).

In case of fermionic ^{167}Er the total electronic angular momentum J couples with the nonzero nuclear spin $I = 7/2$ to form the total angular momentum $\mathbf{F} = \mathbf{J} + \mathbf{I}$. This splits energy levels into a hyperfine structure, see Sec. 2.3.2, and the Landé g-factor has to be calculated according to

$$g_F = g_J \frac{F(F+1) - I(I+1) + J(J+1)}{2F(F+1)} \ ,$$ 2.10

with g_J as given in Table 2.7 for the ground state. The magnetic moment is then given by $\mu = m_F g_F \mu_B$. Here, m_F is the projection of $\mathbf{F}$ on the quantization axis and ranges from $-F$ to $+F$. In the energetically lowest state, with $F = 19/2$ and $m_F = -19/2$, this results in $g_F = 0.735032$ and the magnetic moment of the fermionic ground state is $\mu = -6.982804 \, \mu_B$, which equals the magnetic moment of bosons in the ground state, with $J = 6$ and $m_J = -6$.

2.4.3. Zeeman splitting

In presence of an external magnetic field with field strength B each energy level with total angular momentum quantum number J splits in a total of $2J + 1$ Zeeman substates. Each state has a magnetic quantum number m_J. The Zeeman energy shift, ΔE_Z, with respect to the level at zero magnetic field is given by

$$\Delta E_Z(B) = m_J g_J \mu_B B \ .$$ 2.11

Figure 2.4 shows the Zeeman splitting of bosonic erbium from 0 to 10 G. The energetically lowest state has $m_J = -6$. For low magnetic fields the energy splitting between the two nearest m_J states is linear[10] and has a slope of 1.628879 MHz/G. In fact, the range of linear Zeeman splitting extends to magnetic fields higher than technically achievable in ultracold gas experiments, due to the unusually large spin-orbit coupling constant of erbium of 2242 cm^{-1}, see Ref. [Jud61]. Using radio-frequency fields one can drive transitions from $m_J \rightarrow m_J' = m_J \pm 1$, see Sec. 6.3. In the experiment measurements of the transition frequency from $m_J = -6$ to $m_J' = -5$ are used to calibrate magnetic fields.

---

[10] We have experimentally verified the linearity of the Zeeman splitting up to a magnetic field of 50 G within an uncertainty of 0.02 % using RF spectroscopy of the transition from $m_J = -6$ to $m_J' = -5$.
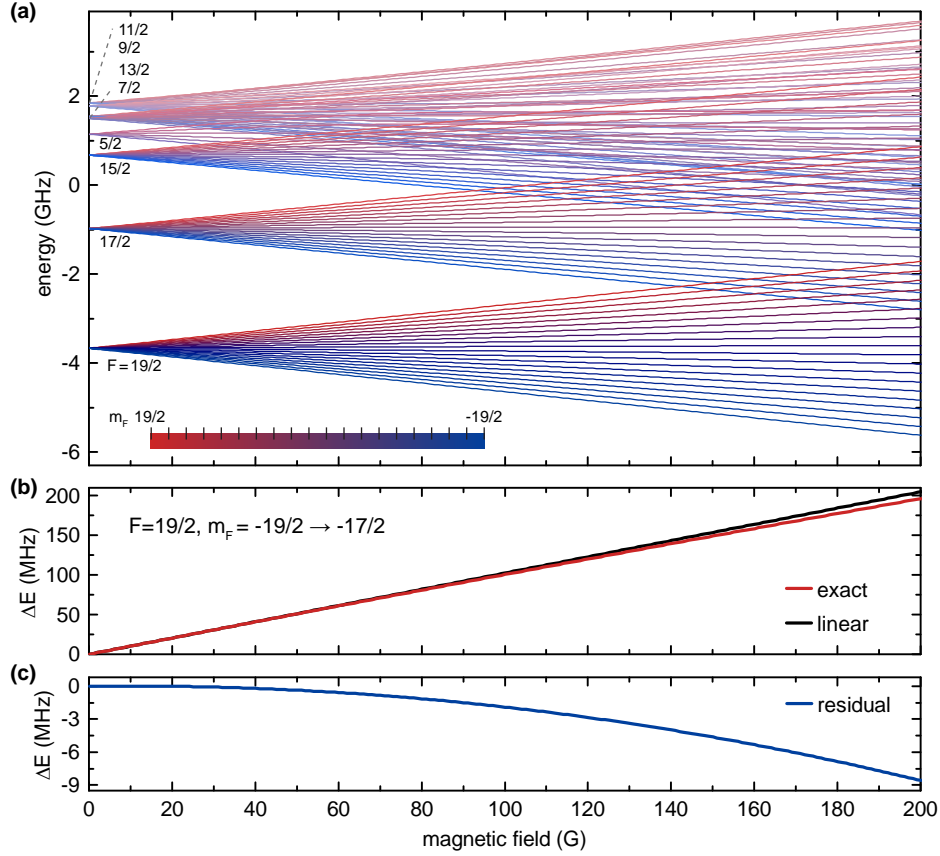
Figure 2.5.: Zeeman splitting of the hyperfine states of fermionic ^{167}Er in the ground state within an external magnetic field. (a) Hyperfine states with a total quantum number F split up in $2F + 1$ magnetic substates with quantum numbers m_F. (b) Energy difference, ΔE, between the two energetically-lowest substates with $m_F = -19/2$ and $-17/2$ derived from exact calculation (red) compared to the linear splitting according to Eq. 2.12 (black). The residual between the two curves is shown in (c).

2.4.4. Hyperfine Zeeman splitting

In case of fermionic erbium each hyperfine state F splits in the presence of a magnetic field B into a manifold of $2F + 1$ substates with quantum numbers m_F from $-F$ to $+F$, see Fig. 2.5. Consequently, the Zeeman energy of the hyperfine substates can be approximated by

$$\Delta E_Z(B) = m_F g_F \mu_B B \ , \qquad\qquad 2.12$$

for magnetic fields below 20 G. Here, g_F is the Landé g-factor from Eq. 2.10. For larger magnetic fields, a decoupling of J and I becomes apparent, which is also known as Paschen-Back effect, and the energy splitting deviates form the linear case. In this regime, the hyperfine energy levels have to be calculated via exact diagonalization of the atomic Hamiltonian, see Ref. [Smi65].

Figure 2.5(b) shows the deviation of the exact calculation from the linear splitting following Eq. 2.12. The residual between these two curves is separately shown in Fig. 2.5(c). The frequency difference of the transitions from $m_F = -19/2$ to $m'_F = -17/2$ and $m_F = -17/2$

to $m'_F = -15/2$ is 65.5 kHz at a magnetic field of 50 G. This separation would be large enough to prevent a population of the $m_F = -15/2$ state when driving a transition from $m_F = -19/2$ to $m'_F = -17/2$ in an ultracold atomic sample using a radio-frequency. This method allows for the preparation of a spin mixture of fermionic erbium atoms.

Chapter
3

Experimental setup

This chapter focuses on the experimental setup used to produce ultracold fermionic and bosonic quantum gases of erbium. The design phase of the experiment started in the second half of 2009. The vacuum chamber and laser system have been installed in 2010 and 2011. We obtained the first erbium magneto-optical trap in late 2011, the first Bose-Einstein condensate in early 2012, and the first degenerate Fermi gas in 2013.

In the following, the erbium apparatus will be described in detail. The chapter is structured in four sections: Section 3.1 reviews the key experimental requirements of the apparatus, Sec. 3.2 offers an overview of the vacuum chamber including a high-temperature effusion cell, Sec. 3.4 introduces the coil system for creating magnetic fields and Sec. 3.5 shows the laser system for laser cooling and trapping.

3.1. Experimental requirements

The erbium machine was designed from scratch with the aim of creating a quantum gas experiment. Several parts of the vacuum chamber were standard to ultracold atom experiments, while other parts required a more careful design. In designing the apparatus the following list of guidelines was taken into account:

- The pressure in the vacuum chamber should allow for a long lifetime of the atomic sample, which corresponds to a collision rate with the background gas below $0.01\,\mathrm{s}^{-1}$. This requires a pressure below $10^{-10}\,\mathrm{mbar}$, i.e. within the ultra-high vacuum regime.

- Because of the high melting point of erbium a high-temperature oven has to be used for evaporating the source material at temperatures of up to $1500\,^{\circ}\mathrm{C}$.

- The amount of source material in the oven should allow for an oven lifetime of more than a year.

- The magneto-optical trap (MOT) should operate on the narrow transition (with wavelength $\lambda = 583\,\mathrm{nm}$ and linewidth $\Delta\nu = 190\,\mathrm{kHz}$) to guarantee temperatures low enough for direct loading into an optical dipole trap.

23

- Hot atoms from the oven have to be slowed to velocities below the capture velocity of the narrow-line MOT. The usage of a Zeeman slower (ZS), operating on a strong transition (with $\lambda = 401\,\text{nm}$ and $\Delta\nu = 30\,\text{MHz}$), ensures a slow atom beam with a high flux at the center of the main chamber.

- For future experiments with a Er-Li mixture, a lithium oven should be attachable to the vacuum chamber, allowing for evaporating lithium at a temperature of up to $500\,^\circ\text{C}$. The two atom beams should be combined in order to require only one ZS.

- The ZS should be usable for both species simultaneously. In case of erbium the ZS should capture atoms with velocities as high as possible to maximize the atomic flux and increase the lifetime of the source material in the oven. This is less critical in case of lithium.

- It should be possible to create homogeneous magnetic fields up to $400\,\text{G}$ for Feshbach spectroscopy[1] and gradient fields above $50\,\text{G/cm}$ for MOT operation and Stern-Gerlach experiments. Additionally, coils should be installed to allow for compensation of external magnetic fields, active reduction of the magnetic field noise, and creation of a small homogeneous polarizing magnetic field in any spatial direction.

- The stability of the experiment should be as high as possible in order to be able to carry out measurements over several days/weeks without significant noise. This includes short-term stability, e.g. by reducing vibrations as well as long-term stability by stable environmental conditions, like temperature, humidity, and external magnetic fields.

During the construction of the erbium machine, we could benefit from various technical developments in other experimental setups in Innsbruck, like the Sr or the FeLiKx experiment, see Refs. [Ste13] and [Wil09], respectively.

3.2. Vacuum chamber design

Figure 3.1 gives an overview of the main parts of the vacuum apparatus. The apparatus can be divided into a high vacuum (HV) section and an ultra-high vacuum (UHV) section. Each individual part of the vacuum chamber will be discussed in the following sections, see Sec. 3.2.1 for the HV and Sec. 3.2.2 for the UHV section.

- **the high vacuum section includes:**

  - the high-temperature effusion cell for erbium
  - the transversal cooling section
  - the low-temperature oven for lithium

---

[1] Nothing was known about the Feshbach spectrum of erbium or other lanthanides at the beginning of the experiment.

  – the atom beam shutter

  – a first pumping stage

- **the ultra-high vacuum section includes:**

  – the Zeeman slower

  – the main chamber

  – a second pumping stage

  – the Zeeman slower mirror

A pressure of about 4×10^{-9} mbar in the HV section and 1×10^{-11} mbar in the UHV section has to be maintained for the experiment. A differential pumping tube connects the two sections and provides a pressure gradient of up to three orders of magnitude. The sections can be disconnected from each other by an all-metal gate valve. This allows for refilling the oven without breaking the vacuum in the UHV section.

The center of the vacuum chamber is situated 200 mm above the surface of an optical table, making the use of two layers of optical setup with a beam height of 75 mm each possible. Solid aluminum bread boards with a thickness of 25 mm support the upper optical layer. Stainless-steel supporting structures are placed on various critical points of the vacuum chamber to suppress mechanical vibrations to a minimum. A welded bellow is introduced at the gate valve to reduce mechanical stress while baking out the main chamber, which leads to a thermal expansion of the vacuum chamber. Furthermore, it allows for a rough alignment of the two sections with respect to each other. This is crucial to point the atom beam into the center of the main chamber.

3.2.1. High vacuum section

Figure 3.2 shows a section view of the main part of the HV section. It consists of the high-temperature erbium oven and a transversal cooling stage, connected by a port aligner. The latter allows for aligning the angle between the axis of the effusion cell and the main axis of the vacuum chamber. It is primarily used to compensate a slight downward bending of the inner parts of the high-temperature oven, which was observed within a few years of operation at high temperatures. For this, the port aligner is oriented such that a single screw changes the angle of the oven axis with respect to the horizontal plane. Each subsection of the high vacuum section will be discussed in more detail in the following.

High-temperature oven   For heating erbium to the required temperatures, a commercially available high-temperature oven is used[2]. The oven consists of two separately controllable sections, the so-called effusion cell and the hot lip that are heated by two independent heating filaments. In the former, solid pieces of erbium (about 10 g) are evaporated and in the latter, a collimated atom beam is formed using a set of apertures. The two heating filaments make

---

[2]   model DFC-40-10-WK-2B, from CreaTec Fischer & Co. GmbH
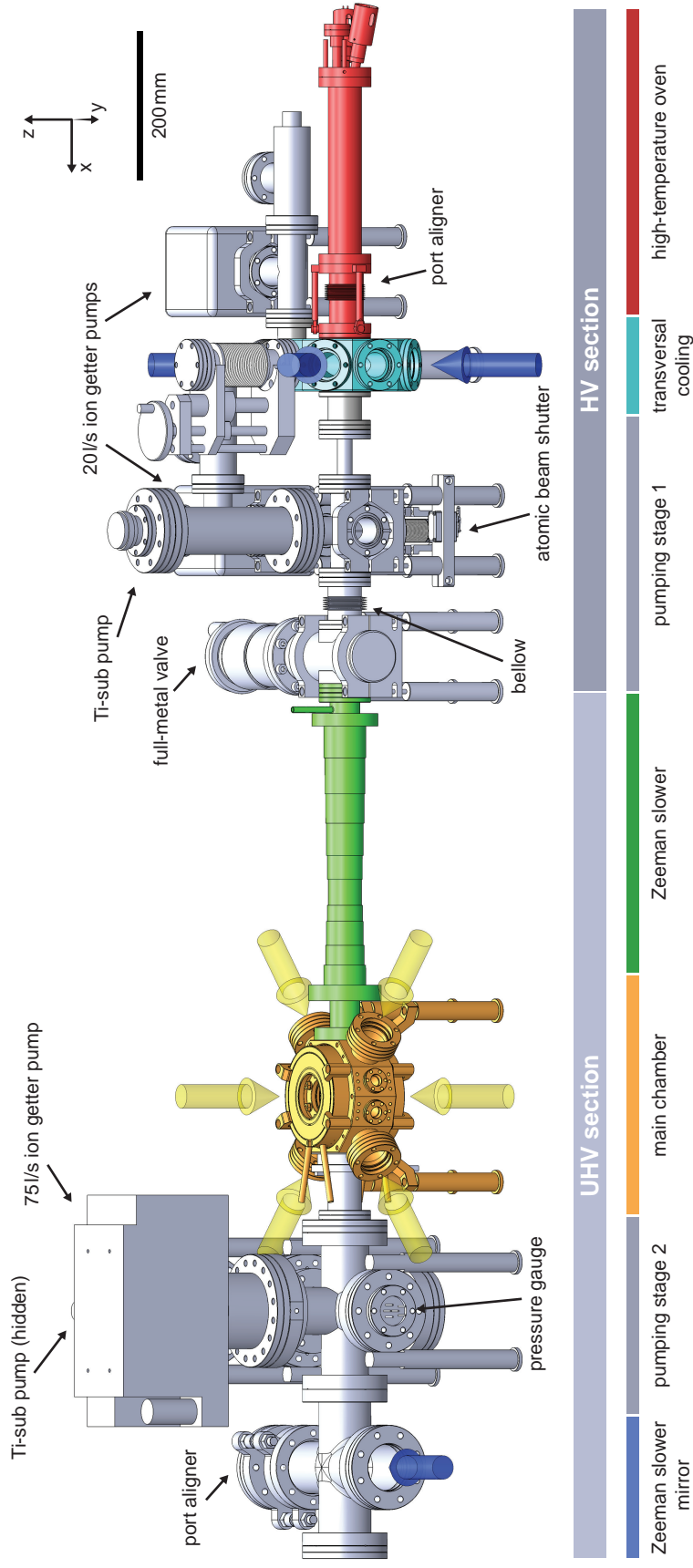
Figure 3.1.: Full model of the vacuum chamber. Individual sections are highlighted in different colors. Laser beams for transversal cooling and Zeeman slowing as well as MOT operation are shown by blue and yellow arrows, respectively. The oven chamber is situated in the high vacuum (HV) section and the main chamber in the ultra-high vacuum (UHV) section. In case of refilling the high-temperature oven, the two sections can be separated from each other by a full-metal gate valve. A differential pumping tube in the center of the Zeeman slower (green) maintains a pressure difference of up to three orders of magnitude. Sufficient pumping is achieved by two 20 l/s (HV section) and one 75 l/s (UHV section) ion getter pumps as well as by one titanium sublimation pump in each section.
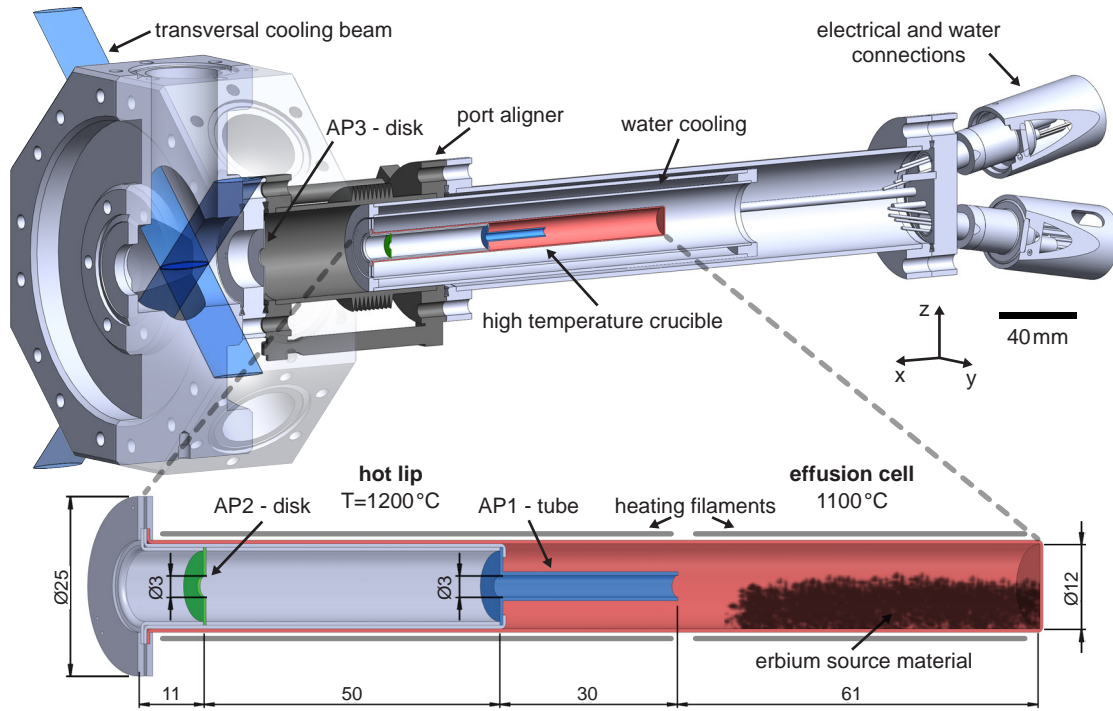
Figure 3.2.: High-temperature oven and transversal cooling section. For a better view the model is shown in a section view. The oven crucible (red) contains pieces of erbium and is shown in the inset with dimensions in mm. Two apertures (AP1 and AP2), the first in shape of a tube (blue) and the second like a disk (green), create a collimated atom beam directed at the center of the main chamber. To prevent clogging of the apertures they are heated to a higher temperature than the effusion cell. A third aperture (AP3) with an inner diameter of 8 mm basically blocks excessive material exiting the oven and keeps the transversal cooling section clean.

it possible to set the temperature of the aperture setup to a higher value compared to that of the effusion cell. Typical operating temperatures are as high as 1100 °C for the effusion cell and 1200 °C for the hot lip, which results in an atom flux density of $10^{14}\,\mathrm{s}^{-1}\mathrm{sr}^{-1}$ at the position of the transversal cooling section, see Ref. [Sch11].

Effusion cell   The effusion cell consists of a tantalum crucible, see inset of Fig. 3.2. Tantalum is used due to its high temperature resistivity, inertness to chemical reactions, and suppression of forming low-melting alloys with erbium[3]. It is filled with small pieces of naturally occurring erbium[4]. A filling volume of $7\,\mathrm{cm}^3$ must not be exceeded to prevent damage of the effusion cell due to thermal expansion of the source material. More details about the oven filling procedure can be found in Appendix B.

Aperture setup   A set of three apertures creates a collimated atom beam, two of which are shown in the inset of Fig. 3.2 (AP1-AP2) and the third aperture (AP3) is located between the high-temperature oven and the transversal cooling section. Like the oven crucible all

---

[3] Any low-melting alloys will destroy the high-temperature oven as they will easily leak out of the crucible in horizontal orientation and short-circuit the heating filaments.

[4] 10 g of erbium distilled dentritic, purchased from Alfa Aesar

apertures are made out of tantalum. The first two apertures are mounted as an inset directly into the crucible. Tantalum cylinders are used as spacers, which are held in place by twisted tantalum wires at the front of the crucible setup. More details about the full characterization of the atom beam and a test of different aperture geometries for optimum collimation of the atom beam can be found in Ref. [Sch11].

2D transversal cooling section   This section allows for laser cooling the atomic beam in both transversal directions, see left-hand side of Fig. 3.2 and Sec. 3.3 for more details. The homemade stainless-steel chamber has an octagonal shape and provides optical access in two orthogonal directions transversally to the atom beam. On top of the transversal cooling chamber an all-metal aluminum mirror is mounted on a linear translation stage, which can be lowered to check the alignment of the Zeeman slower laser beam.

Intermediate pumping stage   An intermediate pumping stage is connected to the transversal cooling section to pump off the volume between the high-temperature oven and the optional lithium oven. Installing the lithium oven setup would strongly reduce the pumping efficiency, therefor this intermediate pumping stage is necessary. It consists of a $20\,\mathrm{l/s}$ ion getter pump[5], a hot-filament ionization gauge[6] for pressure readings, and an angled valve for connecting a pumping station.

Lithium oven   After the transversal cooling section for erbium, it is possible to attach a second oven. It is intended to evaporate lithium, which has a low melting point of $181\,°\mathrm{C}$. To achieve an optimized overlap with the atom beam coming from the high-temperature erbium oven, an oven with a design similar to Ref. [Wil09] is intended to be used. Here, small micro tubes with an inner diameter of $200\,\mu\mathrm{m}$ create a collimated atom beam. The volume of the oven is divided into three sections, separated by thin walls. One section contains the micro tubes, whereas the other two sections are empty and erbium atoms can pass through. This will create a mixed erbium and lithium atom beam. Currently this oven is not installed but replaced by a dummy tube.

Pumping stage 1   A $20\,\mathrm{l/s}$ ion getter pump[5] and a titanium sublimation pump[7] are mounted to the vacuum chamber to provide pressures below $1 \times 10^{-9}\,\mathrm{mbar}$. Furthermore, a hot-filament pressure gauge[6] is connected for pressure monitoring and an angled valve for initial pumping. Due to the large gettering properties of erbium, see Ref. [Mül72], it is not necessary to bake the high vacuum section in order to reach suitable pressures. This makes a refilling of the high-temperature oven very convenient and can be achieved within a single week of pumping, see Appendix B.

---

[5]   VacIon Plus 20 Ion StarCell, from Agilent Technologies
[6]   UHV-24 dual filament gauge, from Agilent Technologies
[7]   TSP Filament Cartridge CF40, from Agilent Technologies

Atom beam shutter   An atom beam shutter is mounted on the lower flange of the pumping stage. After loading the MOT is finished the shutter blocks the atom beam and prevents erbium atoms from entering the UHV section. It consists of a stainless-steel disk with 20 mm diameter and 2 mm thickness, mounted on a homemade wobble stick. The disk can be operated by a servo motor from outside the vacuum utilizing a welded bellow.

Full-metal gate valve   A full-metal gate valve[8] separates the HV section from the UHV section in case of having to break the vacuum in one of the sections.

3.2.2. Ultra-high vacuum section

As is known, collisions with the background gas limit the lifetime of the trapped atomic gas. Only at an ultra-low pressure the lifetime is long enough for ultracold gas experiments. At a typical pressure of 1×10^{-11} mbar in the UHV section the measured lifetime of the trapped atomic gas is longer than 40 s. This lifetime is much longer than the duration of the experimental cycle. Thus collisions with the background gas can be neglected for the experiment. The UHV section consists of four subsections including the main experimental chamber.

Zeeman slower tube   The ZS vacuum tube has a total length of 460 mm and an inner diameter of 24 mm. It contains a single stainless-steel differential pumping tube with a length of 300 mm and a diameter of 8 mm. The differential pumping tube is welded on a CF40 flange, mounted between the gate valve and the ZS tube. Any heating of the vacuum chamber due to an excessive power dissipation of the ZS magnetic field coils would lead to an increase of the pressure in the main chamber. To prevent this, a second tube with 40 mm outer diameter encloses the ZS tube, which creates a 5 mm thick cylindrical spacing along the whole ZS, allowing for water-cooling. The ZS coils are directly mounted onto the outer tube for most efficient cooling. The principle of operation and the design of the ZS will be discussed in Sec. 3.3 in more detail.

Main chamber   Atoms are trapped, cooled, and manipulated in the main chamber. Figure 3.3 shows the main vacuum chamber in a section view. It provides optical access for loading atoms into the MOT, employing various optical dipole traps and optical lattices, and imaging the atoms using CCD cameras. It is an in-house-manufactured stainless-steel[9] chamber with six different optical axes. As the slow atom beam is strongly divergent when it leaves the ZS, the distance from the end of the ZS to the center of the main chamber has to be minimized for a high MOT loading efficiency. This distance is about 120 mm in the current chamber and it was one of the major geometrical restrictions for the design. Two sets of coils are mounted on top and below the main chamber for creating magnetic fields, which are symmetric around the z-axis, see Sec. 3.4. The two sets of coils are mounted in water-cooled copper casings. The height of each casing is 35 mm with an outer diameter of 136 mm.

---

[8]   All-metal gate valve, size CF40, Series 481, from VAT Vacuumvalves AG
[9]   stainless steel code 316LN (after AISI) or 1.4429 (after ESU)
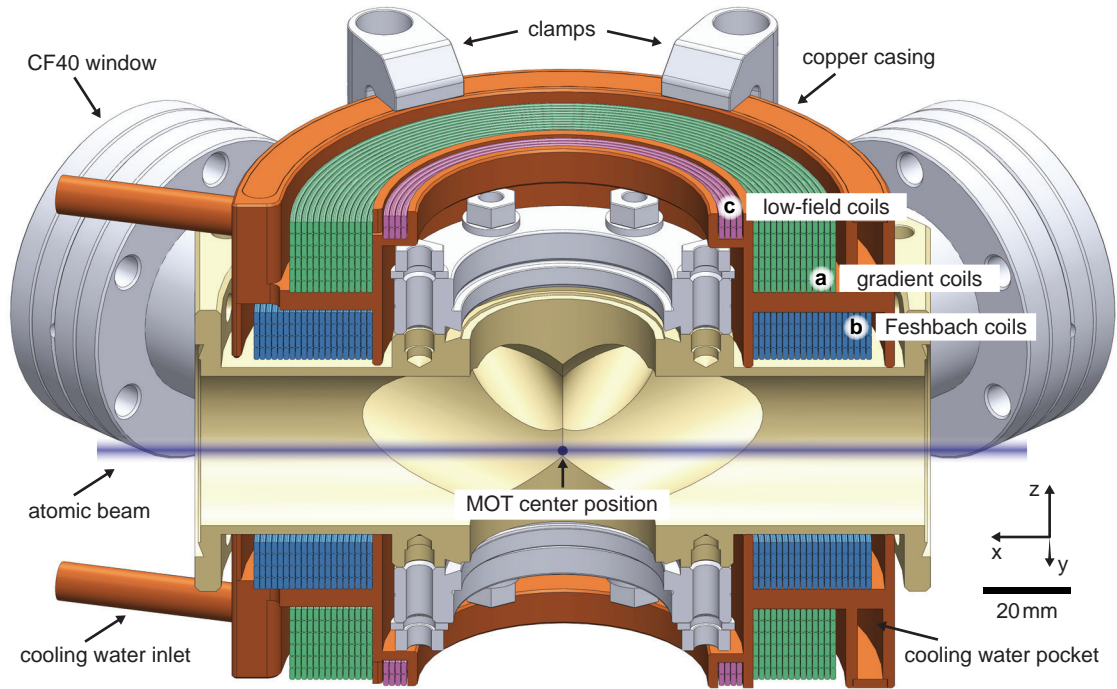
Figure 3.3.: Main vacuum chamber and coil setup shown in a section view. The stainless-steel vacuum chamber (yellow) has a total of ten anti-reflection coated windows for optical access. Additionally, two CF40 flanges are used to connect the Zeeman slower (right side) and the UHV pumping stage (left side), not shown here. The vertical dimension of the chamber between the upper and lower coil casing is only 38 mm. The bores for the atom beam and MOT beams have a diameter of 34 mm. Both, upper and lower coil sets are identically built and consist of three coils each. (a) For operating the MOT, two coils (green) produce a magnetic field gradient in all three spatial directions by a quadrupole field. (b) Two coils in Helmholtz configuration (blue) give a homogeneous magnetic field for Feshbach spectroscopy. (c) A smaller set of coils (purple) is used to create stable homogeneous magnetic fields below 4 G. The coils are held in place by a copper casing (brown), which enables efficient cooling by water flowing through a pocket on the outer side of the casing. For sufficient heat transport the coils are moulded into the casing with a thermally conductive resin.
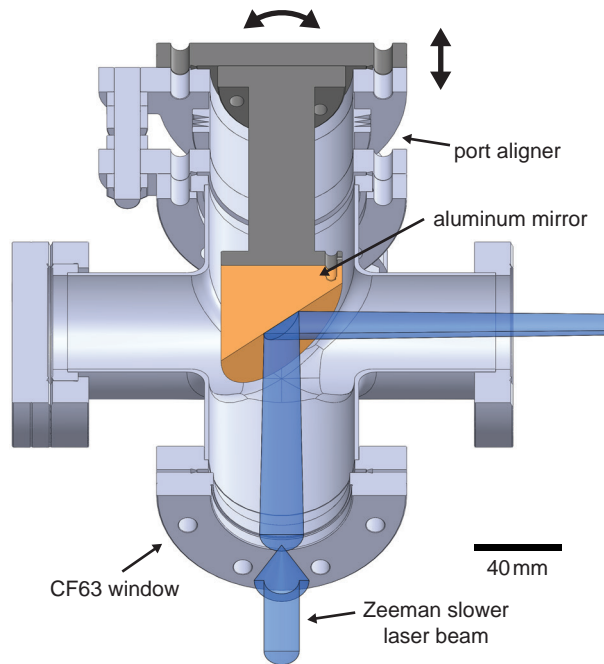
Figure 3.4.: Zeeman slower mirror setup in a section view. The ZS light (blue) enters the vacuum chamber through a CF63 window. It is then reflected by a solid aluminum mirror (orange) and counter propagates to the atom beam through the whole vacuum apparatus. The usage of an aluminum mirror prevents coating of the vacuum window by atoms not being slowed by the ZS and not captured in the MOT. The mirror is mounted on a port aligner that can be moved and tilted for optical alignment.

Pumping stage 2   The UHV pumping stage consists of a 75 l/s ion getter pump[10], a pressure gauge[11], an angled valve, and a titanium sublimation pump[7]. For an optimized pumping speed the titanium sublimation pump is contained within a large CF100 vacuum tube.

Zeeman slower mirror   In many experimental setups the laser light for the Zeeman slower is brought collinear to the atom beam into the vacuum chamber via a vacuum window. In the erbium experiment this would result in an irreversible coating of the window with erbium atoms coming from the atom beam. Compared to alkali and alkali-earth metals, erbium can not be heated off the window due to its high melting point. The transmittance of such a coated window would decrease significantly within a short period of time. A solution for this problem is to use a mirror inside the vacuum and let the laser beam enter the chamber perpendicular to the atom beam. The mirror will get coated by a thin layer of erbium over time but its reflectivity will not suffer much from the coating. Therefore, a solid aluminum mirror[12] is mounted on a port aligner at the end of the vacuum chamber, see Fig. 3.4. We estimated the reduction of the mirror's reflectivity by coating with a thin layer of erbium onto a test mirror to be less than 1.3 %.

---

[10] VacIon Plus 75 Ion StarCell, from Agilent Technologies
[11] UHV-24p dual filament, from Agilent Technologies
[12] diamond fly-cut, optical-grade aluminum mirror, AlMgSi1, manufactured by Kugler GmbH

3.3. Slow atom beam with high flux

The preparation of a slow atom beam with high flux in the main chamber is important for efficient MOT loading. This will result in a larger number of atoms in the MOT, which is advantageous for further experiments. In the erbium experiment an estimated flux of slow atoms[13] of about $4 \times 10^8 \, \mathrm{s}^{-1}$ at the MOT position is achieved by a combination of a two-dimensional transversal cooling (TC) stage and a Zeeman slower (ZS).

The maximum longitudinal velocity of the erbium atom beam exiting the high-temperature oven is about $500 \, \mathrm{m/s}$, see Sec. B.2 in the appendix. The ZS has to be well designed and optimized to slow down atoms close to the MOT capture velocity. The capture velocity is only $5.6 \, \mathrm{m/s}$ because of the narrow-line character of the 583-nm transition, see Sec. 6.1.1. The TC reduces the transversal velocity of the atom beam immediately after leaving the high-temperature oven. Both, ZS and TC, work best on a broad atomic transition, which has a short lifetime of the excited state. This enables a sufficiently large number of scattered photons within the time it takes for the atom to fly through the TC section or the ZS tube. A suitable broad transition in erbium is the blue transition at a wavelength of 401 nm with a linewidth of $29.7 \, \mathrm{MHz}$ corresponding to a lifetime of $5.4 \, \mathrm{ns}$, see Sec. 2.3.

3.3.1. Transversal cooling

After atoms exit the oven they are cooled in the transversal directions by two elliptical laser beams. The ellipticity increases the overlap between the laser beam and the atom beam and maximizes the amount of scattered light. Both laser beams are retro-reflected to form a two-dimensional optical molasses. Each beam has a total power of about $40 \, \mathrm{mW}$ and the light is generated by a slave diode laser, seeded by the blue master laser, see Sec. 3.5.1. The light has a detuning of $-10 \, \mathrm{MHz}$ to the atomic resonance, which was determined by maximizing the MOT loading rate. Under optimal conditions, the TC increases the MOT loading rate by a factor of up to three to four.

3.3.2. Zeeman slower

The ZS reduces the longitudinal velocity of single atoms by exerting a strong light force in opposite direction of the atom's direction of propagation. This is achieved by shining a laser beam in collinear and counter-propagating direction to the atom beam. To keep atoms resonant with the light during the full slowing process one exploits the Zeeman shift of atomic energy levels in a magnetic field. The ZS efficiently reduces the atom's longitudinal velocity from a maximum velocity, so-called *capture velocity*, v_c^{ZS}, down to a final velocity v_f. The capture velocity is given by

$$v_c^{\mathrm{ZS}} = \sqrt{2 a_{\mathrm{ZS}} x_0} \, , \qquad\qquad 3.1$$

---

[13] Here, slow means a velocity close to the capture velocity of the MOT as depicted in Sec. 3.3.3.
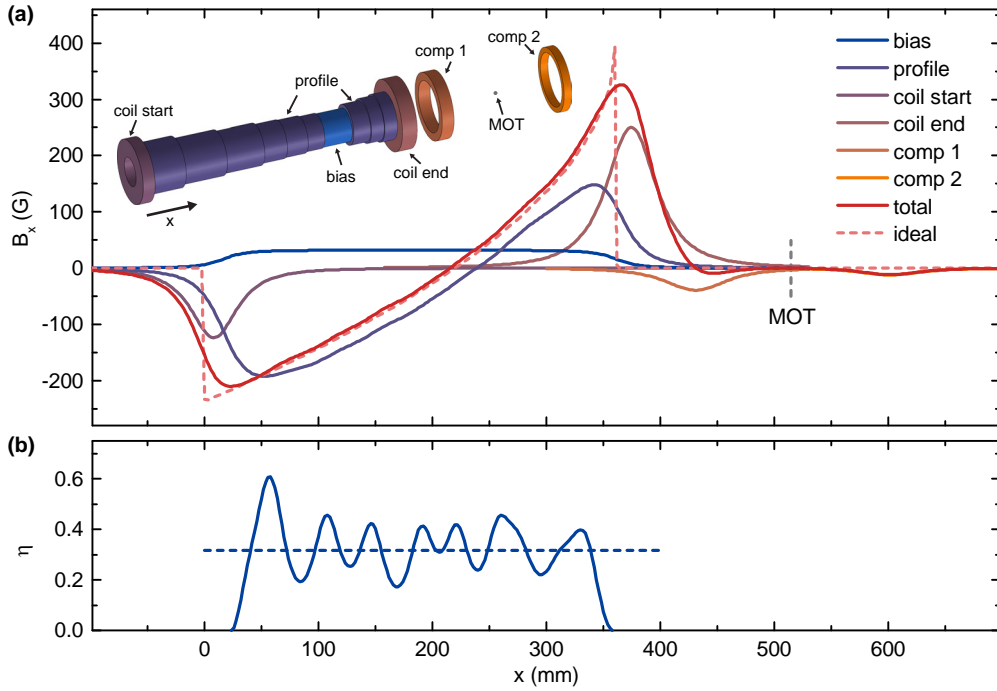
Figure 3.5.: Increasing-field spin-flip Zeeman slower for erbium and lithium. (a) Six separately controllable coils (inset) are used to create the necessary magnetic field. Utilizing a bias coil (blue) for creating a homogeneous magnetic field the capture velocity of the ZS can be tuned (see text). The resulting total magnetic field (red) is calculated and approximates the ideal field (light-red dashed) well except at the beginning and the end of the ZS. Two compensation coils before and after the main chamber (comp 1 and comp 2) are used to reduce the residual magnetic field and its gradient to zero at the position of the MOT (gray dashed). (b) The resulting value for η calculated for erbium (solid line) using the total magnetic field from (a). Its mean value (dashed line) is as large as 0.34.

where a_{ZS} is the actual deceleration acting on the atoms within the ZS and x_0 is the total length of the ZS. The capture velocity predominantly determines the flux of slow atoms leaving the ZS as it gives the upper velocity bound in the Maxwell-Boltzmann distribution of the atom beam coming from the high-temperature oven. The thermal velocity distribution is shown in Fig. B.3 in Appendix B.

The ZS in the erbium experiment is an increasing-field spin-flip ZS with a length of $x_0 = 360\,\mathrm{mm}$, see Fig. 3.5. It is designed for a v_c^{ZS} for erbium of about $400\,\mathrm{m/s}$, which is close to the maximum of the thermal velocity distribution. By using a spin-flip ZS it is possible to have a large capture velocity with moderately low absolute values of the magnetic field. Currently, the ZS is operated with $v_c^{\mathrm{ZS}} = 325\,\mathrm{m/s}$, which is limited by the available light intensity from the injection-locked laser, see Sec. 3.5.1. Furthermore, the ZS can be simultaneously used to slow lithium as a second species. The general principle of operation is similar to existing ZSs for many other elements, see Refs. [Lis99, Kro02, Har03, Gün04, Wil09]. A major difference of the ZS in the erbium experiment to other setups is the ability of changing its capture velocity in a wide range by the utilization of an additional bias field coil. With such a coil setup the slowing efficiency can be easily optimized to its maximum, see Sec. 3.3.3. A consequence of changing the bias field is that the position of the zero-crossing of the magnetic field moves along the axis of the ZS.

In the following, we will summarize the general working principle of the ZS before we discuss the coil setup and the operational parameters of the erbium ZS. For a maximum slowing efficiency atoms with transition frequency ω_0 have to be in resonance with the laser light of frequency ω over the full extension of the ZS. During the slowing process the Doppler shift of the atom changes as the atom's velocity, $v(x)$, changes as a function of position x. The Doppler shift is compensated by a Zeeman shift induced by the external magnetic field $B(x)$. Thus the resonance condition equals

$$\omega_0 - kv(x) + \frac{\mu' B(x)}{\hbar} = \omega \ . \tag{3.2}$$

Here, μ' is the difference of the magnetic moment between the ground and excited state given by $\mu' = (g_e m_e - g_g m_g)\mu_B$ with magnetic quantum numbers m_g, m_e and Landé g-factors g_g, g_e, see Sec. 2.4.3. For the blue transition $\mu' = 1.13719\,\mu_B$ and $k = \frac{2\pi}{\lambda}$ is the wavenumber of the transition with wavelength λ. The maximum possible deceleration, a_{max}, which is given by the light force acting on the atom, depends on the transition parameters as

$$a_{max} = \frac{\hbar k \Gamma}{2m} \ , \tag{3.3}$$

with Γ the natural linewidth of the transition and m the atomic mass. For erbium this gives $a_{max} = 6.6 \times 10^5\,\text{m/s}^2$. A constant deceleration of atoms in the ZS leads to a square-root dependence of the velocity on the position along the ZS by

$$v(x) = v_c^{ZS}\sqrt{1 - \frac{x}{x_0}} \ . \tag{3.4}$$

The necessary ZS magnetic field can therefore be written as

$$B(x) = B_b + B_0\sqrt{1 - \frac{x}{x_0}} \ . \tag{3.5}$$

Here, B_b is a magnetic bias field, which can be understood as a shift of the square-root-like magnetic field profile, and B_0 is the overall height of the profile. Utilizing Eq. 3.2 these two parameters can be calculated by

$$B_b = \frac{\hbar\delta}{\mu'} \quad \text{and} \quad B_0 = \frac{\hbar k v_c^{ZS}}{\mu'} \ , \tag{3.6}$$

where $\delta = \omega - \omega_0$ is the detuning of the ZS laser light. The required total length of the ZS to slow atoms from v_c^{ZS} to a final velocity, v_f, is simply given by

$$x_0 = \frac{(v_c^{ZS} - v_f)^2}{2a_{ZS}} \ . \tag{3.7}$$

The number of scattering events needed for the slowing process can be calculated by

$$N_{sc} = \frac{m(v_i - v_f)}{\hbar k} \ , \tag{3.8}$$

with v_i the initial velocity, which can be in general smaller than v_c^{ZS}. This results for the ZS of erbium in $N_{sc} = 5.4 \times 10^4$ for an assumed $v_f = 5\,\text{m/s}$ and $v_i = v_c^{ZS} = 325\,\text{m/s}$. Atoms which enter the slower with $v_i < v_c^{ZS}$ need a smaller number of scattering events.

According to Eq. 3.3 one wants to have large values of Γ and k, i.e. small values of λ, for a large maximum deceleration. The broad $4f^{12}\,6s^2\,{}^1\mathrm{S}_1$ - $4f^{12}\,6s6p\,{}^1\mathrm{P}_1$ transition fulfills both requirements with $\lambda = 401\,\mathrm{nm}$ and $\Gamma = 2\pi \times 29.7\,\mathrm{MHz}$, see Sec. 2.3. At a first glance, the large number of metastable states in which the excited $4f^{12}\,6s6p\,{}^1\mathrm{P}_1$ state can decay into, see Fig. 2.1, might suggest that this transition is not suitable for slowing at all. However, a careful analysis of the branching ratio of the excited state shows different. The value for the branching probability into metastable states is 7.7×10^{-6}, see Ref. [McC06b]. Comparing this with the required number of scattering events from Eq. 3.8 shows that on average 1/3 of the atoms in this velocity class decays into metastable states and can not be loaded into the MOT. For lower initial velocities the loss fraction decreases, e.g. for $v_i = 150\,\mathrm{m/s}$ the loss fraction is only 18 %. Although this loss fraction seems large it can be easily overcome by slightly increasing the oven temperature to have a sufficiently large flux of slow atoms for loading the MOT[14].

From the right-hand-side expression in Eq. 3.6 one can easily see that a larger B_0 increases the capture velocity of the ZS and by this also the atom flux. As mentioned earlier, the main advantage of a spin-flip ZS is the ability to achieve large values of B_0 with a moderate set of coils as the absolute magnetic fields on both ends of the ZS can be smaller than compared to a non spin-flip ZS. This is achieved by shifting the magnetic field by B_b, see ideal magnetic field in Fig. 3.5(a). To minimize the light force of the ZS laser beam on atoms which are already loaded into the narrow-line MOT the detuning of the ZS light should be as large as possible. Following Eq. 3.6, the detuning δ also fixes the value of B_b. In the experiment, a detuning of about $-530\,\mathrm{MHz}$ corresponding to $\delta = -17.8\Gamma$ is used that results in $B_b = 333\,\mathrm{G}$ and B_0 is tunable by the bias field coil.

If there are too strong deviations from the ideal magnetic field given in Eq. 3.5, it can easily happen that atoms will not be resonant with the ZS light and are not contributing to the slowing process any more. It is therefore advisable for the design of the ZS to assume a deceleration, a_{ZS}, not larger than about 2/3 of the maximum possible deceleration[15]. This ratio is known as deceleration parameter and is written as

$$\eta = \frac{a_{\mathrm{ZS}}}{a_{\mathrm{max}}} \; , \qquad\qquad 3.9$$

where $0 \leq \eta \leq 1$. If the atomic transition is not fully saturated η has to be chosen even smaller due to the limited light force acting on the atoms. Its upper limit is then set by $\eta < \frac{s_0}{1+s_0}$ with the saturation parameter $s_0 = \frac{I}{I_S}$. In the erbium experiment the current maximum power of the ZS beam is limited to about $90\,\mathrm{mW}$, which gives $s_0 = 5$ for a beam waist of the ZS laser of $4\,\mathrm{mm}$. This sets the maximum value of η to 0.83. To ensure reliable slowing at the beginning of the ZS where atoms are fastest the laser beam is slightly focused to increase the intensity at this point and make a larger η possible. Figure 3.5(b) shows the dependence of η over the full length of the ZS calculated for the total magnetic field.

The coil setup of the erbium ZS is as follows. In total six independently supplied coils create the required magnetic field, see Fig. 3.5(a). Most important is the profile coil, which roughly

---

[14] An estimation of the flux of atoms, which can be captured by the MOT, gives a value of $4 \times 10^8\,\mathrm{s}^{-1}$ at a temperature of the oven effusion cell of $1100\,^\circ\mathrm{C}$, see Ref. [Sch11]. Increasing the temperature by $150\,^\circ\mathrm{C}$ will increase the flux by one order of magnitude.

[15] The factor of 2/3 is chosen from the experience of previous experiments.

creates a square-root-like magnetic field according to Eq. 3.5. This is achieved by a variable number of windings dependent on the position along the ZS tube. Secondly, a cylindrical bias coil provides the homogeneous bias field for shifting the profile magnetic field. Two additional coils are located at the beginning and at the end of the ZS. They are constructed such that the magnetic field drops off as fast as possible when moving away from the ZS[16]. Another two coils are used to compensate any residual magnetic field and magnetic field gradient to zero at the MOT position. Figure 3.5(a) shows the magnetic field created by each of the coils and the total magnetic field for $\eta = 0.35$. To tune η the electric current through each of the six coils has to be changed accordingly, which results in a shift of the position of the zero crossing. The value of η can thus be changed from 0.1 to 0.5, which makes the ZS highly versatile.

We wind the ZS coils using standard enameled copper wires with a special coating for high-temperature resistivity and long-term stability[17]. This is important as the ZS coils have been mounted before performing the bake-out of the UHV chamber. This high-grade copper wire easily withstands the bake-out temperature of 200 °C for a time much longer than two weeks. The electrical isolation of low-grade copper wire would degrade at this temperature within a few hours and electrical isolation would not be guaranteed anymore.

Next we will estimate the usability of the ZS for two different atomic species and give the final ZS operating parameters. Equations 3.1, 3.3, and 3.6 can be combined for an expression of the deceleration parameter, which can be written as

$$\eta = \frac{m\mu'^2 B_0^2}{x_0 \Gamma \hbar^3 k^3} \ .$$
                                                                    3.10

An efficient multi-species ZS for two atomic species A and B can be constructed only if η is similar for both species, see Ref. [Wil09]. This can be estimated by the ratio

$$\frac{\eta_A}{\eta_B} = \frac{m_A \mu_A'^2 k_B^3 \Gamma_B}{m_B \mu_B'^2 k_A^3 \Gamma_A} \ ,$$
                                                                    3.11

In case of a dual-species ZS for erbium and lithium $\eta_{\text{Er}}/\eta_{\text{Li}} = 1.091$. Thus it is possible to use the same ZS for both elements and slowing should work efficiently. The final parameters of the currently operating ZS for erbium are

$$v_c^{\text{ZS}} = 325\,\text{m/s} \quad v_f = 5\,\text{m/s} \quad B_b = 333\,\text{G} \quad B_0 = -627\,\text{G} \quad \eta = 0.34 \quad \delta = -17.8\,\Gamma \ .$$

Assuming the same magnetic field parameters, B_b and B_0, this would result in the following parameters for a ZS for lithium with

$$v_c^{\text{ZS}} = 600\,\text{m/s} \quad v_f = 100\,\text{m/s} \quad \eta = 0.31 \quad \delta = -83\,\Gamma \ ,$$

which is very similar to other slowers used for lithium, see Refs. [Joc04, Wil09].

---

[16] This is achieved by a short coil geometry and utilizing a larger current than that for the other coils.

[17] wire class W200, manufactured by Synflex Elektro GmbH
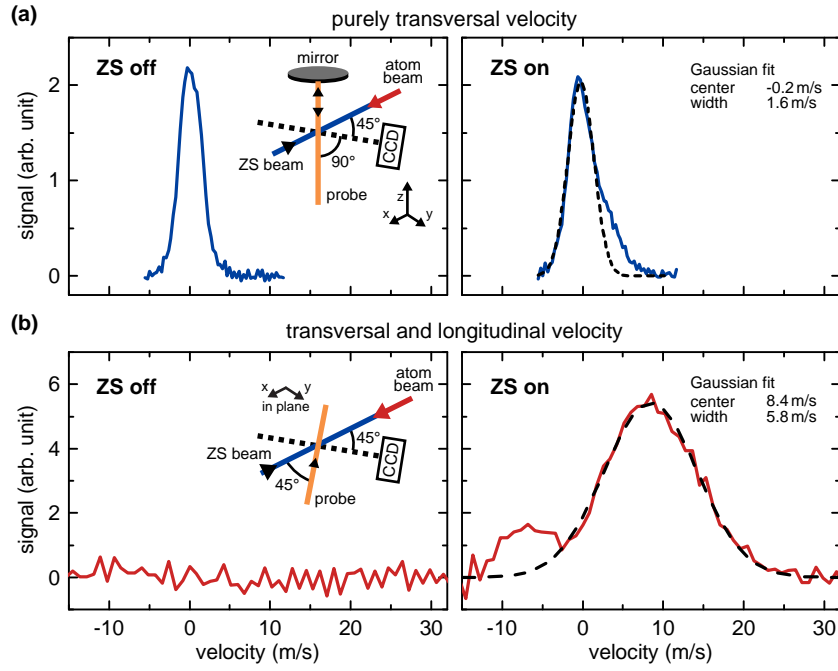
Figure 3.6.: Velocity distribution along probing direction oriented (a) purely transversal and (b) under an angle of 45° with respect to the atom beam (see insets). The measurement was done in the center of the main chamber using a CCD camera for imaging the fluorescent light. The effect of the Zeeman slower (ZS) is clearly seen when turned off (left panels) and on (right panels). The center of the transversal velocity distribution with the ZS switched off is used as a marker for zero-velocity calibration. With turned-off ZS the velocity distribution in (b) is outside the shown range at much larger values because the thermal longitudinal velocity of atoms exiting the oven is about 500 m/s. When the ZS is turned on a distribution of atoms with a maximum at 8.4 m/s can be observed, see Gaussian fit (dashed line). A second peak is appears at negative velocities, which is caused by atoms being stopped by the ZS light and being accelerated back in direction of the oven. Note that also the transversal velocity distribution gets slightly changed and deviates from the Gaussian fit. This is due to transversal heating when the ZS is turned on.

3.3.3. Velocity distribution

For optimizing the operational parameters of the ZS we measured the velocity distribution of erbium atoms after the slowing process in the center of the main chamber. Narrow-linewidth light at a wavelength of 583-nm was shined on the slow atom beam and the fluorescence signal was recorded on a CCD camera. The signal was achieved by integrating pixel values within a small region of interest of about $1 \times 2\,\mathrm{mm}^2$ around the atom beam. Figure 3.6 shows a sketch of the experimental setup and the measured velocity distributions. We oriented the probing laser beam either vertically, i.e. under an angle of 90° to the atom beam, or within the horizontal plane under 45° with respect to the atom beam, see insets in Fig. 3.6. The former setup allowed to probe only the velocity component in transversal direction whereas the latter gave information on both transversal and longitudinal components. The beam in vertical direction was retro-reflected and used as a zero-velocity marker for calibration purposes.

The 401-nm transition in erbium has a linewidth of 29.7 MHz. This is too large to probe the velocity distribution with a desired small resolution of maximal 1 m/s. The narrow-line transition at 583 nm provides a better velocity resolution of 0.1 m/s. For this transition the experienced velocity-dependent Doppler-shift of the atoms, $\delta\nu$, is given by

$$\delta\nu = v\frac{\nu_0}{c} \quad \Rightarrow \quad \frac{v}{\delta\nu} = \frac{c}{\nu_0} = \lambda = 0.58\,\frac{\text{m/s}}{\text{MHz}}\ , \qquad\qquad 3.12$$

where ν_0 is the transition frequency and c is the speed of light. As the frequency of the probing laser could only be detuned within ± 60 MHz using a non-specialized AOM setup the velocity distribution could be recorded between -35 m/s and $+35$ m/s. The velocity distribution in Fig. 3.6(b) shows a clear effect of the ZS as a fluorescence signal appears only when the ZS light is turned on. A fitted Gaussian curve gives a center velocity of 8.4 m/s with a full-width-half-maximum of 13.4 m/s. This nicely covers the capture velocity of the narrow-line MOT of 5.6 m/s, refer to Sec. 6.1.1 and Eq. 6.6. With the ZS turned off the velocity of the atoms is too large and the Doppler shift is larger than the tuning-range of the AOM and thus no signal could be recorded.

The purpose of this measurement was to verify whether atoms with a velocity comparable to the capture velocity of the MOT are indeed available in the main chamber. An optimization of the detuning of the slowing light and the magnetic field was carried out. Final fine-tuning of the ZS was performed by maximizing the atom number and the loading rate of the MOT. Only a small change of the initial values was necessary. These results were promising for setting up the first erbium MOT on the narrow-line transition. The setup of the narrow-line MOT will be described in Chapter 6.

3.4. Coil setup at main chamber

Magnetic fields play a very important role in ultracold gas experiments. Due to the Zeeman shift of atomic energy levels, see Sec. 2.4.3 and 2.4.4, and a spin-dependent force acting on atoms in a magnetic field gradient (so-called Stern-Gerlach experiment) atoms can be conveniently manipulated from outside the vacuum chamber using magnetic fields. At the same time this implies that atoms with a large magnetic moment are very sensitive to unwanted but persistent magnetic field noise.

In particular, three major coil setups are used in the erbium experiment:

- **Zeeman slower coils** for operating the ZS, see previous description in Sec. 3.3.2. Regarding the main chamber there are two coils utilized to compensate the magnetic field and its gradient generated by the ZS at the center position of the main chamber.

- **Main coil setup** consisting of gradient coils for creating a magnetic field gradient, e.g. during MOT operation and Stern-Gerlach experiments, as well as low- and high-field coils for a homogeneous magnetic field, e.g. for Feshbach spectroscopy, see Sec. 3.4.1.

- **Compensation cage** for compensating the Earth's magnetic field as well as other external magnetic fields, e. g. from the static magnets of ion getter pumps. Furthermore, it can be used to rotate the magnetic field with the possibility of leaving its absolute value constant, see Sec. 3.4.2.

The main chamber and attached parts are made of stainless steel with extremely low magnetic permeability[18]. This prevents any residual magnetic stray fields generated by the vacuum chamber after ramping between high and low magnetic fields. The largest amount of periodic magnetic field noise is introduced by the mains electricity with a characteristic frequency of 50 Hz and higher harmonics. Other strong non-periodic noise sources come mostly from neighboring experiments and a mechanical workshop close-by. This magnetic field noise easily turns into a major technical problem especially if the magnetic field should be reduced to very small values close to zero. In this case, an active feedback loop with an ultra-low-noise magnetic field sensor[19] has to be used. Furthermore, a high relative magnetic field stability on the order of 10^{-4} even at large absolute values of the magnetic field is desired for Feshbach spectroscopy. This is achieved by using an actively stabilized current source, which relies on a homemade analog feedback loop with an ultra-stable current transducer[20].

3.4.1. Main coil setup

The main coil setup is used to create homogeneous magnetic fields as well as gradient fields by a set of three coil pairs. Each pair of coils consists of an upper and lower coil. Figure 3.3 shows a schematic overview of the coil geometries and Fig. 3.7 gives a plot of the corresponding magnetic fields, i. e. the total magnetic field $B_{\text{tot}}(r_i)$ and its gradient $\partial_i B_{\text{tot}} = \partial B_{\text{tot}}/\partial r_i$ with $i = x, y, z$, calculated for a unit current of 1 A. All three sets of coils are made up of enameled copper wire[21] placed in a copper casing. For thermal conductivity, the coils are vacuum moulded into the casing using thermally conductive resin[22].

The main coil system is cooled by a water pocket around the perimeter of the copper casing, see Fig. 3.3. Temperature sensors are placed inside and outside the coils as well as inside the copper casing for monitoring purposes. An automatic safety system, the so-called interlock system, switches off the coil power supplies when the coil temperature exceeds a given threshold.

The magnetic fields created by the gradient and the high-field coils can be switched off in a short time by high-current IGBT switches[23]. We measured the switch-off-time of the magnetic field utilizing a pick-up coil. The time is limited to about $5-6$ ms due to eddy currents in the steel chamber. Every pair of wires supplying a single coil is twisted as tight as possible and positioned symmetrically with the other pair of wires of the opposite coil

---

[18] $\mu_r < 1.005$, see Ref. [Lee05], for stainless steel code 316LN (after AISI) or 1.4429 (after ESU)
[19] model Mag-03-MS-70, three-axis magnetic field sensor, noise $< 10\,\text{pT}/\sqrt{\text{Hz}}$, from Bartington Instruments
[20] ITN 12-P, 12.5 A measuring range, 0.0509 % accuracy, from LEM
[21] $2.50 \times 1.00\,\text{mm}^2$ W200 copper wire, outer dimension $2.96 \times 1.22\,\text{mm}^2$, from Synflex Elektro GmbH
[22] type RAKU-POX 22-G110/7-7, two-component electro casting resin, from RAMPF Holding GmbH & Co KG
[23] dual IGBT module 2MBI100U4A-120-50, $I_c = 100\,\text{A}$ and $U_{ce} = 1200\,\text{V}$, from Fuji Electric
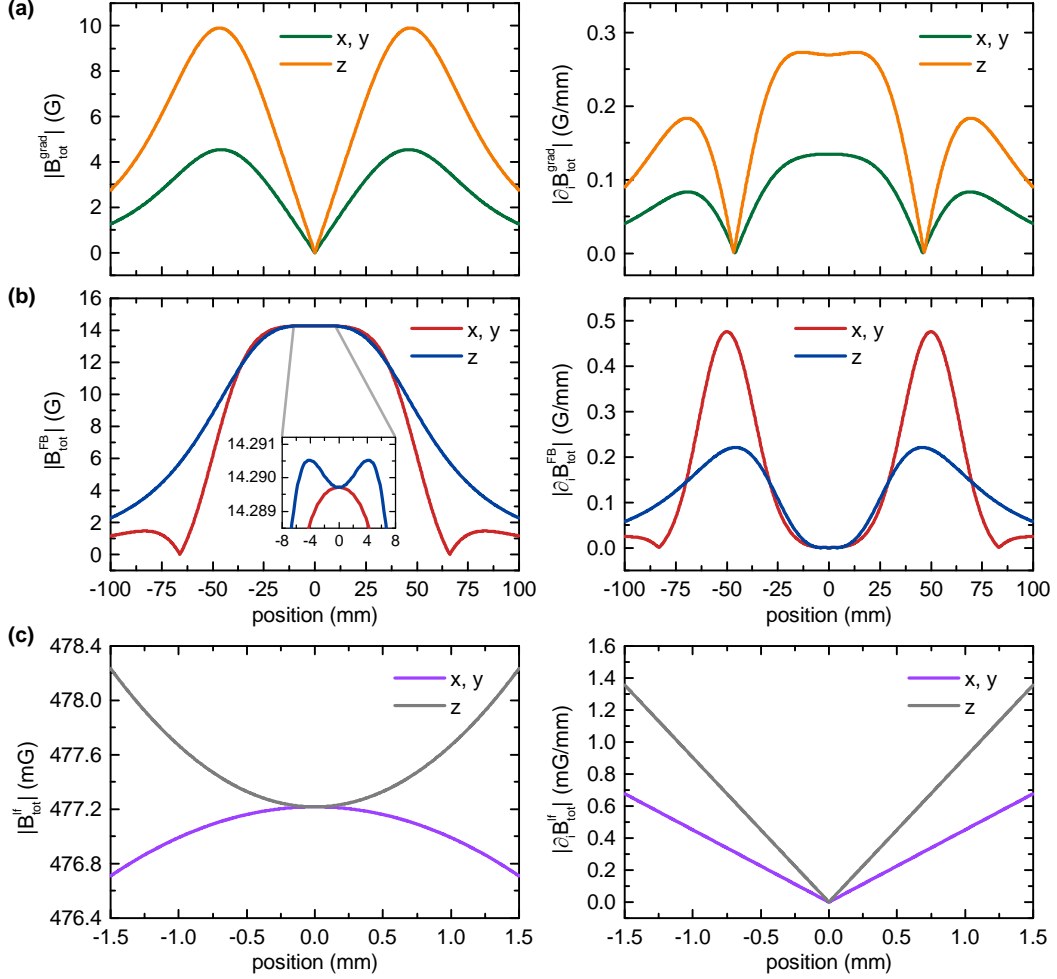
Figure 3.7.: Magnetic field strengths generated by the main coil system. The absolute values of the total magnetic field $B_{\text{tot}}(r_i)$ (left) and its gradient $\partial_i B_{\text{tot}} = \partial B_{\text{tot}}/\partial r_i$ with $i = x, y, z$ (right) along the x-, y-, and z-direction (colors) for a unit current of $1\,\text{A}$ are shown. (a) Magnetic field generated by the gradient coils (grad) for MOT operation and Stern-Gerlach experiments. (b) Homogeneous magnetic field induced by a set of coils in Helmholtz configuration for high-field Feshbach (FB) spectroscopy. (c) Magnetic field of low-field coils (lf) usable up to a maximum field of $4.5\,\text{G}$. Zero position corresponds to the center of the main chamber.

in respect to the center of the main chamber. Doing so, the magnetic field created by the current running into the coil cancels with that of the current returning from the coil. This is intended to reduce any residual magnetic fields created by the power supply wires.

Gradient coils Two coils in anti-Helmholtz configuration create a magnetic field gradient in every spatial direction, i. e. by creating a quadrupole magnetic field. In this configuration the gradient in x- and y-direction is half as large as the one in z-direction. Each coil is made up of six layers with 14 windings each, which makes it possible to use a power supply[24] at a moderate output current, i. e. below $50\,A$ reducing thermal heating. The conversion factor for the magnetic gradient field is about $2.698\,\frac{G/cm}{A}$ in z-direction. The maximum gradient is about $80\,G/cm$, which is limited by thermal heating at a maximum current of $30\,A$. The total resistance of the gradient coils is $440\,m\Omega$. At maximum current the gradient coils dissipate a total power of $400\,W$ in form of heat, which is removed by the water-cooling system.

Feshbach coils The high-field coils are capable of creating a homogeneous magnetic field of up to $500\,G$. Due to its Helmholtz configuration the spatial homogeneity of the magnetic field is better than $0.2\,mG/mm$ at the center of the main chamber, see inset of Fig. 3.7(b). The calculated conversion factor for the Feshbach coil is $14.290\,G/A$. The maximum current is limited to $35\,A$ and the total resistance is $430\,m\Omega$. This corresponds to a dissipated power of about $530\,W$. At maximum current the temperature at the center of the coil stack increases to about $40\,°C$ but due to the water-cooling system the temperature of the copper casing does not exceed $25\,°C$. We measured the frequency response of the high-field coils revealing a cut-off frequency of about $500\,Hz$. High-current relays[25] make it possible to switch between two different power supplies, one for a high and one for a low current operation. The first power supply[26] is capable of driving the maximum current whereas the second power supply[27] is limited to about $5\,A$ giving a maximum magnetic field of $70\,G$. In both cases the current is actively stabilized using a current transducer[28] and a PID control loop to achieve a relative short-term stability of the magnetic field of better than 2×10^{-4} for the low-current power supply. The magnetic field of the Feshbach coils was calibrated using atomic radio-frequency (RF) transitions from $m_J = -6$ to -5. The average magnetic field noise is estimated to be $40\,mG$ for the high-current power supply and $5\,mG$ for the low-current power supply. In both cases the main contribution comes from the power supply itself, which could be replaced by lead-acid batteries for further noise reduction.

Low-field coils A pair of two small coils consisting of two layers with four windings each creates a magnetic field of up to $5\,G$. The conversion factor is $477.22\,\frac{mG}{A}$ and the maximum current should not exceed $10\,A$. Although they are not in perfect Helmholtz configuration the coils have a calculated homogeneity of about $0.9\,mG/mm$. For a typical cloud size of $20\,\mu m$ this would in principle give a spatial deviation of less than $18\,\mu G$, which is much less

---

[24] switching power supply, model SM 18-50, from Delta Elektronika
[25] model G9EA-1-B-24VDC, for 60 A and 400 VDC, from Omron Corporation
[26] switching power supply, model SM 15-200 D, from Delta Elektronika
[27] linear power supply, model EA-PS 1032-10 B, from Elektro-Automatik
[28] IT 60-1000 S (high current) and ITN 12-P (low current), from LEM

than the magnetic field noise. The low-field coils are supplied by a linear power supply[27] with low noise but an active stabilization of the current is not implemented yet. RF-calibration yields a total magnetic field noise of about $600\,\mu\mathrm{G}$. A high precision feedback loop would be necessary for performing low-field experiments below $100\,\mu\mathrm{G}$.

3.4.2. Compensation cage

Three sets of rectangular-shaped coils forming a rectangular cage are used to compensate any residual magnetic field in x-, y-, and z-direction. An external field is for instance generated by Earth and the permanent magnets of the ion pumps. The geometric size of the cage is $1200 \times 1200 \times 850\,\mathrm{mm}^3$. The center of the cage overlaps with the center of the main chamber in x- and y-direction but is shifted by $250\,\mathrm{mm}$ in positive z-direction. The coils are composed of 40 windings in x- and y-direction and 30 windings in z-direction. This results in a total inductance of about $15\,\mathrm{mH}$ for each set of coils.

Additionally, the compensation cage can be used to change the direction of the magnetic field even while keeping the value of the absolute magnetic field constant. Such a magnetic field rotation is limited to absolute magnetic fields smaller than $1.2\,\mathrm{G}$. In the experiment this allows for changing the polarization direction of the magnetic dipoles with respect to the trapping geometry by rotating the orientation of the magnetic field. Due to the large inductance of the coils the frequency response function shows a high-frequency cut-off at about $1\,\mathrm{kHz}$. This limits the maximum speed, at which the magnetic field can be rotated, to about $15\,^\circ/\mathrm{ms}$.

3.5. Laser light setup

For the production of quantum gases of erbium we use laser light at a wavelength of $401\,\mathrm{nm}$ (blue light, see Sec. 3.5.1) for ZS, TC, and imaging and light at $583\,\mathrm{nm}$ (yellow light, see Sec. 3.5.2) for magneto-optical trapping. Additionally, for optical dipole traps we employ far-off-resonance laser light at a wavelength of $1064\,\mathrm{nm}$ and $1570\,\mathrm{nm}$, see Sec. 3.5.3.

3.5.1. Blue laser system

For the 401-nm light we use a master laser and two slave lasers. Figure 3.8 illustrates the optical setup for the master laser whereas Fig. 3.10 shows the optical setup for the slave lasers. The master laser is utilized for the locking setup, seeding the slave lasers, and imaging atoms in the experiment. It is a commercial laser[29]. The light of a diode laser operating at $802\,\mathrm{nm}$ is first tapered-amplified and then frequency-doubled in a bow-tie ring cavity. The maximum output power of the master laser is $210\,\mathrm{mW}$ from which $80\,\mathrm{mW}$ are needed for operating the experiment, see Appendix C. For the ZS- and TC-light injection-locked slave lasers provide

---

[29] TA-SHG-pro system, from Toptica Photonics AG

a high optical power on the experiment table. They are seeded by light coming from the master laser through optical fibers. The master laser is locked by the modulation-transfer technique to a spectroscopy cell in form of a hollow-cathode lamp (HCL). We observe about 40 % absorption in the HCL for typical operating parameters of a voltage of 110 V at a discharge current of 6 mA. The spectroscopy signal contains a clear signal of the transitions of all bosonic isotopes as well as features coming from the hyperfine structure of the fermionic isotope. The modulation-transfer technique creates a signal, which can be conveniently used for laser locking. It is described in Sec. 8.1.2.

In total, five acousto-optic modulators[30] (AOMs) are used to shift the laser light frequency to the desired values, see Fig. 3.8. The master laser is locked on the laser frequency necessary for the ZS. This is achieved by shifting the light used for the spectroscopy cell with one AOM in double-pass (DP) configuration by an amount equal to the ZS-light detuning of -530 MHz. For fermions the spectroscopy signal of the hyperfine transition $m_F = -19/2 \rightarrow -21/2$ is weak and sits on top of the broad background signal of the bosonic isotope ^{166}Er, see Chapter 8. Therefore we lock the laser on the bosonic transition and use an additional DP AOM[31] to shift the light by another $+150$ MHz for experiments with fermionic ^{167}Er.

Because the laser is locked away from the atomic resonance another DP AOM can be used for shifting the light back on or close to resonance with a variable detuning. This is done to prepare light for TC, which needs to have a detuning of about -10 MHz with respect to the atomic transition. The final value of the detuning was determined empirically by maximizing the improvement of the MOT loading rate when TC is switched on. The light for absorption imaging is shifted close to resonance in a similar way with a detuning suitable for the current experiment[32]. Finally, for selectively removing atoms from an atom-molecule mixture a weak blowing (or pushing) beam is prepared. It is tuned exactly on resonance with the atomic transition to have a largest possible light-force acting on the atoms during the blowing sequence. Usually a pulse with a duration of 1 μs and a beam power of 2 mW giving an intensity on the order of the saturation intensity is sufficient to remove all atoms from the sample.

Injection-locked lasers

Two injection-locked diode lasers are used as slave lasers on the experiment table, see Fig. 3.10. Both slave lasers are homemade and share a similar setup. Each one of them delivers 80 mW of laser light after seeding them with about 2 mW from the master laser. The first slave laser is used for the ZS and the second one for TC. In this setup only a low power has to be carried via optical fibers from the laser table to the experiment table. This makes high-power fibers unnecessary resulting in a larger long-term stability of the laser system.

---

[30] For the blue laser system mostly AOMs, model BRI-TEF-270-100-401, from Brimrose Corporation are used, which have a center frequency of $f_c = 270$ MHz and a 3 dB-bandwidth of $B = 100$ MHz.
[31] model BRI-TEF-80-20-583, with $f_c = 80$ MHz and $B = 20$ MHz, from Brimrose Corporation
[32] Off-resonant light is used for imaging optically thick atomic clouds to prevent saturation effects.
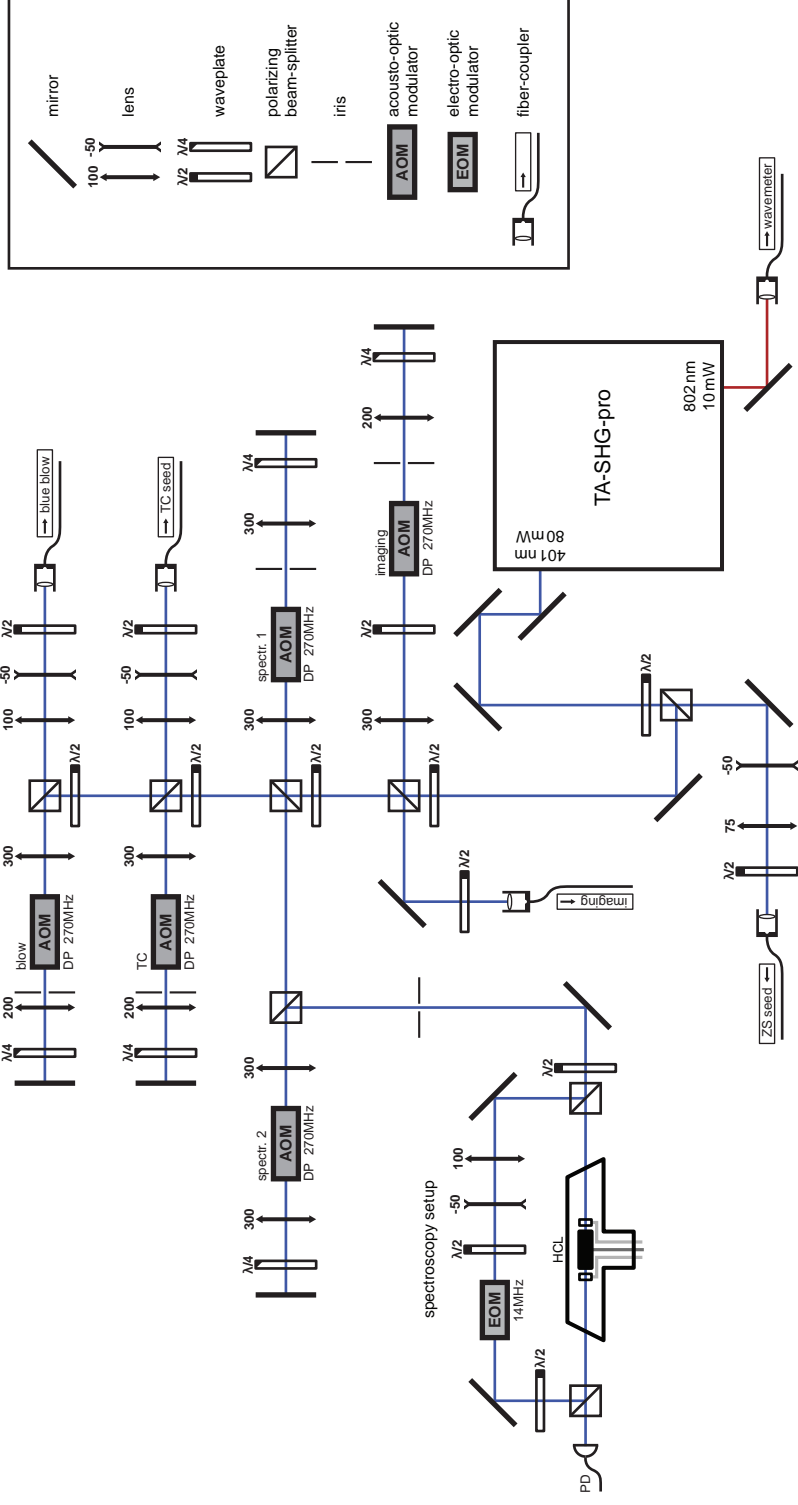
Figure 3.8.: Blue laser setup for the 401-nm transition. A frequency-doubled, tapered-amplified diode laser operating at 802 nm (TA-SHG-pro) is used as a master laser (blue lines). Light for seeding the Zeeman slower (ZS) and transversal cooling (TC) slave lasers, absorption imaging, and resonantly blowing atoms is prepared by frequency-shifting using acousto-optical modulators (AOMs). The master laser is locked to a spectroscopy cell using modulation transfer spectroscopy. It operates off-resonance with a detuning given by the ZS light. Two AOMs in double-pass (DP) configuration are utilized for shifting the laser frequency to resonance for spectroscopy (see text).

For the slave laser a wavelength-selected single-mode laser diode[33] is stabilized in temperature[34] and is powered by a constant current source up to 120 mA. For suppressing unwanted back-reflections into the laser diode the light passes a polarization-dependent optical isolator[35], which is simultaneously used to couple in the light coming from the master laser. To ensure single-mode operation of the slave laser some light is picked-off and sent to a homemade wavemeter.

In the case of the ZS the laser beam from the slave laser is first expanded using two telescopes to a diameter of more than 30 mm before a single lens with a focal length of 1000 mm focuses the light into the vacuum chamber. Here, the focus is situated at the high-temperature oven. A standard quarter-wave plate sets the polarization of the beam to circularly polarized.

For TC the laser beam is first elongated to an aspect ratio of about 10 : 1 using cylindrical lenses before it is split into two beams. The large aspect ratio maximizes photon scattering by simultaneously having a high intensity and a long interaction time with the atom beam. Each laser beam is retro-reflected to form the two-dimensional optical molasses.

Imaging setup

Absorption imaging of the atom cloud can be done either in the horizontal or the vertical direction, see Fig. 3.11. The imaging laser light from the blue laser setup is either sent into the vacuum chamber through a CF16 flange for horizontal imaging or is recoupled into another fiber for vertical imaging. The second fiber carries the light below the vacuum chamber before it enters the vacuum chamber through the lower CF40 window. In both cases the light is circular polarized by quarter-wave plates in front of the windows.

For horizontal imaging an objective with a magnification of 1.9 creates an image on the CCD sensor[36]. The numerical aperture is limited by the geometric size of the CF16 flange to about 0.1 giving a theoretical resolution limit of 2.5 μm. The objective for vertical imaging has a magnification of 2.5 and creates an image on a second CCD sensor[37]. In this case the numerical aperture is determined by the objective and has a value of about 0.08.

3.5.2. Yellow laser system

We use a continuous-wave ring-cavity dye laser[38] with rhodamine 6G as an active medium for a laser light source for the MOT operating at a wavelength of 583 nm. The dye laser is

---

[33] model NDV4313 from Nichia Corporation

[34] by the temperature controller WTC3243, from Wavelength Electronics

[35] model IO-5-405-LP, from Thorlabs

[36] scientific camera model iXon3 897, back-illuminated AR-coated EMCCD, with 512×512 pixel resolution, $16 \times 16 \, \mu\text{m}^2$ pixel size, 14 bit digitization, from Andor Technology

[37] scientific camera model Luca R 604, AR-coated EMCCD in OEM housing, with 1004×1002 pixel resolution, $8 \times 8 \, \mu\text{m}^2$ pixel size, 14 bit digitization, from Andor Technology

[38] CW ring dye laser, from Radiant Dyes

pumped by a 10 W solid-state laser[39] at 532 nm. The bare dye laser has a maximum output power of 1 W, a linewidth of about 1 MHz, and a frequency drift of 100 MHz/h.

For MOT operation the linewidth has to be decreased below 200 kHz, which is given by the natural linewidth of the yellow transition, and a frequency-drift lower than a few kHz/h has to be achieved. The reduction in linewidth is accomplished by introducing an electro-optical modulator (EOM) into the cavity of the dye laser for a fast feedback-loop with a response frequency of up to a few MHz. The error signal is generated from a low-finesse cavity using the Pound-Drever-Hall (PDH) method. We improve the frequency-drift and long-term stability by locking the low-finesse cavity to an ultra-low expansion (ULE) cavity. The ULE cavity consists of a ULE spacer[40] and two fused silica mirrors, which are optically contacted to the spacer. The cavity has a finesse of 1865(6) and a free spectral-range of 998.69(2) MHz, which is similar to the isotope frequency shift of erbium. This turns out to be convenient for locking to different isotopes of erbium. To achieve sufficiently high stability the ULE cavity is put under vacuum and shielded from outside temperature fluctuations by two aluminum shields. The temperature of the ULE spacer is stabilized to its zero-expansion temperature of $-5.65(9)\,°\text{C}$ using four Peltier elements. Utilizing this locking setup the linewidth of the dye laser could be decreased to 45.0(5) kHz within 10 ms and the drift was measured to be 580(70) Hz/h over a timescale of 40 days. A full description of the locking procedure and ULE cavity setup can be found in Ref. [Rie12].

Figure 3.9 shows the optical setup of the yellow laser-system. It consists of the dye laser, the locking setup including the low-finesse and ULE cavities, two DP AOMs for shifting the frequency of the MOT light and yellow blow light, and the MOT distribution setup. The output of the dye laser can be monitored on a wavelength-meter and a power-meter. The dye laser has to be realigned whenever the dye needs to be exchanged. This realignment would lead to a misalignment of the full optical setup. For convenient realignment a short fiber is placed between the dye laser and the rest of the optical setup.

Error signals from the low-finesse and ULE cavities are generated by a standard PDH method using EOMs for sideband creation. The error signal of the ULE cavity is fed to the piezo crystal of the low-finesse cavity controlling the length of the low-finesse cavity. The error signal of the low-finesse cavity is then split up in three signals of different frequency ranges feeding three optical elements inside the dye laser cavity. The low-frequency part, which goes up to a few 100 Hz, drives a Brewster plate, the mid-frequency part, up to several kHz, controls a cavity mirror mounted on a Piezo crystal, and higher frequencies up to a few MHz are applied to the intra-cavity EOM. As the length of the ULE cavity is fixed the frequency of the laser light used for locking has to be shifted by two DP AOMs[41] such that the light generated by the dye laser is on resonance with the atomic transition. The lock-shift setup was designed for a frequency tuning range covering at least the free spectral-range of the ULE cavity of about 1 GHz. One of the two AOMs is used for stabilizing the intensity to about $100\,\mu\text{W}$. This ensures a constant and small heat input to the ULE cavity. The shifted light is then carried to the cavity lock setup using an optical fiber and is modulated by another EOM for the PDH technique.

---

[39] Verdi V10, from Coherent

[40] ULE premiumgrade, length 150 mm and diameter 60 mm, from Hellma Optics

[41] model AOMO 3200-125 with $f_c = 200$ MHz from Crystal Technology, Inc. (now Gooch & Housego)
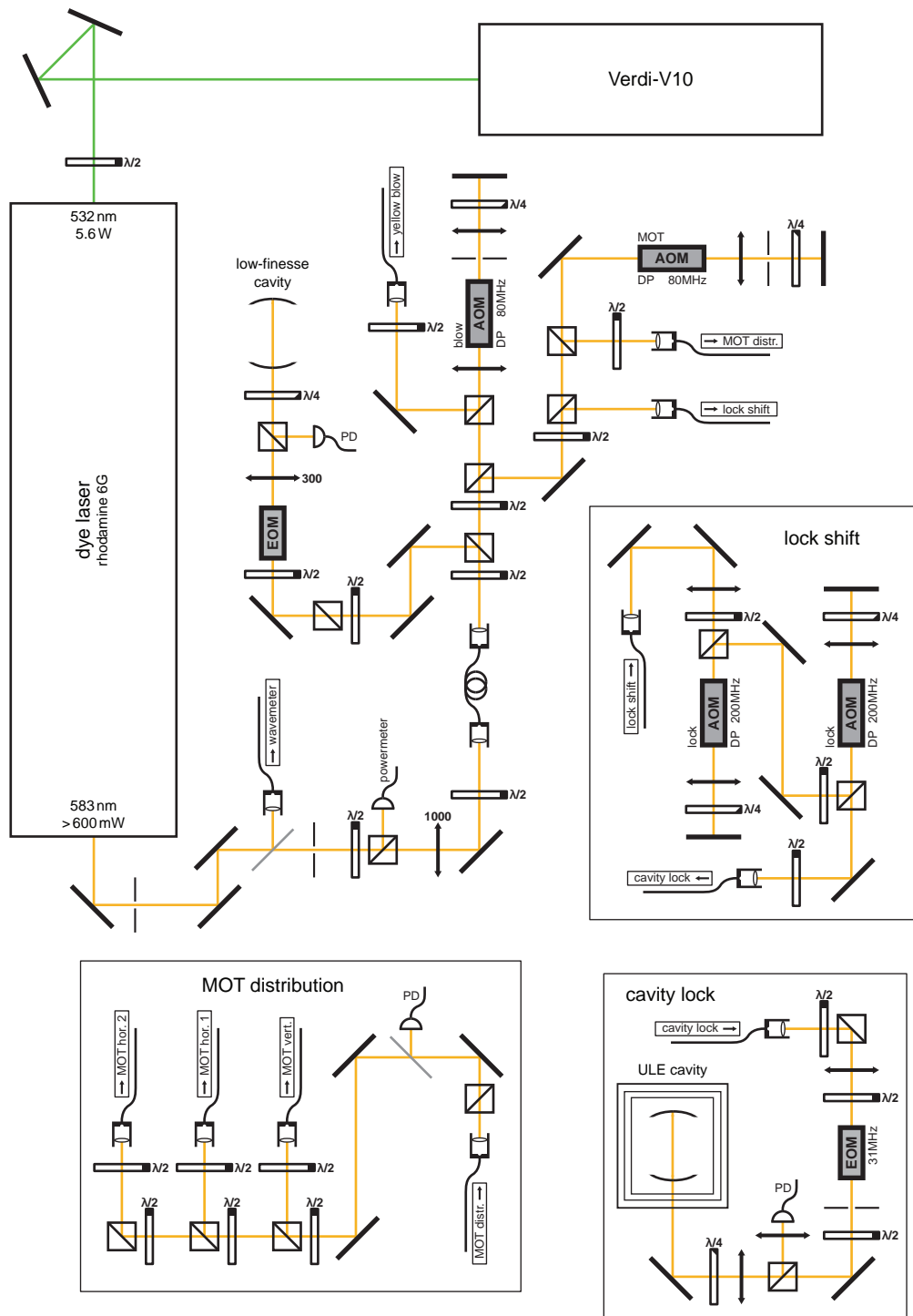
Figure 3.9.: Yellow laser setup for the 583-nm transition. Here, the light source is a dye laser operating with rhodamine 6G (yellow), which is pumped by 532-nm light (green). The light for the three MOT beams can be detuned using an AOM. Furthermore, resonant light is prepared for blowing atoms out of the optical dipole trap. For narrowing the laser linewidth lower than the natural linewidth of the atomic transition an intra-cavity electro-optical modulator (EOM) is utilized (not shown). The laser is locked to a low-finesse cavity, which length is locked to an ultra-low-expansion (ULE) cavity using the Pound-Drever-Hall technique.
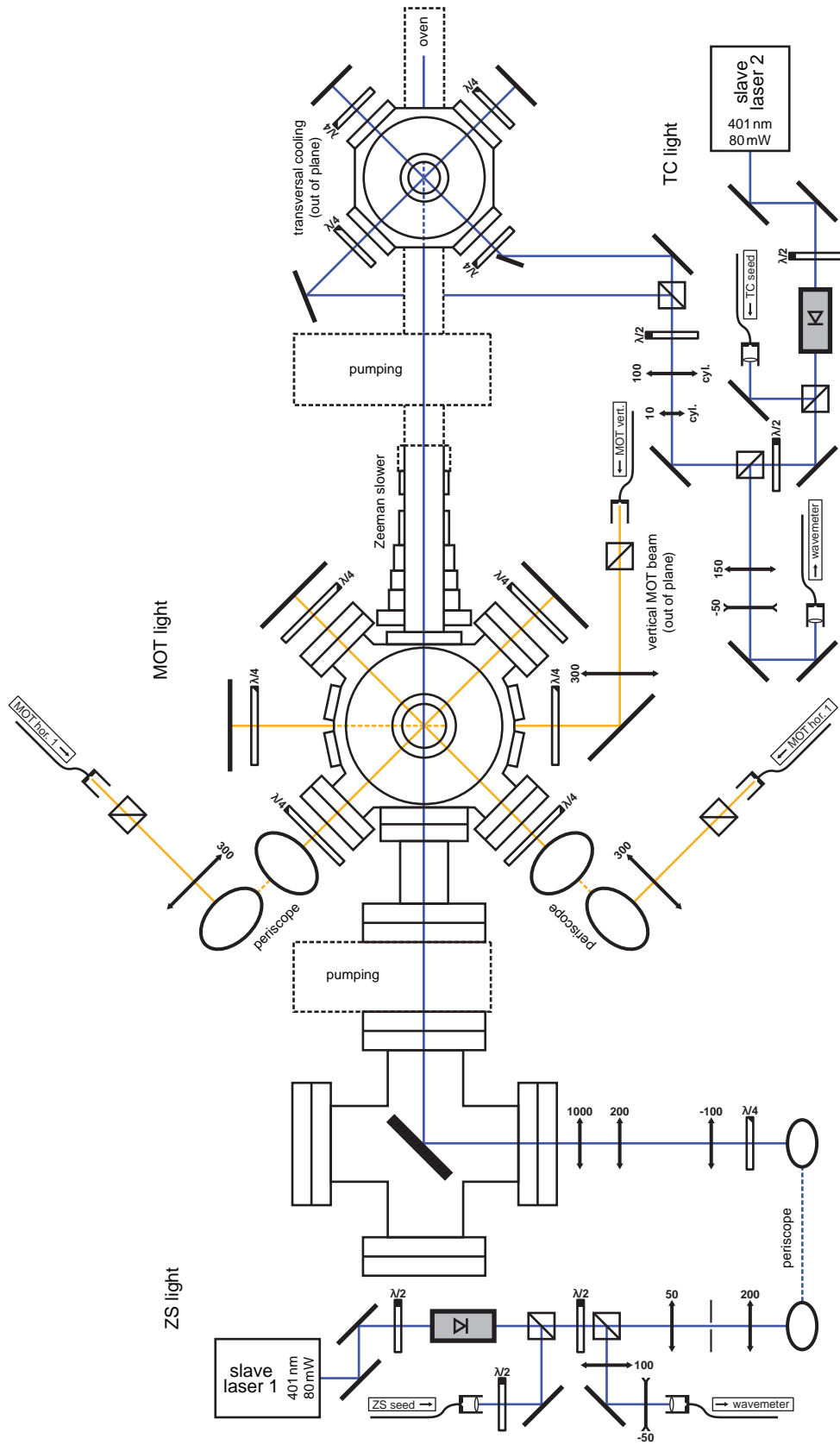
Figure 3.10.: Overview of the laser setup for transversal cooling (TC), Zeeman slowing (ZS), and MOT beams. The vacuum chamber is schematically shown in a top view. The retro-reflection of the MOT beams (yellow) is done in the way such that highest intensities are achieved in the direction against the atom beam as well as against gravity. This ensures maximum loading efficiency into the MOT. The injection-locked slave lasers generate about 80 mW each (blue). The TC beams are highly elliptical and are displaced from each other in direction of the atom beam. This maximizes the scattering force on the atoms.

The frequency of the MOT light can be detuned by an AOM[42] in double-pass configuration. Afterwards, the light is carried to the MOT distribution board in a single fiber. After the fiber a photo-diode monitors the light intensity for intensity stabilization utilizing the AOM. The light is then split up in three beams, which are carried to the experiment table in three separate fibers. Two beams are used for the horizontal MOT direction and the third for the vertical direction. On the experiment table each beam is increased to a diameter of more than 20 mm using a telescope. This increases the capture velocity of the MOT according to Eq. 6.6. The enlarged beams are then brought close to the vacuum chamber using periscopes, see Fig. 3.10. All beams are circularly polarized by achromatic true zero-order quarter-wave plates[43] before entering the vacuum chamber and are retroreflected on the opposite side of the chamber. The minimum total output power of the dye laser has to be at least 600 mW otherwise the intensity of the MOT beams is not high enough for MOT operation. Typically intensity values at the vacuum chamber are as high as $12\,I_S$ for each beam with $I_S = 0.13\,\mathrm{mW/cm^2}$ the saturation intensity of the transition.

3.5.3. Optical dipole traps

After laser cooling atoms in the MOT they are usually loaded into a red-detuned optical dipole trap (ODT) comprising of various trap geometries and laser wavelengths. A so-called scanning setup was implemented to achieve a highly efficient loading from the MOT into the ODT. In this setup the laser beam is deflected in the horizontal, transversal direction by an AOM with a frequency much larger than any trapping frequencies. This creates a time-averaged optical potential, which can be changed by tuning the amplitude and speed of deflection. Using the scanning system the ODT can be increased in size to have a good spatial overlap between atoms in the MOT and the ODT. This optimizes the loading efficiency to about 35 %. Furthermore, the scanning system can be used to adiabatically change the aspect ratio of the ODT, i. e. the ratio of the trapping frequencies in two directions, from 1.5 to 15. A comprehensive description of the scanning system is presented in Ref. [Bai12a].

As soon as atoms are loaded into the ODT further cooling is done via evaporative cooling in a crossed beam setup, which consists of a horizontal and a vertical trapping beam. A detailed description of the evaporation procedure can be found in Sec. 7.1.1 for cooling bosons and in Sec. 9.1.3 for cooling fermions.

In case of fermions the lifetime in the ODT operating at a wavelength of 1064 nm turned out to be too short for evaporative cooling and further measurements. Due to that restriction fermions are loaded from the 1064 nm trap into an ODT at 1570 nm. In this trap the lifetime is about 40 s, which is sufficiently long. The reason for this reduced lifetime of the fermions in the 1064-nm ODT is not understood so far.

The current ODT setup in the erbium experiment consists of five different beams; two beams in horizontal and three in vertical direction. The setup is shown schematically in Fig. 3.11. Each ODT beam is briefly discussed in the following.

---

[42] model BRI-TEF-80-20-583, from Brimrose Corporation
[43] model APAW, usable from $500 - 750$ nm, 40 mm diameter, from Astropribor
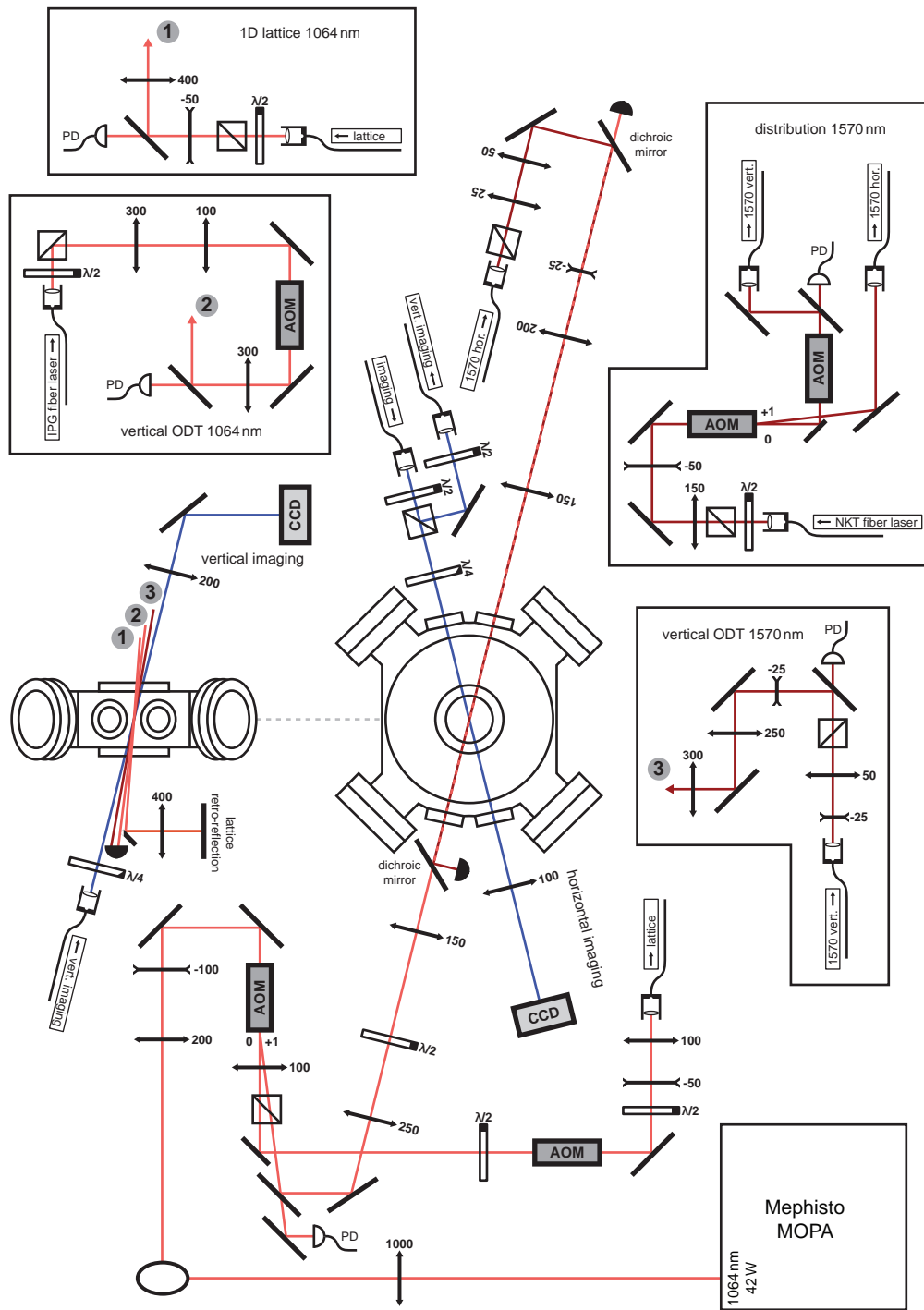
Figure 3.11.: Overview of the laser setup for absorption imaging (blue) and optical dipole-trap (ODT). The main chamber is shown from the front (left side) and from the top (right side). Imaging the atomic cloud can be done in horizontal or vertical direction. The laser light for the horizontal dipole trap and the one-dimensional optical lattice is derived from a single-mode master oscillator power amplifier (MOPA) at 1064 nm (light red). For the vertical dipole trap a Yb fiber laser is utilized operating at 1064 nm. Additionally, a second horizontal and vertical dipole trap from an Er-doped fiber laser at 1570 nm is used for trapping fermions (dark red).

Horizontal 1064 nm ODT The laser light for this ODT has a wavelength of 1064 nm and is generated by a high-power, single-mode, ultra-narrow linewidth laser[44]. Light with a total power of 42 W is sent through a high-power AOM[45]. The zeroth-order beam is used for the vertical lattice, see later. For the above mentioned scanning system the first-order beam is deflected by the AOM. This deflection can be translated into a parallel displacement by putting the AOM in the focal point of a lens, see Ref. [Bai12a]. The beam is then collimated by a second lens with a focal length of 250 mm before it is focused into the main chamber by a third 150 mm lens. This results in a beam waist of $w_x = 16.1\,\mu$m and $w_y = 24.2\,\mu$m without scanning. The beam waist in the x-direction can be increased with the scanning system by up to a factor of ten. Using this ODT with a maximum power of up to 20 W traps with potential depths of more than $k_{\mathrm{B}} \times 1\,$mK can be created without scanning and $k_{\mathrm{B}} \times 180\,\mu$K with maximum scanning. The largest scanning is very suitable for loading atoms from the MOT into the ODT because of two reasons. First, the large trap provides a good spatial overlap with the MOT and second, atoms in the MOT have an initial temperature of $15\,\mu$K, which is one order of magnitude smaller than the trap depth. A minimum trap depth of a factor of ten higher than the initial MOT temperature is required for a high loading efficiency.

Vertical 1064 nm ODT This trap is created by light coming from a broadband Yb fiber laser[46] operating at 1064 nm with a maximum output power of 10 W. The vertical beam is focused by a 400 mm lens and has waists of $w_x = 224\,\mu$m and $w_y = 140\,\mu$m.

Horizontal 1570 nm ODT A second horizontal trapping beam is created by light from a single-mode, Er-doped fiber laser[47] at 1570 nm. The light is split up using an AOM and carried to the vacuum chamber by high power, polarization-maintaining fibers[48]. The first diffraction order from the AOM is used for the horizontal beam, which is overlapped with the horizontal 1064 nm trapping beam using dichroic mirrors.

Vertical 1570 nm ODT The light for this beam is taken from the zeroth diffraction order from the AOM in the horizontal 1570 nm setup. The light is frequency-shifted by a second AOM to prevent interference with the horizontal beam. The same AOM is used to control and stabilize the laser power. The beam is then focused into the chamber by a 300 mm lens.

Vertical 1D lattice with 1064 nm light For confining atoms in a quasi-2D geometry a one-dimensional optical lattice with a lattice constant of 532 nm can be created in the erbium experiment. An array of pancake-shaped traps is formed by retro-reflecting the lattice beam. Light coming from the zeroth order of the AOM of the horizontal 1064 nm trap is sent through

---

[44] model Mephisto MOPA, 42 W at 1064 nm, from Innolight (now Coherent)
[45] model 3110-197, numerical aperture of 3 mm, from Crystal Technology, Inc. (now Gooch & Housego)
[46] model PYL-10-1064-LP, 10 W at 1064 nm, from IPG Photonics
[47] model Koheras Boostik HPA C15, System PM Pzt, 10 W at 1570 nm, from NKT Photonics GmbH
[48] LMA-PM-15, from NKT Photonics GmbH

a second AOM for detuning the frequency with respect to the horizontal beam preventing unwanted interference effects. Furthermore, an intensity stabilization is implemented using the AOM. The light is then coupled into a high-power fiber for mode-cleaning. It is brought above the vacuum chamber before it is focused into the chamber by a 400 mm lens. On the other side of the chamber the beam is collimated again and retro-reflected forming an optical standing wave. Monitoring the amount of laser light traveling in backward direction through the fiber is a convenient method for optimizing the quality of retro-reflection. In the final setup the lattice beam has a waist of $250\,\mu$m and gives a trap frequency of up to 31 kHz in the direction of strong confinement for a power of 8 W. The radial trap frequencies in the lattice are as low as 33 Hz.

4

Ultracold dipolar scattering

Since the very first experiments on ultracold quantum gases have been carried out the scattering properties of particles were of fundamental importance. The reason for this is the fact that scattering properties reveal explicit information on the interaction between particles. At small collision energies, which are only achievable with ultracold gases, one can explore the regime of lowest partial waves. In this regime, the contact interaction between two particles has been extensively studied during the last years. It is an isotropic and short-range interaction and can be described by a collision of two hard spheres.

The dipole-dipole interaction (DDI) fundamentally changes the scattering properties of particles. Its long-range and anisotropic character has strong influences on the scattering cross section at ultracold temperatures. A new length scale, which is set by the dipole moment of the particle and its mass, comes into play, the so-called *dipole length*. The stronger the DDI, the larger its contribution to the particle interaction is, up to a point, where it becomes the dominant interaction in the system. A convenient method exists in ultracold gas experiments to tune the relative strength between contact interaction and DDI. This tunability is induced by the existence of *Feshbach resonances*.

One of the most striking features of the DDI is that the anisotropic nature of the dipole potential causes the elastic scattering cross section not to vanish for decreasing collision energies. This *is* the case for contact interaction, except for the well-known *s*-wave scattering of bosons. But with DDI, the contribution of higher partial waves can not be neglected, even in case of identical fermions. Here, the scattering length will rather converge for lower collision energies to a universal value, which is independent of temperature. These novel scattering properties are summarized under the term *universal dipolar scattering*.

In this chapter, we will discuss the scattering physics of dipoles at low collision energies. The first section is dedicated to anisotropic interactions, i. e. the dipole-dipole interaction and the anisotropic dispersion interaction between atoms. Then the theory of dipolar scattering is presented in Sec. 4.2 with the aim of developing a framework for universal dipolar scattering. Finally, anisotropy induced Feshbach resonances are subject for discussion in Sec. 4.3.

4.1. Anisotropic interactions

The interaction potential U of two dipolar atoms separated by a distance $\mathbf{r}$ has two main contributions. On the one hand, there is the dipole-dipole interaction U_{dd} and on the other hand, the van der Waals interaction U_{vdW}.

$$U(\mathbf{r}) = U_{\mathrm{dd}}(\mathbf{r}) + U_{\mathrm{vdW}}(\mathbf{r}) \qquad 4.1$$

Here, higher order interactions, like quadrupole-quadrupole or dipole-quadrupole, have been neglected. The DDI is intrinsically anisotropic as the sign and the strength of interaction depends on the orientation of the two dipoles. The van der Waals interaction is isotropic for simple atoms, like alkali metals, but it can also be anisotropic for atoms with complex electronic structure, like for lanthanides. Both interactions will be discussed in the following.

4.1.1. Dipole-dipole interaction

The dipole-dipole interaction is an anisotropic and long-range interaction. Its anisotropic nature makes the DDI dependent on the geometry the system. Due to these reasons, it gained large interest in the field of atomic physics within the last few years. The interaction potential U_{dd} between two dipoles of identical dipole moment pointing in directions $\mathbf{e}_1$ and $\mathbf{e}_2$, see Fig. 4.1(a), can be described in a general form by

$$U_{\mathrm{dd}}(\mathbf{r}) = \frac{C_{\mathrm{dd}}}{4\pi} \frac{(\mathbf{e}_1 \cdot \mathbf{e}_2)r^2 - 3(\mathbf{e}_1 \cdot \mathbf{r})(\mathbf{e}_2 \cdot \mathbf{r})}{r^5} \ . \qquad 4.2$$

Here, $r = |\mathbf{r}|$ is the distance between the two dipoles and C_{dd} the dipolar coupling constant. The coupling constant is given by $\mu_0 \mu^2$ for particles with a permanent magnetic dipole moment μ, as in case of magnetic atoms, and $C_{\mathrm{dd}} = d^2/\epsilon_0$ for particles with an electric dipole moment d, e. g. for heteronuclear molecules. The magnetic constant μ_0 and the electric constant ϵ_0 are used here. The magnetic dipole moment is usually expressed in units of μ_{B}, whereas an electric dipole moment is given in units of Debye[1], D, due to convenience. The conversion factor[2] between magnetic and electric dipole moments is $1 \, \mu_{\mathrm{B}} \approx 9.274 \times 10^{-3} \, \mathrm{D}$.

The dipolar coupling constant for electric dipoles with a dipole moment of $1 \, \mathrm{D}$ is much larger than that for magnetic dipoles with a dipole moment of $1 \, \mu_{\mathrm{B}}$. This becomes obvious by expressing the magnetic and electric dipole moments by the fundamental definitions of μ_{B} and the Bohr radius[3], a_0. The ratio of magnetic to electric coupling constant is given by

$$\frac{\mu_0 \mu^2}{d^2/\epsilon_0} \approx \frac{\alpha^2}{1.6} \approx 3 \times 10^{-5} \ , \qquad 4.3$$

---

[1] A Debye is defined in SI units as $1 \, \mathrm{D} = \frac{1}{c} 10^{-21} \, \mathrm{C/m}$, with c the speed of light.

[2] The conversion factor can be calculated by setting $d^2/\epsilon_0 = \mu_0 \mu^2$ and using $\sqrt{\epsilon_0 \mu_0} = 1/c$, which gives for $d = 1 \, \mathrm{D}$ and $\mu = 1\mu_{\mathrm{B}}$ the following relation $\frac{1}{c\mathrm{D}} \mu_{\mathrm{B}} = 10^{21} \frac{e\hbar}{2m_e} \approx 9.274 \times 10^{-3}$.

[3] The Bohr radius is defined as $a_0 = \frac{4\pi\epsilon_0 \hbar^2}{m_e e^2} \approx 0.529 \times 10^{-10} \, \mathrm{m} \approx 0.05 \, \mathrm{nm}$, with m_e the electron rest mass and e the elementary charge.
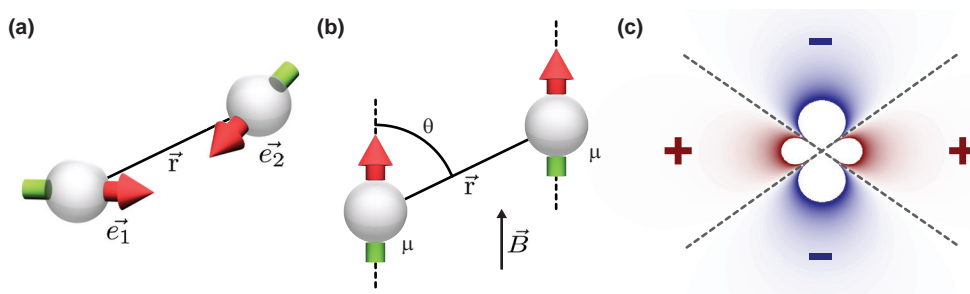
Figure 4.1.: Dipole-dipole interaction (DDI) between two dipoles. Schematic view of the geometry of two interacting dipoles (a) in the unpolarized case and (b) in the polarized case. (c) Interaction strength of the DDI, showing its anisotropic character. Regions where two dipoles repel each other are shown in red (positive potential) and where they attract one another are shown in blue (negative potential). The central white region is an artifact coming from a cutoff in the interaction strength used for plotting. It directly shows the *d*-wave angular symmetry. Dashed lines depict the angle at which the DDI is zero.

with α the fine-structure constant[4]. From now on, we will focus on atomic magnetic dipoles unless otherwise stated.

In presence of an external magnetic field, the dipoles will align along the direction of the field such that the atomic sample gets polarized, see Fig. 4.1(b). For two aligned dipoles, Eq. 4.2 simplifies to

$$U_{\mathrm{dd}}(\mathbf{r}, \theta) = \frac{\mu_0 \mu^2}{4\pi} \frac{1 - 3\cos^2\theta}{r^3} \ . \tag{4.4}$$

Here, θ is the angle between the orientation of the dipoles with respect to the interatomic axis and r denotes the distance between two dipoles. At $\theta_{\mathrm{m}} \approx 54.7^\circ$ the DDI vanishes. When changing θ from 0 to $\pi/2$ the interaction changes its sign. For angles smaller than θ_{m} the potential is negative and dipoles attract each other, whereas above θ_{m} the potential is positive, which leads to a repulsion between dipoles. The term $1 - 3\cos^2\theta$ ranges from -2 to 1, i. e. maximum attraction is twice as large as maximum repulsion. A configuration with $\theta = 0$, is called a *head-to-tail* configuration and with $\theta = \pi/2$ a *side-by-side* configuration of dipoles. It is interesting to note that the angular symmetry of the DDI equals the Legendre polynomial $P_2(\cos\theta)$ of second order and the interaction is thus *d*-wave symmetric, see Fig. 4.1(c).

The classification of the DDI as a long-range interaction is subtle as it depends on the dimensionality of the system. Following an approach in Ref. [Ast08], a classification can be done by checking whether the interaction energy of a system is extensive or intensive. An extensive energy is given when the integral of the interaction potential $U(\mathbf{r})$ converges,

$$\int_{r_0}^{\infty} U(\mathbf{r}) d^D r \ , \tag{4.5}$$

with D the dimensionality of the system and r_0 some short-distance cutoff parameter. If the integral does not converge, one speaks of an intensive energy. For a system with extensive energy the chemical potential μ depends only on the particle density n with $\mu = \mu(n)$. In

---

[4] The fine-structure constant is given by $\alpha = \frac{\hbar}{m_e c a_0} \approx \frac{1}{137}$.

contrast, for a system with intensive energy the chemical potential also depends on the total number of particles N and such $\mu = \mu(N, n)$. This difference is used in the following to classify short-range and long-range potentials. For interaction potentials decaying as $1/r^i$ at large distances, the integral in Eq. 4.5 converges if $D < i$. This means that the DDI with $i = 3$ has long-range character in three dimensions and the chemical potential is an extensive property of the system. In one and two dimensions the DDI has to be considered as short-range. As shown later, the van der Waals interaction has $i = 6$ and such it can be fully considered as a short-range interaction, even in three dimensions.

4.1.2. Anisotropic dispersion interaction

In the simplest case the attractive electronic interaction of two atoms is given by the dispersion potential[5], also known as van der Waals potential,

$$U_{\text{disp}}(\mathbf{r}) = -\frac{C_6}{r^6} \, , \qquad\qquad 4.6$$

where r is the internuclear distance and C_6 is a constant called the van der Waals coefficient. The potential is attractive, drops off with r^{-6} and is usually spherically symmetric. It is a short-range interaction and is caused by the interaction of the electrons of the two atoms. Its exact shape can be calculated from spectroscopic data, especially in case of alkali, alkali-earth, and alkali-earth-like atoms. For this, the well-known Born-Oppenheimer (BO) approximation is applied, in which the electronic part is decoupled from the nuclear part of the molecular wave function. Solving the full interaction Hamiltonian with the BO approximation gives the full electronic interaction potential, known as Born-Oppenheimer potential.

For lanthanide atoms, the dispersion interaction is anisotropic and the calculation of the BO potentials is more difficult than for alkali atoms as the electronic structure of the ground state is very complex and has many energy levels. Nevertheless, the group of S. Kotochigova at Temple University (USA) pioneered in calculating the dispersion potential for dysprosium atoms, see Ref. [Kot11]. The same approach was also applied to erbium atoms, see Ref. [Kot14].

Due to the strong spin-orbit coupling of lanthanide atoms in the ground state, their electron spin S is coupled to their electron orbital angular momentum L, such that the total atomic electron angular momentum $\mathbf{j}$ is formed. In the following, two colliding atoms with a total angular momentum $\mathbf{j_1}$ and $\mathbf{j_2}$ are investigated. Due to the strong magnetic field created by each of the atoms during a collision, $\mathbf{j_1}$ and $\mathbf{j_2}$ precess around the internuclear axis and give rise to the magnetic quantum numbers m_1 and m_2, see Fig. 4.2(a).

The collisional state is defined by the total angular moment $\mathbf{J} = \mathbf{j_1} + \mathbf{j_2}$, its projection M along the magnetic field, and its projection Ω along the internuclear axis, see Fig. 4.2(b). Values of Ω range from $0, 1, \ldots, J$. Each projection of J onto the internuclear axis gives rise

---

[5] The dispersion interaction, also known as London dispersion, describes only the attractive part of the Lennard-Jones potential. Its repulsive part becomes important at very small values of r and is not considered in Eq. 4.6
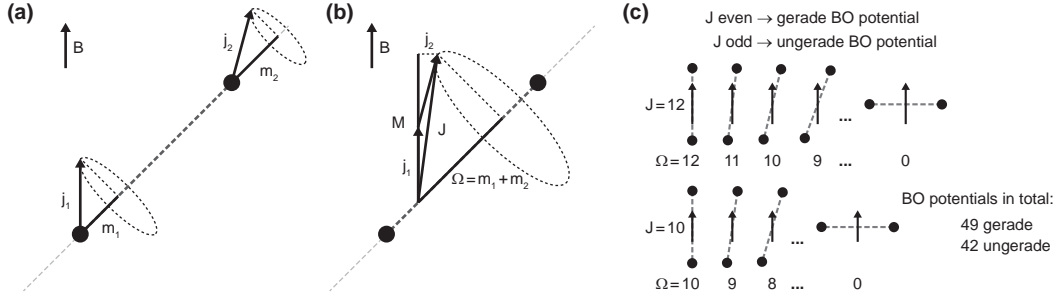
Figure 4.2.: Total angular moments $\mathbf{j_1}$ and $\mathbf{j_2}$ of two colliding atoms (shown as black dots) in an external magnetic field B. The internuclear axis is shown as gray dashed line. (a) The projection of $\mathbf{j_1}$ and $\mathbf{j_2}$ onto the nuclear axis is labeled with m_1 and m_2. (b) Both angular moments are coupled and form $\mathbf{J}$, which precesses around the internuclear axis and results in the projection Ω. Its projection in the direction of the magnetic field is called M. (c) Different values of Ω for $J = 12$ and 10. Even values of J give rise to 49 gerade Born-Oppenheimer (BO) potentials and odd values to 42 ungerade BO potentials (see text).

to a separate BO potential, see Fig. 4.2(c). Only the projections on the internuclear axis are good quantum numbers during a collision process, see Ref. [Kot11]. The quantum numbers m_1 and m_2 can change in a collision to m_1' and m_2' as long as $\Omega = m_1 + m_2 = m_1' + m_2'$ stays conserved.

For two erbium atoms, having $j = j_1 = j_2 = 6$ and $J = 12$, there are $(2j + 1) - \Omega$ different potentials with gerade and ungerade parity for each value of Ω. This results in a total of 91 BO potentials for Er$_2$. There are 49 potentials with gerade and 42 potentials with ungerade symmetry. Gerade BO potentials correspond to even values of J and ungerade potentials to odd values.

In case of colliding bosons with the same value of j_i, only gerade states have to be considered. Using atomic spectroscopy data, the BO potentials have been calculated within an ab initio relativistic, multi-reference configuration-interaction method developed in Ref. [Kot97]. This results in a *matrix* of van der Waals coefficients, $\boldsymbol{C_6}$, dependent on the quantum numbers m_1, m_2, m_1', and m_2'. Using this matrix, the dispersion potential has be written as

$$U_{\mathrm{disp}}(\mathbf{r}) = -\frac{\boldsymbol{C_6}(m_1 m_2, m_1' m_2')}{r^6} \ , \qquad 4.7$$

with r the separation between the atoms. The dispersion coefficients are calculated by evaluating the coupling from the initial state $|j_1 m_1, j_2 m_2\rangle$ to the final state $|j_1 m_1', j_2 m_2'\rangle$ by coupling through all possible electronic states $|n_a j_a m_a, n_b j_b m_b\rangle$ of intermediate electron configurations a and b. Here, n denotes the main quantum number of the electronic states. This calculation can be formally written as, see Ref. [Kot11],

$$\begin{aligned}
\langle j_1 m_1, j_2 m_2 | U_{\mathrm{disp}} | j_1 m_1', j_2 m_2'\rangle = \sum_{\substack{n_a j_a m_a \\ n_b j_b m_b}} \frac{1}{(E_1 + E_2) - (E_{n_a j_a} + E_{n_b j_b})} \\
\times \langle j_1 m_1, j_2 m_2 | U_{\mathrm{dd}} | n_a j_a m_a, n_b j_b m_b\rangle \\
\times \langle n_a j_a m_a, n_b j_b m_b | U_{\mathrm{dd}} | j_1 m_1', j_2 m_2'\rangle \ ,
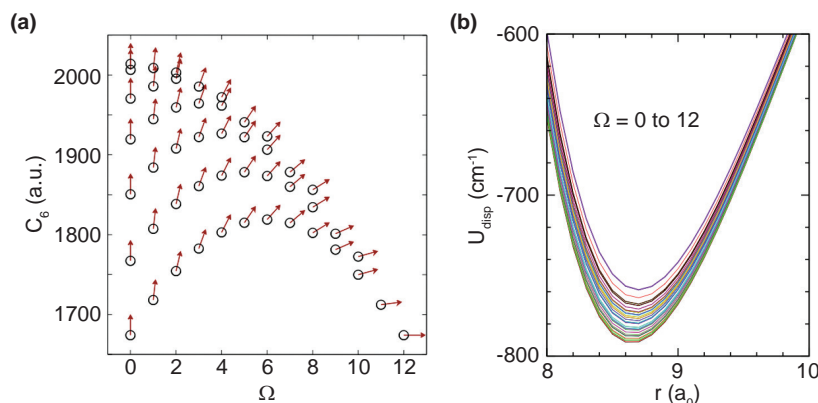\end{aligned} \qquad 4.8$$

Figure 4.3.: Van der Waals C_6 coefficients of erbium. (a) Different values of the C_6 coefficients of the 49 gerade BO potentials of Er_2 dependent on Ω. The red arrows show the orientation of J, when the internuclear axis is taken to be along the horizontal direction. (b) Born-Oppenheimer potential minima dependent on the internuclear distance r. In this graph, the different potential depth of all 49 gerade BO potentials is shown. Both graphs are taken from Ref. [Kot14].

with $E_{n_a j_a}$ and $E_{n_b j_b}$ the energies of the electron configuration a and b, and E_1 and E_2 the ground state energies of the colliding atoms. The coupling between two electronic states is induced by the electric dipole-dipole interaction as

$$U_{dd}(\mathbf{r}) = \frac{1}{4\pi\epsilon_0} \frac{\mathbf{d}_1 \cdot \mathbf{d}_2 - 3d_1 d_2}{r^3} \ .$$

4.9

Here, $\mathbf{d}_i$ are the electric dipole operators and d_i their projection along the internuclear axis.

Figure 4.3 shows the values of all calculated C_6 coefficients of the 49 gerade BO potentials of erbium dependent on the quantum number Ω. Note, that for different values of Ω a different number of C_6 coefficients exist, as shown in Fig. 4.2(c). The spread of the coefficients is caused by the anisotropic electric dipole interaction between electrons according to Eq. 4.9, which is in case of lanthanide atoms due to electrons in the $4f$ shell. It is often referred to as anisotropic dispersion interaction (ADI). The amount of anisotropy in the C_6 coefficients can be characterized by introducing ΔC_6. Results of the calculation for erbium atoms are $C_6 = 1723\,\text{a.u.}$ and $\Delta C_6 \approx 350\,\text{a.u.}$, see Ref. [Kot14].

Figure 4.4 gives an overview of relevant interaction terms for the collision of two erbium atoms. For comparison, the energy of the Zeeman splitting for a typical magnetic field of $B = 1\,\text{G}$ and $100\,\text{G}$ is shown additionally. Spin-changing collisions can only occur at internuclear distances where the anisotropic interaction terms, i.e. magnetic dipole-dipole interaction and anisotropic dispersion interaction, become larger than the Zeeman splitting, which is the case for distances of $r < 170\,\text{a}_0$ at $B = 1\,\text{G}$ but $r < 45\,\text{a}_0$ at $B = 100\,\text{G}$.

One of the most important consequences of anisotropic interactions, namely both DDI and ADI, is the fact, that they provide a coupling between electronic degrees of freedom and molecular rotation. The DDI couples rotational states with $\Delta\ell = 2$ and the ADI with $\Delta\ell = 4$, see Ref. [San03b]. This means, that during a collision, the m quantum numbers can change as long as the total projection quantum number $M_{tot} = m_1 + m_2 + m_\ell$ stays conserved.
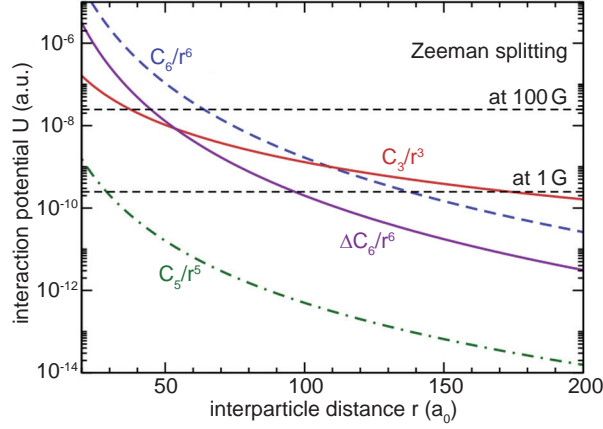
Figure 4.4.: Comparison of interaction potentials U in atomic units (a. u.) of two colliding erbium atoms dependent on the interparticle distances r. Here, we compare the magnetic dipole-dipole interaction $\frac{C_3}{r^3}$ (solid red), the electrostatic quadrupole-quadrupole interaction $\frac{C_5}{r^5}$ (dash-dotted green), the isotropic dispersion interaction $\frac{C_6}{r^6}$ (dashed blue), and the anisotropic dispersion interaction $\frac{\Delta C_6}{r^6}$ (solid purple). The quadrupole-quadrupole interaction can be neglected due to its small value. The long-range character of the dipole-dipole interaction can be observed, whereas at short-distances the dispersion interaction dominates. Taken from Ref. [Kot14].

This will be of importance, when we discuss the emergence of Feshbach resonances induced by anisotropic interactions, see Sec. 4.3.

In conclusion, the peculiar electron configuration of lanthanides leads to a highly anisotropic dispersion interaction potential. In combination with the DDI, these two interactions effectively couple atomic electronic states with molecular rotational states.

4.2. Dipolar scattering

The scattering process of two particles can be in the simplest case described by writing the total wave function as the sum of an incoming plane wave and an outgoing scattered wave. From the knowledge of the scattering amplitude, $f(\theta)$, one can calculate the differential cross section, i. e. the cross section per unit solid angle. The amplitude of the outgoing wave depends on the angle θ with respect to the incoming wave. The differential cross section is defined by

$$\frac{d\sigma}{d\Omega} = |f(\theta)|^2 \ . \tag{4.10}$$

The scattering cross section can then be calculated by integration, giving

$$\sigma = \frac{4\pi}{k^2} \sum_{\ell=0}^{\infty} (2\ell + 1) \sin^2 \delta_\ell \ , \tag{4.11}$$

with k the wave number of the incoming wave and δ_l the phase shift at $r \to \infty$ between the incoming and outgoing wave with an angular momentum quantum number[6] ℓ. The collision energy is given by

$$E = \frac{\hbar^2 k^2}{2m_r} \ .$$
     4.12

Here, m_r is the reduced mass with $m_r = \frac{m_1 m_2}{m_1 + m_2}$ for two particles of mass m_1 and m_2, which simplifies to $m_r = \frac{m}{2}$ for particles with identical mass m.

In case of an anisotropic interaction potential, a multichannel description of the scattering process has to be used, because the scattering problem can not be reduced to only one single channel, see Ref. [Mar98]. This would usually be the s-wave channel with $\ell = 0$ for colliding bosons. A calculation of the total elastic cross section between identical particles can then be carried out by

$$\sigma_{\text{el}\,(F)}^{B} = 8\pi \sum_{\substack{\ell,\ell'=(odd)}}^{even} \sum_{m_\ell, m_\ell'} |\mathbf{t}_{\ell m_\ell}^{\ell' m_\ell'}|^2 \ ,$$
     4.13

for bosons (B) and fermions (F), respectively. Here, m_ℓ is the projection of the angular quantum number and $\mathbf{t}_{\ell m_\ell}^{\ell' m_\ell'} = \mathbf{T}_{\ell m_\ell}^{\ell' m_\ell'}/k$ are the reduced T-matrix elements, which contains the asymptotic phase shift, δ_ℓ, of each partial wave. Note, that in the limit of spherically symmetric collisions, i.e. without any dipole-dipole interaction potential, the matrix reduces to $\mathbf{t}_{\ell m_\ell}^{\ell' m_\ell'} = -a_s \delta_{\ell 0} \delta_{\ell' 0} \delta_{m_\ell 0} \delta_{m_\ell' 0}$, with δ_{ij} the Kronecker delta.

In the case of a short-range potential, the phase shift changes as $\delta_\ell \propto k^{2\ell+1}$ for small k according to the Wigner threshold law. Assuming an interaction potential varying like r^{-i} at large distances this is only true for partial waves with $\ell < \frac{i-3}{2}$. For higher partial waves $\delta_\ell \propto k^{i-2}$, see Refs. [Lan77, Pet02]. The scattering phase shift for partial waves can be written as

$$\tan \delta_\ell \propto A k^{2\ell+1} + B k^{i-2} \ ,$$
     4.14

with constants A and B, which are determined by the interaction potential. The first term describes the action of the short-range potential, whereas the second is due to long-range scattering taking place outside the centrifugal barrier, see Ref. [Sad00].

For a van der Waals interaction potential with $i = 6$, this argument implies that all phase shifts of partial waves other than the s-wave become negligible small as $k \to 0$. In this case, the s-wave scattering cross section σ_s is only determined by the s-wave scattering length, a_s, and the phase shift can be written as $\delta_0 = -ka_s$. From Eq. 4.11 and also from Eq. 4.13 follows by approximation the well-known result for identical bosons[7] of

$$\sigma_{\text{el B}} = \sigma_s = \frac{8\pi}{k^2} \delta_0^2 = 8\pi a_s^2 \ .$$
     4.15

The fact that the s-wave scattering length is one of the most important parameters for collisions in the ultracold regime can be described by the following. Due to the large size of the thermal de Broglie wavelength, given by $\lambda_{\text{dB}} = h/\sqrt{2\pi m k_{\text{B}} T}$, at low temperatures T the

---

[6] The notation of partial waves follows the usual rule for labeling an angular momentum quantum number using $s, p, d, f, g, \dots$ for $\ell = 0, 1, 2, 3, 4, \dots$.

[7] For bosons, Eq. 4.11 has to be multiplied by two due to the symmetrization of the wave function.

inner-lying small-scale structure of the interaction potential can not be resolved anymore. Therefore, the shape of the potential does not matter as long as it gives the same value for the scattering length and such it can be replaced by a simpler model with the same effective interaction. This is known as the so-called *hard-core* model describing the contact interaction between particles.

In presence of DDI the picture of the scattering process changes fundamentally, see Ref. [Mar98]. Its long-range character dropping off as r^{-3} implies, that for all partial waves, the phase shift $\delta_\ell \sim k$ for small k and thus the phase shift does *not* vanish. It is explicitly shown in Ref. [Deb01], that the reduced T-matrix elements from Eq. 4.13 stay non-zero for $k \to 0$. This means that all partial waves contribute to the scattering amplitude and the scattering cross section contains a sum over phase shifts of all higher partial waves.

A direct consequence arising from dipolar scattering can be nicely observed using a Fermi gas in a single spin state. Namely, the scattering cross section of identical, dipolar fermions does not vanish at low temperatures. It rather approaches a constant, nonzero value when going to zero temperature as will be shown in the following. This is in stark contrast to the ordinary situation without DDI, for which $\sigma_{\mathrm{el\,F}} = 0$ for $T \to 0$. The consequence of the nonzero value is that scattering can be used to accomplish evaporative cooling of a single-state dipolar Fermi gas, which had been predicted by theory and was recently experimentally shown, see Ref. [Mar98] for theory and Chapter 9 for the experimental results.

4.2.1. Universal dipolar scattering

Dipolar scattering theories predict an energy-independent elastic scattering cross section in the regime of low energies, see Refs. [Lan77, Sad00, Bar08]. In this regime, σ_{el} takes a constant value, which is for fermions purely determined by the strength of the dipole-dipole interaction and the particle mass, whereas for bosons the *s*-wave contribution from contact interaction has to be added. When the DDI becomes the dominant interaction, i. e. when the scattering process is insensitive to short-range interactions, the emergence of an *universal* behavior can be observed, see Ref. [Tic08]. This causes different dipolar systems, bosonic as well as fermionic ones, to show basically the same scattering behavior. According to Ref. [Boh09], a universal scaling law can be found in two distinct regimes. The first regime is at low collision energies with a constant scattering cross section, whereas the second one is found at large collision energies. To estimate the transition point between these two regimes, it is important to compare the collision energy from Eq. 4.12 with the energy scale set by the DDI as

$$E_D = \frac{C_{\mathrm{dd}}}{4\pi a_D^3} = \frac{16\pi^2 \hbar^6}{m_r^3 \mu_0^2 \mu^4} \; . \tag{4.16}$$

Here, a_D is a typical length scale for characterizing two colliding dipoles[8]. This gives

$$a_D = \frac{m_r C_{\mathrm{dd}}}{4\pi \hbar^2} \; , \tag{4.17}$$

---

[8] It can be obtained by equating the centrifugal energy $E_Z = \frac{\hbar^2}{m_r a_D^2}$ with the dipolar energy E_D. Its definition is similar to the dipole length, a_d, with the only difference that for two colliding dipoles the reduced mass has to be considered.

which results for two colliding ^{168}Er atoms in $a_D = 99.4\,a_0$. Taken this into account, the dipolar energy of ^{168}Er is $E_D = k_B \times 209\,\mu$K and for fully polarized KRb as low as $k_B \times 83$ nK. Temperatures below this energy belong to the *ultracold* and above to the *cold* regime. Only in the ultracold regime, purely elastic threshold scattering can be observed, whereas in the cold regime inelastic collision have to be taken into account.

The second universal behavior can be observed for collisional energies larger than the dipolar energy, i. e. outside the threshold region. In this cold regime, the cross section scales as $\sigma \sim a_D/k$. Here k is the wave number of relative motion of the two collision partners and thus σ drops off as $1/\sqrt{E}$. At even higher temperatures, the collision becomes semiclassical.

By applying the Born approximation to the scattering of dipoles one can calculate expressions for the elastic cross section in the ultracold limit with a collision energy $E < E_D$. The Born approximation assumes that the incoming scattering wave is not substantially changed by the interaction potential, which is true for long-range scattering outside the centrifugal barrier, see Refs. [Sha72, Gao99, Gao08]. The result for the total elastic cross section, σ_{el}, depends on whether scattering occurs in even or odd partial waves with

$$
\begin{aligned}
\sigma_{\mathrm{el}}^{\mathrm{e}} &= \sigma_{\mathrm{Born}}^{\mathrm{e}} + \sigma_s = \frac{16\pi}{45}a_D^2 + 4\pi a_s^2 \,, & \text{even} \quad \text{(i. e. for bosons)} \\
\sigma_{\mathrm{el}}^{\mathrm{o}} &= \sigma_{\mathrm{Born}}^{\mathrm{o}} = \frac{16\pi}{15}a_D^2 \,, & \text{odd} \quad \text{(i. e. for fermions)} \,.
\end{aligned}
\tag{4.18}
$$

For even partial waves the second term gives the contribution coming from the contact interaction characterized by the s-wave scattering length a_s. For indistinguishable particles both cross sections in Eq. 4.18 have to be multiplied by two. For distinguishable particles in different partial waves both cross sections of even and odd partial waves have to be added. In case of s-wave scattering of identical bosons the elastic cross section reads

$$
\sigma_{\mathrm{el\,B}} = \frac{32\pi}{45}a_D^2 + 8\pi a_s^2 \,,
\tag{4.19}
$$

whereas for identical fermions colliding in p-wave the cross section reads

$$
\sigma_{\mathrm{el\,F}} = \frac{32\pi}{15}a_D^2 \,.
\tag{4.20}
$$

It is remarkable that σ_{el} only depends on the dipole length a_D and on a_s for bosons, but is independent of energy and temperature. The universal behavior of the scattering length was studied in detail with a deeply degenerate Fermi gas of ^{167}Er for the first time, see Chapter 9. Signatures of this effect have been observed in an experiment using ^{161}Dy, see Ref. [Lu12].

4.3. Anisotropy-induced Feshbach resonances

Feshbach resonances (FR) are well-studied in collisions of alkali-metal atoms, see Ref. [Chi10] for a review. They are used in many applications in ultracold-gas experiments and have developed to a standard tool within the last decade. The existence of FR allows for example to tune the particle's scattering length and convert a weakly interacting gas into a strongly

interacting gas of atoms. Alternatively, the scattering length can be tuned to zero, which essentially turns off interactions and an ideal Bose or Fermi gas can be prepared. FRs had also been the key element in observing the crossover from a molecular BEC to a degenerate Fermi gas, the so-called BEC-BCS crossover [Bar04]. Furthermore, two particles can be associated to a weakly-bound molecule using a FR [Köh06], which is the first step in creating ultracold polar molecules in its rovibronic ground state by transferring them with the help of the stimulated Raman adiabatic passage (STIRAP) technique [Dan08, Lan08, Tak14]. As a last example, FRs make it possible to study three-body Efimov physics [Kra06, Fer11]. In most applications, FRs are either induced magnetically/electrically by an external magnetic/electric field or optically by a light field. The method of using a magnetic field is commonly implemented because of its ease of use in the experiment and will be the focus of this thesis.

The exotic interaction properties of erbium give rise to a very rich Feshbach spectrum, see Ref. [Kot14]. It is instructive to compare FRs in erbium with those in ordinary alkali metals. In the latter case, FRs are induced by a different magnetic moment of different molecular hyperfine states. For bosonic erbium, FRs occur due to the coupling of rotational bound states because hyperfine structure is missing here. The coupling is achieved by the anisotropic dispersion potential as well as the anisotropic dipole-dipole interaction, see Ref. [San03b]. Calculations have shown that both interactions give significant contributions to the Feshbach spectrum, see Ref. [Pet12] and Fig. 4.6. The very same argument also applies to the collision of dysprosium atoms, but does not apply to chromium atoms, as in this case anisotropic dispersion interaction is absent.

FRs can be studied only at ultracold temperatures, where losses due to inelastic three-body collisions are suppressed. In case of bosonic erbium, all atoms are prepared in the lowest Zeeman sublevel with a total atomic angular momentum of $j_1 = j_2 = 6$ and its projection along the magnetic field $m_{j1} = m_{j2} = -6$. There is no hyperfine structure for bosons due to zero nuclear spin quantum number. For collisions of atoms in this *stretched* state exists only one collision channel with zero relative nuclear orbital angular momentum quantum number ℓ, resembling a *s*-wave collision. FRs only appear due to the coupling to bound states with $\ell \neq 0$, see Ref. [Pet12]. The Hamilton operator describing the collision can be written as

$$\hat{H} = -\frac{\hbar^2}{2m_r}\frac{d^2}{dr^2} + \frac{\hat{\boldsymbol{\ell}}^2}{2m_r r^2} + g_j\mu_B(m_{j1} + m_{j2})B + \hat{V}(\mathbf{r}, \tau) \, , \qquad 4.21$$

with m_r the reduced mass and B a homogeneous magnetic field along the z-direction. Here the first two terms give the relative kinetic and rotational energies of the collisional state and the third term denotes the Zeeman interaction energy, with g_j the g-factor. The electronic Hamiltonian, $\hat{V}(\mathbf{r}, \tau)$, is anisotropic and depends on the orientation and separation between the two atoms, with an electronic configuration labeled by τ. It consists of the magnetic dipole-dipole and quadrupole-quadrupole interaction as well as the anisotropic dispersion interaction. As shown in Sec. 4.1.2, the anisotropic dispersion interaction is caused for lanthanides by electrons distributed in the $4f$ shells. These shells lie deep within the atom's electron cloud and do not overlap with the electron cloud of the nearby atom. Thus, the bonding of lanthanide molecules is mainly due to an overlap of the outer-lying isotropic $6s$ shells.
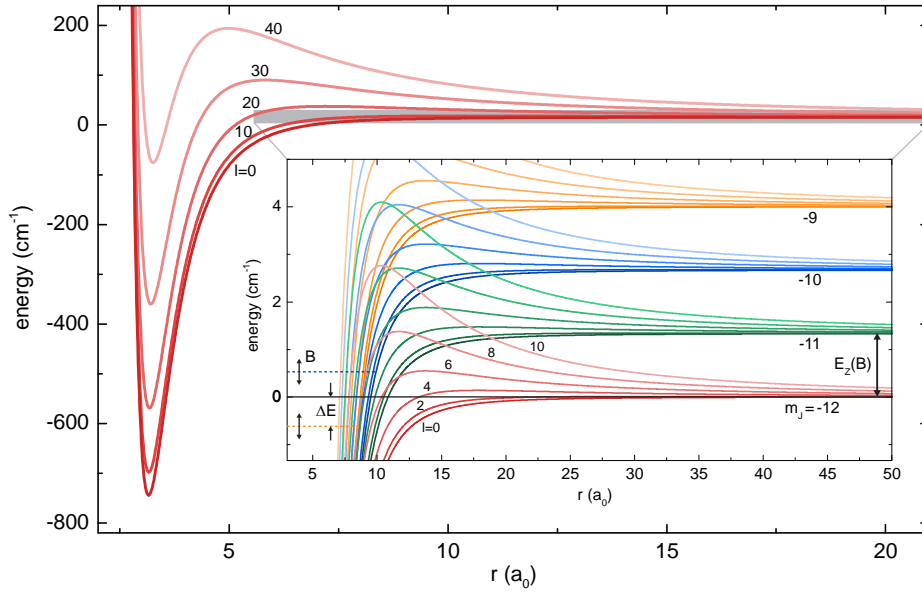
Figure 4.5.: Anisotropy-induced Feshbach resonances of bosonic erbium atoms. The molecular potential, which depends on the internuclear distance r, is shown only for selected values of ℓ. In principle, 49 different BO potentials are present for every value of ℓ, as in Fig. 4.3(b), but for simplicity only the molecular potential for $\Omega = 12$ is plotted. The red lines show rotational states up to $\ell = 40$ in steps of ten for the energetically lowest magnetic state with $m_J = -12$. The Zeeman splitting $E_Z(B)$ for a magnetic field of $50\,\mathrm{G}$ is only visible after scaling the gray shaded area of the plot, see inset. Here, the open channel is shown as a solid black line, and closed channels by dotted lines. States with different magnetic quantum numbers m_J are coded in color. As the Zeeman splitting depends on B, the energy of each bound state is tunable with B (indicated by arrows). A FR appears, whenever the energy of a bound state crosses the threshold of the open channel making $\Delta E = 0$. Due to the large number of magnetic states and the coupling of rotational states up to $\ell \approx 50$, the density of accessible closed channels is extremely high. This large density can't be observed with alkali metals.

As shown in Ref. [Pet12], coupled-channel (CC) calculations can be performed in the basis $|(j_1 j_2)j m_j, \ell m_\ell\rangle = Y_{\ell m}(\theta, \phi)\,|(j_1 j_2)j m_j\rangle$, with $Y_{\ell m}(\theta, \phi)$ the spherical harmonic functions and the angles θ and ϕ give the orientation of the internuclear axis with respect to the magnetic field. The Hamiltonian of Eq. 4.21 conserves $M_{\mathrm{tot}} = m_J + m_\ell$ and is invariant under parity operation, so that only even or odd ℓ states are being coupled with each other. In case of homonuclear collisions only basis states with even $J + \ell$ exist and for s-wave collisions of erbium atoms it gives $M_{\mathrm{tot}} = -12$.

Figure 4.5 shows the magnetic tunability of molecular potentials, which is a necessary premise for the existence of magnetic FRs. States with a rotational quantum number up to $\ell = 40$ are shown in the figure. A change of ℓ is possible due to strong anisotropic interactions between the two atoms, which couples rotational states with $\Delta \ell = \pm 2$. Atoms collide in an incoming or open channel and can be resonantly transferred into a bound molecular state or closed channel, when the energies of both channels are degenerate. The separation between the two channels, ΔE, is tunable by an external magnetic field B via the Zeeman shift.

Early CC calculations of the scattering length have revealed many FRs at magnetic fields below $200\,\mathrm{G}$ already when taking only up to $\ell = 10$ partial waves into account, see Fig. 4.6.
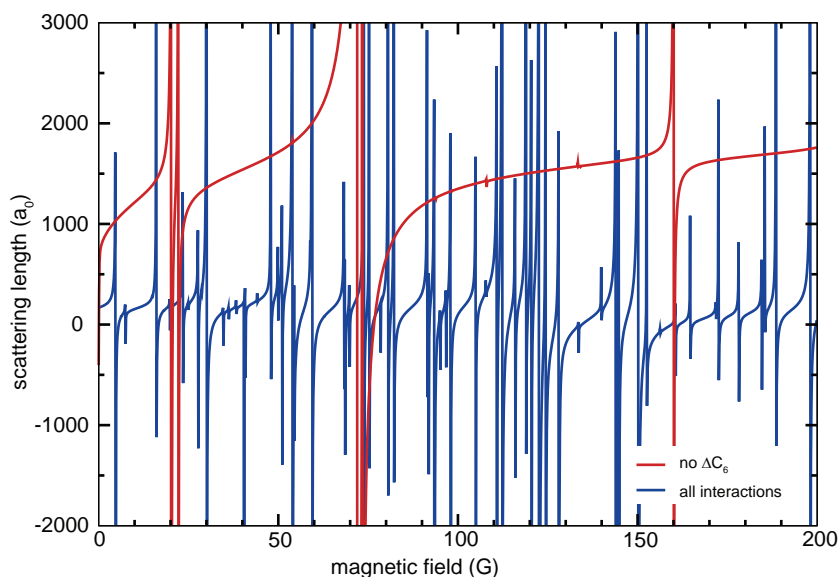
Figure 4.6.: Preliminary calculated scattering length of ^{168}Er dependent on the magnetic field to show the important role of the anisotropic dispersion interaction. When neglecting the anisotropic dispersion interaction (red), the number of FRs is strongly decreased compared to the case, in which all interactions are taken into account (blue). Only rotational states up to $\ell = 10$ have been considered for coupled-channel calculations. This calculation was carried out for a temperature of 30 nK and zero collision energy. Taken from Ref. [Kot].

A qualitative analysis showed that more resonances appear as more and more partial waves were included in the calculations. Recent measurements verified a number of resonances corresponding to a density of about three per Gauss, see Refs. [Bau14, Pfa] for dysprosium and Chapter 10 for erbium. An estimation using a random quantum defect theory approach suggests that up to $\ell \approx 50$ partial waves need to be included for describing the experimental results.

Within the coupled-channel calculations, not only the density of resonances changes with increasing values of ℓ but also the position of a resonance shifts significantly. The position converges within a few Gauss for a partial wave number being four larger than the partial wave number at which the resonance has initially appeared. This behavior with increasing ℓ and the strong coupling of rotational states can not be observed in ultracold gas experiments with alkali-metal atoms or chromium. Moreover, it even requires a new way of labeling FRs. It was suggested in Ref. [Pet12] to use the specific ℓ value at which a FR appears in calculations for labeling purposes. Recent work has shown that measuring the magnetic moment of the bound state might be utilized to assign rotational quantum numbers for specific FRs, see Refs. [Aik14a, Kot].

As mentioned earlier, a FR occurs when the energy of the closed state, $E_c = \Delta E$, is equal to the energy of the open channel, such that $E_c = \delta\mu(B - B_c) = 0$. Here, $\delta\mu$ is the magnetic moment of the molecular state with respect to the magnetic moment of the atomic threshold and B_c is the magnetic field, at which the uncoupled closed channel crosses the threshold. Then the bound state is strongly coupled to the open channel and the scattering length
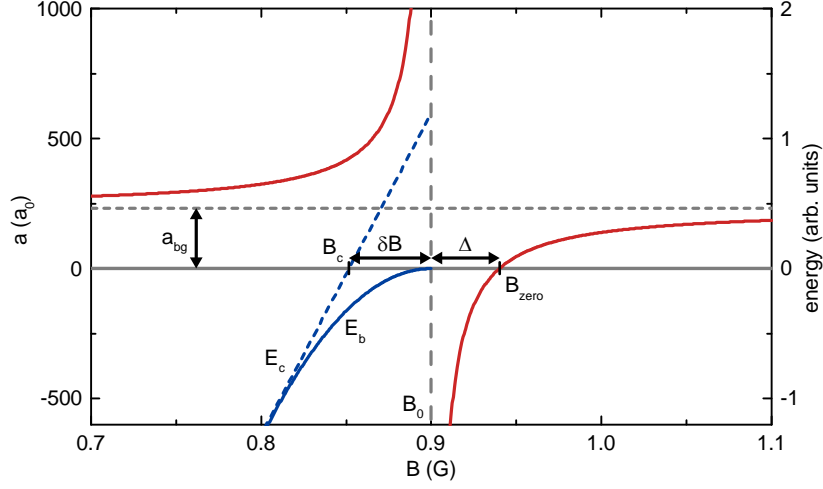
Figure 4.7.: Scattering length (red) and binding energy (blue) close to a Feshbach resonance of ^{168}Er. The scattering length diverges at the position of the resonance B_0 and has a zero crossing at B_{zero}, which is characterized by the resonance width Δ. The resonance position is shifted by δB due to coupling between open and closed channels. The bound state energy, E_b, varies quadratically close to the resonance, whereas the energy of the bare, uncoupled closed channel, E_c, depends linearly and crosses the threshold at B_c.

depends on the magnetic field like, see Ref. [Chi10],

$$a(B) = a_{\mathrm{bg}} \left(1 - \frac{\Delta}{B - B_0} \right) \; , \qquad\qquad 4.22$$

where $\Delta = |B_{\mathrm{zero}} - B_0|$ is the width and B_0 is the position of the resonance, see Fig. 4.7. Here B_{zero} is the magnetic field at which $a = 0$. The background scattering length a_{bg} characterizes the scattering length away from the resonance. The position of the FR, B_0, at which a diverges, is shifted away from the position without coupling, which is denoted by B_c, due to the coupling between the closed and open channel. The shift is given by $\delta B = -\delta E / \delta \mu$, which results in $B_0 = B_c + \delta B$.

Note that in case of alkali atoms only the van der Waals interaction determines a_{bg}, whereas for dipolar systems an additional dipolar contribution to the scattering length has to be considered. See Sec. 7.3.1 for a measurement of the scattering length of different erbium isotopes via the cross-dimensional rethermalization method.

Close to the FR the energy of the bound state depends quadratically on the magnetic field with

$$E_b = -\frac{\hbar^2}{2 m_r a^2} \; . \qquad\qquad 4.23$$

Further away from the FR, the energy of the closed channel E_c varies linearly with the magnetic field as

$$E_c = -\delta \mu B \; . \qquad\qquad 4.24$$

The binding energy of the closed channel can be measured relative to the two-atom threshold energy by magnetic field modulation spectroscopy. In the erbium experiment, this technique

was recently used to measure the magnetic moment of five different molecular states at FRs below 2.5 G. The values of the measured molecular magnetic moments range from $\mu = 7.96\,\mu_B$ to $11.8\,\mu_B$, see Ref. [Aik14a].

In principle, for higher magnetic fields the magnetic moment of the molecular state can be any combination of the magnetic moment of two atoms in some m_J states. The maximum magnetic moment would be twice the magnetic moment of atoms in $m_J = -6$, which results in a maximum magnetic moment of $13.96\,\mu_B$ for the Er_2 molecule. This molecular state lies parallel to the atomic threshold and is difficult to prepare by ramping the magnetic field because it has to be entered utilizing another molecular state with lower magnetic moment. But preparing such a molecular state will be interesting in future, as this gives a maximally large dipole length four times as large as that for atoms making Er_2 molecules competitive to current experiments using polar heteronuclear molecules.

C h a p t e r

5

Random matrix theory

Random matrix theory (RMT) was introduced by Wigner in the 1950s, see Refs. [Wig51a, Wig51b]. RMT was developed to describe statistical properties of neutron scattering spectra. This approach was necessary as the recorded nuclear spectra revealed unprecedented complexity and an exact theoretical description was not possible. Early experiments in the 1930s revealed numerous narrow resonances in the neutron scattering on light nuclei, see Refs. [Fer34, Fri36]. It was the insight of Bohr that these spectra could only be explained by a nucleus of great complexity with strongly interacting constituents, see Ref. [Boh36]. Later this idea led to the discovery of the nuclear shell model in 1949.

The main advantage of RMT is that one can describe generic spectral properties without the knowledge of the Hamiltonian governing the system's behavior. This is done by substituting the real Hamiltonian by an ensemble of randomly generated Hamiltonians, whose matrix elements obey a certain probability distribution, hence the name random matrices. According to the symmetry of the underlying system these Hamiltonians belong to a specific ensemble, e. g. real and symmetric matrices in the case of time-reversal symmetry. A comprehensive theory of the statistical properties of RMT was developed in the 1960s by Dyson and Mehta, see Refs. [Dys62a, Dys62b, Dys62c, Dys63, Meh63]. Such statistical properties include the character of spectral fluctuations, which are revealed by spacing distributions and number variances.

It was speculated in Ref. [Bro81] that the study of spectral fluctuations in complicated systems can be applied to other many-body systems outside nuclear physics. In 1984 a behavior according to RMT was found in a classical scattering experiment as well as in its quantum-mechanical analog, see Ref. [Boh84b]. This led to a strong connection between quantum physics and classical chaos theory by the formulation of the so-called *Bohigas-Giannoni-Schmit* (BGS) conjecture. The field of studying spectral fluctuations and correlations in quantum few- and many-body systems is today known as *quantum chaos* and has since the BGS conjecture acquired much attention.

In the following section we will give a short introduction to the theoretical formalism of RMT. Secction 5.2 presents the connection between classical chaos and quantum chaos and Sec. 5.3 provides an application of RMT to ultracold scattering processes.

68
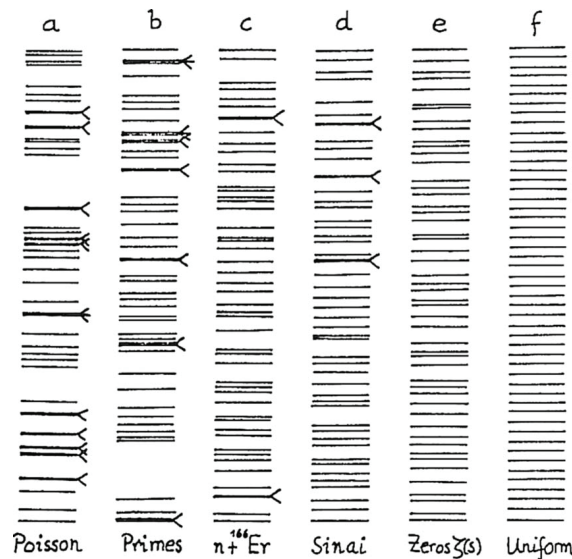
Figure 5.1.: Six different level spectra for various types of level correlations but with the same mean level density. In (a) the levels are fully uncorrelated (Poisson), whereas in (c) (neutron scattering on ^{166}Er atoms) and (d) (Sinai billiard, see Sec. 5.2) the level distribution follows the GOE prediction. In (f) all levels are uniformly distributed. Taken from Ref. [Boh84a].

5.1. Introduction to RMT

5.1.1. General idea of RMT

Trying to tackle a complex system either from the experimental or the theoretical point of view can be very difficult, especially if the exact Hamiltonian of the system is unknown in the first place. Applying RMT to these problems can certainly *not* provide an exact solution, e.g. predicting the position of individual resonances, but what it *can do* is offering a first insight into 'global' properties of the system. There exists a strong similarity between RMT and thermodynamics in the sense that only a few global properties define a rather complex system. This implies some sort of universality in the application of the random matrix approach, which allows it to be used in many different fields, see Refs. [Ros60, Guh98]. The most intriguing consequence of RMT is that levels or eigenstates of the system are correlated. This correlation is revealed by a characteristic fingerprint in several of the system's statistical properties.

Providing an example for this correlation Fig. 5.1 shows different sets of level spectra from the fully uncorrelated case, to level distributions according to RMT, to uniformly distributed levels. These sets have all the same level density but they are distinguishable by analyzing the degree of correlation between levels.

5.1.2. Applications of RMT

Above mentioned universality makes the RMT applicable to many different fields beyond its origin in nuclear physics. The general predictions of RMT were found in many complex systems ranging from analyzing financial correlation matrices [Lal99, Bou09], to wireless multiuser communication techniques [Tul04, Mül13], electric grid topology planning [Mar10], neural networks [Raj06], to RNA folding theories [Orl02], just to name a few.

5.1.3. Symmetry groups and Gaussian ensembles

RMT classifies systems by their symmetry properties, see Ref. [Wei09]. A system with N correlated energy levels is described by a Hamiltonian H of size $N \times N$ with entries H_{nm}. All entries are randomly chosen according to a Gaussian distribution. As defined in Ref. [Dys62a] there are three possible Gaussian symmetry classes available within RMT. These symmetry classes are labeled by the Dyson index β. In the case of time reversal and rotational symmetry (e.g. when the system has integer spin) the matrix H is real symmetric ($\beta = 1$). For half-integer spin rotational symmetry is broken and H is self-dual with quaternionic entries ($\beta = 4$). For a non time-reversal symmetric system all H_{nm} are complex numbers ($\beta = 2$).

Diagonalizing the random matrix $H = U^{-1}xU$ gives N eigenvalues $x = \text{diag}(x_1, \ldots, x_N)$. The diagonalizing matrix U belongs to the orthogonal group $\text{O}(N)$ for $\beta = 1$, to the unitary group $\text{U}(N)$ for $\beta = 2$, and to the unitary-symplectic group $\text{USp}(2N)$ for $\beta = 4$. Due to the use of a Gaussian distribution for constructing the random Hamiltonian the ensembles are therefore called *Gaussian orthogonal* (GOE), *unitary* (GUE), and *symplectic ensemble* (GSE) for $\beta = 1, 2, 4$, respectively.

Each entry of H is chosen randomly from a Gaussian distribution with a probability density function $\mathcal{P}_N^{(\beta)}(H)$. It has a zero mean value and a variance fixed by λ. The probability density is given as

$$\mathcal{P}_N^{(\beta)}(H) = C_N^{(\beta)} \exp\left(-\frac{N\beta}{4\lambda^2}\,\text{tr}H^2\right) \ . \tag{5.1}$$

Here, the constant λ sets the energy scale, which is defined by the level density, see Eq. 5.3, and the constant $C_N^{(\beta)}$ ensures normalization. Note that no basis set had to be chosen for constructing $\mathcal{P}_N^{(\beta)}(H)$ and thus H only depends on its eigenvalues, for which $\mathcal{P}_N^{(\beta)}(H) = \mathcal{P}_N^{(\beta)}(x)$ holds.

The mean level density of a spectrum, $\bar{\rho}(x)$, is defined as

$$\bar{\rho}(x) = \overline{\sum_i \delta(x - x_i)} \ , \tag{5.2}$$

with i an index over individual levels at position x_i, δ the delta function, and the bar denoting an average value. It is equivalent to the density of states of the system and is for Gaussian
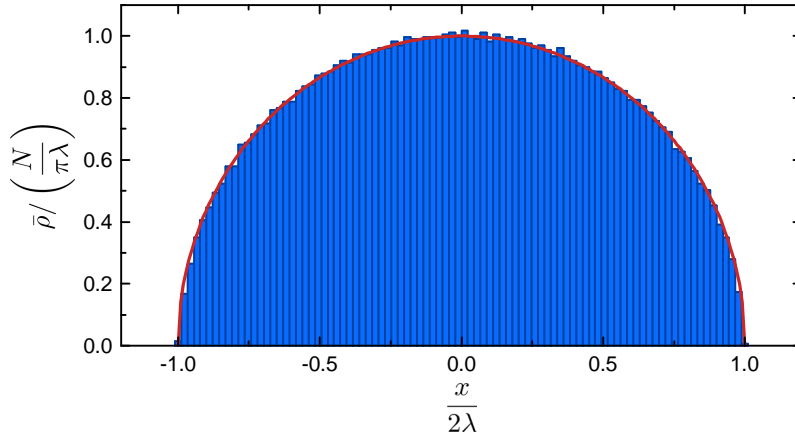
Figure 5.2.: Histogram of the calculated mean level density $\overline{\rho}(x)$, for 10,000 individual random matrices of size 10,000 × 10,000 (blue). Spectrum according to Eq. 5.3 (red line). The semicircular shape of the spectrum is clearly visible.

ensembles given by

$$\overline{\rho}(x) = \begin{cases} \frac{N}{2\pi\lambda^2}\sqrt{4\lambda^2 - x^2} & \text{if } |x| \leq 2\lambda \\ 0 & \text{if } |x| > 2\lambda \ . \end{cases} \qquad 5.3$$

This equation is known as the *semicircle law*, which was found by Wigner, see Refs. [Wig57a, Wig58]. The spectrum of $\rho(x)$ has the shape of a semicircle with radius 2λ and a mean level density at the center of the semicircle of $\overline{\rho}(0) = \frac{N}{\pi\lambda}$, see Fig. 5.2. Usually the limit $N \to \infty$ has to be taken to suppress cutoff effects in the spectrum. In reality almost no physical system has a bound spectrum in shape of a semicircle as one can always observe resonances at larger values of x and thus $\overline{\rho}(x)$ is not zero even for $\frac{x}{2\lambda} > 1$, see Ref. [Guh98]. But for small values of $\frac{x}{2\lambda}$ the semicircle is a good approximation.

The mean level spacing between consecutive levels is defined by

$$\overline{d}(x) = \frac{1}{\overline{\rho}(x)} \ . \qquad 5.4$$

It tends to zero as $N \to \infty$ for constant λ because N eigenvalues have to fit into a finite energy interval from -2λ to $+2\lambda$. For $x = 0$ the mean level spacing equals $\overline{d}(0) = \frac{\pi\lambda}{N}$.

5.1.4. Statistical properties

RMT was developed to describe the statistical properties of energy spectra recorded in nuclear scattering experiments, see Ref. [Wei09]. There exists a great number of tools for analyzing these statistical properties. A comprehensive description of most relevant observables can be found in Refs. [Bro81, Wei09]. More recently developed methods include for example analyzing the $1/f$ noise of quantum chaotic spectra, see Ref. [Rel02], or the usage of maximum likelihood methods for correcting possibly missed levels, see Ref. [Mul11]. Only a small selection of the most important measures of RMT is discussed in the following. Some quantities show the short-range correlations, like the nearest-neighbor spacing probability,
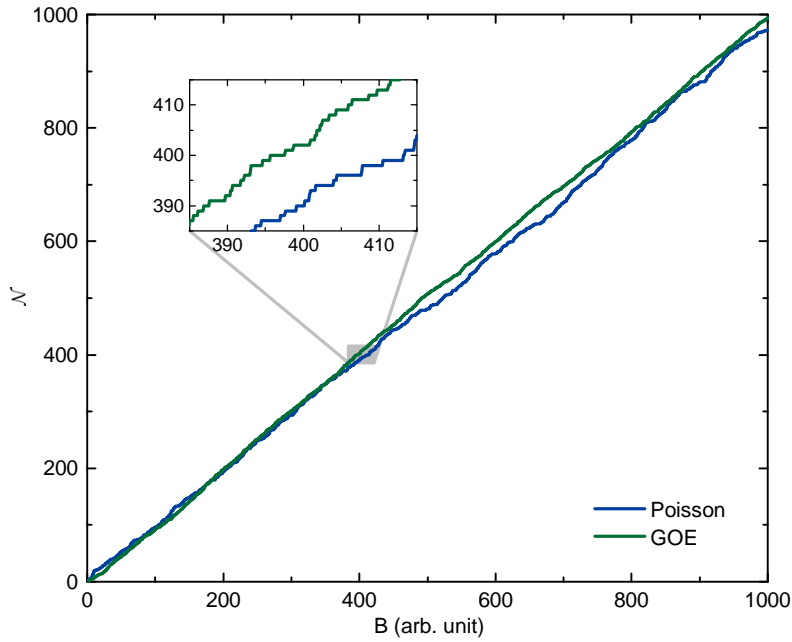
Figure 5.3.: Simulated staircase function of uncorrelated levels (Poisson) and levels according to a Gaussian orthogonal ensemble (GOE), both assuming a density of resonances of unity. The inset emphasizes the integer nature of the staircase function. Note the larger fluctuations of levels in the case of a Poisson distribution compared to levels following a GOE, which are visible as larger deviations from a line with unity slope.

whereas others probe the long-range correlation of the spectrum, e. g. the number variance and the two-gap correlation function. For applying these methods to Feshbach spectra we will redefine all necessary statistical properties in terms of a dependence on the magnetic field B.

It is common in the RMT data analyzing process to first plot the position of resonances in the so-called *staircase function*, see Ref. [Wei09]. This step-like function counts the number of resonances up to some magnetic field value. It is defined as

$$\mathcal{N}(B) = \int\limits_0^B dB' \sum_i \delta(B' - B_i) \, , \qquad\qquad 5.5$$

with δ being the delta function and B_i the position of the i-th resonance. Figure 5.3 shows the staircase functions for two randomly generated sets of data of uncorrelated and correlated resonances with a density of one per unit. It can easily be seen that the staircase function of correlated resonances deviates less from a line with unity slope than the staircase function of uncorrelated resonances.

One of the central observables to discriminate uncorrelated from correlated resonances in a spectrum is to calculate the nearest-neighbor spacing (NNS) distribution $P(s)$, see Fig. 5.4(a). Here, s is the actual spacing between levels in units of the mean level spacing $\bar{d}$. As shown in Refs. [Ber77, Bro81] the probability distribution of a system with uncorrelated classical
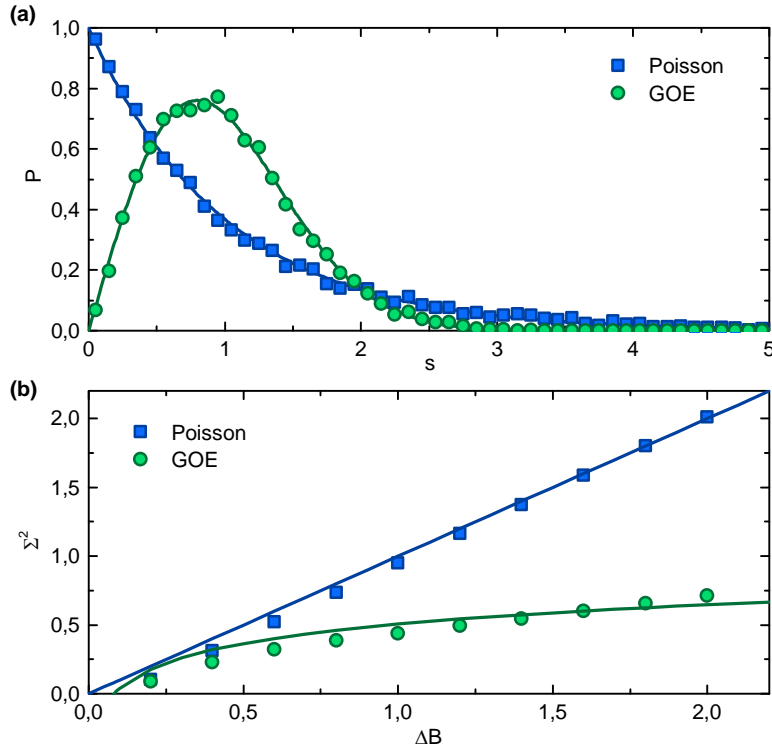
Figure 5.4.: (a) Nearest-neighbor spacing distribution for uncorrelated levels (Poisson) and levels according to a Gaussian orthogonal ensemble (GOE). Lines show the distributions given by Eq. 5.6 and 5.7. Points are calculated from a randomly generated dataset of 100,000 levels assuming a Poisson or Wigner-Dyson distribution, respectively. (b) Number variance of levels according to a Poisson and Wigner-Dyson distribution. Lines show the theoretical values from Eq. 5.12 and 5.13 and points show calculated values of the generated dataset.

dynamics is simply given by the Poisson distribution

$$P_{\mathrm{P}}(s) = \exp(-s) \ . \qquad\qquad 5.6$$

An exact expression for the spacing distribution of a Gaussian orthogonal ensemble can not be written down in a simple form but according to the *Wigner surmise*, see Ref. [Wig57b], a good approximation is provided by the Wigner-Dyson distribution

$$P_{\mathrm{WD}}(s) = \frac{\pi}{2}s \exp(-\pi s^2/4) \ . \qquad\qquad 5.7$$

Note that both distributions are not only normalized with $\int ds\, P(s) = 1$ but they have also the same mean value as $\int ds\, s\, P(s) = 1$. What makes them differ strongly from each other is their variance. For the Poisson distribution it is $\int ds\, (s-1)^2 P_{\mathrm{P}}(s) = 1$ whereas for the Wigner-Dyson distribution the variance is 0.5224, see Ref. [Gut90]. This difference in variances can be easily probed by analyzing the local fluctuations of levels, i. e. analyzing the level correlations.

Regarding the NNS distribution the properties of the other two Gaussian ensembles, i. e. GUE and GSE, differ from the GOE as $P(s)$ shows a dependence on s, which is proportional to

s^β for small values of s. This means that for a GOE $P(s)$ shows a linear increase, see Fig. 5.4(a), whereas for a GUE it increases quadratically, and for a GSE it increases with the fourth power. This implies that the eigenvalues of a GUE and a GSE are even stronger correlated and repel each other more than in the GOE case. Uncorrelated levels show no repulsion at all and are often referred to by $\beta = 0$.

In Ref. [Bro73] an empirical function was introduced to interpolate between P_P and P_{WD}. It is called the Brody distribution and has a single fitting parameter η. It quantifies the tendency (but not the degree of chaoticity) of the observed distribution to be more Poisson-like ($\eta = 0$) or more Wigner-Dyson-like ($\eta = 1$). The Brody distribution is defined by

$$P_B(s) = As^\eta \exp(-\alpha s^{\eta+1}) \qquad 5.8$$

$$A = (\eta + 1)\alpha \qquad 5.9$$

$$\alpha = \left[\Gamma\left(\frac{\eta+2}{\eta+1}\right) \right]^{\eta+1} , \qquad 5.10$$

where Γ denotes the Gamma function.

To calculate the NNS probability distribution $P(s)$ from a measured spectrum a histogram of level spacings has to be constructed using an appropriate bin size or number of bins N_{bin} for distinguishing between the two distributions. There is no fixed rule for choosing an optimum bin size for an arbitrary histogram, see Ref. [Tay97]. Using a number of bins of $N_{bin} = \sqrt{N_{res}}$ where N_{res} is the number of observed resonances usually provides reasonably good results. A too small bin size increases the error on each value of the histogram and a too large bin size makes it difficult to differentiate between different distributions.

For a reliable statistical analysis following RMT one has to make sure that the staircase function increases linearly over a large range. If this is not the case a so-called *unfolding procedure* has to be carried out before further analysis to artificially 'linearize' the staircase function, see Ref. [Bro81]. A reliable unfolding procedure requires knowledge on the average density of resonances over a large range of the spectrum, see Refs. [Wei09, Mor11]. In the case of a Feshbach spectrum of ultracold erbium atoms there is no physical model available up to now, describing the density of resonances. Due to this limitation an unfolding procedure can not be carried out in the present case. Luckily, the staircase function of erbium is indeed linear above a magnetic field of $30\,G$ and the problem of unfolding can be circumvented by only considering resonances above that value for further analysis.

A second statistical quantity of interest is the number variance Σ^2, representing the variance of number of resonances within a certain range of the spectrum. The number variance depends on long-range correlations between resonance spacings within an interval ΔB and is defined by

$$\Sigma^2(\Delta B) = \overline{n^2(B_0, \Delta B)} - \overline{(n(B_0, \Delta B))^2} , \qquad 5.11$$

with $n(B_0, \Delta B) = \mathcal{N}(B_0 + \Delta B) - \mathcal{N}(B_0)$ giving the number of resonances in the interval $[B_0, B_0 + \Delta B]$ and the bar denotes the mean value over all possible B_0. It follows for a Poisson distribution that

$$\Sigma_P^2 = \Delta B . \qquad 5.12$$

In contrast, for a spectrum according to the GOE one expects for large ΔB

$$\Sigma^2_{\text{WD}} = \frac{2}{\pi^2}\left(\ln(2\pi\Delta B) + \gamma + 1 - \frac{\pi^2}{8}\right) \tag{5.13}$$

$$\approx \frac{2}{\pi^2}\ln(\Delta B) + 0.442 , \tag{5.14}$$

where $\gamma = 0.5772...$ is Euler's constant, see Ref. [Dys63]. Figure 5.4(b) shows a plot of Σ^2 for the Poisson and GOE case. The fact that $\Sigma^2_{\text{WD}} \propto \ln(\Delta B)$ shows that there are only very small fluctuations around an average number of resonances within a given interval of size ΔB. This suppression of fluctuations is often referred to as *spectral rigidity*. Compared to the NNS distribution the number variance is more suitable to probe long distances in the spectrum including many resonances. A clear signature of level repulsion on the one hand and a large spectral rigidity on the other hand are central properties of strong correlations between levels.

In contrast to analyzing the NNS distribution and number variance an unfolding independent method was developed in Refs. [Oga07, Kol10]. This method consists of calculating the ratio of two consecutive gaps between resonances. The so-called *two-gap correlation function* is defined by

$$0 \leq r_i = \frac{\min(d_i, d_{i-1})}{\max(d_i, d_{i-1})} \leq 1 , \tag{5.15}$$

with d_i the spacing between two neighboring resonances. As long as the density of states does not vary on the scale of the mean level spacing an unfolding procedure is not needed for calculating this quantity. A Poisson distribution of resonances shows a two-gap correlation distribution following $P(r) = 2/(1+r)^2$ with a mean value of $\langle r \rangle_{\text{P}} = 2\ln 2 - 1 \approx 0.386$. In contrast, the mean value of a Wigner-Dyson distribution can be calculated to be $\langle r \rangle_{\text{WD}} \approx 0.53(1)$, see Ref. [Kol10]. Utilizing the mean values of both distributions we can introduce a quantity η_r which is proportional to the proximity to either a Poisson distribution ($\eta_r = 0$), a Wigner-Dyson distribution ($\eta_r = 1$), or any intermediate value by

$$\eta_r = \frac{\langle r \rangle - \langle r \rangle_{\text{P}}}{\langle r \rangle_{\text{WD}} - \langle r \rangle_{\text{P}}} . \tag{5.16}$$

In general, a larger sample size increases the significance of statistical observables. Since the early years of RMT the number of nuclear resonances in the 'Nuclear Data Ensemble' has increased to several thousands, see Refs. [Haq82, Guh98]. Also theoretical simulations offer a much greater number of resonances, e. g. the Sinai billiard, as shown in Sec. 5.2.2, or the zeros of the Rieman zeta function, see Ref. [Tim06].

5.2. Quantum chaos

Following Bohr's correspondence principle a quantum mechanical system in its macroscopic limit shows coinciding behaviors with a classical system. This might easily suggest that signatures of classical chaos can be found in quantum mechanical systems as well. But
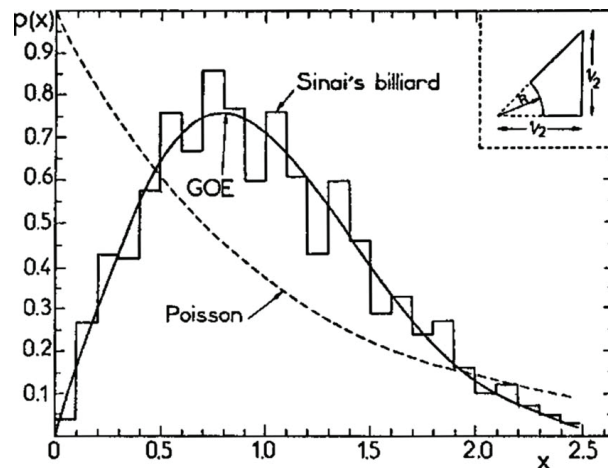
Figure 5.5.: The nearest-neighbor spacing distribution of eigenmodes of the Sinai billiard (histogram) follows a Wigner-Dyson distribution (solid line) instead of a Poisson distribution (dashed line). The inset shows the actual form of the billiard walls; it has a triangular shape with one rounded corner. Note that the normalized level spacing is denoted by x instead of s. Taken from Ref. [Boh84b].

one of the central properties of classical chaotic systems namely the strong dependence of the system's state on initial parameters is not present in quantum mechanical systems. Despite its probabilistic nature and the fundamental limit of the uncertainty principle in quantum mechanics an analog to the classically extremely sensitive evolution in time caused by uncertainties adding up exponentially can not be found in quantum mechanical systems.

But it turns out that there exist quantum mechanical systems, for which the corresponding classical Hamiltionian indeed exhibits chaotic behavior. The field of studying and describing such systems is referred to as the field of *quantum chaos*. Since its origin in the middle of the 1980s various experiments confirmed quantum chaotic systems with high precision. One of the most intriguing examples is the study of resonances in two-dimensional microwave resonators, commonly known as *Sinai billiard*. These experiments are described in Sec. 5.2.2. A nice introduction into the subject of quantum chaos can be found in Refs. [Pec84, Jen92].

5.2.1. Bohigas-Giannoni-Schmit conjecture

The origin of quantum chaos can be traced back to the publication of the Bohigas-Giannoni-Schmit (BGS) conjecture, see Ref. [Boh84b]. The eigenmodes of a classical particle in a flat triangular-shaped billiard, depicted as Sinai billiard system, had been calculated. From this spectrum the NNS probability distribution and the number variance had been derived and both were found to comply with the predictions of RMT for the case of a GOE. Figure 5.5 shows the calculated NNS distribution and the billiard system. Within the quantum mechanical viewpoint the classical particle can be described by a wavefunction with the Schrödinger equation giving the evolution in time.

This result has lead to the formulation of the BGS conjecture, conveying two central messages. First, the level fluctuations of a quantum mechanical system with a corresponding

classical Hamiltonian showing chaotic behavior can be described using RMT. Second, these fluctuation laws are universal for complex single-, few-, and many-body quantum systems.

Recently the BGS conjecture was formally proven for the special case of time-reversal invariant graphs in Refs. [Plu13, Plu14]. Although a general proof is not yet found the conjecture is by now numerically well established. There are also strong theoretical efforts to prove the conjecture following a semiclassical approach in Refs. [Sie01, Mül04] based on the Gutzwiller's periodic orbit theory, see Ref. [Gut90].

5.2.2. Sinai billiard

An extensively studied example of a single-body quantum system, showing chaotic behavior in the corresponding classical limit, is the case of Sinai billiard (SB). After the theoretical investigation, which built the foundation of the BGS conjecture, experimentalists realized such a system and measured the absorption spectrum of a microwave field confined in a flat superconducting resonator of irregular shape, see Refs. [Grä92, Alt95]. The recorded spectrum shows several thousand absorption dips and its statistical properties fully comply with the description by RMT. It is possible to access two regimes with SB-type experiments. The first one is the regime of non-overlapping resonances and the second one is the regime of weakly overlapping resonances where Ericson fluctuations start to be prominent, see Refs. [Die08, Mit10]. In a recent study a hexagonal structure inside the superconducting resonator, mimicking the structure of graphene, makes it possible to study quantum chaos with a relativistic time evolution given by the Dirac equation, see Ref. [Bit12].

After injecting an electromagnetic field, which is tunable in the GHz range, at one site of the resonator, the amplitude and phase at another site is measured using a vector network analyzer. By varying the frequency of the input microwave and recording the spectrum with high resolution one can reconstruct the full scattering matrix of the superconducting resonator SB system including the phase shift between incoming and outgoing waves. The position of input and output sites are kept fixed during measurements. Such a resonator, having an entrance as well as an exit port for the microwave, models a scattering system of two particles with an incoming and outgoing channel, e.g. a system of a neutron colliding with a compound nucleus, see Ref. [Mit10], or colliding ultracold particles as it is the case in the present thesis.

In the following we will outline the analogy of the classical SB-type experiment and a quantum mechanical particle with boundary conditions. As described in Ref. [Ber81] theories and measurements of SB-type experiments determine the energy eigenvalues E_n of the stationary Schrödinger equation

$$\Delta \Psi_n + \frac{2mE_n}{\hbar^2} \Psi_n = 0 \;, \qquad\qquad 5.17$$

with Ψ_n the wave function. For convenience the wave number k_n and the rescaled energy $\mathcal{E}_n$ is defined by

$$k_n^2 = \frac{2mE_n}{\hbar^2} = 4\pi^2 \mathcal{E}_n \;. \qquad\qquad 5.18$$

Dirichlet boundary conditions are assumed as the wave function has to vanish at the walls of the resonator. The classical limit of the Schrödinger equation corresponds to the limit $\hbar \to 0$ and this leads to $k_n \to \infty$ and $\mathcal{E}_n \to \infty$. By this, Eq. 5.17 can be rewritten to

$$\Delta\Psi_n + k_n^2\Psi_n = 0 \ , \qquad\qquad 5.19$$

which resembles the Helmholtz equation of a static microwave field in the resonator. It was shown that this classical system reveals chaotic properties and thus its quantum mechanical analog can be called quantum chaotic.

5.2.3. Quantum chaos in atomic physics

First hints to quantum chaos in the field of atomic physics were given in Ref. [Ros60]. Here, the repulsion of energy levels for the complex atomic spectra of atoms with strong spin-dependent forces, such as Hf, Ta, W, Re, Os, and Ir, were investigated and the fingerprints of Wigner-Dyson distributions were found. The study of quantum chaos in many-electron atoms is described in Ref. [Con97] and a more recent measurement of energy levels in singly ionized thorium can be found in Ref. [HS13].

Another system showing quantum chaos was found in Ref. [Has89] by studying the diamagnetic Kepler problem, which can be mimicked by highly-excited Rydberg atoms in a homogeneous magnetic field as realized in Ref. [Jia96]. In particular, quantum chaos was observed measuring the Stark spectrum of atomic lithium in Ref. [Cou95]. A transition to chaos can be driven by increasing the electric field, responsible for the Stark splitting. This is in contrast to the regular Stark system of hydrogen. A possible explanation for this discrepancy is offered by the scattering of electrons into many trajectories when passing the nucleus and thus is able to explore the full phase space. These multiple scattering processes are known as so-called closed-orbit recurrences.

5.3. Ultracold resonant scattering

Complex systems such as lanthanide atoms and atom-dimer or dimer-dimer mixtures support a large number of Feshbach resonances (FR). In particular, for lanthanide atoms this originates from the strong anisotropic interaction between two atoms, mixing higher angular momentum states, see Sec. 4.3 and Refs. [Kot11, Pet12]. For atom-dimer and dimer-dimer mixtures the large number of FRs is due to the additional ro-vibrational structure of molecules. Applying RMT to ultracold collision processes allows for deriving statistical properties of these complex Feshbach spectra, which can be compared with experimental values. Specifically, theoretical calculations were carried out for atom-dimer and dimer-dimer mixtures in Refs. [May12, May13] and first experimental signatures of RMT were found for erbium atom-atom collisions within the present work of this thesis, see Chapter 10.

Due to the strong coupling between rotational molecular states many of these states can be explored by the collision constituents within a single collision process. During this time of

'exploration' the constituents are quasi-bound and form the so-called *collision complex*. The dissociation of this complex is described by the Rice-Ramsberger-Kassel-Marcus (RRKM) theory, see Ref. [Lev05]. The mean rate of dissociation, k_{RRKM}, of a particular configuration of the complex is expressed as

$$k_{\mathrm{RRKM}} = \frac{1}{2\pi} \frac{N_a}{\hbar \rho_E} \; . \tag{5.20}$$

Here, ρ_E denotes the density of states with respect to energy and N_a is the number of all available quantum states, which can be explored during the collision. Following Ref. [May12] the mean lifetime of the collision complex, τ, can be calculated by

$$\tau = \frac{2\pi \hbar \rho_E}{N_o} \; . \tag{5.21}$$

Here, N_{o} is the number of open channels, available for outgoing collision products after the collision process. In the ultracold regime N_o can be as small as one, resulting in a lifetime of the complex on the order of a few μs and in the case of two colliding dimers on the order of 1–10 ms. During this long lifetime collisions with other particles become probable, ultimately leading to a loss of complexes. This loss process has to be considered in experiments with ultracold molecules.

For low-energy atom-dimer collisions it was just recently shown in Ref. [Cro14] that a fractal-like structure can be observed in the lifetime of the collision complex dependent on the angle between the interatomic axis of the dimer and the collision direction of the two collision partners. An extensive study of the fractal dimension versus collision energy suggests a transition from a classical to a chaotic collision process when energies are smaller than about $k_{\mathrm{B}} \times 400$ K. Thus, ultracold gases are supposed to be deep in the regime of chaotic collisions. For these calculations only the van der Waals coefficient C_6 and the well depth D_e of the Lennard-Jones potential need to be taken into account.

In Ref. [May12] a multichannel quantum defect theory (MQDT) approach is utilized to derive the scattering matrix $\boldsymbol{S}^{\mathrm{phys}}$ for alkali atom-dimer collisions. A set of parameters is required for MQDT. Once this set of parameters is acquired for a given class of molecular potentials it gives a direct connection between the short-range reactance matrix $\boldsymbol{K}^{\mathrm{sr}}$, valid for distances $R < R_m$, and $\boldsymbol{S}^{\mathrm{phys}}$, valid for $R \to \infty$, see Fig. 5.6. Here, R_m is a characteristic distance, splitting the interaction range into a short-range and long-range part. In the short-range region forms the collision complex at $R < R_m$ and incomming channels a are strongly mixed with each other. In the long-range region the scattering channels are assumed to be independent. The long-range interaction is of the form

$$V_a(R) = -\frac{C_6}{R^6} + \frac{\hbar^2 L_a(L_a + 1)}{2m_r R^2} + E_a(B) \; , \tag{5.22}$$

where C_6 denotes the isotropic van der Waals coefficient and m_r is the reduced mass of the scattering partners. Here, $E_a(B)$ is the energy threshold, which depends on some external magnetic field B, and L_a is the angular momentum of channel a.

The wavefunction of a scattering process from the incoming channel a into the outgoing channel a' can be written as

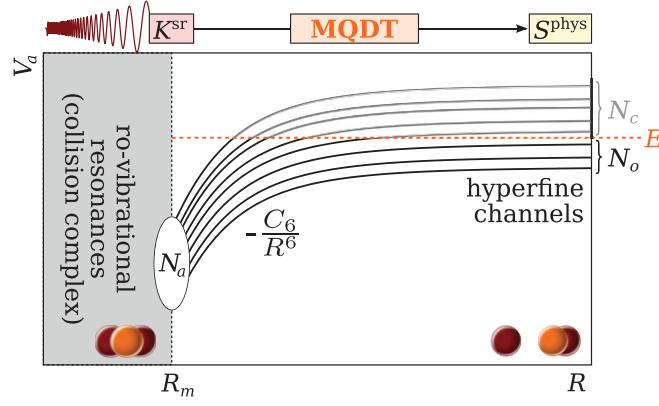$$\Psi_{a'}^{(a)}(R) = \delta_{a'a} f_a^-(R) - \boldsymbol{S}_{a'a}^{\mathrm{phys}} f_{a'}^+(R) \; , \tag{5.23}$$

Figure 5.6.: MQDT approach to resonant scattering of alkali atom-dimer collisions. The MQDT treatment connects the short-rage K matrix $\boldsymbol{K}^{\mathrm{sr}}$, containing information about the ro-vibrational resonances, to the physical scattering matrix $\boldsymbol{S}^{\mathrm{phys}}$ at long ranges, where only hyperfine channels are taken into account. From $\boldsymbol{S}^{\mathrm{phys}}$ elastic and inelastic cross sections can be deduced, which are observable in the experiment. For $R \to \infty$ the number of energetically closed and open channels is given by N_c and N_o, respectively. The collision complex forms at distances $R < R_m$. Taken from Ref. [May12].

with

$$f_a^\pm = \sqrt{\frac{2m_r}{\pi\hbar^2 k_a}} e^{\pm i(k_a R - L_a \pi/2)} \ ,$$ 5.24

the incoming (+) and outgoing (-) spherical waves.

For a given number of hyperfine channels N_a at short ranges there are only N_o open channels at long ranges available for scattering products to exit to infinity as the energy is above threshold with $E_a > E$. The remaining $N_c = N_a - N_o$ channels are energetically closed. Closed channels have to be removed within the MQDT formalism by eliminating them. For accomplishing this $\boldsymbol{K}^{\mathrm{sr}}$ is partitioned in a first step into

$$\boldsymbol{K}^{\mathrm{sr}} = \begin{pmatrix} \boldsymbol{K}^{\mathrm{sr}}_{oo} & \boldsymbol{K}^{\mathrm{sr}}_{oc} \\ \boldsymbol{K}^{\mathrm{sr}}_{co} & \boldsymbol{K}^{\mathrm{sr}}_{cc} \end{pmatrix} \ .$$ 5.25

Then a closed-channel MQDT parameter $\boldsymbol{\beta}$ is introduced and the modified reactance matrix $\widetilde{\boldsymbol{K}}$ is defined by

$$\widetilde{\boldsymbol{K}} = \boldsymbol{K}^{\mathrm{sr}}_{oo} - \boldsymbol{K}^{\mathrm{sr}}_{oc}(\boldsymbol{K}^{\mathrm{sr}}_{cc} + \tan\boldsymbol{\beta})^{-1}\boldsymbol{K}^{\mathrm{sr}}_{co} \ .$$ 5.26

The modified reactance matrix can be transformed into an energy-normalized long-range representation by

$$\boldsymbol{K} = \boldsymbol{A}^{\frac{1}{2}}\widetilde{\boldsymbol{K}}(1 + \boldsymbol{\mathcal{G}}\widetilde{\boldsymbol{K}}^{-1})\boldsymbol{A}^{\frac{1}{2}} \ .$$ 5.27

$\boldsymbol{A}$, $\boldsymbol{\mathcal{G}}$, $\boldsymbol{\eta}$, and $\boldsymbol{\beta}$ are diagonal matrices containing the relevant MQDT parameters. The physical scattering matrix $\boldsymbol{S}^{\mathrm{phys}}$ is finally achieved by

$$\boldsymbol{S}^{\mathrm{phys}} = e^{i\boldsymbol{\eta}}(1 + i\boldsymbol{K})(1 - i\boldsymbol{K})^{-1}e^{i\boldsymbol{\eta}} \ .$$ 5.28

The MQDT has been extensively used for describing resonant scattering processes at ultracold temperatures in Refs. [Bur98, Mie00, Gao05, Gao08]. The reason for the success of

MQDT lies within the fact that at a matching radius of $R = R_m$ classically closed states at $R \to \infty$ become open. Thus the reactance matrix $\boldsymbol{K}$ exhibits only a weak dependence on the energy and complex spectra can be described. The connection to the scattering matrix $\boldsymbol{S}^{\text{phys}}$ can then be established by the use of MQDT.

In the case of atom-atom collisions of lanthanides or atom-dimer collisions of alkali-metal atoms the exact details about the interaction potential as in Eq. 5.22 are not known and thus the short-range reactance matrix $\boldsymbol{K}^{\text{sr}}$ can not be determined. A possible solution to this problem is to use a fully statistical $\boldsymbol{K}$ matrix according to RMT.

As shown in Refs. [May12, Mit10] in great detail such a statistical $\boldsymbol{K}$ matrix can be received by writing

$$\boldsymbol{K}^{\text{sr}}_{a,b} = -\pi \sum_{\mu=1}^{N} \frac{\boldsymbol{W}_{a\mu}\boldsymbol{W}_{\mu b}}{E - E_\mu} \ , \qquad 5.29$$

with $\boldsymbol{W}$ an energy-independent coupling-matrix, representing the coupling between short-range resonances. Here, a and b are the asymptotic channels and μ denotes intermediate states. A mean coupling strength of channel a to short-range resonances can be written as

$$R_a^{(0)} = \frac{\pi}{2} \rho_E \overline{\Gamma}_a \ , \qquad 5.30$$

where ρ_E is the density of states at incident energy E and

$$\overline{\Gamma}_a = \frac{2\pi}{N} \sum_{\mu=1}^{N} |\boldsymbol{W}_{\mu a}|^2 \qquad 5.31$$

the partial width of channel a.

As $\boldsymbol{K}^{\text{sr}}$ is expressed in the frame, where the corresponding Hamiltonian is diagonal, the coupling $\boldsymbol{W}$ becomes a random process and can be constructed as a random matrix, where its elements have a zero mean value and a variance of ν_a^2, see Ref. [Mit10] and Sec. 5.1.3. With $\overline{\Gamma}_a = 2\pi\nu_a^2$ the variance is only defined by the density of states ρ_E and the mean coupling strength $R_a^{(0)}$ by

$$\nu_a^2 = \frac{R_a^{(0)}}{\rho_E \pi^2} \ . \qquad 5.32$$

According to Ref. [May12] it can be assumed that $R_a^{(0)} = 1$ as this gives a transmission coefficient of $T_a = 1$ between short-range and long-range channels by

$$T_a = \frac{4R_a^{(0)}}{\left(1 + R_a^{(0)}\right)^2} \ . \qquad 5.33$$

In fact, $R_a^{(0)}$ can be left as a fitting parameter to some real spectra, giving more information on short-range physics of complex collision processes. The expression of $\boldsymbol{W}$ by a random matrix directly leads to a distribution of energy levels with a NNS distribution, resembling a Wigner-Dyson distribution as shown in Eq. 5.7.

An estimation of the density of states for atom-dimer collisions for various combinations of alkali-metal atoms can be found in Ref. [May12]. Much higher density of states, like on the order of 10^3 per Gauss, are predicted for dimer-dimer collisions, e.g. $^{87}\text{Rb}^{133}\text{Cs} + {}^{87}\text{Rb}^{133}\text{Cs}$ or $^{40}\text{K}^{87}\text{Rb} + {}^{40}\text{K}^{87}\text{Rb}$, see Ref. [May13]. In this regime resonances start to overlap and can not be individually resolved any more. This leads to strong and random fluctuations of the scattering cross section, which are known as *Ericson fluctuations*, see Ref. [Eri60].

6

Publication: Narrow-line laser cooling of erbium

6.1. Introduction

Narrow-line magneto-optical traps (MOTs) are a very powerful tool to reach low temperatures. The Doppler temperature, T_{D}, directly depends on the natural linewidth, Γ, of the laser-cooling transition with $T_{\mathrm{D}} = \frac{\hbar\Gamma}{2k_{\mathrm{B}}}$. For comparison, an ordinary MOT of alkali atoms, operating on the D_2 transition with a linewidth, $\Delta\nu = \Gamma/(2\pi)$, of a few MHz, provides typical temperatures of $150\,\mu\mathrm{K}$. Multi-valence-electron species have a richer energy structure than alkali atoms and offer a number of different opportunities for laser cooling. For instance, a MOT of ytterbium atoms is realized with a narrow-line transition, i.e. an intercombination line with $\Delta\nu = 200\,\mathrm{kHz}$ resulting in $T_{\mathrm{D}} = 4.8\,\mu\mathrm{K}$, and an narrow-line MOT, with $\Delta\nu$ of a few kHz and T_{D} as low as a few hundred nK, has been realized with strontium, see Ref. [Kat99]. In case of ytterbium, atoms from a Zeeman slowed atom beam are directly captured by the MOT, while in the case of strontium the narrow-line MOT acts as a second cooling stage within a two-stage MOT setup.

Although the electron structure of lanthanides is much more complicated than compared to ytterbium it is possible to implement a narrow-line MOT with erbium. To provide an overview, typically achievable temperatures in the presented erbium MOT are as low as $10\,\mu\mathrm{K}$ with a maximum atom number of a few 10^8 atoms. This narrow-line cooling of erbium is presented in the following.

Magnetic lanthanides have several broad and narrow transitions usable for laser cooling as discussed in Chapter 2. One difference to simple systems, like alkali, alkaline-earth, and alkaline-earth-like elements, is the existence of many metastable states, in which an excited state can decay into, see Fig. 2.1. In general, the number of possible decay channels increases the shorter the transition wavelength is. However, pioneering work with erbium by the group of J.J. McClelland at NIST (USA) demonstrated a MOT operating on the open transition at a wavelength of 401 nm. Similar results have been obtained in later experiments with dysprosium, see Ref. [Lu10]. Atoms participating in the cooling cycle are trapped and cooled in the MOT. Part of these atoms decay into some metastable state, become dark, and do not

scatter the MOT light anymore until they return into the ground state again via relaxation. But due to the large atomic magnetic moment atoms in metastable states stay trapped in the magnetic gradient field of the MOT. The dynamics of such a MOT with a reservoir of magnetically trapped atoms was studied in Ref. [McC06b]. In a later experiment erbium atoms were then loaded from this broad-line MOT into a narrow-line MOT operating at a wavelength of 841 nm. Typical final temperatures after this two-stage erbium MOT were as low as $2\,\mu$K, see Ref. [Ber08].

We use a different approach with erbium, inspired by the successful demonstration of the ytterbium MOT, see Ref. [Kuw99]. The transition $4f^{12}\,6s^2\,^1\mathrm{S}_1$ - $4f^{12}\,6s6p\,^3\mathrm{P}_1$ has a wavelength of 583 nm and a linewidth of 190 kHz, which is very similar to the transition in ytterbium. It was not fully clear from the beginning, whether this cooling approach would work out because of two issues. First, there are two metastable states below the excited $4f^{12}\,6s6p\,^3\mathrm{P}_1$ state of erbium, into which the excited state can decay. However, the calculated branching ratio into these two states is negligible small. Second, the narrow linewidth of this transition results in a small capture velocity of the MOT of 5.6 m/s, which makes loading the MOT with an atom beam from a high-temperature oven a delicate issue. As shown in Sec. 3.3.2 one can indeed prepare a slow atom beam with a velocity smaller than the capture velocity of this narrow-line transition. This makes it possible to load the narrow-line erbium MOT directly from the ZS. The erbium narrow-line cooling strategy is very simple and robust. The final temperature of the atoms in the MOT is as low as $10\,\mu$K and the peak density is $1.5\times10^{11}\,\mathrm{cm}^{-3}$, which corresponds to a phase-space density of 1.2×10^{-5}. Another advantage of our narrow-line MOT approach is an automatic spin-polarization of the atoms without the need of optically repumping them into their lowest spin state. We successfully realized the directly-loaded narrow-line MOT for erbium atoms in our group for the first time in late 2011 and the group in Stuttgart just recently used a similar idea for dysprosium atoms, see Ref. [Mai14].

In the following, we describe the creation of a narrow-line MOT operating on the 583-nm transition for different erbium isotopes. In Sec. 6.1.1 we discuss its relevant experimental parameters and then we show a measurement of the spin purity of atoms in the MOT measured by a Stern-Gerlach experiment in Sec. 6.3.1.

6.1.1. Narrow-line cooling

The narrow-line MOT for the bosonic isotopes ^{164}Er, ^{166}Er, ^{168}Er, and ^{170}Er and the fermionic isotope ^{167}Er operates on the yellow 583-nm transition. The natural linewidth of this transition is $\Delta\nu = \frac{\Gamma}{2\pi} = 190$ kHz, which results in a Doppler temperature of $4.6\,\mu$K, see Sec. 2.3.1. Figure 6.1 shows two real-color photographs of the fluorescence of trapped atoms. Figure 6.2 summarizes the experimental sequence for the MOT, e. g. the light detuning and intensity, the magnetic gradient field, and the homogeneous magnetic field. In the following we will first describe the erbium MOT loading procedure and then discuss the theory of narrow-line cooling.

The ZS laser beam travels in collinear direction with the atom beam through the vacuum chamber and overlaps with the center of the MOT. Schemes that combine a broad transition
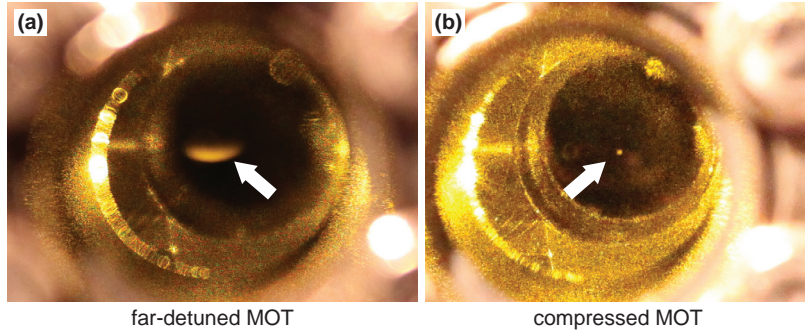
Figure 6.1.: Real-color photographs of the narrow-line erbium MOT. (a) The typical bowl-shaped MOT is due to the narrow-line laser-cooling transition in combination with a large detuning and the gravitational sag. In this picture the cloud contains approximately 10^7 atoms. (b) After finishing loading the MOT the atomic cloud is compressed into the center of the trap and gets spherically symmetric. The much smaller volume of the MOT enables one to load atoms efficiently into an optical dipole trap for further experiments.

for ZS and a narrow transition for MOT potentially suffer from an undesired light force, acting on atoms from the ZS light during the MOT loading[1]. To avoid this effect we spatially separate the MOT from the ZS laser beam by the use of a large detuning of the MOT laser light in combination with the proper magnetic field gradient. This shifts the atoms out of the trap center and effectively prevents any light force of the ZS laser beam acting on the atoms. For erbium a detuning as large as $\delta = -7.6\,\mathrm{MHz} \approx -40\,\Delta\nu$ and a gradient of $\partial_z B = \frac{\partial B}{\partial z} = 2.6\,\mathrm{G/cm}$ is needed, see Fig. 6.2. At such a large detuning compared to the natural linewidth atoms in the MOT will not feel a homogeneous light force over the full volume of the MOT but will rather be resonant with the light on an ellipsoid of constant magnetic field. Adding the gravitational potential the trapped atoms will accumulate at the lower part of this ellipsoid. Figure 6.3 gives a schematic view of this MOT working principle. The so-called *gravitational sag* will create a characteristic 'bowl-shaped MOT', see Fig. 6.1(a). Dependent on the laser detuning, $\Delta = 2\pi\delta$, the position of the cloud in z-direction, z_0, will adjust itself such that the effective detuning $\Delta - \mu\partial_z B z_0$ stays constant, see Ref. [Lof04]. Here, μ is the atomic magnetic moment. An important consequence of the narrow-line MOT is that the damping and diffusion coefficients of atoms in the MOT are independent of the laser light detuning. This is in contrast to broad-line MOTs and strongly affects the equilibrium temperature in the MOT as it will be shown below.

After loading sufficiently many atoms into the MOT the ZS light and ZS magnetic field are switched of and the atom beam is blocked by a shutter. Atoms are then being shifted towards the center position, which creates a nearly-symmetric compressed MOT (cMOT), see Fig. 6.1(b). The cMOT is achieved by ramping the laser-light detuning closer to resonance, decreasing the light intensity, and reducing the magnetic field gradient[2]. This is achieved in a sequence of two linear ramps. During the first ramp, which has a duration of only

---

[1] The ZS light gives a scattering force on the atoms, which is two orders of magnitude larger than for the MOT light. This estimation is based on the actual experimental parameters for light intensity and detuning for the blue and yellow transition, respectively.

[2] It has to be noted here that this is in contrast with most other schemes for MOT compression, in which the gradient is usually increased.
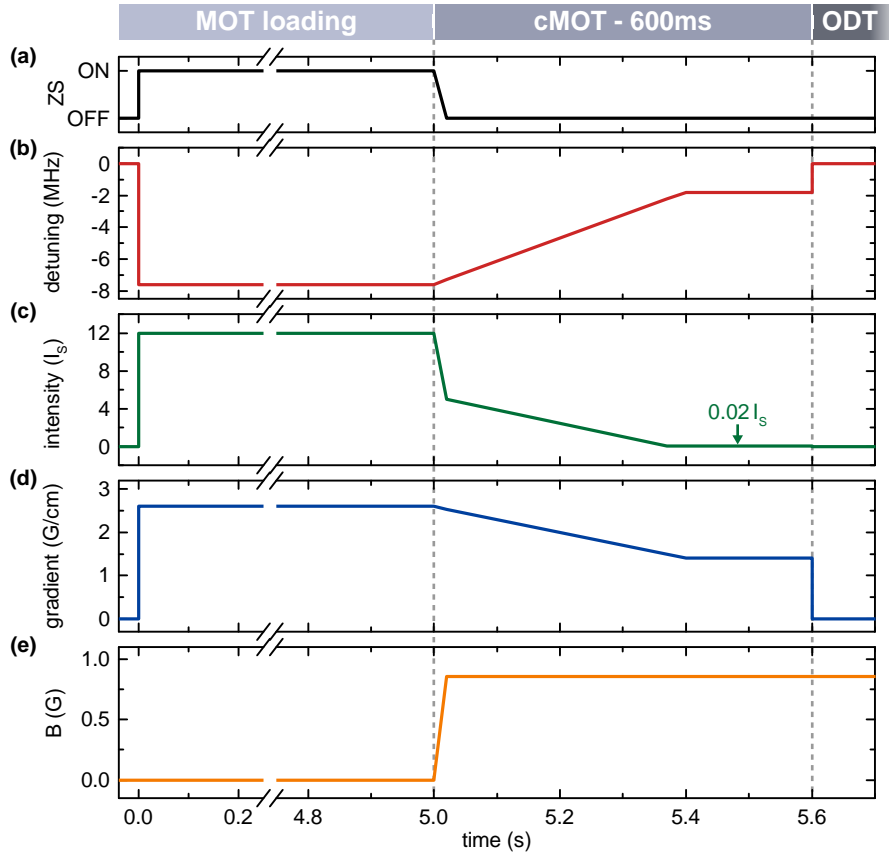
Figure 6.2.: Relevant parameters for MOT loading and compressing. The MOT loading is shown for a loading time of 5 s, which is varied dependent on the specific isotope or experimental needs whereas the cMOT ramping procedure is kept unchanged. (a) After switching off the Zeeman slower (ZS) a two-stage ramp is used to compress the MOT (cMOT). (b) This involves changing the detuning, (c) the intensity (in units of the saturation intensity, I_S), and (d) the gradient field (in z-direction). After an additional holding time of 200 ms a final temperature of as low as 10 μK can be achieved in the cMOT. The atoms are then loaded into an optical dipole trap (ODT) for further experiments. (e) A homogeneous magnetic field is ramped up within 10 ms at the beginning of the cMOT stage, to keep the atomic sample fully spin-polarized.

Figure 6.3.: Working principle of the narrow-line MOT. (a) Position-dependent detuning in the MOT, shown in one direction for a simplified MOT with a $J = 0 \to J' = 1$ transition. Due to the small linewidth trapped atoms fulfill the resonance condition only in a small region far outside the center of the gradient field (yellow regions). The distance from the center is set by the de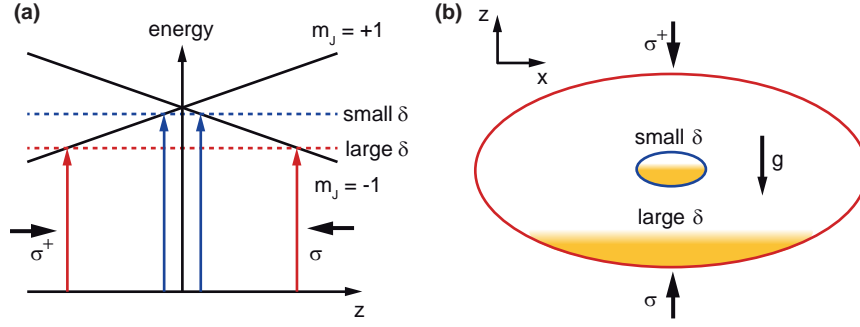tuning (see text). (b) In three dimensions atoms are resonant on an ellipsoid. The gravitational force pulls the atoms to the lower part of the ellipsoid, where they preferably scatter σ^--polarized light from the lower MOT beam and the sample automatically gets spin polarized.

10 ms, the laser beam peak intensity is ramped to $4\,I_\mathrm{S}$ with I_S the saturation intensity and a homogeneous magnetic field of $0.9\,\mathrm{G}$ is introduced. Within the second ramp with a duration of 390 ms the magnetic field gradient is changed to $1.4\,\mathrm{G/cm}$, the light intensity to $0.02\,I_\mathrm{S}$ and the detuning to $-1.8\,\mathrm{MHz}$. In the following holding time of 200 ms the atoms are further cooled in the cMOT until they reach their final temperature. To achieve low temperatures the peak intensity of the cooling laser beams has to be chosen small, see Fig. 6.4. Figure 6.2 shows a full list of necessary parameters for loading the MOT and ramping to the cMOT.

A very convenient consequence of a narrow-line MOT, operated with a large detuning, is its ability to intrinsically spin-polarize the atoms. In such a narrow-line MOT the lower vertical laser beam[3] supports the atoms against gravity and atoms predominantly scatter light from this beam as demonstrated in Fig. 6.3(b). This beam happens to be σ^--polarized, which successively transfers all atoms into the energetically lowest Zeeman sublevel $m_J = -6$. As long as they do not scatter light from the upper vertical beam they stay polarized in this stretched spin state. A homogeneous magnetic field during compressing the MOT and loading it into the optical dipole trap (ODT) preserves the spin polarization, see Fig. 6.2(e). The degree of spin polarization in the ODT is verified by a Stern-Gerlach measurement, which is presented in Sec. 6.3.1.

Now we will discuss the theory of narrow-line MOT cooling. The total force along the z-direction, acting on atoms with velocity v_z at position z in the MOT, is given by, see Ref. [Lof04],

$$F_{\mathrm{MOT}}(v_z, z) = F_{\mathrm{sc}} + F_g = \frac{\hbar k \Gamma}{2} \left[\frac{s}{1 + s' + \frac{4(\Delta - kv_z - \mu \partial_z B z)^2}{\Gamma^2}} \right] - mg \,. \qquad 6.1$$

The first term is due to light scattering whereas the second term gives the gravitational force with m the atomic mass and g the gravitational acceleration. The scattering force, F_{sc},

---

[3] For perfect spin polarization it is very important that the vertical MOT axis is oriented along the direction of gravity.

depends on the transition linewidth Γ, the laser light detuning $\Delta = 2\pi\delta$, and $\partial_z B$. Here, $k = \frac{2\pi}{\lambda}$, $s = \frac{I}{I_S}$ is the saturation parameter, $s' \geq s$ takes care of saturation effects induced by beams in other directions, and I is the single-beam peak intensity. We will now derive an expression for the damping coefficient in the narrow-line MOT from which the capture velocity and the equilibrium temperature of the MOT can be calculated.

Dependent on the detuning of the MOT light one has to distinguish between two regimes in which the MOT dynamics turn out to be completely different, see Ref. [Lof04]. For a detuning, being larger than the power-broadened natural linewidth $\Gamma_E = \Gamma\sqrt{1 + s}$ and $|\Delta| > \Gamma_E$, atoms can be treated in a free flight picture with hard walls as boundaries induced by the MOT. This regime is called regime (I). The hard walls are located far outside the MOT center where atoms are resonant with the cooling light and experience a strong light force, see Fig. 6.3. Including the gravitational potential atoms will sag to the lower part of the trap and scatter mostly the lower beam. This applies during the erbium MOT loading procedure as well as in the cMOT, as for both stages $\Delta \approx -10\,\Gamma_E$. The regime (II) is reached for small detunings when $|\Delta| < \Gamma_E$. In this case atoms experience a radiative force over the full volume of the trap. The resulting restoring force changes linearly with the position in the trap, which is described by damped harmonic motion, see Ref. [Xu02]. This is usually the case, e.g. for a MOT of alkali-metal atoms and lanthanides, where the MOT is operated on a broad transition.

Atoms in the MOT experience a cooling power, P_{cool}, which is proportional to the square of their velocity, v, see Refs.[Let89, Sch03]. The power can be written as

$$P_{\text{cool}} = \left(\frac{dE}{dt}\right)_{\text{cool}} = F_{\text{sc}}v = -\alpha v^2 \ , \qquad 6.2$$

where $F_{\text{sc}} = -\alpha v$ is the friction force in the MOT given by Eq. 6.1 with $(\partial F_{\text{sc}}/\partial v) = \alpha$ evaluated at $v_z = 0, z = z_0$. Here, α is the damping coefficient. Accordingly, the kinetic energy of the atoms, $E = \frac{1}{2}mv^2$, will decrease exponentially with a time constant τ, the so-called *thermal equilibration time*. Utilizing Eq. 6.2 the cooling rate in the MOT can be calculated by

$$\frac{1}{\tau} = -\frac{P_{\text{cool}}}{E} = \frac{2\alpha}{m} \qquad 6.3$$

The thermal equilibration time has to be considered when optimizing the MOT ramping parameters. As shown in Ref. [Lof04] α is given in regime (I) by

$$\alpha = \frac{2\hbar k^2\sqrt{Rs - s' - 1}}{R^2 s} \ , \qquad 6.4$$

with $R = \frac{\hbar k \Gamma}{2mg}$. Note that in this regime α depends on the atomic mass, m. Using this result the equilibration time for the erbium MOT is about $78\,\text{ms}$ and for the cMOT $\tau = 3.6\,\text{ms}$. For completeness, in regime (II) α is according to ordinary Doppler theory given by, see Ref. [Xu02],

$$\alpha = \frac{4}{3}\hbar k^2 \frac{I_t}{I_S} \frac{|\Delta|}{\Gamma} \left(1 + \frac{I_t}{I_S} + 4\frac{\Delta^2}{\Gamma^2}\right)^{-2} \ , \qquad 6.5$$

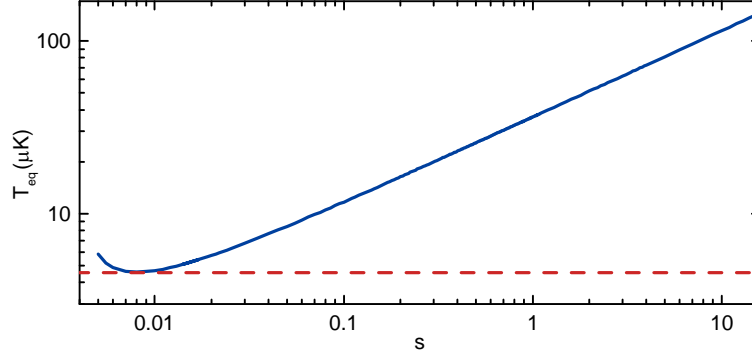where I_t is the total intensity of all six MOT beams.

Figure 6.4.: Equilibration temperature of ^{168}Er in the MOT (solid line). Note that the equilibration temperature is independent of the detuning and only depends on the saturation parameter, s, in a square-root-like behavior for large values of s, according to Eq. 6.8. The lower temperature limit is set by the Doppler temperature (dashed line).

Utilizing the result for α one can estimate the capture velocity of the MOT, v_c, which is the maximum velocity that atoms can have when entering the MOT and they will still be captured by the MOT. The capture velocity is given by

$$v_c = \frac{2d\alpha}{m} \ ,$$
6.6

and depends on the size of the capture volume of the MOT, which is simply set by the beam diameter d. A Value for v_c for the narrow-line transition of erbium is $5.6\,\text{m/s}$ for $d = 25\,\text{mm}$. This result is important for the design of the Zeeman slower as depicted in Sec. 3.3.2.

From Eq. 6.1 an expression for the diffusion coefficient in regime (I) can be derived as, see Ref. [Lof04],

$$D_p = \frac{\hbar^2 k^2 \Gamma}{2R} \ .$$
6.7

Using this expression one can calculate the equilibrium temperature T_{eq} as the ratio between diffusion and damping coefficient. The former results in an effective heating process whereas the latter cools the atomic sample. Equilibrium is reached when both heating and cooling balance each other. Taking the damping coefficient from Eq. 6.4 the equilibrium temperature in the narrow-line MOT is thus,

$$T_{\text{eq}} = \frac{D_p}{k_B |\alpha|} = \frac{\hbar \Gamma \sqrt{s}}{2 k_B} \frac{R}{2\sqrt{R - s'/s - 1/s}} \ .$$
6.8

Note, that T_{eq} is independent on the detuning of the MOT light put is a function of s. Figure 6.4 shows the dependence of T_{eq} on the laser-beam intensity. During the erbium MOT loading stage this gives $T_{\text{eq}} = 126\,\mu\text{K}$ for $s = s' = 12$ and in the cMOT the theoretical equilibrium temperature is as small as $5.7\,\mu\text{K}$ for $s = s' = 0.02$, which is close to the Doppler temperature of $T_D = \frac{\hbar \Gamma}{2 k_B} = 4.6\,\mu\text{K}$.

Utilizing this simple and efficient approach to a narrow-line MOT we could successfully demonstrate a directly loaded MOT with up to 2×10^8 erbium atoms at a temperature of $10\,\mu\text{K}$ and a peak density of $1.5 \times 10^{11}\,\text{cm}^{-3}$, corresponding to a phase-space density of about 1.2×10^{-5}.

6.2. Publication:
Narrow-line magneto-optical trap for erbium[†]

Albert Frisch,[1] Kiyotaka Aikawa,[1] Michael Mark,[1] Alexander Rietzler,[1] Johannes Schindler,[1] Eric Zupanič,[1,2] Rudolf Grimm,[1,3] and Francesca Ferlaino[1]

[1] *Institut für Experimentalphysik and Zentrum für Quantenphysik, Universität Innsbruck, Technikerstraße 25, 6020 Innsbruck, Austria*

[2] *Jožef Stefan Institute, Jamova 39, SI-1000 Ljubljana, Slovenia*

[3] *Institut für Quantenoptik und Quanteninformation, Österreichische Akademie der Wissenschaften, 6020 Innsbruck, Austria*

[†] The author of the present thesis constructed the experimental apparatus together with J. S. and A. R., performed the measurements with K. A. and M. M., analyzed the data, and contributed in writing the manuscript.

Narrow-line magneto-optical trap for erbium

A. Frisch,[1] K. Aikawa,[1] M. Mark,[1] A. Rietzler,[1] J. Schindler,[1] E. Zupanič,[1,2] R. Grimm,[1,3] and F. Ferlaino[1]

[1]*Institut für Experimentalphysik and Zentrum für Quantenphysik, Universität Innsbruck, Technikerstraße 25, A-6020 Innsbruck, Austria*
[2]*Jožef Stefan Institute, Jamova 39, SI-1000 Ljubljana, Slovenia*
[3]*Institut für Quantenoptik und Quanteninformation, Österreichische Akademie der Wissenschaften, A-6020 Innsbruck, Austria*

We report on the experimental realization of a robust and efficient magneto-optical trap for erbium atoms, based on a narrow cooling transition at 583 nm. We observe up to $N = 2 \times 10^8$ atoms at a temperature of about $T = 15\,\mu$K. This simple scheme provides better starting conditions for direct loading of dipole traps as compared to approaches based on the strong cooling transition alone, or on a combination of a strong and a narrow kHz transition. Our results on Er point to a general, simple, and efficient approach to laser cool samples of other lanthanide atoms (Ho, Dy, and Tm) for the production of quantum-degenerate samples.

PACS number(s): 37.10.De, 67.85.−d, 37.10.Vz

Laser cooling of non-alkali-metal atoms has become a very active and challenging field of research. The great appeal of unconventional atomic systems for experiments on ultracold atomic quantum gases stems from the possibility of engineering complex interactions and of accessing rich atomic energy spectra. Both features are at the foundation of a number of novel and fascinating phenomena. For instance, the energy spectra of two-valence-electron species, such as alkaline-earth-metal and alkaline-earth-metal-like atoms, feature narrow and ultranarrow optical transitions, which are key ingredients for ultraprecise atomic clocks [1], efficient quantum computation schemes [2], and novel laser cooling approaches, as demonstrated in experiments with Sr, Yb, and Ca [3–5].

As a next step in complexity, multivalence-electron atoms with a non-*S* electronic ground state such as lanthanides are currently attracting increasing experimental and theoretical interest. Among many, one of the special features of lanthanides is the exceptionally large magnetic dipole moment of atoms in the electronic ground state (e.g., $7\mu_B$ for Er and $10\mu_B$ for both Dy and Tb), which provides a unique chance to study strongly dipolar phenomena with atoms. Highly magnetic atoms interact with each other not only via the usual contact interaction but also via an anisotropic and long-range interaction, known as the dipole-dipole interaction [6]. Chromium was the first atomic species used for experiments on atomic dipolar quantum gases [7,8], and the even more magnetic lanthanides are nowadays in the limelight thanks to laser cooling experiments on Er and Tm [9,10] and to the recent realization of quantum-degenerate Dy gases [11,12].

Similarly to Yb and the alkaline-earth-metal atoms, the atomic energy spectra of magnetic lanthanides include broad, narrow, and ultranarrow optical transitions. This collection of lines is reflected in a wide choice of possible schemes for laser cooling experiments. However, all experiments on Zeeman slowing and cooling in a magneto-optical trap (MOT) with magnetic lanthanides so far have relied on an approach that is essentially based on the strongest cycling transition [9,10,13]. This broad transition typically lies in the *blue* between 400 and 430 nm and has a linewidth on the order of few tens of MHz. As a consequence, the Doppler temperature is close to 1 mK. Such a high temperature makes direct loading

from a MOT into a dipole trap difficult and inefficient, even when sub-Doppler mechanisms take place [14,15]. To further decrease the temperature of atoms prior to the dipole trap loading, an additional MOT stage based on an ultranarrow kHz-linewidth transition was applied in Refs. [11,13], making the whole experimental procedure more involved.

Taking advantage of the rich atomic spectrum of lanthanides, we identify a different transition to be the most suitable one for MOT operation toward production of a quantum-degenerate gas. This transition, which for Er lies at 583 nm and has a linewidth of 190 kHz, represents an intermediate case between the broad (blue) and the ultranarrow (red) transitions available in the lanthanide spectra and has very similar properties to the Yb intercombination line [16,17]. Based on this narrow yellow line, we demonstrate a MOT of 2×10^8 Er atoms at a temperature as low as 15 μK. Our approach, inspired by Yb experiments [4], provides better starting conditions for direct loading into a dipole trap than the conditions achieved in other experiments with magnetic lanthanides [11].

Erbium is a heavy rare-earth element of the lanthanide series. It has six stable isotopes, among which the three bosonic isotopes ^{166}Er (34%), ^{168}Er (27%), and ^{170}Er (15%) and the fermionic isotope ^{167}Er (23%) have a high natural abundance. The Er electronic configuration is characterized by a xenonlike core, an inner open $4f$ shell, and an outer closed $6s$ shell, $[\text{Xe}]4f^{12}6s^2$. The electron vacancies in the inner f shell are a common feature of all the lanthanides (with the exception of Yb) and are at the origin of the strong magnetism as well as various interesting collisional effects [18–20].

The atomic level spectrum of Er is shown in Fig. 1. In the ground state, Er has a highly anisotropic electronic density distribution with a large orbital angular momentum $L = 5$ (H state) and a total electronic angular momentum $J = 6$. The bosonic isotopes have zero nuclear spin ($I = 0$) and consequently do not exhibit a hyperfine structure. On the contrary, the fermionic isotope ^{167}Er has a nuclear spin $I = 7/2$, leading to eight hyperfine levels, from $F = 5/2$ to $F = 19/2$, in the electronic ground state.

In Ref. [22], five different $J \rightarrow J + 1$ laser cooling transitions were identified with linewidths ranging from tens of MHz to a few Hz. Here we focus on the blue and
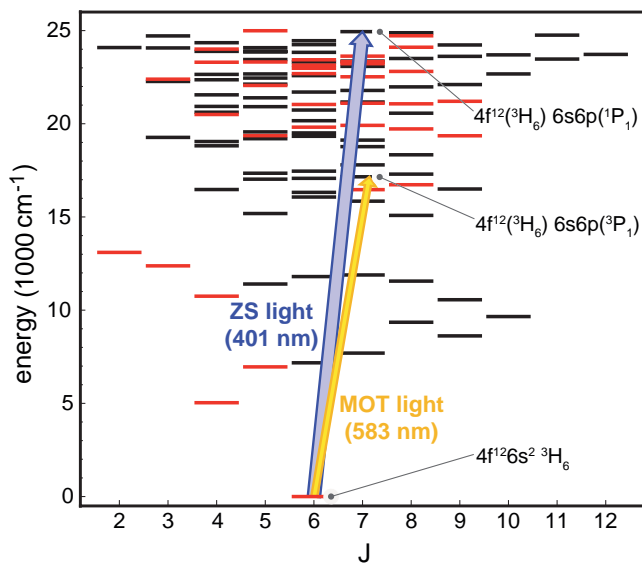
FIG. 1. (Color online) Energy levels of atomic erbium up to $25\,000$ cm^{-1} for different total electronic angular momentum quantum numbers J [21]. States with odd (even) parity are indicated by black (red/gray) horizontal lines. The two relevant laser cooling transitions at 401 and 583 nm are indicated by arrows [22].

the yellow transition at 401 and 583 nm, respectively; see the arrows in Fig. 1. The corresponding excited levels are the singlet $^1P_1$ and triplet $^3P_1$ states coming from the transition of an s electron into a p shell. The strong blue transition at 401 nm has a linewidth of $\Gamma_{401}/2\pi = 27.5$ MHz [23], corresponding to a Doppler temperature of $\hbar\Gamma_{401}/(2k_B) = 660\,\mu$K. We use the blue light for both Zeeman slowing and transversal cooling of the Er atomic beam. The MOT operates on the narrow yellow transition at 583 nm, which has a natural linewidth of $\Gamma_{583}/2\pi = 190$ kHz and a corresponding Doppler temperature of 4.6 μK. The line may exhibit weak leaks from the excited level into two intermediate levels with very low calculated leakage rates (0.017 and 0.0049 s^{-1}) [22]. Note that we find these losses irrelevant for all practical purposes. For ^{167}Er the hyperfine structure in the 401- and 583-nm excited states gives rise to eight levels ranging from $F' = 7/2$ to $F' = 21/2$. For the 583-nm line, the hyperfine constants are known [26]. On the contrary the hyperfine constants for the 401-nm line are currently unknown, making the operation of the fermionic MOT more challenging.

We generate the blue light from two independent blue diode lasers injection locked to a master laser. The master laser light is produced by frequency doubling methods based on a tapered amplified diode laser at 802 nm. The blue light from the master laser is locked to a hollow-cathode discharge lamp [4] via modulation transfer spectroscopy. With this setup we spectroscopically resolve the lines of the four most abundant bosonic isotopes as well as the hyperfine structure of the fermionic isotope ^{167}Er. Since the hyperfine constants of the excited level at 401 nm are unknown, we could not assign the absorption features to specific hyperfine transitions. We derive the yellow light from a dye laser operating with

Rhodamin 6G. By using an intracavity electro-optic modulator (EOM) and an external reference cavity, we stabilize the laser to a linewidth of about 50 kHz. By additionally locking the laser to an ultralow-expansion cavity, we achieve a long-term stability better than 30 kHz within a day [27].

Our experimental procedure is as follows. We load the Zeeman slowed atomic beam from an effusive, high-temperature oven directly into the narrow-line MOT. Our commercial oven typically operates at a temperature of 1300 °C, which is about 200 °C below the Er melting point. Two 3-mm apertures, separated by 50 mm, provide a geometrical collimation of the atomic beam. In addition, the atomic beam is further collimated and transversally cooled by a two-dimensional (2D) optical molasses, working on the broad 401-nm transition with a total power of about 100 mW. The beams are elliptically shaped to increase the interaction time between the atoms and the light. Thanks to the transversal cooling stage, we increase the loading flux by almost an order of magnitude.

The atomic beam then enters the Zeeman slower (ZS). Because of the limited capture velocity (a few m/s) imposed by the narrow cooling transition used for the MOT, it is crucial to design a ZS that provides enough atomic flux at low velocities [4]. We build a 360-mm-long spin-flip Zeeman slower, which can slow the atoms from 500 to about 5 m/s. The ZS light is focused at the oven position and has a total power of about 60 mW. At the MOT position, we estimate a beam diameter of about 11 mm, corresponding to an intensity of about one $I_{s,401}$, where $I_{s,401} = 56$ mW/cm^2 is the saturation intensity. Our ZS operates with light detuned by about $-20\Gamma_{401}$ (-540 MHz) from the unshifted resonance.

The narrow-line MOT is operated in a standard six-beam configuration with retroreflected beams. To increase the capture velocity of the MOT, we use large MOT beam diameters of about 30 mm. Typical MOT loading parameters include a magnetic field gradient B' (along the symmetry axis) of 4 G/cm, a laser intensity of $12I_{s,583}$ per beam with $I_{s,583} = 0.13$ mW/cm^2, and a detuning δ_{583} from the atomic transition of $-50\Gamma_{583}$ (-9.5 MHz). To measure the number of atoms in the MOT after loading, we optically compress the MOT by reducing δ_{583} to $-0.5\Gamma_{583}$ and we apply standard absorption imaging on the blue transition.

A special feature of our narrow-line MOT is the large detuning of the MOT light (typically $-50\Gamma_{583}$) needed for optimal loading. At this detuning, we observe a very strong effect of gravity on the position and shape of the atom cloud [3]. The atoms are located well below the center of the magnetic quadrupole field, and the cloud takes the form of a large semishell. To elucidate the reason for the large detuning, we monitor the loading dynamics and the lifetime of the MOT; see Fig. 2. Our measurements focus on the ^{166}Er isotope, but we have observed the same qualitative behavior also for the other isotopes.

Figure 2(a) shows the atom number in the MOT as a function of the loading time for different values of δ_{583}. We fit our data by using a standard loading rate equation [28], which includes a capture rate R and a decay rate γ; the latter accounts for both collisions between trapped atoms and collisions with the background gas. For a detuning of $-50\Gamma_{583}$ the atom number approaches its steady state in about 10 s with $N_{ss} \approx 2 \times 10^8$. For a lower value of the detuning
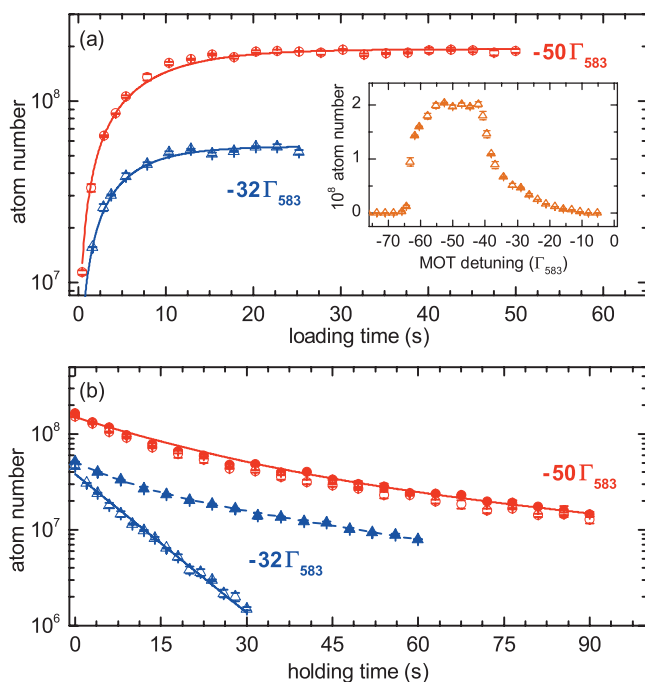
FIG. 2. (Color online) Loading (a) and decay (b) of the narrow-line MOT with ^{166}Er atoms for $\delta_{583} = -50\Gamma_{583}$ (circles) and $\delta_{583} = -32\Gamma_{583}$ (triangles). (a) Atom numbers are plotted as a function of the MOT loading time. The solid lines are fits to the data using $N(t) = N_{ss}(1 - e^{-\gamma t})$ with $N_{ss} = R/\gamma$. From the fits we obtain $\gamma = 0.137(2)$ s^{-1}, $R = 2.6(4) \times 10^7$ s^{-1}, and $\gamma = 0.200(4)$ s^{-1}, $R = 1.1(1) \times 10^7$ s^{-1} for $-50\Gamma_{583}$ and $-32\Gamma_{583}$, respectively. The inset shows the atom number after 10-s loading time as a function of the MOT detuning. (b) Atom numbers are plotted as a function of the holding time in the MOT in presence (open symbols) and absence of the ZS light (solid symbols). The solid lines are fits to the data using a double-exponential function; see text.

to $-32\Gamma_{583}$ we observe a substantial decrease of the atom number to $N_{ss} \approx 5 \times 10^7$. This behavior is clearly shown in the inset, where we monitor the number of atoms N_{ss} for a fixed loading time of 10 s as a function of the MOT light detuning. For detunings exceeding $\delta_{583} = -30\Gamma_{583}$ we observe a rapid increase in the atom number. When further increasing the detuning, N_{ss} first stays constant and then rapidly decreases.

We believe that the large detuning of the MOT light serves to minimize the detrimental effects of off-resonant pumping processes driven by the ZS light. According to the Zeeman shift in the quadrupole field of the MOT, we observe a spatial displacement of the atomic cloud with δ_{583} of about 1.4 mm/MHz [29]. For large detunings, this shift becomes so large that the atoms can no longer be kept in the MOT. For intermediate detunings in the range from -40 to $-55\Gamma_{583}$, the cloud displacement is advantageous for MOT operation since the atoms become spatially separated from the region of interaction with the ZS light. For small detunings, the ZS light leads to substantial losses of atoms.

The effect of the ZS light also shows up in lifetime measurements, where we monitor the number of atoms in the MOT as a function of the holding time with the ZS light being present or absent; see Fig. 2(b). For these measurements we

switch off the ZS magnetic field and the atomic beam after 10 s of MOT loading. For large detuning ($\delta_{583} = -50\Gamma_{583}$) the evolution of the atom number is not affected by the ZS light. In both cases, i.e., with the ZS light on and off, we observe faster losses in the earlier stage of the decay, which we attribute to inelastic two-body collisional processes, and a slower decay at a later time, which is finally limited by background collisions. For simplicity we use a double-exponential fit function to estimate the time constants [30]. We extract time constants of 19(3) and 80(20) s for the fast and slow dynamics, respectively. At lower MOT detuning ($-32\Gamma_{583}$), the ZS light strongly affects the decay. When the blue light is turned off, our observations are qualitatively similar to the ones at $-50\Gamma_{583}$ while with the blue light turned on the atomic loss dramatically increases. In this case the decay curve is well described by a single exponential function with a time constant $\tau = 9.0(1)$ s. This decay time is consistent with a simple estimate of pumping losses. By considering the absorption rate Γ_a of the 401-nm light at the actual intensity and detuning [31] and the branching ratio b for decay from the excited state to all the possible metastable states [9], we estimate a decay rate $1/\tau = b\Gamma_a$ of the order of 0.1 s^{-1}.

We could also demonstrate trapping of all the other Er isotopes, with the exception of the rare ^{162}Er (0.1% natural abundance). For all the bosonic isotopes we used about the same values for the detuning of the ZS and the MOT light. Figure 3(a) shows the atom number in the MOT for the different isotopes as a function of their natural abundance. For a long loading time of 20 s we observe similar atom numbers exceeding 10^8 for the three most abundant bosonic isotopes, indicating that saturation effects might apply. For a short loading time of 5 s, the atom number increases with the natural abundance. However, we observe a more complicated
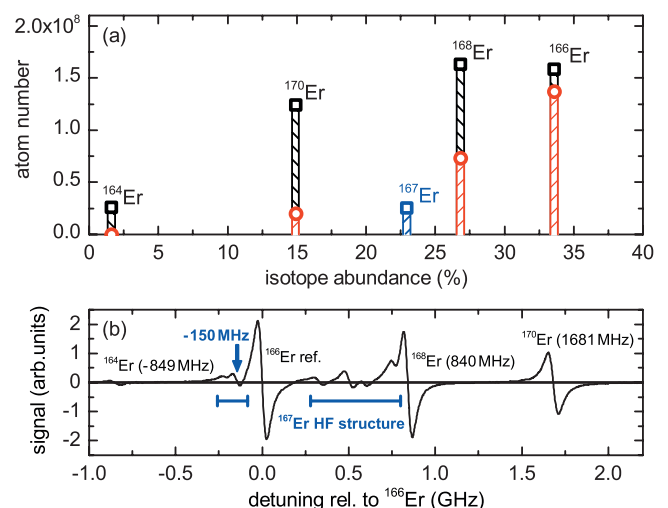
FIG. 3. (Color online) Behavior of different Er isotopes. (a) MOT atom number for the four most abundant bosonic isotopes as well as for the ^{167}Er fermionic isotope is plotted as a function of the natural abundance for 20-s (squares) and 5-s (circles) loading times. (b) Spectroscopy signal of the blue transition shows the isotope shifts for the bosonic isotopes and the HF structure of ^{167}Er. The arrow indicates the locking point used for the ZS light to produce the ^{167}Er MOT.

behavior than the expected linear growth. This might be due to slight differences in the optimal MOT parameters, but may also point to differences in scattering and collisional properties among the different isotopes.

For the fermionic isotope [167]Er we observe a MOT with atom number of about 3×10^7, which is substantially lower than the numbers measured for the bosonic isotopes. A simple explanation of this behavior can be that we decelerate and cool only atoms in the $F = 19/2$ hyperfine state, which has a statistical weight of about 20%. Note that a similar behavior has been observed with the fermionic [161]Dy MOT, which also shows lower atom numbers than the ones of bosonic MOTs [13]. An additional complication stems from the unknown hyperfine splitting of the 401-nm line. From the spectroscopic signal we could not identify *a priori* where to lock the Zeeman slower light to be resonant with the desired $F = 19/2 \rightarrow F' = 21/2$ hyperfine transition. To produce the [167]Er MOT, we had to proceed blindly by first locking the 583-nm MOT light on the cooling transition and then by trying different locking points for the ZS light until the MOT was visible. We finally succeed in creating a MOT by locking the ZS light to the spectroscopic line located 150 MHz below the blue transition frequency of the [166]Er isotope; see the arrow in Fig. 3(b).

After loading the MOT we apply a stage of compression to reduce the temperature of the atomic cloud and to achieve good starting conditions for direct loading of an optical dipole trap. With the optimized parameters $\delta_{583} = -0.5\Gamma_{583}$, $I = 0.16 I_{s,583}$, and $B' = 0.8 \, \text{G/cm}$, we measure a temperature of 15 μK via time-of-flight experiments. In addition, Stern-Gerlach experiments indicate that atoms in the compressed MOT phase are naturally pumped in the lowest Zeeman sublevel $m_J = -6$ by the MOT light. This can be explained by considering a combined effect of the narrow cooling transition used for the MOT and of gravity. The latter pushes the atoms

downward, creating an effective imbalance in the trap and leading to a preferential absorbtion of the σ^- polarized light from the lower vertical beam. For 2×10^8 atoms at $T = 15 \, \mu$K we estimate a peak number density of the polarized sample of $1.5 \times 10^{11} \, \text{cm}^{-3}$, corresponding to a phase-space density of about 4×10^{-6}. These values are similar to the ones observed in Yb experiments using the intercombination light [4]. Compared to other experiments on magnetic lanthanides, such as Dy [11], our much simpler approach based on a single cooling light for the MOT provides higher atom numbers and similar final temperatures. We suggest that this scheme can be successfully implemented with Dy, Ho, and Tm, using the 626-nm ($\Gamma/2\pi = 135$ kHz) [32], the 598-nm ($\Gamma/2\pi = 146$ kHz) [33], and the 531-nm ($\Gamma/2\pi = 370$ kHz) [34] transitions, respectively.

In conclusion, we have demonstrated an efficient and simple approach for an Er MOT based on a single narrow-line transition. Our scheme works with all abundant Er isotopes and allows for direct loading of an optical dipole trap. In first experiments we were able to load up to 10^7 Er atoms into the dipole trap in a single focused-beam configuration. Optimization of the dipole trap loading and evaporative cooling experiments are under way in our laboratory.

[1] T. Ido and H. Katori, Phys. Rev. Lett. **91**, 053001 (2003).

[2] A. J. Daley, M. M. Boyd, J. Ye, and P. Zoller, Phys. Rev. Lett. **101**, 170504 (2008).

[3] H. Katori, T. Ido, Y. Isoya, and M. Kuwata-Gonokami, Phys. Rev. Lett. **82**, 1116 (1999).

[4] T. Kuwamoto, K. Honda, Y. Takahashi, and T. Yabuzaki, Phys. Rev. A **60**, R745 (1999).

[5] E. A. Curtis, C. W. Oates, and L. Hollberg, Phys. Rev. A **64**, 031403 (2001).

[6] T. Lahaye, C. Menotti, L. Santos, M. Lewenstein, and T. Pfau, Rep. Prog. Phys. **72**, 126401 (2009).

[7] A. Griesmaier, J. Werner, S. Hensler, J. Stuhler, and T. Pfau, Phys. Rev. Lett. **94**, 160401 (2005).

[8] Q. Beaufils, R. Chicireanu, T. Zanon, B. Laburthe-Tolra, E. Maréchal, L. Vernac, J.-C. Keller, and O. Gorceix, Phys. Rev. A **77**, 061601 (2008).

[9] J. J. McClelland and J. L. Hanssen, Phys. Rev. Lett. **96**, 143005 (2006).

[10] D. Sukachev, A. Sokolov, K. Chebakov, A. Akimov, S. Kanorsky, N. Kolachevsky, and V. Sorokin, Phys. Rev. A **82**, 011405 (2010).

[11] M. Lu, N. Q. Burdick, S. H. Youn, and B. L. Lev, Phys. Rev. Lett. **107**, 190401 (2011).

[12] M. Lu, N. Q. Burdick, and B. L. Lev, e-print arXiv:1202.4444.

[13] S. H. Youn, M. Lu, U. Ray, and B. L. Lev, Phys. Rev. A **82**, 043425 (2010).

[14] A. J. Berglund, J. L. Hanssen, and J. J. McClelland, Phys. Rev. Lett. **100**, 113002 (2008).

[15] D. Sukachev, A. Sokolov, K. Chebakov, A. Akimov, N. Kolachevsky, and V. Sorokin, JETP Lett. **92**, 703 (2010).

[16] Y. Takasu, K. Honda, K. Komori, T. Kuwamoto, M. Kumakura, Y. Takahashi, and T. Yabuzaki, Phys. Rev. Lett. **90**, 023003 (2003).

[17] Y. Takasu, K. Maki, K. Komori, T. Takano, K. Honda, M. Kumakura, T. Yabuzaki, and Y. Takahashi, Phys. Rev. Lett. **91**, 040404 (2003).

[18] R. V. Krems, G. C. Groenenboom, and A. Dalgarno, J. Phys. Chem. A **108**, 8941 (2004).

[19] C. B. Connolly, Y. S. Au, S. C. Doret, W. Ketterle, and J. M. Doyle, Phys. Rev. A **81**, 010702 (2010).

[20] S. Kotochigova and A. Petrov, Phys. Chem. Chem. Phys. **13**, 19165 (2011).

[21] Y. Ralchenko, A. Kramida, J. Reader, and N. A. Team, NIST Atomic Spectra Database, 2011.

[22] H. Y. Ban, M. Jacka, J. L. Hanssen, J. Readerand, and J. J. McClelland, Opt. Express **13**, 3185 (2005).

[23] In Ref. [24] a linewidth of $\Gamma_{401}/2\pi = 36$ MHz has been measured via fluorescence spectroscopy on atomic beams while in Ref. [25] a value of $\Gamma_{401}/2\pi = 29.5$ MHz has been obtained from lifetime measurements. We measure a linewidth of 27.5(4) MHz by using an absorption imaging technique on magneto-optically trapped atoms in the regime of low saturation parameters.

[24] J. J. McClelland, Phys. Rev. A **73**, 064502 (2006).

[25] J. E. Lawler, J.-F. Wyart, and E. A. D. Hartog, J. Phys. B **43**, 235001 (2010).

[26] W. J. Childs, L. S. Goodman, and V. Pfeufer, Phys. Rev. A **28**, 3402 (1983).

[27] Although we could clearly observe the spectroscopic signals for the different Er isotopes using a hollow-cathode lamp, we prefer to lock the 583-nm light to an ultralow-expansion cavity in order to reach higher-frequency stability.

[28] J. Weiner, V. S. Bagnato, S. Zilio, and P. S. Julienne, Rev. Mod. Phys. **71**, 1 (1999).

[29] The atomic cloud displacement Δ_x from the trap center is given by $\Delta\mu B'\Delta_x = \hbar\Delta_{583}$, where $\Delta\mu$ is the difference in magnetic moments between the ground and excited state.

[30] The standard rate equation approach is problematic, because the distorted (semishell) shape of the MOT makes it difficult to extract reliable values for the density and because the MOT may be in the high-density limit regime [28].

[31] H. J. Metcalf and P. van der Straten, *Laser Cooling and Trapping* (Springer, New York, 1999).

[32] M. Lu, S. H. Youn, and B. L. Lev, Phys. Rev. A **83**, 012510 (2011).

[33] M. Saffman and K. Mølmer, Phys. Rev. A **78**, 012336 (2008).

[34] D. Sukachev, K. Chebakov, A. Sokolov, A. Akimov, N. Kolachevsky, and V. Sorokin, Opt. Spectrosc. **111**, 633 (2011).

6.3. Further work

6.3.1. Spin polarization

As pointed out earlier an advantage of the narrow-line MOT with large detuning is that the atomic sample gets spin-polarized without the need for an extra repumping laser[1]. This effect is related to the gravitational sag in the MOT, which causes the atoms to preferably scatter the lower MOT beam, see Fig. 6.3(b). Dependent on the polarization of the lower beam atoms get pumped into a stretched Zeeman state, which is in case of σ^--polarized light for the lower beam the energetically lowest $m_J = -6$ state of erbium.

The polarization of the spin state happens already during MOT loading. By applying an homogeneous magnetic field of 855 mG at the beginning of the cMOT stage, see Fig. 6.2(e), the spin-polarization can be easily maintained also when one turns off the magnetic field gradient for loading into the ODT. The degree of spin-polarization was checked by performing a Stern-Gerlach-type experiment. Atoms are first loaded from the cMOT into the ODT where forced evaporation was performed. This results in a final temperature of 140 nK. To separate different m_J states a magnetic field gradient of about 5 G/cm was applied for 4 ms after switching off the trap. The magnetic field gradient leads to a spin-dependent force, which spatially separates different spin states. Further separation happens during a subsequent time-of-flight of another 16 ms such that different spin components can be separately imaged on the CCD.

Figure 6.5(a) shows the result of this measurement. The spin-purity is determined by the ratio between the area of a Gaussian fit to $m_J = -6$ and the overall area enclosed by the data points. This gives a spin purity of 99(1)%. By driving a radio-frequency transition in resonance with the energy of the Zeeman splitting energetically higher m_J-states can be intentionally populated, see Fig. 6.5(b-d). This was done in presence of a homogeneous magnetic field of 855 mG.

---

[1] Due to a finite branching ratio into unwanted spin states in case of alkali metals and unwanted electric states in case of alkali-earth metals during the MOT loading, repumping lasers have to be used to bring atoms into the desired spin state at the end of MOT loading.
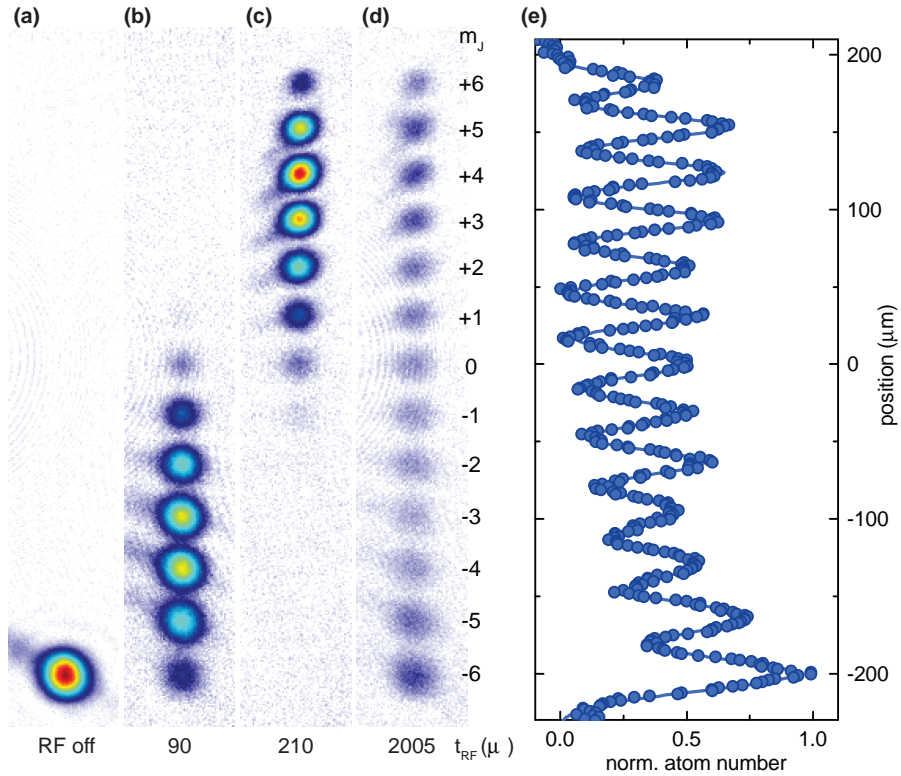
Figure 6.5.: Population of Zeeman sub-states in an ultracold thermal sample measured in a Stern-Gerlach-type experiment. (a) When no radio-frequency (RF) is applied only the lowest spin state is populated and thus spin polarization of the atomic sample is verified. (b) When applying a RF for $90\,\mu$s at a power of $23\,$dBm energetically higher-lying Zeeman states are populated. (c) After $210\,\mu$s mostly states with $m_J \geq 0$ are populated. (d) For even longer RF durations the atoms are distributed equally in all Zeeman sub states. (e) Integrated atom number from (d) is fitted by Gaussian peaks for each m_J state (line). Small deviations in the spacing between different m_J-peaks are due to a spatial inhomogeneity of the magnetic gradient field.

Chapter 7

Publication: Bose-Einstein condensation of erbium

7.1. Introduction

The successful demonstration of narrow-line laser cooling using the transition at a wavelength of 583 nm was important to further proceed with achieving a Bose-Einstein condensate (BEC) of erbium atoms for the first time. After preparing the compressed MOT (cMOT), atoms are loaded into an optical dipole trap (ODT) where they undergo forced evaporative cooling. Regarding dipolar lanthanide atoms, the approach of forced evaporation has been also applied to prepare a dipolar BEC of dysprosium atoms, published in Ref. [Lu11].

Since the atomic polarizability of erbium was not known in the beginning a first crossed ODT was set up using two fiber-amplified lasers operating at a wavelength of 1064 nm and 1070 nm. The first laser was used to create a trapping beam in horizontal direction whereas the second one was used in vertical direction. Atoms had been loaded with an efficiency of about 10 % from the cMOT into the ODT within the first 150 ms with only a small heating of up to a temperature of $42\,\mu$K. After a total loading time of 600 ms forced evaporative cooling was performed. Initial experiments on ^{166}Er showed insufficient thermalization rates. Later it was found out that this isotope has only a small background scattering length. Changing the isotope to ^{168}Er lead directly to the observation of a bimodal distribution at low temperatures[1], which is the smoking gun of the appearance of a condensed phase. An onset of condensation was seen at a temperature of about 400 nK with 2×10^5 atoms. Finally, a pure BEC was achieved with 6.8×10^4 atoms by further evaporation, showing its characteristic Thomas-Fermi density distribution and an inversion of the aspect ratio after releasing it from the trap. A Feshbach scan at magnetic fields below 3 G revealed up to six Feshbach resonances and gave important information about the scattering properties for optimizing the evaporation procedure. The BEC was mutually brought to collapse by ramping from above closer and closer to a prominent Feshbach resonance at 914 mG. This revealed the tunability of the s-wave scattering length as well as the presence of dipole-dipole interaction by the observation of an anisotropic d-wave pattern in the absorption image.

---

[1] The first observation of the erbium BEC was made on the 8th of March 2012, about two years after starting to design and set up the experiment.

In the following section an improved evaporation procedure will be described. Section 7.2 contains the publication on the erbium BEC. In Sec. 7.3 further additional work is presented. In the first half of that section the cross-dimensional rethermalization method used for measuring the scattering length for various isotopes of erbium is discussed. In the second half the mass dependence of the s-wave scattering length for various isotopes is shown and fitted by a theoretical model.

7.1.1. Evaporative cooling

Due to the small phase-space density in the MOT atoms need to be evaporatively cooled in the ODT to produce a degenerate quantum gas, see Ref. [Ket99]. The phase-space density[2] of a quantum gas is defined as

$$\mathrm{PSD} = n_0 \lambda_{\mathrm{dB}}^3 \, , \qquad\qquad 7.1$$

where n_0 is the peak number density of the gas and λ_{dB} the thermal de Broglie wavelength, which is proportional to $1/\sqrt{T}$. The transition into the condensed phase happens when a macroscopically large number of bosons occupy the ground state and the phase-space density[3] approaches a value of 2.6. A large value of the phase-space density requires both low temperature and high density of the gas. In a harmonic trapping potential with trap frequencies ω_i with $i = x, y, z$ in the three spatial directions and geometrical mean trap frequency $\overline{\omega} = (\omega_x \omega_y \omega_z)^{1/3}$ the peak number density can be calculated as

$$n_0 = N \overline{\omega}^3 \left(\frac{m}{2\pi k_{\mathrm{B}} T} \right)^{\frac{3}{2}} \, , \qquad\qquad 7.2$$

with N being the total atom number. The phase-space density can be expressed by using this equation as

$$\mathrm{PSD} = N \overline{\omega}^3 \left(\frac{\hbar}{k_{\mathrm{B}} T} \right)^3 \, . \qquad\qquad 7.3$$

Increasing the PSD by evaporative cooling is based on actively truncating the thermal Maxwell-Boltzmann distribution by removing only hot particles from the system and letting the residual atoms rethermalize via elastic collisions. In dipolar systems the elastic cross section arises from the long-range dipole-dipole interaction (DDI). Refer to Sec. 4.2.1 and Eqs. 4.19 and 4.20 for expressions of the elastic cross section of bosons and fermions, respectively. Note that for bosons the DDI gives an additional contribution to the contact-interaction cross section whereas for fermions it causes the cross section to be nonzero in contrast to non-dipolar fermions. This opens the possibility to evaporatively cool of indistinguishable fermions, see Chapter 9. In both cases the truncation of hot particles can be easily achieved by adiabatically lowering[4] the potential depth of the ODT. Increasing the phase-space density by evaporative cooling relies on a favorable ratio of elastic to inelastic

---

[2]   The phase-space density relates the mean particle distance, expressed by n_0, to the extension of the particle, given by $\lambda_{\mathrm{dB}} = h/\sqrt{2\pi m k_{\mathrm{B}} T}$.

[3]   For a 3D gas in a harmonic trapping potential, one would expect the onset of condensation at a critical phase-space density of PSD = 1.2, see Ref. [Pet02], but it can be shown that for $k_{\mathrm{B}} T \ll \hbar \omega$ the critical phase-space density is 2.6, see Ref. [Cas01].

[4]   It is crucial to lower the potential depth adiabatically because of two reasons. First, the gas has to have enough time to rethermalize and second, excitations in the trap have to be avoided.
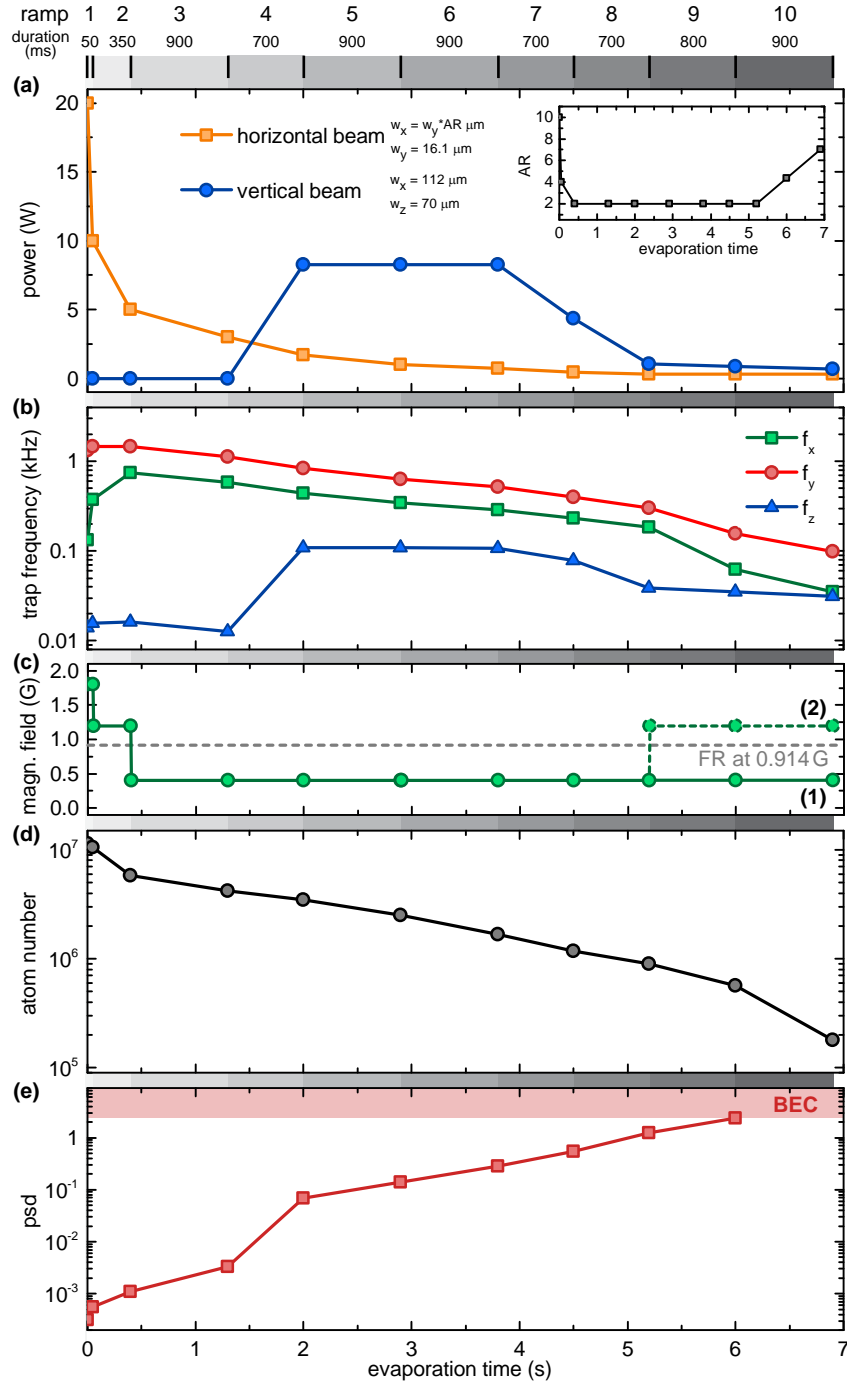
Figure 7.1.: Evaporation trajectory after loading ^{168}Er into the ODT. Parameters of each ramp have been optimized to achieve the largest possible increase of the phase-space density (e) with the smallest loss of atom number (d). (b) Trap frequencies are calculated from the laser power (a) and measured waists of the horizontal and vertical beams. (c) The magnetic field is shown with the position of a Feshbach resonance (FR) at 914 mG (gray dashed line). Evaporative cooling is mostly carried out at 0.4 G (1) but for special applications, e. g. where the cloud has to be prepared above the FR, we jump to 1.2 G at the beginning of the ninth ramp. This is indicated by the dashed line (2).

collision rates. The former is needed to provide efficient rethermalization between atoms within a reasonable time whereas the latter leads to losses especially at high densities and should therefore be small.

A major improvement of the loading from the cMOT into the ODT was made by replacing the initially used multi-mode fiber laser in the horizontal direction by a single-mode diode-pumped solid state laser[5] and implementing the scanning system for the horizontal trapping beam, see Ref. [Bai12a] and Sec. 3.5.3. By deflecting the trapping beam in a fast way using an accusto-optical modulator a time-averaged potential is created. This lets one optimize the spatial overlap between the cMOT and the ODT and improves the loading efficiency from 10% to 35%. Furthermore, it allows for a dynamical change of the aspect ratio of the ODT during the experiment.

For efficient evaporation it is important to find an optimum set of parameters for an adiabatic ramp of the potential depth. Lowering the trapping potential depth is done by decreasing the trapping laser power. As described in Sec. 3.5.3 atoms are initially loaded from the cMOT into a single horizontal trapping laser beam. Typical conditions at this stage are 1.2×10^6 atoms at a temperature of $22 \, \mu\text{K}$, which corresponds to a PSD of 3.1×10^{-4}. The power of the horizontal laser beam is decreased in an exponential-like piecewise linear ramp consisting of a total of ten steps. Figure 7.1 presents the important ramp parameters for every evaporation step, including the laser power, trap frequencies, homogeneous magnetic field, atom number, and phase-space density. During the first two ramps the aspect ratio of the horizontal beam is lowered from a value of ten, used for loading from the MOT, to two, see inset in Fig. 7.1. This spatially compresses the sample before evaporation is performed. At the fourth step the power of the vertical beam[6] is ramped up, which gives a much stronger confinement in the axial direction of the horizontal beam and thus a strong increase of the density as well as the phase-space density is observed, see Fig. 7.1(e). The magnetic field is usually changed to $0.4 \, \text{G}$ after the third ramp, which gives a more favorable scattering length during evaporation of about $240 \, a_0$. As shown in Fig. 7.1(c) there is a Feshbach resonance (FR) located at $914 \, \text{mG}$. For special applications, which require to be at a magnetic field above the FR, like for driving the dipolar collapse or creating Er_2 molecules via magneto-association, we jump back above the FR to $1.2 \, \text{G}$ for the last two evaporation stages, see Fig. 7.1(c). After completing the full evaporation ramp up to 2×10^5 atoms are prepared in an almost pure BEC within $7 \, \text{s}$. Final laser powers are $0.3 \, \text{W}$ for the horizontal and $0.7 \, \text{W}$ for the vertical trapping beam, giving trap frequencies of $(\omega_x, \omega_y, \omega_z) = 2\pi \times (35, 98, 31) \, \text{Hz}$. An in-detail description of the evaporation process and its optimization can be found in Ref. [Bai12a].

The evaporation efficiency equals the order of magnitude increase of the phase-space density at the expense of an order of magnitude of atom number, see Ref. [Ket96]. It is given by

$$\gamma = -\frac{d(\ln \text{PSD})}{d(\ln N)} \ . \tag{7.4}$$

The evaporation efficiency can be easily determined by plotting the phase-space density against the atom number in a log-log plot, as seen in Fig. 7.2. The slope of a linear fit gives

---

[5] model Mephisto MOPA, $42 \, \text{W}$ at $1064 \, \text{nm}$, from Innolight (now Coherent)
[6] created by a fiber laser, model PYL-10-1064-LP, $10 \, \text{W}$ at $1064 \, \text{nm}$, from IPG Photonics
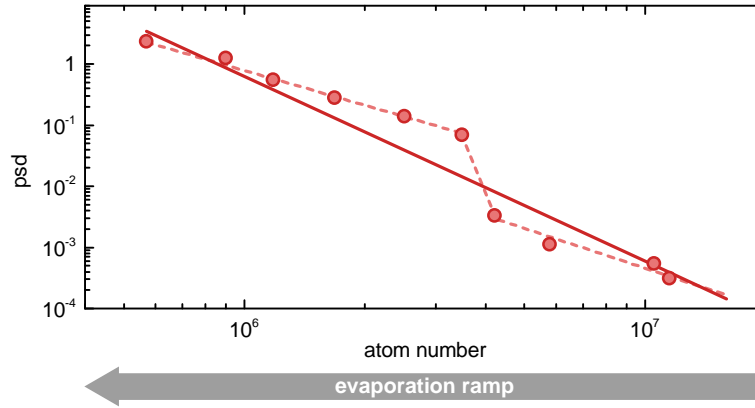
Figure 7.2.: Evaporation efficiency of cooling ^{168}Er. The increase of the phase-space density is plotted against the loss of atom number. Evaporative cooling proceeds along the direction following an increasing phase-space density, indicated by the arrow. The slope of the linear fit following Eq. 7.4 (solid line) gives an overall efficiency of the evaporation process of $\gamma = 3.4$. For the final evaporation at small atom numbers the efficiency is about two (upper dashed line), which is similar to the efficiency at the beginning of evaporation (lower dashed line).

the overall evaporation efficiency, which is in case of ^{168}Er evaluated to be $\gamma = 3.4$. The sudden increase of the phase-space density is caused by the ramping of the vertical trapping beam during the fourth evaporation ramp. This evaporation efficiency is among the highest efficiencies available in modern quantum gas experiments and is usually achievable by using a so-called *dimple technique* or other more elaborate techniques. For non-dipolar systems in a simple crossed dipole trap, like in the presented case, typical values for γ range from about one up to two.

7.1.2. Dipolar Bose-Einstein condensate

At the many-body level the s-wave contact interaction is given by the contact potential

$$U_{\text{cont}}(\mathbf{r}) = \frac{4\pi\hbar^2 a_s}{m}\delta(\mathbf{r}) = g\delta(\mathbf{r}) \; , \qquad\qquad 7.5$$

with δ the delta function and $g = \frac{4\pi\hbar^2 a_s}{m}$ the coupling constant. The contact interaction can be changed by tuning the s-wave scattering length a_s. The s-wave scattering length can be compared to the dipolar scattering length, a_D, see Eq. 4.17, by calculating the dipolar constant ϵ_{dd} as

$$\epsilon_{\text{dd}} = \frac{2}{3}\frac{a_D}{a_s} \; . \qquad\qquad 7.6$$

It is important that ϵ_{dd} is non negligible if dipolar effects should be observable in a system of ultracold particles. Some numerical values of a_D and ϵ_{dd} for magnetic and electric dipolar systems are summarized in Table 7.1.

A Bose-Einstein condensate with contact *and* dipole-dipole interaction is described by the

species	dipole moment	a_D (a_0)	$\epsilon_{\rm dd}$
^{87}Rb	$1\,\mu_{\rm B}$	1.1	0.007
^{52}Cr	$6\,\mu_{\rm B}$	24	0.2
^{168}Er	$7\,\mu_{\rm B}$	99	0.3
^{164}Dy	$10\,\mu_{\rm B}$	196	0.7
KRb	$0.6\,{\rm D}$	3.0×10^3	20
HCN	$3.0\,{\rm D}$	3.6×10^4	240

Table 7.1.: Dipolar scattering length a_D and dipolar constant $\epsilon_{\rm dd}$ for different systems in comparison. To observe dipolar effects at ultracold temperatures $\epsilon_{\rm dd}$ should be non-negligible. Most of the data was taken from [Lah09].

following Gross-Pitaevskii equation,

$$i\hbar\frac{\partial\psi}{\partial t} = -\frac{\hbar^2}{2m}\Delta\psi + \left(U_{\rm ext} + g|\psi|^2 + \Phi_{\rm dd}\right)\psi \;, \qquad 7.7$$

with ψ the many-body wave function, $U_{\rm ext}$ an external trapping potential, and $\Phi_{\rm dd}$ the dipolar contribution. The dipolar contribution can further be written as

$$\Phi_{\rm dd}(\mathbf{r}, t) = \int |\psi(\mathbf{r}', t)|^2 U_{\rm dd}(\mathbf{r} - \mathbf{r}') d^3\mathbf{r}' \;, \qquad 7.8$$

with $U_{\rm dd}$ the dipole-dipole interaction potential, see Eq. 4.2. In case of a spherically symmetric cloud of radius $R = R_i$ with $i = x, y, z$ trapped in an ODT with trapping frequency $\omega = \omega_i$ the dipolar contribution $\Phi_{\rm dd}$ can be written to first order in $\epsilon_{\rm dd}$ as, see Ref. [Gio02],

$$\Phi_{\rm dd}(\mathbf{r}) = \epsilon_{\rm dd}\frac{m\omega^2}{5}(1 - 3\cos^2\theta)\begin{cases} r^2 & \text{if } r < R \\ \frac{R^5}{r^3} & \text{if } r > R \;. \end{cases} \qquad 7.9$$

Thus the dipolar mean-field potential has the shape of a saddle with two minima along the direction of the dipole orientation. This means that the cloud will be elongated in that direction because it is energetically more favorable.

The elongation is the most obvious example for an effect of the DDI in a harmonically confined BEC. The effect is often called *magnetostriction* and was predicted in Ref. [San00]. The first observation of this effect was made using a BEC of ^{7}Li atoms in spite of its small magnetic moment of $1\,\mu_{\rm B}$, see Ref. [Pol09]. Magnetostriction stems from magnetic forces within the cloud, which change the cloud's shape and volume.

A second effect of the DDI is the emergence of a *d*-wave pattern when the BEC collapses. The numeric factor in Eq. 7.6 is chosen such that a BEC will become unstable with $\epsilon_{\rm dd} \geq 1$. The contact interaction can be tuned in a broad range by an external magnetic field using a Feshbach resonance and thus also $\epsilon_{\rm dd}$ can be changed. Utilizing this tunability a stable condensate can be mutually brought to collapse. This demonstration of a collapse is used as a smoking gun for a tunable *and* dipolar quantum gas and was first demonstrated by the group of T. Pfau in Stuttgart (Germany) in Ref. [Lah08] for a gas of chromium atoms. A confirmation of the erbium BEC collapse is given within the publication in the following section.

7.2. Publication: Bose-Einstein Condensation of Erbium[†]

Kiyotaka Aikawa,[1] Albert Frisch,[1] Michael Mark,[1] Simon Baier,[1] Alexander Rietzler,[1] Rudolf Grimm,[1,2] and Francesca Ferlaino[1]

[1] *Institut für Experimentalphysik and Zentrum für Quantenphysik, Universität Innsbruck, Technikerstraße 25, 6020 Innsbruck, Austria*
[2] *Institut für Quantenoptik und Quanteninformation, Österreichische Akademie der Wissenschaften, 6020 Innsbruck, Austria*

[†] The author of the present thesis made strong contributions in constructing the experimental apparatus together with A. R., S. B., K. A. and M. M., analyzing the data, and writing the manuscript.

Bose-Einstein Condensation of Erbium

K. Aikawa,[1] A. Frisch,[1] M. Mark,[1] S. Baier,[1] A. Rietzler,[1] R. Grimm,[1,2] and F. Ferlaino[1]

[1]*Institut für Experimentalphysik and Zentrum für Quantenphysik, Universität Innsbruck, Technikerstraße 25, 6020 Innsbruck, Austria*
[2]*Institut für Quantenoptik und Quanteninformation, Österreichische Akademie der Wissenschaften, 6020 Innsbruck, Austria*
(Received 6 April 2012; published 21 May 2012)

We report on the achievement of Bose-Einstein condensation of erbium atoms and on the observation of magnetic Feshbach resonances at low magnetic fields. By means of evaporative cooling in an optical dipole trap, we produce pure condensates of ^{168}Er, containing up to 7×10^4 atoms. Feshbach spectroscopy reveals an extraordinary rich loss spectrum with six loss resonances already in a narrow magnetic-field range up to 3 G. Finally, we demonstrate the application of a low-field Feshbach resonance to produce a tunable dipolar Bose-Einstein condensate and we observe its characteristic d-wave collapse.

Ultracold quantum gases have proven to be ideal systems for observing spectacular many- and few-body quantum effects. The large majority of these phenomena rely on the high degree of control over the interparticle interaction achieved with ultracold atoms. In the widely used alkalis, ultracold atoms interact isotropically via a short-range contact potential. A novel exciting frontier in quantum gas experiments is to access unexplored physical scenarios based on the anisotropic and long-range dipole-dipole interaction (DDI) [1,2]. A dipolar quantum gas is expected to exhibit fascinating phenomena, including novel many-body quantum phases [3–6]. The DDI acts in systems having sizable electric or magnetic dipole moments [1].

In the context of ultracold atomic quantum gases, pioneering experimental work on strong DDI has been carried out with chromium atoms [7–9]. Magnetic lanthanides offer new possibilities for dipolar physics. In such systems, the combination of a large magnetic moment and a large atomic mass leads to a particularly strong dipolar character. The demonstration of the first magneto-optical trap of erbium atoms [10] stimulated growing interest in such species for quantum gas experiments. Very recently, a Bose-Einstein condensate (BEC) and a degenerate Fermi gas of dysprosium have been produced [11,12]. We choose erbium as a promising candidate for experiments on dipolar quantum gases. This species has a number of very appealing features, including a large magnetic moment μ of 7 times the Bohr magneton, several stable isotopes, a rich energy level scheme [13] with a non-S electronic ground state [14], and interesting cold collisional phenomena [15,16].

In strongly magnetic atoms, the competition between the DDI and the contact interaction is very important and gives rise to many intriguing phenomena. The contact interaction is determined by the s-wave scattering length a and can be often tuned with external magnetic fields via Feshbach resonances [17]. Tuning of a also controls the balance of these two interactions. In the case of a novel species in

quantum gas experiments, Feshbach resonances and scattering lengths are *a priori* unknown. Magnetic lanthanides such as erbium with their large magnetic moments and their non-S electronic ground states present a completely unexplored terrain in ultracold scattering physics. Here the anisotropic interaction is expected to give rise to novel scattering scenarios, which are not accessible with alkali atoms [18,19].

In this Letter, we report on the attainment of Bose-Einstein condensation of erbium atoms and on the observation of Feshbach resonances in the region of low magnetic fields. We obtain pure optically trapped BECs of ^{168}Er containing 7×10^4 atoms. The remarkably high efficiency of evaporative cooling in a standard optical dipole trap indicates favorable scattering properties of the ^{168}Er isotope. In addition, the magnetic Feshbach spectroscopy provides first valuable information on the scattering behavior of submerged-shell atoms at ultralow temperatures. Moreover, we demonstrate low-field Feshbach tuning of the contact interaction in our strongly dipolar BEC.

Our experimental procedure to create a BEC of Er follows a simple and straightforward scheme, inspired by work on Yb atoms [20,21]. Our starting point is the narrow-line *yellow* magneto-optical trap (MOT) described in our very recent work [22]; it operates on the 583 nm line (natural linewidth 190 kHz). We choose this approach because narrow-line MOTs permit us to obtain samples with a large number of atoms at temperatures in the lower microkelvin region. This allows a direct and efficient transfer of atoms into optical dipole traps without the need for additional cooling stages [20,21]. Our MOT gives about 10^8 atoms at a temperature of 15 μK [23].

An additional very advantageous feature of our approach is that the MOT light automatically pumps the atoms into the lowest Zeeman sublevel $m_J = -6$, where m_J is the projection quantum number of the total electronic angular momentum $J = 6$. This effect results from the interplay between gravity and weak radiation pressure, which leads to a spatial down shift with respect to the zero of the

magnetic quadrupole field [24] and thus to a preferential absorption of the vertical MOT beam with σ^- polarization [22]. The polarization of the sample is confirmed by Stern-Gerlach-type measurements.

Our optical dipole trap geometry follows the concepts originally applied in experiments with Yb BEC [20]. The trap is created by crossing a tightly confining horizontal beam (y axis) and a less focused vertical beam (z axis). The basic idea is that initially the atoms are predominantly trapped by the horizontal beam, whereas the vertical beam provides confinement relevant in the final stage of evaporation. The horizontal beam is derived from a 100 W broadband Yb fiber laser operating at 1075 nm and has an initial power of 10 W. The beam has an elliptic cross section with a waist of 30(40) μm along the vertical (horizontal) direction. The vertical beam is produced by a 10 W Yb fiber laser source at 1064 nm and has an initial power of 8 W. The beam profile is elliptic with a waist of 55(110) μm along (perpendicular to) the axis of the horizontal beam.

We load the dipole trap during the MOT compression phase. We observe that the time period in which the compressed MOT and dipole trap coexist is crucial for efficient loading. The number of atoms in the optical dipole trap exponentially approaches its maximum value with a time constant of about 150 ms. After 600 ms of loading, we turn off the MOT beams and the quadrupole magnetic field, and we switch on a weak homogeneous magnetic field of about 300 mG along the vertical direction to preserve the spin polarization of the sample. We obtain 2.6×10^6 atoms at a temperature of 42 μK in the optical dipole trap. At this point, the atoms are mainly trapped by the horizontal beam. We measure oscillation frequencies (ν_x, ν_y, ν_z) = (1.3, 0.016, 1.95) kHz; the potential depth is estimated to be 560 μK. The peak density and the peak phase-space density are 1.7×10^{13} cm^{-3} and 1.6×10^{-4}, respectively. These are our starting conditions for the evaporative cooling process.

Forced evaporative cooling is performed by reducing the power of the trapping beams in a nearly exponential ramp. The overall evaporation sequence has a duration of 5.5 s [25]. We then turn off the trapping beams and let the atomic cloud expand before applying standard absorption imaging. For imaging, we illuminate the atomic cloud with a 50-μs probe beam pulse [26]. The probe beam propagates horizontally at an angle of 14° with respect to the propagation axis (y axis) of the horizontal trapping beam.

The phase transition from a thermal cloud to BEC manifests itself in a textbooklike bimodal distribution in the time-of-flight absorption images. Figure 1 shows the absorption images and the corresponding linear density profiles for different final temperatures, i.e., for different stages of the evaporation. At higher temperatures the atomic distribution is thermal with the expected Gaussian profile resulting from the Maxwell-Boltzmann distribution; see Fig. 1(a).
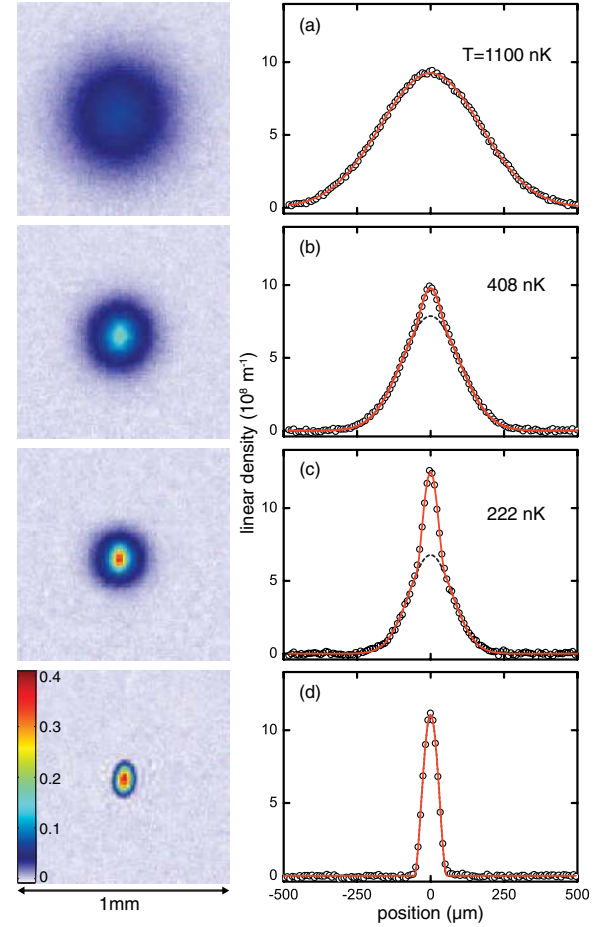

FIG. 1 (color online). Absorption images and integrated density profiles showing the BEC phase transition for different evaporation times. The absorption images are an average of four images taken after 24 ms of expansion. The color bar shows the optical density. The solid lines are fits to the data using Gaussian (a), bimodal (b) and (c), and Thomas-Fermi (d) distribution. The dotted lines represent the Gaussian part of the bimodal fit, describing the thermal atoms. From the fit we extract: $N = 3.9 \times 10^5$, $T = 1100$ nK (a), $N = 2.1 \times 10^5$, $T = 408$ nK (b), $N = 1.6 \times 10^5$, $T = 222$ nK (c), $N = 6.8 \times 10^4$ (d), where N is the total atom number. For (b) and (c), we extract a condensate fraction of 5% and 20%, respectively.

By cooling the atomic sample below the critical temperature, we clearly observe that the atomic density distribution has a bimodal profile with a narrower and denser peak at the center, which represents the BEC (b). By further evaporating the sample, the BEC fraction continuously increases (c) until the thermal component is not anymore discernible and an essentially pure BEC is formed with 7×10^4 atoms (d).

To analyze our data, we fit a bimodal distribution to the integrated time-of-flight absorption images. This distribution consists of a Gaussian function, which accounts for the thermal atoms, and an inverted integrated parabolic function for the BEC component in the Thomas-Fermi limit.

Just after the onset of quantum degeneracy (BEC fraction $\sim 5\%$), we measure trap frequencies of $(\nu_x, \nu_y, \nu_z) = (208, 70, 299)$ Hz, atom number of $N = 2.1 \times 10^5$, and a temperature of $T = 408$ nK. The critical temperature of 417 nK as calculated from standard BEC theory (without interaction shift) is consistent with this observation.

The evaporation efficiency is found to be remarkably high as 3.5 orders of magnitude in phase-space density are gained by losing a factor of 10 in atom number. This observation already points to favorable scattering parameters of the ^{168}Er isotope. First evaporative cooling experiments on the most abundant ^{168}Er isotope reveal a lower efficiency in the final stage of evaporation, suggesting that a different strategy might be needed to reach BEC.

To gain insight into the ultracold collisional properties of erbium we perform Feshbach spectroscopy [17] at low magnetic fields. This measurement is done in a way that allows us to identify both the poles and zero crossings of Feshbach resonances [27,28]. The basic idea here is to prepare the system at a variable target value of the magnetic field and then to rapidly (50 ms) decrease the depth of the optical dipole trap by almost a factor of 2. The sample stays near thermal equilibrium with an effective temperature of 2.2 μK but features a truncated energy distribution. We then let the system evolve at a constant trap depth for 250 ms, during which plain evaporative cooling and inelastic losses can occur depending on the scattering length. We finally switch off the trap and take time-of-flight images to determine the temperature and number of the atoms. The measurement is then repeated for variable magnetic-field values. Such a Feshbach scan shows resonance poles as loss features and zero crossings as temperature maxima.

Figure 2 shows the loss spectrum and the corresponding temperatures in the low magnetic-field range up to 3.2 G [29]. Already in this narrow magnetic-field range, the loss spectrum is very rich. We identify six pronounced resonant minima in the atom number that we interpret as being caused by Feshbach resonances. For convenience, we determine the resonance positions with Gaussian fits, yielding 0.72, 0.91, 1.51, 2.16, 2.48, and 2.85 G. The loss features show different strengths and widths. For the three broader resonances at 0.91, 2.16, and 2.48 G, we also observe the appearance of temperature maxima to the right of the loss minima (arrows in Fig. 2). These temperature maxima mark the zero crossings of the scattering length. The other loss features are too narrow to provide clear signatures of the zero crossing. From the difference in positions between the minima in the atom number and the maxima in temperature we estimate the widths Δ of the resonances. We find $\Delta = 65, 60,$ and 180 mG for the resonances at 0.91, 2.16, and 2.48 G, respectively.

In a strongly dipolar atomic gas, universal dipolar scattering is present [30–32], so that the total cross section for elastic scattering does not vanish at the zero crossings of
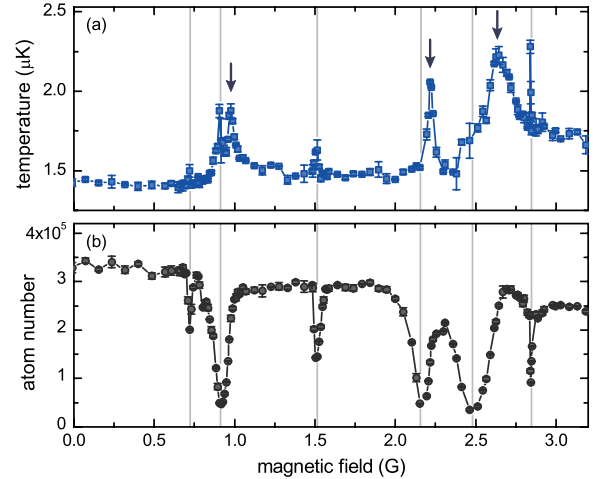

FIG. 2 (color online).   Observation of Feshbach resonances in Er-Er collisions. The measured temperature (a) and atom number (b) are plotted as a function of the magnetic field. The minima in the atom number indicate the Feshbach resonance poles, marked by the thin vertical lines. The maxima in the temperatures to the right of the three stronger loss features (arrows) are attributed to the respective zero crossings of the scattering length. The varying background in the atom number is presumably due to ramping effects caused by the sweep of the magnetic field across the resonances.

the scattering length. For Er, a minimum cross section $\sigma_{\text{dip}} = 8\pi(30a_0)^2$ results from universal dipolar scattering, where a_0 is the Bohr radius. The fact that we observe temperature maxima near the zero crossings suggests a dominant role of s-wave scattering and not of dipolar scattering. Preliminary cross-dimensional thermalization measurements indeed point to a scattering length between 150 and $200a_0$.

The existence of Feshbach resonances at low magnetic fields makes the manipulation of the contact interaction in the Er BEC very convenient and straightforward. As a proof-of-principle experiment, we explore the controlled d-wave collapse of the BEC, following the procedure successfully applied by the Stuttgart group [7]. We first produce a pure BEC by evaporative cooling at 1.2 G, which is above the position of the first broad Feshbach resonance (0.91 G). Here we obtain 3×10^4 atoms in the BEC, indicating that forced evaporation at this magnetic field is slightly less efficient. We then ramp down the magnetic field within 2 ms to a variable target value and let the sample evolve for 2 ms before switching off the trap. The magnetic field is kept constant at its target value during the first stage of the expansion (15 ms), where the main dynamics happens. We then set the magnetic field along the y axis and we image the atomic cloud after an additional 11 ms of expansion. Our results are summarized in Fig. 3, where we show time-of-flight absorption images for different values of the target magnetic field. We observe a dramatic change in the shape of the condensate when the
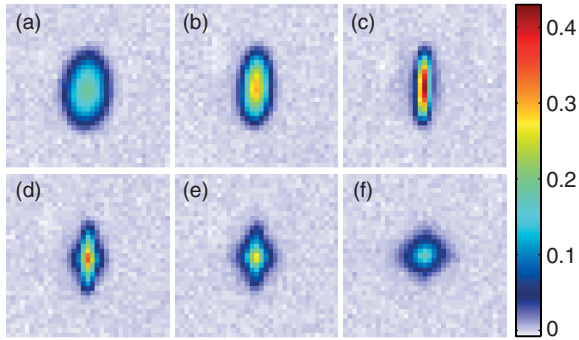
FIG. 3 (color online).   Absorption images showing the *d*-wave collapse of the BEC. The field of view is 290 μm $\times$ 290 μm. The images are an average of eight pictures. The color bar shows the optical density. The images are taken for different target values of the magnetic field: 1.208 G (a), 0.963 G (b), 0.947 (c), 0.942 G (d), 0.939 G (e), and 0.934 G (f). We note that the actual magnetic-field value might be slightly higher (10 mG) because of ramping issues and eddy currents [7].

magnetic field is reduced towards the zero crossing of the scattering length. At the magnetic field of evaporation, the aspect-ratio of the cloud is close to the one observed at zero magnetic field; see Fig. 3(a). By changing the magnetic field to lower target values, the BEC shows a more and more anisotropic shape (b) and (c). Below a critical magnetic-field value, the BEC develops a complicated *cloverleaf* pattern (d)–(f) which is the striking signature of the *d*-wave collapse in a dipolar BEC [7].

In conclusion, we have demonstrated the first BEC of Er atoms and the tunability of its interparticle interaction via Feshbach resonances. Our scattering data provide first sensitive input to understand the complex collisional behavior of submerged-shell atoms. The observation of the *d*-wave collapse is very encouraging in view of future experiments dedicated to the rich phenomena expected in strongly dipolar quantum gases.

[1] T. Lahaye, C. Menotti, L. Santos, M. Lewenstein, and T. Pfau, Rep. Prog. Phys. **72**, 126401 (2009).
[2] M. A. Baranov, Phys. Rep. **464**, 71 (2008).
[3] K. Goral, K. Rzazewski, and T. Pfau, Phys. Rev. A **61**, 051601 (2000).
[4] B. Damski, L. Santos, E. Tiemann, M. Lewenstein, S. Kotochigova, P. Julienne, and P. Zoller, Phys. Rev. Lett. **90**, 110401 (2003).
[5] G. Pupillo, A. Micheli, H. P. Büchler, and P. Zoller, in *Cold Molecules: Theory, Experiment, Applications*, edited by R. V. Krems, W. C. Stwalley, and B. Friedrich (CRC Press, Boca Raton, 2009), Chap. 12.
[6] D. S. Jin and J. Ye, Phys. Today **64**, 27 (2011).
[7] T. Lahaye, J. Metz, B. Fröhlich, T. Koch, M. Meister, A. Griesmaier, T. Pfau, H. Saito, Y. Kawaguchi, and M. Ueda, Phys. Rev. Lett. **101**, 080401 (2008).
[8] T. Lahaye, T. Koch, B. Fröhlich, M. Fattori, J. Metz, A. Griesmaier, S. Giovanazzi, and T. Pfau, Nature (London) **448**, 672 (2007).
[9] B. Pasquiou, G. Bismut, E. Maréchal, P. Pedri, L. Vernac, O. Gorceix, and B. Laburthe-Tolra, Phys. Rev. Lett. **106**, 015301 (2011).
[10] J. J. McClelland and J. L. Hanssen, Phys. Rev. Lett. **96**, 143005 (2006).
[11] M. Lu, N. Q. Burdick, S. H. Youn, and B. L. Lev, Phys. Rev. Lett. **107**, 190401 (2011).
[12] M. Lu, N. Q. Burdick, and B. L. Lev, arXiv:1202.4444 [Phys. Rev. Lett. (to be published)].
[13] H. Y. Ban, M. Jacka, J. L. Hanssen, J. Readerand, and J. J. McClelland, Opt. Express **13**, 3185 (2005).
[14] The Er electronic configuration is [Xe] $4f^{12}6s^2$. The electronic ground state is a $^3H_6$ state, meaning $L = 5$ (*H* state), $S = 1$, and $J = 6$. *L*, *S*, *J* denote the quantum numbers for the orbital angular momentum, for the spin, and for the total electronic angular momentum, respectively. ^{168}Er has zero nuclear spin ($I = 0$) and consequently does not exhibit a hyperfine structure.
[15] R. V. Krems, G. C. Groenenboom, and A. Dalgarno, J. Phys. Chem. A **108**, 8941 (2004).
[16] C. B. Connolly, Y. S. Au, S. C. Doret, W. Ketterle, and J. M. Doyle, Phys. Rev. A **81**, 010702 (2010).
[17] C. Chin, R. Grimm, P S. Julienne, and E. Tiesinga, Rev. Mod. Phys. **82**, 1225 (2010).
[18] S. Kotochigova and A. Petrov, Phys. Chem. Chem. Phys. **13**, 19165 (2011).
[19] A. Petrov, E. Tiesinga, and S. Kotochigova, arXiv:1203.4172.
[20] Y. Takasu, K. Maki, K. Komori, T. Takano, K. Honda, M. Kumakura, T. Yabuzaki, and Y. Takahashi, Phys. Rev. Lett. **91**, 040404 (2003).
[21] T. Fukuhara, S. Sugawa, and Y. Takahashi, Phys. Rev. A **76**, 051604(R) (2007).
[22] A. Frisch, K. Aikawa, M. Mark, A. Rietzler, J. Schindler, E. Zupanic, R. Grimm, and F. Ferlaino, arXiv:1203.1460 [Phys. Rev. A (to be published)].
[23] The MOT stage includes a 15 s loading phase, in which the light is red detuned by -9.5 MHz, and a compression phase, in which we reduce the detuning to -0.8 MHz and the MOT beam intensity by about a factor of 400. The compression phase is used to obtain colder and denser samples and it is optimized for loading efficiency into the dipole trap.
[24] H. Katori, T. Ido, Y. Isoya, and M. Kuwata-Gonokami, Phys. Rev. Lett. **82**, 1116 (1999).
[25] Initially only the power of the horizontal beam is reduced to its final value of 230 mW, while the vertical beam power is reduced during the last 600 ms of evaporation to its final

value of 1.5 W.

[26] We use the strong blue transition at 401 nm for imaging.

[27] S. Jochim, M. Bartenstein, G. Hendl, J. H. Denschlag, R. Grimm, A. Mosk, and W. Weidemüller, Phys. Rev. Lett. **89**, 273202 (2002).

[28] M. Zaccanti, C. D'Errico, F. Ferlaino, G. Roati, M. Inguscio, and G. Modugno, Phys. Rev. A **74**, 041605 (2006).

[29] The magnetic field is calibrated via rf-spectroscopy between Zeeman sublevels. From the calibration we estimate a short-term stability of 1 mG and a long-term stability of about 10 mG.

[30] V. Roudnev and M. Cavagnero, Phys. Rev. A **79**, 014701 (2009).

[31] J. L. Bohn, M. Cavagnero, and C. Ticknor, New J. Phys. **11**, 055039 (2009).

[32] K. K. Ni, S. Ospelkaus, D. Wang, G. Quemener, B. Neyenhuis, M. H. G. de Miranda, J. L. Bohn, J. Ye, and D. S. Jin, Nature (London) **464**, 1324 (2010).

7.3. Further work

7.3.1. Cross-dimensional rethermalization

The cross-dimensional rethermalization method is a powerful method for determining the scattering length of an atomic sample at ultracold temperatures, see Ref. [Mon93]. For this the atomic cloud has to be in thermal equilibrium before it is brought out of equilibrium in one spatial direction. This can be achieved by increasing the temperature in one direction via a sudden compression of the cloud. When the cloud is placed in a crossed ODT this compression can be easily realized by increasing the power of the vertical trapping beam. To reduce systematic errors care has to be taken that only one direction is affected and no collective oscillations are excited by this compression. The temperature increase in the direction of compression will eventually be distributed in the other directions as the kinetic energy of the particles will be 'distributed' by elastic collisions and the gas will reach thermal equilibrium again, i.e. a rethermalization process happens across different spatial dimensions.

The timescale of the rethermalization can be conveniently measured in the experiment by observing the change of the size of the atomic cloud in the direction orthogonal to the direction of excitation. In the experiment the cloud is usually excited in the horizontal direction (y-direction) and the rethermalization is observed in the vertical direction (z-direction). Figure 7.3 shows the increase of the vertical size after compression. It is described by an exponential function with time constant τ, which equals the thermalization time of the cloud. It is inversely proportional to the elastic scattering cross section, σ_{el}, with

$$\tau = \frac{\alpha}{\overline{n}\sigma_{\mathrm{el}}v} \ . \tag{7.10}$$

Here, the term $\overline{n}\sigma_{\mathrm{el}}v$ gives a collision rate with the mean number density

$$\overline{n} = \frac{n_0}{\sqrt{8}} \ , \tag{7.11}$$

where n_0 is the peak density in a harmonic trapping potential, see Eq. 7.2 and Ref. [Sch03], and the mean relative thermal velocity, v, at temperature T with reduced mass m_r is given by

$$v = \sqrt{\frac{8k_{\mathrm{B}}T}{\pi m_r}} \ . \tag{7.12}$$

In Eq. 7.10 the dimensionless constant α has been introduced, which is often referred to as the number of collisions necessary for rethermalization. It can be computed from the known differential cross section and depends on the probability of two horizontally colliding particles to exit the collision in the vertical direction. It has been shown theoretically by Monte-Carlo simulations and also experimentally that for alkali-metal atoms $\alpha = 2.7$ and $\alpha = 4.17$ for s- and p-wave collisions, respectively, see Refs. [Mon93, DeM99a]. For particles with a large dipole moment the scattering amplitude is anisotropic and thus α depends on the angle θ between the excitation direction and the orientation of the dipoles set by a polarizing magnetic or electric field, see Ref. [Boh14]. This angular dependence of α has been demonstrated in a cross-dimensional rethermalization measurement using a dipolar Fermi gas of ^{167}Er atoms, see Ref. [Aik14b]. Surprisingly, α can be as small as one for $\theta = 45°$ for
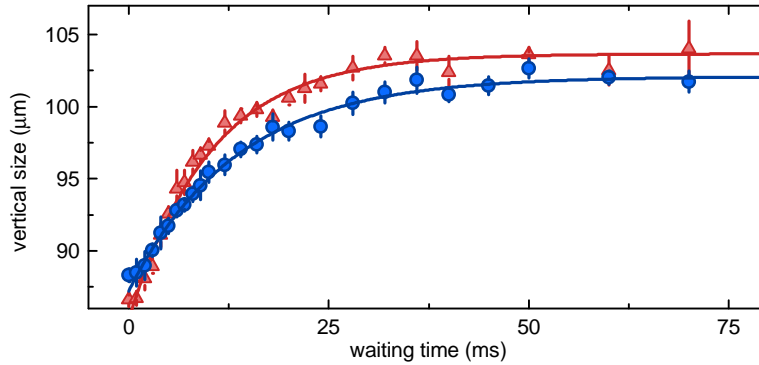
Figure 7.3.: A typical cross-dimensional rethermalization measurement for isotopes ^{168}Er (blue circles) and ^{170}Er (red triangles). The time constant for thermalization is extracted by an exponential fit (solid lines).

fermions, which makes rethermalization extremely efficient. The angle dependence is quite different for bosons. In this case the minimum of α can be found at an angle of $90°$ with a value of about two whereas in the fermionic case it is largest at exactly this angle with $\alpha = 4$. In both fermionic and bosonic cases α further depends on the initial degree of temperature anisotropy T_y/T_z, which is being induced by the trap compression and is usually as large as two, see Ref. [Boh14].

The cross-dimensional rethermalization method was used to determine the total elastic scattering cross section, σ_{el}, away from Feshbach resonances for various bosonic isotopes of erbium. Atoms were trapped in the crossed ODT and a holding time of $500\,\mathrm{ms}$ ensured thermal equilibrium. Then the power of the vertical beam was ramped from $1.6\,\mathrm{W}$ to $8.0\,\mathrm{W}$ within $5\,\mathrm{ms}$ in a parabolic way to prevent collective oscillations. Typical final trap frequencies were $(\omega_x, \omega_y, \omega_z) = 2\pi \times (61, 35, 260)\,\mathrm{Hz}$. The angle was set to $\theta = 90°$ which corresponds to a value for $\alpha = 2$. Two examples of a measurement of the cloud size in z-direction versus the waiting time after compression in the y-direction can be found in Fig. 7.3.

By using Eqs. 4.17 and 4.19 one can estimate a value for the s-wave scattering length, a_s, by subtracting the contribution of the dipole-dipole scattering length, a_D, from the measured scattering length, a. Using the expression for the elastic cross section $\sigma_{\mathrm{el}} = 8\pi a^2$ we get

$$a_s = \sqrt{a^2 - \frac{2.234}{8\pi} a_D^2} \; . \qquad 7.13$$

Experimental values of the scattering length for the bosonic isotopes ^{164}Er, ^{166}Er, ^{168}Er, and ^{170}Er are measured via the cross-dimensional rethermalization method and are summarized in Table 7.2.

7.3.2. Scattering length mass scaling

The scattering length depends on the atomic mass of different isotopes in a tangent-like manner. This was derived and supported by measurements using ytterbium in Ref. [Kit08]

isotope	magn. field	scattering length		
(amu)	(G)	a (a_0)	a_D (a_0)	a_s (a_0)
164	0.8, 1.0	86(10)	97.0	81(10)
166	0.4, 0.7	78(12)	98.2	72(13)
168	0.4	202(23)	99.4	200(23)
170	0.4, 0.5	223(22)	100.5	-221(22)

Table 7.2.: Homonuclear scattering lengths for four bosonic erbium isotopes determined by the cross-dimensional rethermalization method. The measured scattering length is given by a, the dipole length is a_D, and the s-wave scattering length by a_s. The values for the scattering length are averaged over a few measurements at different magnetic fields far away from Feshbach resonances. The values of the magnetic field at which measurements were taken are given. The sign of a for ^{170}Er was determined by locating the zero crossing of the scattering length on the left-hand side of the nearest Feshbach resonance, which was found at 0.858 G.

and strontium in Ref. [Ste13]. The mass scaling is given by a simple expression as

$$a = \bar{a} \left[1 - \tan \left(\Phi - \frac{\pi}{8} \right) \right] \ , \tag{7.14}$$

with the characteristic length $\bar{a}$, which is associated to the van der Waals potential by

$$\bar{a} = 2^{-3/2} \left[\frac{\Gamma(3/4)}{\Gamma(5/4)} \right] \left(\frac{2 m_r C_6}{\hbar^2} \right)^{1/4} \ . \tag{7.15}$$

Here, Γ is the gamma function and $m_r = m/2$ the reduced mass. The semiclassical phase Φ in Eq. 7.14 is defined by

$$\Phi = \frac{\sqrt{2 m_r}}{\hbar} \int\limits_{r_0}^{\infty} \sqrt{-U(r)} dr \ , \tag{7.16}$$

where $U(r)$ is the adiabatic Born-Oppenheimer interaction potential between two atoms and r_0 is the inner classical turning point at zero energy. By knowing Φ one can calculate the number of bound states N by, see Ref. [Fla99],

$$N = \left[\frac{\Phi}{\pi} - \frac{5}{8} \right] + 1 \ . \tag{7.17}$$

The brackets denote taking only the integer part. Given these relations the scattering length for different isotopes can be derived by the knowledge of a and N of one single isotope. Figure 7.4 shows a plot of the values for a_s for four bosonic isotopes of erbium together with a fit of the mass scaling following Eq. 7.14. For fitting the value for C_6 was assumed to be 1723 a.u., see Ref. [Kot14]. The value for Φ is extracted from the fit, which yields for the number of bound channels $N = 142(1)$.

In initial experiments, the thermalization of ^{166}Er was insufficiently working, which can be understood by its small scattering length of $78(12)$ a_0. A BEC of erbium atoms was finally successfully produced using the isotope ^{168}Er. Its scattering length of $a = 202(23)$ a_0 made the evaporative cooling very efficient. After knowing the scattering lengths and Feshbach resonance spectra of isotopes ^{166}Er and ^{170}Er it was possible to evaporatively cool these two isotopes to a BEC using slightly modified evaporation procedures.
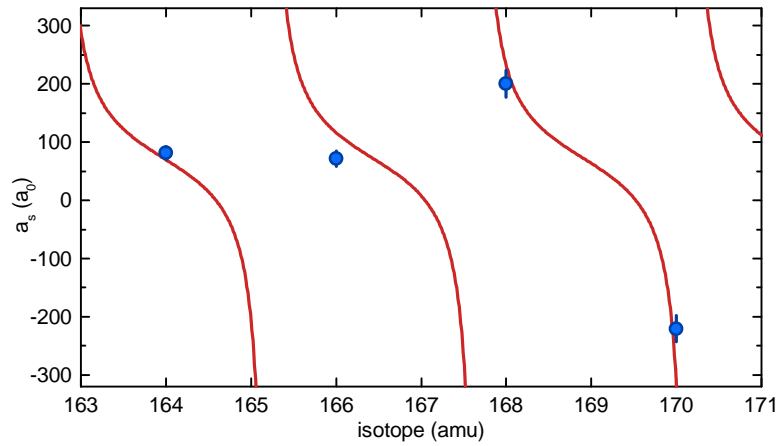
Figure 7.4.: Mass scaling of the scattering length. Measurements of the scattering length for four bosonic isotopes have been carried out by cross-dimensional rethermalization measurements away from Feshbach resonances (blue circles). A tangent function according to Eq. 7.14 with a fixed value for $C_6 = 1723$ a.u. (solid red line) is fit to the data.

Identifying the s-wave scattering length, a_s, with the background scattering length, a_{bg}, and combining this with the Feshbach resonance properties, like positions and widths, we can estimate the scattering length dependent on the magnetic field. Figure 7.5 shows a plot of this dependence from 0 to 5 G for the isotopes ^{166}Er, ^{168}Er, and from 0 to 1.6 G for ^{170}Er.
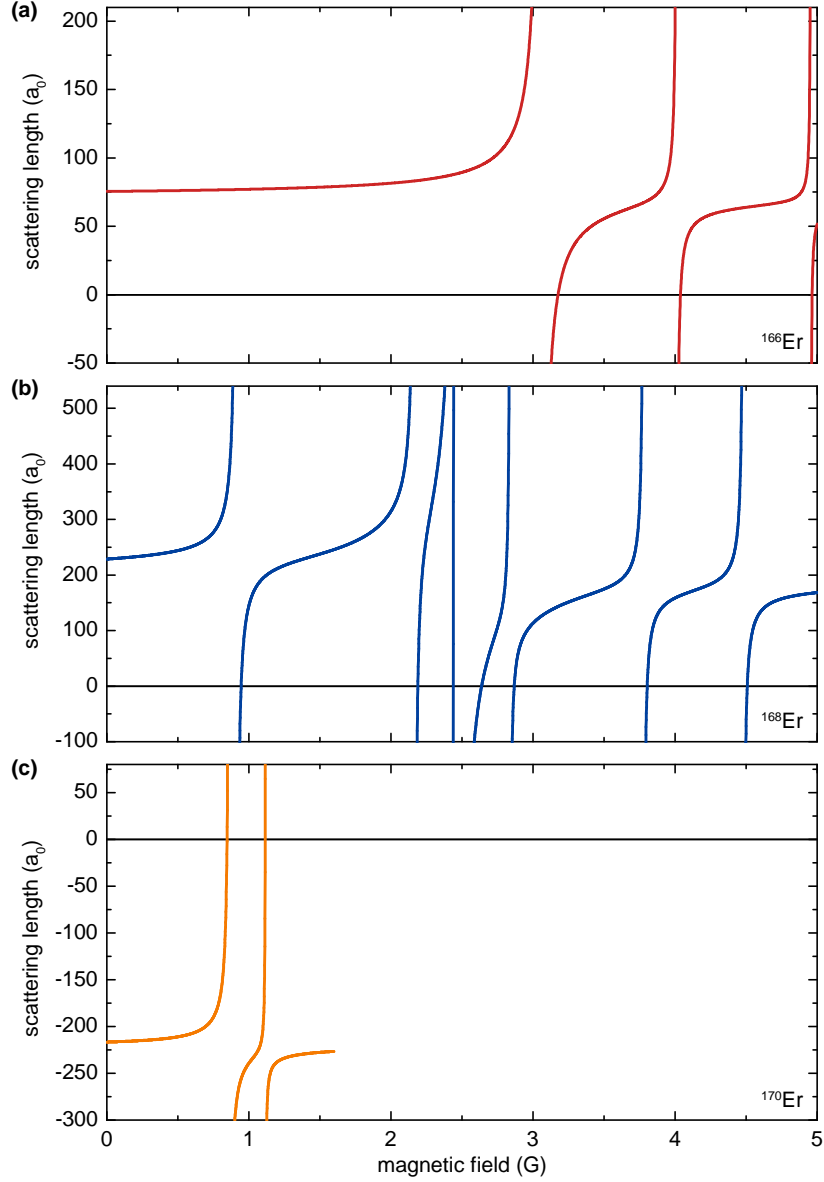
Figure 7.5.: The s-wave scattering length, a_s, dependent on the magnetic field for the three bosonic isotopes ^{166}Er (a), ^{168}Er (b), and ^{170}Er (c). These plots are intended as a rough estimation of the scattering length due to the large error of the background scattering length in Table 7.2. The plots were generated using Eq. 4.22 for multiple resonances assuming a constant background scattering length over the full plotting range. Positions and widths of Feshbach resonances are given in Appendix D. For ^{170}Er the Feshbach scan was only carried out between 0 and 1.6 G.

8

Publication: Hyperfine structure of fermionic erbium

8.1. Introduction

In contrast to bosonic erbium the fermionic isotope has a nonzero nuclear spin of $I = 7/2$. This gives rise to the hyperfine structure of the ground and excited states. Knowledge of the hyperfine energy structure is fundamental for laser cooling experiments. For erbium only poor knowledge exists of its hyperfine structure. The hyperfine coefficients of the excited state of the 401-nm transition have not been known at all, which made a determination with spectroscopic measurements necessary. In the presented publication the hyperfine structure and isotope shifts for the 401-nm and 583-nm transitions were recorded using modulation transfer spectroscopy. We carried out a fitting of the measured spectra using a theoretical model in order to assign quantum numbers to the spectral features and extract values for the hyperfine A and B coefficients.

In the following section the spectroscopic setup utilizing a hollow-cathode lamp is described and the technique of modulation-transfer spectroscopy is briefly discussed. In Sec. 8.2 the publication is presented.

8.1.1. Hollow-cathode lamp

Hollow-cathode lamps (HCLs) have been used extensively in spectroscopic setups as a spectral line source since the 1960s. In such setups the plasma, which is created in the HCL, is used as an emitter of incoherent light that can be used as a frequency reference. Nowadays, hollow-cathode lamps are commonly utilized as spectroscopy cells in ultracold gas experiments also for elements other than erbium, like calcium [Han05], chromium [Chr09], and ytterbium [WL11].

Figure 8.1 shows a photograph and a schematic view of a HCL. The working principle of a HCL is the following: the hollow cathode is formed by a metallic cylinder with a center bore in axial direction. It can be either made of a solid piece of the desired metal or its surface
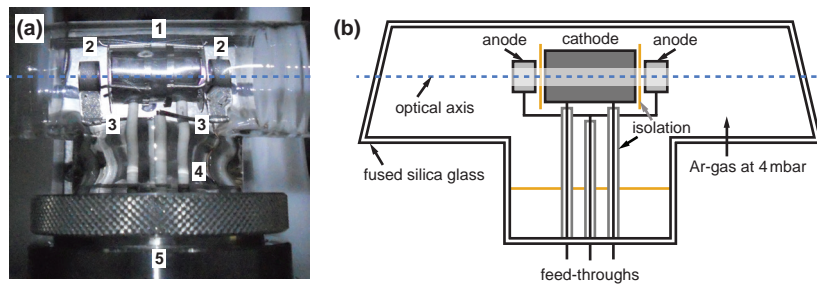
Figure 8.1.: (a) The photograph of the hollow-cathode lamp shows the cathode (1), the two anodes (2), the electrical connections via feedthroughs (3), the glass body (4), and the lamp holder (5). (b) The schematic view highlights the mechanical construction and shows the optical axis (dotted line). The lamp is filled with an Ar-gas at a pressure of 4 mbar. Electric isolation between the cathode and anodes is achieved by thin mica insulator disks (orange) and ceramic tubes (gray).

can be coated with the desired metal. In the latter case, the lifetime of the HCL will be much shorter because of the small layer thickness. Two anodes are mounted on each side next to the cathode. The full setup is inside a glass cell, which is filled with a buffer gas at a pressure of a few millibar. Nobel gases are best suited as a buffer gas. In our case the lamp is filled with argon at a pressure of 4 mbar. A high voltage of 110 V is applied between the cathode and the anodes. This creates a plasma discharge by electric-field ionization of atoms in the buffer gas. Positively charged ions are then accelerated into the center of the hollow cathode. When an argon ion with sufficient kinetic energy hits the surface of the cathode neutral atoms are emitted. This is known as a so-called *sputtering effect*, which was studied in Ref. [Mus62]. Electrical isolation between the two electrodes is realized by two thin mica insulator disks. This is important to direct the plasma into the center of the cathode and maximize the number of target atoms along the optical axis.

Hollow-cathode lamps can be acquired from a manufacturer with almost any metallic element forming the cathode. This broad availability was the reason to use such lamps as spectroscopy cells instead of light sources. In the beginning spectroscopy was done in a setup taking advantage of the optogalvanic effect, see Ref. [Bar90]. Later HCLs were slightly modified as see-through HCLs such that they can be used in Doppler-free absorption spectroscopy setups, see Ref. [Law81]. A major drawback of the HCL is given by the large pressure of the buffer gas, which broadens the natural linewidth by several MHz. The usage of HCLs as frequency references has been nowadays surpassed by modern optical frequency standards, like high-finesse cavities and frequency combs. But its simple operation makes it advantageous for providing a source of elements for spectroscopic setups. This saves the construction of a high-temperature oven in case of elements with high melting point. Lasers for broad transitions can be reliably stabilized on the spectroscopy signal coming from a HCL whereas narrow transitions suffer from line broadening effects.

The electrical current, at which the plasma discharge is operated, should not exceed 20 mA to prevent arc discharges inside the lamp. Typical values of the discharge current for its purpose as a spectroscopy cell are below 10 mA. A too high current will reduce the lifetime of the lamp significantly. The current can be controlled by changing the applied voltage. When turning on the lamp it requires a higher voltage of about 400 V for ignition of the

plasma discharge. Typical guaranteed lifetimes are specified to be around 1000 hrs but it was observed that even after 3 years of daily use in the lab, which corresponds to about 15.000 operating hours, spectroscopy still works well. However, strong signs of degradation are already visible, like a deposition of black metallic vapor on the inside of the lamp as well as an increase of the plasma discharge volume.

8.1.2. Modulation-transfer spectroscopy

Compared to other spectroscopic methods, e.g. saturated absorption spectroscopy, modulation-transfer spectroscopy (MTS) produces a Doppler-free signal with a flat background, which can be directly used for laser-locking purposes. One of the main advantages of MTS is that it directly gives dispersive-shaped curves with zero crossings at the frequencies of atomic transitions.

The optical setup consists of a high-power pump beam, which is aligned through the center of the atomic vapor in the center of the HCL[1], and a weaker probe beam in counter-propagating direction. Both laser beams are derived from the same laser source. The pump beam is phase-modulated via an electro-optical modulator (EOM) and thus contains additional sidebands in the frequency spectrum. These sidebands are transfered onto the probe beam when the laser frequency is close to resonance with an atomic cycling-transition. The modulation-transfer happens due to an optical four-wave mixing process in a sufficiently nonlinear gas, see Ref. [Shi82]. The probe beam is recorded using a photodiode (PD) and its sidebands are detected by mixing the signal of the PD with a local oscillator (LO) from which also the initial modulation frequency is derived. Dependent on the phase delay between signal and LO a signal proportional to either the dispersion or the absorption of the atomic gas can be recorded, i.e. it is sensitive to either the in-phase or quadrature component.

For laser-locking the dispersion signal is used. This signal can be optimized to largest steepness around a spectroscopic feature and a maximum signal-to-noise ratio (SNR) by choosing the right modulation frequency, f_{mod}, see Refs. [Ebl07, McC08]. The optimum is found when f_{mod} equals half of the natural linewidth of the atomic transition to be probed. In case of the 401-nm transition of erbium this sets $f_{\text{mod}} \approx 15\,\text{MHz}$. Strongest contributions in the spectroscopy signal come from the bosonic isotopes of erbium, which makes locking to these features convenient and reliable. But also the hyperfine structure of the fermionic isotope is observed as presented in the publication in the next section. The shape of features in the dispersion signal equals the expected shape of a differentiated Lorentzian curve.

The spectroscopy signal from MTS is Doppler-free but can be affected by other broadening effects, like pressure and power broadening. This has to be considered when using MTS in combination with a HCL as spectroscopy cell. Due to the large background pressure the collisional broadening can be as large as 8.2 MHz. Because of the small erbium atom number density inside the HCL it is difficult to achieve a sufficiently large SNR for stable locking. For a large signal the intensity of the pump laser has to be chosen quite large, leading to a significant power broadening. Typical broadening factors are as large as $\sqrt{1 + I/I_S} = 2.3$

---

[1] see-through HCL 3QQAYEr, from Heraeus Noblelight

with I the total intensity of pump and probe beam and I_S the saturation intensity of the transition. These two effects broaden the natural linewidth from 30 MHz to about 81 MHz. Nevertheless, the steepness of the spectroscopy signal is estimated to be 2 MHz/V, which allows for reliable laser-locking with a sufficiently high stability.

In summary, modulation transfer spectroscopy on a hollow-cathode lamp is a very reliable and easy-to-use spectroscopic technique, which can be used for direct laser-locking on atomic transitions with a natural linewidth of several MHz. For narrower transitions, like the 583-nm transition with a linewidth of 190 kHz, a signal can only be observed if the intensity of the laser beam is strongly increased. This causes a significant broadening of the transition of up to a factor of 100, making laser locking impossible.

As shown, locking a laser on a broad transition using a HCL can be done even for elements, which would otherwise require a high-temperature oven for spectroscopy or different spectroscopic techniques, like locking to a reference cavity. A setup, which is very similar to the one described above is presented in Ref. [Bra12] but the spectroscopy signal suffers from an unusually high discharge current of 70 mA at an applied voltage of 1.3 kV. Here, the HCL is operated at a lower pressure of 1 mbar intended to increase the signal amplitude and SNR to a usable magnitude.

8.2. Publication:
Hyperfine structure of laser-cooling transitions in fermionic erbium-167[†]

Albert Frisch,[1] Kiyotaka Aikawa,[1] Michael Mark,[1] Francesca Ferlaino,[1] Ekaterina Berseneva,[2] and Svetlana Kotochigova[2]

[1] *Institut für Experimentalphysik and Zentrum für Quantenphysik, Universität Innsbruck, Technikerstraße 25, 6020 Innsbruck, Austria*
[2] *Department of Physics, Temple University, Philadelphia, Pennsylvania 19122, USA*

[†] The author of the present thesis developed the experimental procedures, performed the measurements together with K. A., analyzed the data, and contributed in writing the manuscript. The theoretical calculations of this publication were contributed by E. B. and S. K.

Hyperfine structure of laser-cooling transitions in fermionic erbium-167

Albert Frisch, Kiyotaka Aikawa, Michael Mark, and Francesca Ferlaino

Institut für Experimentalphysik and Zentrum für Quantenphysik, Universität Innsbruck, Technikerstraße 25, 6020 Innsbruck, Austria

Ekaterina Berseneva[*] and Svetlana Kotochigova

Department of Physics, Temple University, Philadelphia, Pennsylvania 19122, USA

(Received 11 April 2013; published 13 September 2013)

We have measured and analyzed the hyperfine structure of two lines, one at 583 nm and one at 401 nm, of the only stable fermionic isotope of atomic erbium as well as determined its isotope shift relative to the four most-abundant bosonic isotopes. Our work focuses on the $J \to J+1$ laser cooling transitions from the $[Xe]4f^{12}6s^2(^3H_6)$ ground state to two levels of the excited $[Xe]4f^{12}6s6p$ configuration, which are of major interest for experiments on quantum degenerate dipolar Fermi gases. From a fit to the observed spectra of the strong optical transition at 401 nm we find that the magnetic dipole and electric quadrupole hyperfine constants for the excited state are $A_e/h = -100.1(3)$ MHz and $B_e/h = -3079(30)$ MHz, respectively. The hyperfine spectrum of the narrow transition at 583 nm, was previously observed and accurate A_e and B_e coefficients are available. A simulated spectrum based on these coefficients agrees well with our measurements. We have also determined the hyperfine constants using relativistic configuration-interaction *ab initio* calculations. The agreement between the *ab initio* and fitted data for the ground state is better than 0.1%, while for the two excited states the agreement is 1% and 11% for the A_e and B_e constants, respectively.

I. INTRODUCTION

The field of ultracold quantum gases has historically heavily relied on alkali-metal atoms. Only recently, the use of non-alkali-metal atoms has gained attention as a means to explore fascinating quantum phases of matter that are not accessible with alkali-metal species. Species with multiple unpaired valence electrons have rich atomic energy spectra and exhibit various types of coupling between the electronic angular momentum $\vec{J}$ and the nuclear spin $\vec{I}$ of the atom. For instance, fermionic alkaline-earth-metal atoms have $J = 0$ and $I \neq 0$ and the electronic and nuclear angular momenta decouple. This decoupling is at the center of proposals for efficient quantum simulation [1–3] and quantum magnetism [4–7]. Recently, degenerate Bose and Fermi gases of Ca [8], Sr [9–11], and the alkaline-earth-metal-like Yb atoms [12,13] have been realized.

Lanthanides with submerged $4f$-shell electrons are a novel class of atoms that attract attention in the field of ultracold quantum physics. Lanthanide atoms can have an exceptionally large electronic angular momentum $\vec{J}$ resulting from the alignment of the angular momenta of the submerged electrons. Consequently, these species can have strong magnetic moments μ as large as $10\mu_B$, where μ_B is the Bohr magneton. The mutual interaction is dominated by long-range magnetic dipole-dipole forces. Their dipolar character can be one hundred times larger than that for alkali-metal atoms. This key property makes lanthanides prime candidates for the study of atomic dipolar physics [14–16]. Dy [17,18] and Er [19], with $\mu = 10\mu_B$ and $7\mu_B$, respectively, have been recently brought to quantum degeneracy, while others are under investigation [20–22].

The success of quantum-degenerate-gas experiments relies on a precise understanding of the atomic properties, such as energy levels, hyperfine structures, and atomic polarizabilities. However, for unconventional atomic species, such as lanthanides, the available knowledge is in many instances insufficient for laser-cooling and trapping purposes. Therefore, dedicated experiments need to be conducted en route to quantum degeneracy [21,23–25].

In this paper, we present a combined experimental and theoretical investigation of the hyperfine structure of the only stable fermionic erbium isotope, ^{167}Er. In particular, we obtain the magnetic dipole, A, and electric quadrupole, B, hyperfine structure constants for the ground and two electronically excited states of ^{167}Er, which are relevant for laser-cooling experiments [23,26]. The two electronic excited states investigated are the one at a wavelength of 582.67 nm [corresponding to photon energy $E/(hc) = 17\,157.307$ cm^{-1}] and one at 400.796 nm [$E/(hc) = 24\,943.272$ cm^{-1}] from the ground state [27]. Here h is Planck's constant and c is the speed of light. In addition to the study of the hyperfine constants, we also obtained the isotope shift of ^{167}Er relative to the most-abundant bosonic isotopes. Our work provides important information for future experiments on quantum-degenerate Fermi gases of strongly dipolar Er atoms.

In a previous work, we used the optical transitions at about 401 nm and 583 nm for Zeeman slowing (ZS) and magneto-optical trapping (MOT) applications [26]. We demonstrated efficient laser cooling for five Er isotopes, including the fermionic one. However, the realization of a MOT of fermionic Er isotope was challenging, since only the hyperfine structure of the ground and the 583-nm-excited state were known [28,29], while the one of the state at 401 nm was unknown prior to this work. To operate the Zeeman slower and the transversal cooling stage we had in fact to proceed empirically and try different locking points for the light at 401 nm before being able to produce a MOT of fermions.

---

[*]Present address: Division of Quantum Mechanics, St. Petersburg State University 198904, Russia.
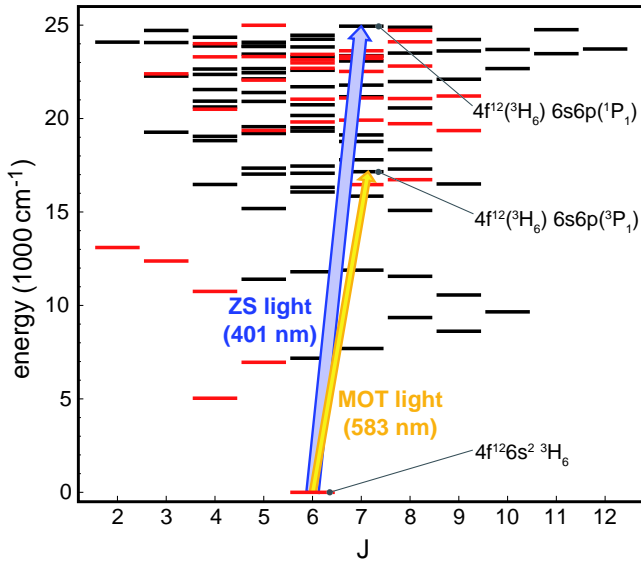
FIG. 1. (Color online) Energy levels of atomic Er up to $E/(hc) = 25000$ cm^{-1} for different electronic angular momentum quantum numbers J [27,30]. States with odd (even) parity are indicated by black (red) horizontal lines. The two relevant laser-cooling transitions at 401 nm and 583 nm are indicated by arrows.

Figure 1 shows the atomic level scheme of Er. The electronic ground state belongs to the [Xe]$4f^{12}6s^2$ configuration and has a large orbital angular momentum quantum number $L = 5$ (H state) and a total electronic angular momentum quantum number $J = 6$. The excited states at 401 nm and 583 nm belong to the [Xe]$4f^{12}6s6p$ configuration and have singlet $^1P_1$ and triplet $^3P_1$ character for the outer two valence electrons, respectively. Both excited states have a total electron angular momentum $J = 7$. Erbium has six stable isotopes with natural abundance being 33.6% for ^{166}Er, 26.8% for ^{168}Er, 23.0% for ^{167}Er, 14.9% for ^{170}Er, 1.61% for ^{164}Er, and 0.14% for ^{162}Er. ^{167}Er is the only stable fermionic isotope. The bosonic isotopes have zero nuclear spin ($I = 0$), while the fermionic one has $I = 7/2$ and shows hyperfine structure. All three electronic states of ^{167}Er have eight hyperfine levels ranging from $F = J - 7/2$ to $F = J + 7/2$, where $\vec{F} = \vec{J} + \vec{I}$.

This paper is structured as follows. Section II describes our experimental methods to investigate the hyperfine structure of the relevant states. Section III reports on our least-squares fitting procedure to obtain the hyperfine constants and isotope shifts from the measured spectra. Section IV describes our *ab initio* relativistic configuration-interaction calculations and compares the *ab initio* hyperfine constants with the fitted values. We present our conclusions in Sec. V.

II. ATOMIC SPECTROSCOPY

We measure the hyperfine structure of the ^{167}Er isotope using modulation-transfer spectroscopy [31]. The spectroscopy is performed on an atomic Er vapor created with a hollow cathode discharge lamp (HCL). The HCL, based on a sputtering process, has the advantage of providing atomic vapors without the need of a high-temperature atomic source.

We use a commercially available HCL, which is filled with an argon gas at a fixed pressure of 4 mbar [32]. By applying a high voltage on the electrodes, the argon gas is ionized and accelerated into the center of the Er-coated cathode. When hitting the surface the kinetic energy of the Ar ions is high enough to free neutral erbium atoms by sputtering processes [33]. We typically operate the HCL with a voltage of 110 V, giving a discharge current of 9.2 mA.

We perform a Doppler-free modulation-transfer spectroscopy in the HCL [34,35]. The laser beam is split into a pump and a probe beam, as shown in Fig. 2(a). The pump light is modulated with an electro-optical modulator (EOM) driven by a local oscillator (LO) at a frequency of 14.2 MHz and with a power of 23 dBm [36]. A four-wave mixing process transfers the sidebands from the modulated pump beam onto the counterpropagating probe beam [37]. We acquire the
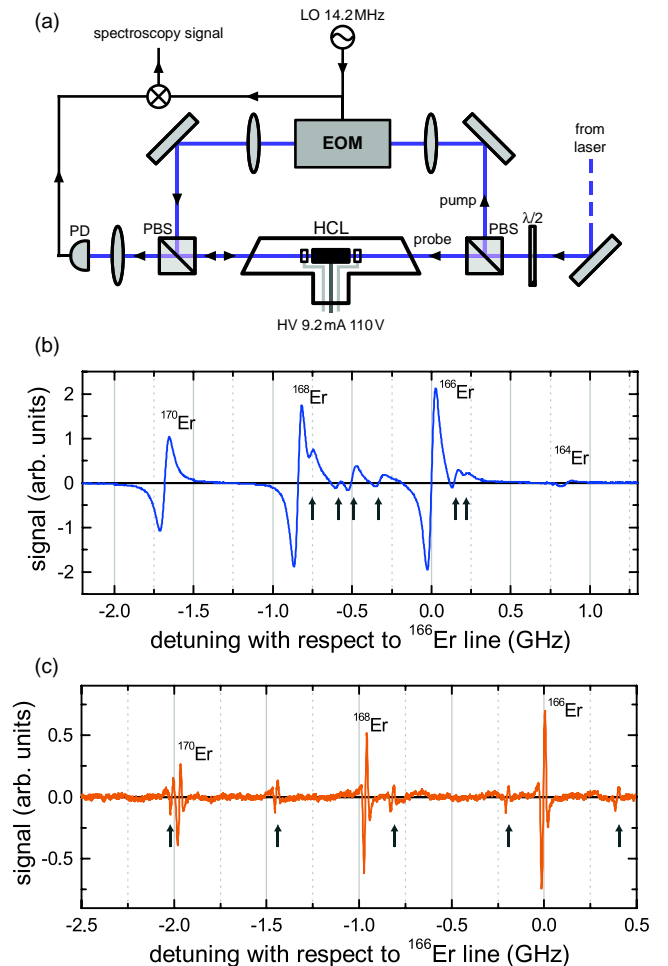
FIG. 2. (Color online) Modulation transfer spectroscopy of Er for the 401 nm and 583 nm transitions. (a) Laser setup for spectroscopy on a hollow cathode discharge lamp (HCL); see text. The pump (probe) light has a power of 3.3 mW (0.6 mW) for the 401 nm transition and 20 mW (1 mW) for the 583 nm transition. (b), (c) Obtained spectroscopy signals for the 401 nm and the 583 nm transitions of different isotopes. Signals related to the hyperfine structure of ^{167}Er are indicated by arrows. The relative amplitudes of the observed signals reflect the natural isotope abundances.

spectroscopy signal by mixing the LO signal with the probe beam signal detected by a photodiode (PD). By setting the LO and the signal either in phase or shifted by π, one can obtain a signal proportional to the dispersion or to the absorption of the atomic sample, respectively. In our setup we use the dispersion signal.

In a first set of experiments, we measure the hyperfine structure and the isotope shift of the excited state at 401 nm, with a natural linewidth of $2\pi \times 29.7(5)$ MHz [38–40]. A frequency-doubled diode laser is used for the spectroscopy. Figure 2(b) shows the dispersive spectroscopy signal for this transition. The signal is averaged over 16 scans with a scanning speed of 2.4 GHz/s [41].

Our measurement reveals the full hyperfine structure for the fermionic ^{167}Er. The discussion and the assignment of the observed spectral features are given in Sec. III. In addition, we determine the isotope shifts for the bosonic isotopes relative to ^{166}Er. We measure a shift of $-1681(14)$ MHz for ^{170}Er, $-840(14)$ MHz for ^{168}Er, and $+849(17)$ MHz for ^{164}Er, which is in good agreement with Ref. [42]. The linewidths are extracted by fitting the derivative of a Lorentzian curve to the data. This gives an averaged value of $2\pi \times 88(8)$ MHz, corresponding to about three times the natural linewidth. This broadening of the transition can be explained as a combined effect of collisional and power broadening. For a number density of about 10^{17} cm^{-3} and an argon background pressure of 4 mbar, we calculate a collisional broadening of $2\pi \times 8.2$ MHz. Considering a total intensity of the pump and probe beams of $\mathscr{I} = 250$ mW/cm^2, we estimate a power broadening of a factor of $\sqrt{1 + \mathscr{I}/\mathscr{I}_0} = 2.3$ with $\mathscr{I}_0 = 60.3$ mW/cm^2 being the saturation intensity. Combining the two contributions, we estimate a broadened linewidth of $2\pi \times 81$ MHz, which is in agreement with the observed value.

In a second set of measurements, we focus on the hyperfine structure of the excited state at 583 nm, with a linewidth of $2\pi \times 186$ kHz [43]. The spectroscopy is performed with a dye laser, which is frequency stabilized to an ultralow expansion cavity within 30 kHz [26]. We use a spectroscopy setup similar to the one described above for the 401 nm transition. Figure 2(c) shows the corresponding spectroscopy signal.

Despite the narrow-line nature of the transition, we could observe five features related to the hyperfine structure of the fermionic isotope and three features for the bosonic ones. The discussion of the hyperfine structure is given in Sec. III. We measure an isotope shift of $-975(15)$ MHz for ^{168}Er and $-1966(14)$ MHz for ^{170}Er relative to ^{166}Er, respectively. These values are in good agreement with Ref. [29].

For this transition, we extract an averaged value for the linewidth of $2\pi \times 23(5)$ MHz, corresponding to about 120 times the natural linewidth. This large broadening can again be explained in terms of collisional and power broadening. Considering the saturation intensity of $\mathscr{I}_0 = 0.13$ mW/cm^2 and our total intensity of $\mathscr{I} = 1.3 \times 10^3$ mW/cm^2, we calculate a power broadening of a factor of 100. Adding the effect of collisional broadening, we obtain an overall linewidth of $2\pi \times 19.3$ MHz, which is in agreement with the measured value. Because of this large broadening, we could operate the modulation-transfer spectroscopy at the same LO frequency as the one used for the 401 nm transition.

III. ANALYSIS OF HYPERFINE STRUCTURE

In this section we describe our fitting procedure to the observed spectra of the five most abundant Er isotopes and we present the resulting hyperfine-structure constants A_e and B_e for ^{167}Er. The bosonic features are easily assigned as shown in Fig. 2. The remaining weaker features, which sometimes overlap with those from the bosonic isotopes, are due to ^{167}Er.

We start with the definition of the transition energies between the ground and an excited state of ^{167}Er including hyperfine interactions [44]

$$\hbar\omega_{F_e F_g} = \Delta_{167} + \hbar\omega_{166} + E_e(F_e, J_e, I) - E_g(F_g, J_g, I), \quad (1)$$

where Δ_{167} is the ^{167}Er isotope shift relative to the transition energy $\hbar\omega_{166}$ of the bosonic ^{166}Er atom, the most abundant isotope, and $E_e(F_e, J_e, I)$ and $E_g(F_g, J_g, I)$ are hyperfine energies of the excited and ground state, respectively. The quantum numbers F_i and J_i with $i = e$ or g are the total atomic and electronic angular momentum of the excited and ground state, respectively, and

$$E_i(F_i, J_i, I) = \frac{1}{2} A_i C_i$$
$$+ \frac{1}{2} B_i \frac{3C_i(C_i + 1) - 4I(I + 1)J_i(J_i + 1)}{2I(2I - 1)2J_i(2J_i - 1)}, \quad (2)$$

where $C_i = F_i(F_i + 1) - J_i(J_i + 1) - I(I + 1)$. Finally, the transition energies $\Delta_A + \hbar\omega_{166}$ define the isotope shift for bosonic Er isotopes with atomic number A.

In addition to the resonance positions, we can calculate the line shape of the fermionic spectral features $S(\omega)$ by noting that the signal is well approximated by

$$S(\omega) \propto -\sum_{F_e F_g} Q_{F_e, F_g} \frac{d}{d\omega} \mathcal{L}(\omega - \omega_{F_e F_g}, \gamma) \quad (3)$$

as a function of laser frequency ω, where the sum is over all (F_g, F_e) hyperfine lines, and $\mathcal{L}(\omega, \gamma)$ is a Lorentzian centered around zero with linewidth γ [45]. Consequently, for an isolated line the resonance occurs when the signal is zero. The fluorescence line strength Q_{F_e, F_g} is

$$Q_{F_e, F_g} = \sum_{M_e M_g q} |\langle (J_g I) F_g M_g | d_{1q} | (J_e I) F_e M_e \rangle|^2$$
$$= \hat{F}_g \hat{F}_e \hat{J}_g \begin{pmatrix} F_g & F_e & 1 \\ J_e & J_g & I \end{pmatrix}^2 |\langle J_g || d || J_e \rangle|^2, \quad (4)$$

where the M_i are magnetic quantum numbers, d_{1q} is the electric dipole-moment operator, and we have assumed equal population for all hyperfine states $F_e M_e$ of the electronic excited state. Finally, $\hat{F} = 2F + 1$, $\begin{pmatrix} \vdots \end{pmatrix}$ is a six-j symbol, and $\langle J_g || d || J_e \rangle$ is a reduced dipole matrix element independent of F_g and F_e.

We use a nonlinear least-squares fit to the experimental spectra to determine the hyperfine constants and isotope shift Δ_{167} of the excited states. The fit is based on six resolved hyperfine features for the 401 nm line and five resolved features for the narrow 583 nm line. In our analysis, we hold the hyperfine constants for the ground state to the literature values of $A_g/h = -120.487(1)$ MHz and
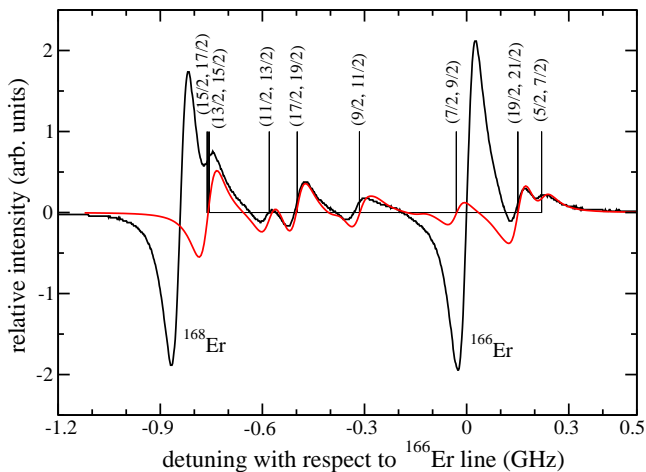
FIG. 3. (Color online) Spectroscopy signal and hyperfine assignment of the 401 nm transition of the fermionic [167]Er. The black solid line is the recorded line. The red line is a simulated line shape obtained using a nonlinear fit to the line positions and a linewidth of $\gamma/(2\pi) = 90$ MHz. The simulated line shape is a sum of the first derivative of several Lorentzians, one for each hyperfine transition, whose relative strength is given by a theoretical estimate of the line strength. We scaled the overall size of the simulated line shape to fit to the experiment. The assignment of the P-branch transitions $(F_g \rightarrow F_e = F_g + 1)$ is shown by vertical lines and pairs (F_g, F_e). The hyperfine coefficients of the excited state are $A_e/h = -100.1$ MHz and $B_e/h = -3079$ MHz.

FIG. 4. (Color online) Spectroscopy signal and hyperfine assignment of the 583 nm transition of the fermionic [167]Er. The solid black line is the experimental spectrum, while the red line is a simulated line shape using a linewidth of $\gamma/(2\pi) = 20$ MHz. The P-branch transitions $(F_g \rightarrow F_e = F_g + 1)$ are assigned by pairs (F_g, F_e). Three P-branch resonances and several Q-branch $(F_g \rightarrow F_e = F_g)$ resonances are predicted to lie outside of the measurement range. The simulated line shape is a sum of the first derivative of several Lorentzians, one for each hyperfine transition, whose relative strength is given by a theoretical estimate of the line strength. We scaled the overall size of the simulated line shape to fit to the experiment. The hyperfine coefficients of the excited state are $A_e/h = -172.7$ MHz and $B_e/h = -4457.2$ MHz.

$B_g/h = -4552.984(10)$ MHz [28], which have significantly lower uncertainties than those for the excited states.

Figures 3 and 4 are the results of our fit for the 401 nm and 583 nm line, respectively. We observe remarkable agreements between the simulated and experimental spectra. For the excited 401 nm level, we extract the best value for the hyperfine coefficients to be $A_e/h = -100.1(3)$ MHz and $B_e/h = -3079(30)$ MHz. Using these coefficients and those for the ground state, we obtain resonance positions that agree to better than 11 MHz with the experimental values. For the excited 583 nm level, we fit the line shape of the spectral features while the resonance positions are calculated by using the hyperfine constants of the excited states, $A_e/h = -172.7$ MHz and $B_e/h = -4457.2$ MHz, from Ref. [29]. We note that the additional structure in the experimental data, which is not fitting to the theoretical curve, originates from a slightly misadjusted phase of the local oscillator in the spectroscopy setup. Table I compares the theoretical and experimental hyperfine energies $\Delta_{167} + E_e(F_e, J_e, I) + E_e(F_g, J_g, I)$ for the 583 nm and 401 nm transitions in [167]Er and lists the corresponding quantum numbers of F_g and F_e. Table II and Fig. 5 show the resulting isotope shifts Δ_A as a function of the mass number A relative to the energy of the [166]Er isotope.

IV. *ab initio* HYPERFINE CONSTANTS

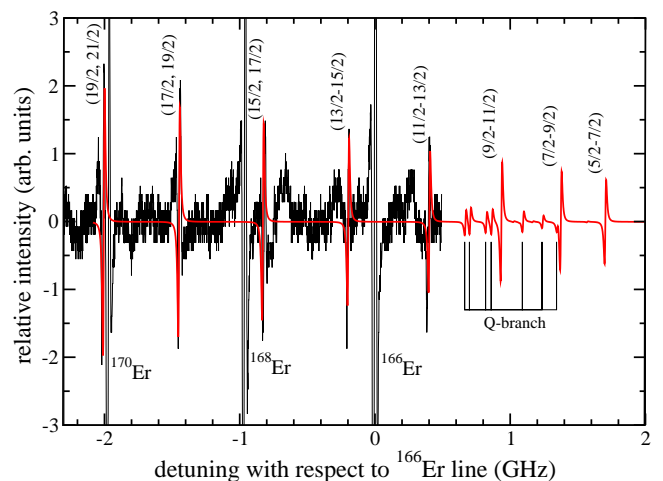In conjunction with the experimental measurements and fits, we have performed extensive *ab initio* electronic structure calculations of the magnetic dipole A and electric quadrupole B hyperfine constants. They describe the coupling of the nuclear spin $\vec{I}$ to the total electron angular momentum $\vec{J}$, due to the magnetic dipole and electric quadrupole interaction, respectively. The latter originates from the electric-field gradient created by the electrons at the nuclear location. We

TABLE I. Observed and calculated hyperfine energies $\Delta_{167} + E_e(F_e, J_e, I) + E_e(F_g, J_g, I)$ for the 583 nm and 401 nm lines in [167]Er. The theoretical values are based on the hyperfine coefficients $A_e/h = -172.7$ MHz and $B_e/h = -4457.2$ MHz [29] for the 583 nm line and our values $A_e/h = -100.1$ MHz and $B_e/h = -3079$ MHz for the 401 nm line.

Obs. energy (MHz)	Calc. energy (MHz)	(F_g, F_e)	Obs. energy (MHz)	Calc. energy (MHz)	(F_g, F_e)
	583 nm			401 nm	
−2011	−2011	(19/2, 21/2)	−761	−762	(15/2, 17/2)
−1449	−1454	(17/2, 19/2)		−757	(13/2, 15/2)
−820	−834	(15/2, 17/2)	−589	−580	(11/2, 13/2)
−200	−203	(13/2, 15/2)	−498	−498	(17/2, 19/2)
393	396	(11/2, 13/2)	−325	−315	(9/2, 11/2)
	941	(9/2, 11/2)		−31	(7/2, 9/2)
	1369	(7/2, 9/2)	150	150	(19/2, 21/2)
	1709	(5/2, 7/2)	220	220	(5/2, 7/2)

TABLE II. Observed isotope shift of the Er isotopes for the 583 nm and 401 nm lines. The transition energy for the bosonic isotope ^{166}Er is taken as energy reference. The isotope shift of the center of gravity of fermionic ^{167}Er was obtained from fitting.

Isotope	Obs. energy (MHz)	Calc. energy (MHz)	Obs. energy (MHz)	Calc. energy (MHz)
	583 nm		401 nm	
170	−1966(14)		−1681(14)	
168	−975(15)		−840(14)	
167		−337(11)		−297(6)
166	0		0	
164			+849(17)	

were interested to reproduce the known constants for the Er ground state as well as those of the excited state at the 583 nm line obtained by Refs. [28,29]. We can then confirm our measurement of the unknown constants of the excited level at the 401 nm line.

The *ab initio* calculations of the hyperfine structure constants have been performed using a relativistic multiconfiguration Dirac-Fock (MCDF) method [46]. In this method we perform an all-electron calculation of the wave function leading to an accurate description of the electron-spin density near the nucleus. The eigenfunctions are superpositions of nonorthogonal many-electron determinants of one-electron Dirac-Fock functions for the core and valence orbitals and Sturm functions for virtual orbitals. Both types of one-electron orbitals are optimized for either the $4f^{12}6s^2$ ground or $4f^{12}6s6p$ excited-state reference configurations.

The hyperfine splittings of atomic levels are due to interactions between electrons and nuclear multipole moments. In the configuration-interaction picture and using atomic units the A
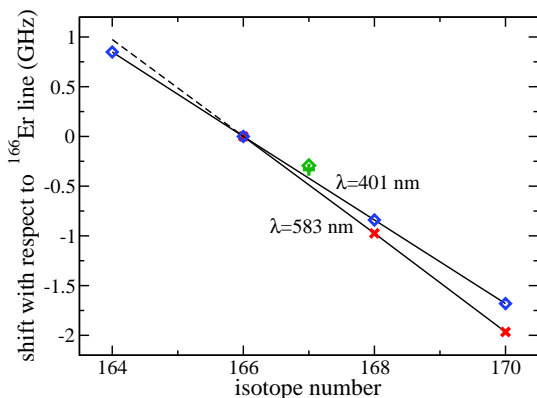
and B constants are given by

$$A(J) = \frac{g_I \mu_N}{M_J} \langle \Psi, J M_J | \sum_i \frac{[\vec{r}_i \times \vec{\alpha}_i]_{00}}{r_i^3} | \Psi, J M_J \rangle, \quad (5)$$

$$B(J) = \frac{2Q}{M_J} \sqrt{\frac{2J(2J-1)(2J+1)}{(2J+2)(2J+3)}}$$

$$\times \langle \Psi, J M_J | \sum_i \frac{Y_{20}(\hat{r}_i)}{r_i^3} | \Psi, J M_J \rangle, \quad (6)$$

where the sum i is over all electrons with positions $\vec{r}_i$ with respect to the nucleus, $Y_{\ell m}(\hat{r})$ are spherical harmonics, and $\vec{\alpha}_i$ is the Dirac matrix for electron i. Furthermore, g_I is the nuclear g factor, μ_N is the nuclear magneton in atomic units, and Q is the nuclear quadrupole moment. The relativistic electronic eigenfunctions $|\Psi, J M_J\rangle = \sum_\beta c_\beta |\phi_\beta, J M_J\rangle$, obtained from the configuration-interaction calculations with relativistic determinants $|\phi_\beta, J M_J\rangle$ and CI coefficients c_β, have total angular momentum J and projection M_J.

When an atom has open or unfilled electron shells, it leads to an unbalanced electron-spin density near the location of the nucleus. As hyperfine constants are proportional to the difference in electron-spin densities this leads to nonzero A and B coefficients. To account for this effect we use a model, where the single-electron orbitals differ for each spin direction or more precisely for each spinor of the Dirac-Fock equation. Alternatively, this implies different exchange potentials for electrons with spin up or down.

We use three restricted active spaces (RAS) to classify the electron Dirac-Fock and Sturm orbitals, ensuring an efficient and compact CI expansion that, nevertheless, remains accurate. The first group of orbitals, RAS1, contains the occupied spinors of the relevant reference configuration. We have studied convergence of the hyperfine structure constants as the active set of orbitals was systematically increased. For our most-precise Er atom calculation RAS1 includes the occupied $1s^2, 2s^2, 2p_{1/2}^2, 2p_{3/2}^4, \ldots$, and $4f_{5/2}^6$ shell electrons. We allow up to one electron to be excited out of RAS1 into the two other active spaces. The second group, RAS2, contains the open-shell $4f_{7/2}^6$, $6s_{1/2}^2$, and $6p_{1/2}, 6p_{3/2}$ spinors, while the third group, RAS3, contains spinors that are unoccupied in the reference configuration. These latter virtual Sturm orbitals are the high-lying s-wave spinors from $7s$ up to $13s$, p-wave spinors from $7p$ up to $11p$, and the $5d$ spinor. For both RAS2 and RAS3 we allow up to two electrons to enter or leave.

With this basis our finite-nuclear-size and finite-nuclear-mass corrected *ab initio* values of the A and B hyperfine constants are −120.42 MHz and −4554 MHz for the ground-state level, −174 MHz and −4057 MHz for the excited level at 583 nm, and −100 MHz and −3424 MHz for the excited level at 401 nm, respectively. Consequently, the *ab initio* A constants agree with experimentally determined values to better than 1%, whereas the B constants differ by up to 11% for the two excited states. For the ground state the agreement for the B constant is also better than 1%.

FIG. 5. (Color online) Isotope shifts for the 583 nm and 401 nm lines of the isotopes ^{164}Er up to ^{170}Er as a function of mass number where the transition energy for the bosonic isotope ^{166}Er is taken as energy reference. The isotope shift of the bosonic isotopes falls on a single straight line, with the isotope shift of the center of gravity of the fermionic ^{167}Er isotope, green cross and green square, is slightly displaced from this linear dependence.

V. CONCLUSIONS

We have used laser modulation-transfer spectroscopy on atomic Er as well as performed *ab initio* electronic structure

TABLE III. Summary of the relevant hyperfine *A* and *B* constants for ground and excited states (e.s.) usable for laser cooling of ^{167}Er.

State	J	A/h (MHz)	B/h (MHz)	Ref.
Ground state	6	$-120.487(1)$	$-4552.984(10)$	[28]
Ab initio		-120.42	-4554	This work
583 nm e.s.	7	$-172.70(7)$	$-4457.2(29)$	[29]
Ab initio		-174	-4057	This work
401 nm e.s.	7	$-100.1(3)$	$-3079(30)$	This work
Ab initio		-100	-3424	This work

calculations of Er to obtain the magnetic dipole and electric quadrupole constants for the only stable fermionic isotope, ^{167}Er. We focused on transitions from the $4f^{12}6s^2$ ($J = 6$) ground state to two $J = 7$ levels within the excited $4f^{12}6s6p$ configuration. A least-squares algorithm applied to the experimentally measured hyperfine-structure energies gives accurate values for the two constants as well as values for the isotope shift of five isotopes. The *ab initio* calculation is based on a multiconfiguration Dirac-Fock method where we allow no more than two electrons to be excited from and between the active spaces. The method has no further adjustable parameters.

Our results are summarized in Table III and Fig. 6. We find that the *ab initio* A coefficients for all three states and the B coefficient for the ground state agree to better than 1% with the experimental values, which is in a surprisingly good agreement considering the complex electron-shell structure of the Er atom. We note that the *ab initio* electric quadrupole constants B for the two excited states exhibit a larger deviation from the experimental values. This might be a consequence of missing key configurations: the excited states have three open shells, $4f^{12}$, $6s$, and $6p$, from which more than two electrons might need to be excited. In addition, Sternheimer shielding (e.g., distortions in the electron shells by the nuclear quadrupole moment), which is not considered in our MCDF theory, might cause significant corrections.
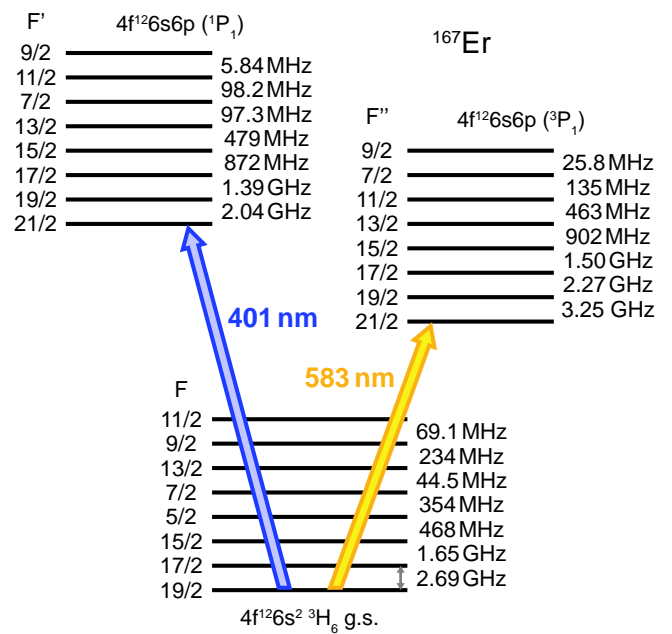
FIG. 6. (Color online) Hyperfine levels of the ground (g.s.) and two excited states of ^{167}Er with particular interest for laser cooling. The level splitting was calculated using A and B constants given in Table III for the respective transitions. The arrows depict two laser-cooling transitions. The transition at 401 nm used for Zeeman slowing is shown in blue and the transition used for magneto-optical trapping at 583 nm is shown in yellow.

[1] A. J. Daley, M. M. Boyd, J. Ye, and P. Zoller, Phys. Rev. Lett. **101**, 170504 (2008).

[2] R. Stock, N. S. Babcock, M. G. Raizen, and B. C. Sanders, Phys. Rev. A **78**, 022301 (2008).

[3] A. V. Gorshkov, A. M. Rey, A. J. Daley, M. M. Boyd, J. Ye, P. Zoller, and M. D. Lukin, Phys. Rev. Lett. **102**, 110503 (2009).

[4] M. Hermele, V. Gurarie, and A. M. Rey, Phys. Rev. Lett. **103**, 135301 (2009).

[5] A. Gorshkov, M. Hermele, V. Gurarie, C. Xu, P. Julienne, J. Ye, P. Zoller, E. Demler, M. D. Lukin, and A. M. Rey, Nat. Phys. **6**, 289 (2010).

[6] M. Foss-Feig, M. Hermele, V. Gurarie, and A. M. Rey, Phys. Rev. A **82**, 053624 (2010).

[7] H.-H. Hung, Y. Wang, and C. Wu, Phys. Rev. B **84**, 054406 (2011).

[8] S. Kraft, F. Vogt, O. Appel, F. Riehle, and U. Sterr, Phys. Rev. Lett. **103**, 130401 (2009).

[9] S. Stellmer, M. K. Tey, B. Huang, R. Grimm, and F. Schreck, Phys. Rev. Lett. **103**, 200401 (2009).

[10] Y. N. Martinez de Escobar, P. G. Mickelson, M. Yan, B. J. DeSalvo, S. B. Nagel, and T. C. Killian, Phys. Rev. Lett. **103**, 200402 (2009).

[11] S. Stellmer, R. Grimm, and F. Schreck, Phys. Rev. A **84**, 043611 (2011).

[12] Y. Takasu, K. Maki, K. Komori, T. Takano, K. Honda, M. Kumakura, T. Yabuzaki, and Y. Takahashi, Phys. Rev. Lett. **91**, 040404 (2003).

[13] T. Fukuhara, Y. Takasu, M. Kumakura, and Y. Takahashi, Phys. Rev. Lett. **98**, 030401 (2007).

[14] M. A. Baranov, Phys. Rep. **464**, 71 (2008).

[15] T. Lahaye, C. Menotti, L. Santos, M. Lewenstein, and T. Pfau, Rep. Prog. Phys. **72**, 126401 (2009).

[16] M. A. Baranov, M. Dalmonte, G. Pupillo, and P. Zoller, Chem. Rev. **112**, 5012 (2012).

[17] M. Lu, N. Q. Burdick, S. H. Youn, and B. L. Lev, Phys. Rev. Lett. **107**, 190401 (2011).

[18] M. Lu, N. Q. Burdick, and B. L. Lev, Phys. Rev. Lett. **108**, 215301 (2012).

[19] K. Aikawa, A. Frisch, M. Mark, S. Baier, A. Rietzler, R. Grimm, and F. Ferlaino, Phys. Rev. Lett. **108**, 210401 (2012).

[20] M. Saffman and K. Mølmer, Phys. Rev. A **78**, 012336 (2008).

[21] D. Sukachev, A. Sokolov, K. Chebakov, A. Akimov, S. Kanorsky, N. Kolachevsky, and V. Sorokin, Phys. Rev. A **82**, 011405 (2010).

[22] D. Sukachev, K. Chebakov, A. Sokolov, A. Akimov, N. Kolachevsky, and V. Sorokin, Opt. Spectrosc. **111**, 633 (2011).

[23] J. J. McClelland and J. L. Hanssen, Phys. Rev. Lett. **96**, 143005 (2006).

[24] S. H. Youn, M. Lu, U. Ray, and B. L. Lev, Phys. Rev. A **82**, 043425 (2010).

[25] V. A. Dzuba, V. V. Flambaum, and B. L. Lev, Phys. Rev. A **83**, 032502 (2011).

[26] A. Frisch, K. Aikawa, M. Mark, A. Rietzler, J. Schindler, E. Zupanic, R. Grimm, and F. Ferlaino, Phys. Rev. A **85**, 051401 (2012).

[27] Y. Ralchenko, A. Kramida, J. Reader, and N. A. Team, NIST Atomic Spectra Database (2011).

[28] W. J. Childs, L. S. Goodman, and V. Pfeufer, Phys. Rev. A **28**, 3402 (1983).

[29] W. G. Jin, T. Horiguchi, M. Wakasugi, and Y. Yoshizawa, J. Phys. Soc. Jpn. **59**, 3148 (1990).

[30] H. Y. Ban, M. Jacka, J. L. Hanssen, J. Reader, and J. J. McClelland, Opt. Express **13**, 3185 (2005).

[31] J. H. Shirley, Opt. Lett. **7**, 537 (1982).

[32] Manufacturer Heraeus Noblelight GmbH, model number 3QQAYEr.

[33] T. Musha, J. Phys. Soc. Jpn. **17**, 1440 (1962).

[34] J. E. Lawler, A. Siegel, B. Couillaud, and T. W. Hansch, J. Appl. Phys. **52**, 4375 (1981).

[35] H. Brammer, J. Ulitzsch, R. Bourouis, and M. Weitz, Appl. Phys. B **106**, 405 (2012).

[36] The modulation frequency is chosen such that the steepness of the spectroscopy signal is maximized, according to [37].

[37] D. J. McCarron, S. A. King, and S. L. Cornish, Meas. Sci. Technol. **19**, 105601 (2008).

[38] Prior to our work on ultracold atoms, two values of the natural linewidth were available in literature, $2\pi \times 35.6(1.2)$ MHz [39] and $2\pi \times 29.5(1.6)$ MHz [40]. Our measurement is based on absorption imaging experiments on magneto-optically trapped atoms of three bosonic isotopes. Our value of $2\pi \times 29.7(5)$ MHz confirms the findings of Ref. [40]. We note that our previous value of $2\pi \times 27.5(4)$ MHz [26] was affected by calibration issues.

[39] J. J. McClelland, Phys. Rev. A **73**, 064502 (2006).

[40] J. E. Lawler, J.-F. Wyart, and E. A. D. Hartog, J. Phys. B: At. Mol. Opt. Phys. **43**, 235001 (2010).

[41] The frequency is monitored during recording the spectroscopy signal and the systematic uncertainty due to nonlinear scanning is estimated to be 12 MHz.

[42] C. B. Connolly, Y. S. Au, S. C. Doret, W. Ketterle, and J. M. Doyle, Phys. Rev. A **81**, 010702 (2010).

[43] E. A. D. Hartog, J. P. Chisholm, and J. E. Lawler, J. Phys. B **43**, 155004 (2010).

[44] E. Arimondo, M. Inguscio, and P. Violini, Rev. Mod. Phys. **49**, 37 (1977).

[45] Pressure broadening, giving a Gaussian contribution to the full profile, is small and can thus be neglected.

[46] P. Villemoes, R. van Leeuwen, A. Arnesen, F. Heijkenskjöld, A. Kastberg, M. O. Larsson, and S. A. Kotochigova, Phys. Rev. A **45**, 6241 (1992).

9

Publication: Degenerate Fermi gas of erbium

9.1. Introduction

In 1999 the group of D. Jin at JILA (USA) produced a degenerate Fermi gas (DFG) of neutral atoms for the very first time, see Ref. [DeM99b]. The atomic species chosen in this pioneering experiment was potassium, one of the two fermionic species available in the series of alkali-metal atoms. Since then many experiments on DFGs have been built all around the world and many spectacular effects have been observed.

Prior to our work the only fermionic species, which had been brought to quantum degeneracy were potassium and lithium from the alkali metals, ytterbium and dysprosium from the lanthanide series, strontium from the alkali-earth metals and helium. The latter opened the fascinating possibility to study dipolar effects with fermions, which could not be done with chromium before. Above mentioned experiments use sympathetic cooling of fermions with either another spin state or a second species. In case of fermions with a large dipole moment elastic collisions between identical fermions driven by dipolar interactions are not suppressed at low temperatures, see Sec. 4.2. This offers the new approach in preparing a degenerate Fermi gas with high densities and low temperatures by *direct evaporative cooling*. Additionally to erbium this idea has been recently applied for Dy [Lu12] and RbK [Ye]. With erbium we demonstrated very efficient direct evaporative cooling down to deep degeneracy for the first time.

9.1.1. Degenerate dipolar Fermi gas

Quantum degeneracy in Fermi gases arises as a smooth crossover when the thermal energy, $k_{\mathrm{B}}T$, reaches the Fermi energy, E_F. The associated Fermi temperature reads

$$T_{\mathrm{F}} = \frac{E_{\mathrm{F}}}{k_{\mathrm{B}}} = \frac{\hbar\overline{\omega}(6N)^{1/3}}{k_{\mathrm{B}}} \ , \tag{9.1}$$

for harmonically trapped atoms with $\overline{\omega}$ the mean trap frequency and N the number of particles. At $T = 0$ the Fermi energy equals the energy of the highest occupied level. For temperatures $T < T_{\mathrm{F}}$ the gas is said to be quantum degenerate. In the current erbium experiment temperatures of down to $0.11(1)\,T_{\mathrm{F}}$ are usually achieved with an atomic sample consisting of 3×10^4 particles with $T_{\mathrm{F}} = 1.06(5)\,\mu\mathrm{K}$, see Ref. [Aik14b]. From E_{F} the Fermi wave number can be derived via

$$k_{\mathrm{F}} = \sqrt{\frac{2mE_{\mathrm{F}}}{\hbar^2}} = \sqrt{\frac{2m\overline{\omega}(6N)^{1/3}}{\hbar}} \ . \qquad 9.2$$

The Fermi wave number resembles the radius of the Fermi surface in reciprocal space and relates to the Fermi momentum by $p_{\mathrm{F}} = \hbar k_{\mathrm{F}}$. In a recent experiment we observe a deformation of the Fermi surface caused by the strong magnetic DDI, see Chapter 11. This is a purely many-body quantum effect and vanishes for high temperatures around T_{F}.

9.1.2. Collisions between identical fermions

As shown in Eq. 4.20 the elastic scattering cross section for dipolar fermions is energy independent. Its non-zero value causes identical fermions to collide even at low temperatures. At temperatures below T_F collisions get more and more suppressed by the Pauli exclusion principle. Although the DDI reduces the p-wave barrier the effective barrier height for erbium, which is about $k_{\mathrm{B}} \times 7\,\mu\mathrm{K}$, is still much larger than the collision energy. This prevents atoms from getting close and efficiently suppresses losses induced by three-body collisions, requiring short-range interactions.

These two features, namely the non-vanishing elastic scattering and a suppression of losses by three-body collisions, make a fermionic gas of dipolar atoms to make an ideal candidate for preparing a strongly-correlated degenerate Fermi gas.

9.1.3. Evaporative cooling of fermions

Observing elastic collisions between identical fermions opens the possibility of employing evaporative cooling of a single spin-component Fermi gas. This strongly simplifies the preparation of a degenerate Fermi gas. We cool the fermionic sample like in the bosonic case by loading atoms from the magneto-optical trap (MOT) into an optical dipole trap (ODT) and applying evaporative cooling in a straightforward way.

We drive direct evaporative cooling in a crossed ODT, consisting of a horizontal and a vertical beam. Both beams are operated at a wavelength of 1570 nm. See Sec. 3.5.3 for the optical setup. The setup is similar to the one used for bosons but the trapping beams have smaller waists to increase the particle density for a more efficient evaporation. The horizontal beam has a waist of $15\,\mu\mathrm{m}$ and the vertical beam of $33\,\mu\mathrm{m}$.

Figure 9.1 summarizes the parameters of our evaporation procedure starting from the MOT. As we are using a tightly focused ODT for evaporation we have to introduce an intermediate
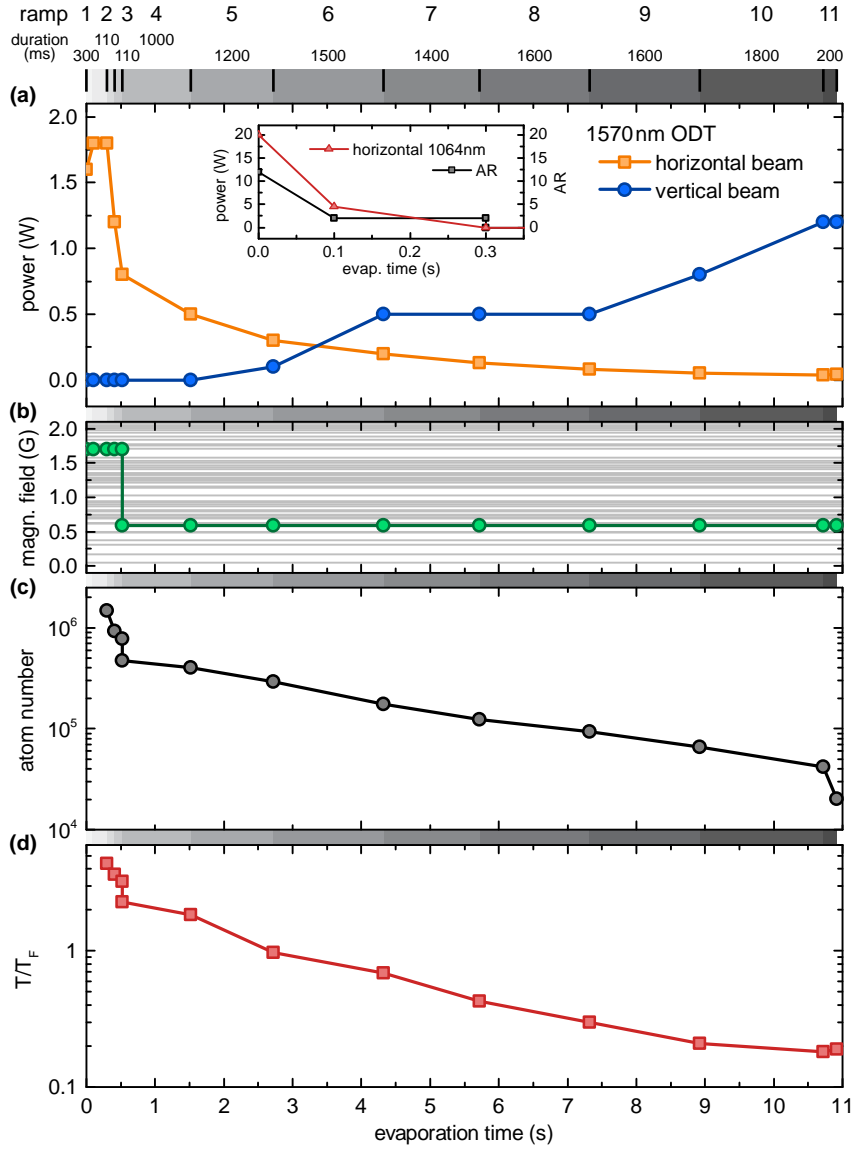
Figure 9.1.: Evaporative cooling of a ^{167}Er Fermi gas in an ODT operated at 1570 nm. (a) Atoms are initially loaded from the MOT into a single-beam ODT at 1064 nm and after initial compression within 300 ms into the horizontal beam at 1570 nm (see inset). This intermediate step makes loading from the MOT more efficient. Forced evaporation is accomplished by ramping down the horizontal trapping beam (orange) in an exponential manner and ramping up the vertical trapping beam to compress the trap in x- and y-direction and preserve a large density. Typical trapping frequencies at the end of evaporation are $(\nu_x, \nu_y, \nu_z) = (398, 282, 304)$ Hz. (b) At the beginning the magnetic field is changed to 0.59 G. The positions of Feshbach resonances are highlighted by gray lines. (c) Atom number and (d) temperature of the cloud are measured at the end of every evaporation step.
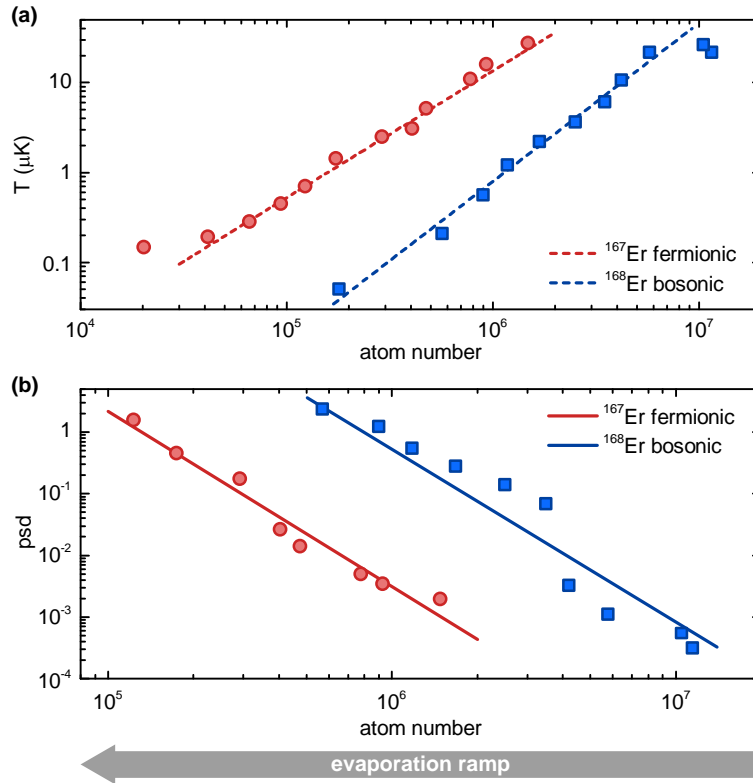
Figure 9.2.: Comparison between evaporation trajectories of fermionic ^{167}Er (red) and bosonic ^{168}Er (blue). (a) Temperature and (b) phase-space density are shown in dependence on the atom number. In both panels the path of evaporation is from right to left (arrow). The overall evaporation efficiencies, given by a linear fit in the log-log plot (lines), are roughly equal for both isotopes. We determine the efficiency for the fermionic isotope to be 3.5.

step by loading the atoms first from the MOT into the horizontal ODT operating at 1064 nm. Then we compress the cloud by decreasing the aspect ratio of the ODT with the scanning system before we can load the sample into the 1570-nm ODT. This intermediate loading step is done within the first 300 ms. In the 1570-nm ODT the power of the horizontal beam is then reduced in a piecewise exponential-like manner and the power of the vertical beam is stepwise ramped up. Note that due to the high density of Feshbach resonances it is not easy to find a suitable spot for evaporation. We change the magnetic field after 520 ms to 0.59 G for a better evaporation efficiency. The full evaporation procedure usually takes up to 11 s to achieve temperatures of $0.11\,\mathrm{T_F}$ with 3×10^4 atoms.

Atom number and temperatures are measured at each evaporation step, see Fig. 9.1(c-d). These values are used to compare the evaporation trajectory of fermionic ^{167}Er with the one of bosonic ^{168}Er, see Fig. 9.2. A linear fit to the log-log plot of the phase-space density versus atom number gives the evaporation efficiency, γ, similar as in Sec. 7.1.1. Remarkably, we observe that fermions can be cooled just like bosons with an efficiency of $\gamma = 3.5$.

9.2. Publication:
Reaching Fermi degeneracy via universal dipolar scattering[†]

Kiyotaka Aikawa,[1] Albert Frisch,[1] Michael Mark,[1] Simon Baier,[1] Rudolf Grimm,[1,2] and Francesca Ferlaino[1]

[1] *Institut für Experimentalphysik and Zentrum für Quantenphysik, Universität Innsbruck, Technikerstraße 25, 6020 Innsbruck, Austria*
[2] *Institut für Quantenoptik und Quanteninformation, Österreichische Akademie der Wissenschaften, 6020 Innsbruck, Austria*

[†] The author of the present thesis helped in taking the data, analyzed the data together with K. A., and contributed in writing the manuscript.

Reaching Fermi Degeneracy via Universal Dipolar Scattering

K. Aikawa,[1] A. Frisch,[1] M. Mark,[1] S. Baier,[1] R. Grimm,[1,2] and F. Ferlaino[1]

[1]*Institut für Experimentalphysik and Zentrum für Quantenphysik, Universität Innsbruck, Technikerstraße 25, 6020 Innsbruck, Austria*
[2]*Institut für Quantenoptik und Quanteninformation, Österreichische Akademie der Wissenschaften, 6020 Innsbruck, Austria*

We report on the creation of a degenerate dipolar Fermi gas of erbium atoms. We force evaporative cooling in a fully spin-polarized sample down to temperatures as low as 0.2 times the Fermi temperature. The strong magnetic dipole-dipole interaction enables elastic collisions between identical fermions even in the zero-energy limit. The measured elastic scattering cross section agrees well with the predictions from the dipolar scattering theory, which follow a universal scaling law depending only on the dipole moment and on the atomic mass. Our approach to quantum degeneracy proceeds with very high cooling efficiency and provides large atomic densities, and it may be extended to various dipolar systems.

Identical fermions with short-range interaction do not collide at very low temperatures [1]. According to the rules of quantum mechanics, the requirement of antisymmetry of the fermionic wave function causes the scattering cross section to vanish in the ultracold regime. This makes ultracold fermions special in many respects. For instance, they realize perfectly noninteracting quantum systems, which can serve for sensitive interferometers [2] and ultraprecise atomic clocks [3]. From another point of view, the absence of collisions means that direct evaporative cooling cannot work.

The inapplicability of direct evaporative cooling to fermions challenged scientists to develop alternative strategies. The common solution is to use mixtures of two distinguishable atomic components [4]. In this scheme, fermions are sympathetically cooled through elastic *s*-wave collisions with fermions in other spin states [4–8], with atoms belonging to a different isotope [9–13], or with atoms of a different chemical element [14–17].

The scenario is completely different in the presence of the long-range dipole-dipole interaction (DDI). While the effect of the short-range van der Waals interaction still freezes out at low temperatures, as it does for nondipolar fermions, the DDI prevents the elastic cross section between identical fermions from vanishing. The corresponding Wigner threshold law, governing the threshold behavior of two-body scattering, gives a finite and energy-independent elastic cross section [18–20]. As a key consequence, identical dipolar fermions can collide even in the zero-temperature limit.

Ultracold dipolar scattering is currently attracting a renewed interest in connection with recent experiments on polar molecules [21,22] and strongly magnetic atoms [13,23,24]. Early theoretical work on H atoms and atoms in electric fields suggested that dipolar scattering could provide an elastic cross section that is large enough for direct evaporative cooling of identical fermions [25–28]. Recent theoretical work has elucidated the universal character of the dipolar scattering [29–31] and found that the elastic dipolar cross section is determined only by the mass and the dipole moment of the particles [30]. Recent experiments on fermionic ground-state polar KRb molecules have tested this prediction and have obtained evidence for the anisotropic character of the DDI [21]. Experiments on using dipolar scattering for evaporative cooling have been reported for fermionic Dy [13] and KRb molecules [32], both reaching temperatures on the order of the Fermi temperature T_F.

In this Letter, we report on the creation of a quantum degenerate dipolar Fermi gas of ^{167}Er atoms. We demonstrate a powerful approach in which the underlying cooling mechanism relies solely on dipolar scattering between spin-polarized fermions. We observe a remarkably high cooling efficiency, leading to very dense Fermi gases with typically 6.4×10^4 atoms at a temperature of $T/T_F = 0.2$ and a peak density of 4×10^{14} cm^{-3}. Finally, we confirm the prediction of the universal dipolar scattering theory [29,30] by measuring the Er elastic cross section in spin-polarized fermions via cross-dimensional thermalization [33]. Our work opens up a conceptually novel pathway to quantum degeneracy in dipolar systems that can be generalized not only to other strongly magnetic atoms but also to ground-state polar molecules, for which the implementation of sympathetic cooling might be difficult.

The strong dipolar character of Er originates from its large magnetic moment μ of $7\mu_B$, where μ_B is the Bohr magneton, and its large mass [20,34]. Among the six stable isotopes, Er has one fermionic isotope, ^{167}Er, with a large natural abundance of 23%. While the bosonic isotopes have no hyperfine structure, ^{167}Er has a nuclear spin $I = 7/2$, giving rise to a manifold of eight hyperfine levels and 104 magnetic sublevels in the electronic ground state [35]. In spite of the much more complex energy structure of the fermionic isotope, our approach to quantum degeneracy

is very similar to the one we have successfully used to condense the bosonic isotope ^{168}Er [24,36]. It consists of a laser cooling stage followed by direct evaporative cooling in an optical dipole trap (ODT). The fundamental difference with respect to the bosonic case is that the thermalization between spin-polarized fermions proceeds solely through dipolar elastic collisions. In the present work, we focus on spin-polarized fermions in the lowest hyperfine sublevel $|F = 19/2, m_F = -19/2\rangle$, where F is the total spin quantum number and m_F is its projection along the quantization axis.

Our laser cooling scheme relies on a Zeeman slower operating at 401 nm and on a magneto-optical trap (MOT) based on a narrow line at 583 nm [36]. Both light fields act on transitions with quantum numbers $F = 19/2 \rightarrow F' = 21/2$, which are sufficiently closed for laser cooling. In our scheme, fermions in the MOT are naturally spin-polarized into the lowest magnetic sublevel $|19/2, -19/2\rangle$ because of a combined effect of gravity and the MOT light [36]. We typically capture 1×10^7 atoms at $T = 7$ μK in the MOT. All measurements in the present work are performed by absorption imaging on the 401-nm transition.

For evaporative cooling, we first transfer the atoms from the MOT into a single-beam large-volume ODT at 1064 nm and then into a tightly focused ODT at 1570 nm. The first trap is used as an intermediate step to increase the transfer efficiency from the MOT. It consists of a single horizontal beam with a power of 20 W and elliptical focus. The beam waists are approximately 20 and 200 μm in the vertical and horizontal direction, respectively. The corresponding trap depth is roughly 100 μK. From the large-volume trap, the atoms are loaded into a tightly focused ODT at 1570 nm. This second trap is made of a single horizontal beam, which is collinear to the large-volume trapping beam and has a waist of 15 μm. The initial power of the 1570-nm beam is 1.8 W, corresponding to trap frequencies of $(\nu_x, \nu_y, \nu_z) = (2147, 51, 2316)$ Hz and a trap depth of about $k_B \times 190$ μK. Here, z is the direction of gravity. At this stage, we have 1.5×10^6 atoms at $T/T_F = 4.4$ with $T = 28$ μK and a peak density of about 1.2×10^{14} cm^{-3}. The Fermi temperature is defined as $T_F = h\bar{\nu}(6N)^{1/3}/k_B$, where $\bar{\nu}$ is the geometric mean of the trap frequencies and h is the Planck constant. We force evaporation by reducing the power of the horizontal beam in a near-exponential manner. When T_F is reached, we introduce a vertical beam at 1570 nm to confine the fermions into the crossed region created by the two beams and to preserve the atomic density. Its power is gradually increased and reaches 1.2 W at the end of the evaporation. The vertical beam has a beam waist of 33 μm. During evaporation, we apply a homogeneous guiding magnetic field to maintain the spin polarization in the system. At high temperature, the magnetic field value is about 1.7 G, which is large enough to avoid any thermal excitation into higher spin states. For

temperature below $3.2T_F$, we decrease the value of the magnetic field to 0.59 G, where we observe a slightly better evaporation efficiency. After 10 s of forced evaporation, we obtain a deeply degenerate Fermi gas.

Figure 1 shows a typical time-of-flight (TOF) absorption image of a degenerate dipolar Fermi gas of $N = 6.4 \times 10^4$ and a peak density of $n_0 = 4 \times 10^{14}$cm^{-3} at $T/T_F = 0.21(1)$ with $T_F = 1.33(2)$ μK. At this point, our trap frequencies are (470,346,345) Hz. Fermi degeneracy reveals itself in a smooth change of the momentum distribution from a Maxwell-Boltzmann to a Fermi-Dirac distribution [37]. Correspondingly, the atomic density profile is expected to change its Gaussian shape into a polylogarithmic one. A fit to TOF images reveals that at temperatures above $\approx 0.5T_F$ the Gaussian and polylogarithmic function are hardly distinguishable from each other and both describe the data well. By further decreasing the temperature, we observe a gradually increasing deviation from the Gaussian shape. This deviation is evident in Fig. 1, which shows a density profile at $T/T_F = 0.21(1)$. A Gaussian fit to the outer wings of the cloud, i.e., outside the disk with radius w, with w being the $1/e$ diameter of the Gaussian fit to the entire cloud, clearly overestimates the population at the center of the cloud. This is a fingerprint of Fermi degeneracy, meaning that the population of low-energy levels is limited by the Pauli exclusion principle.

In all our measurements, we extract T/T_F from fits to the density profiles by using either a polylogarithmic or a Gaussian function. In the former case, the fit gives both the fugacity ζ and the parameter σ characterizing the width of the distribution. The fugacity directly gives $T/T_F = [-6 \times \text{Li}_3(-\zeta)]^{-1/3}$, with Li_n being the nth-order polylogarithmic function [7,9]. The parameter σ is related to the atomic temperature by $T = m\sigma^2/(k_B t_{\text{TOF}}^2)$, where t_{TOF} is the time of flight and m is the mass of ^{167}Er,
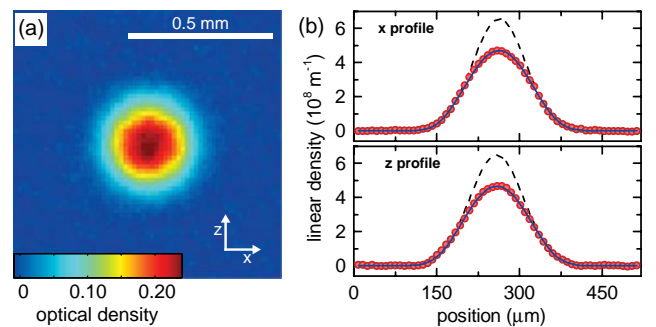
FIG. 1 (color online). Time-of-flight absorption image of a degenerate Fermi gas of Er atoms at $T/T_F = 0.21(1)$ after $t_{\text{TOF}} = 12$ ms of expansion (a) and its density distribution integrated along the z direction (upper panel) and x direction (lower panel) (b). The observed profiles (circles) are well described by fitting a polylogarithmic function to the data (solid lines), while they substantially deviate from a fit using a Gaussian distribution to the outer wings of the cloud, i.e., w (dashed lines). The absorption image is averaged over six individual measurements.

and together with T_F, calculated from N and $\bar{\nu}$, gives a more indirect value for T/T_F. We determine T/T_F by using both methods, which show well consistent results.

To get deeper insights into the evaporation process and the underlying collisional properties, we study the evaporation trajectory. Figure 2 summarizes our results. We observe that the evaporation first proceeds with high efficiency down to temperatures well below T_F and then plateaus at about $T/T_F = 0.2$. The latter behavior suggests that further cooling is limited by Pauli blocking [4,6,7,9] and that more thoroughly optimized evaporation ramps might be needed to reach even lower temperatures. The deepest degeneracy we attained is $T/T_F = 0.19(1)$ with $N = 4.0 \times 10^4$. From the slope of the evaporation trajectory, we obtain the efficiency parameter γ. This parameter quantifies the gain in phase-space density (PSD) at the expense of the atom number and can be written as $\gamma = -d(\ln \text{PSD})/d(\ln N) = -3 \times d(\ln T/T_F)/d(\ln N)$. From a linear fit to the data down to $T/T_F = 0.2$, we find $\gamma = 3.5(2)$. This remarkably large number is in the league of the best evaporation efficiencies observed in experiments with ultracold atoms based on s-wave scattering, including our experiments with the bosonic ^{168}Er [24] and experiments on strongly interacting two-component Fermi gases [5,38,39].

Our interpretation of the cooling process in terms of dipolar scattering relies on the full spin polarization of the sample. Another spin state being present would lead to s-wave collisions in the sample. Therefore it is important to make sure that we do not have any other spin state present. For this reason, we carry out a dedicated set of Stern-Gerlach-type measurements at various stages of the evaporation. During the whole evaporation sequence, we never observe any po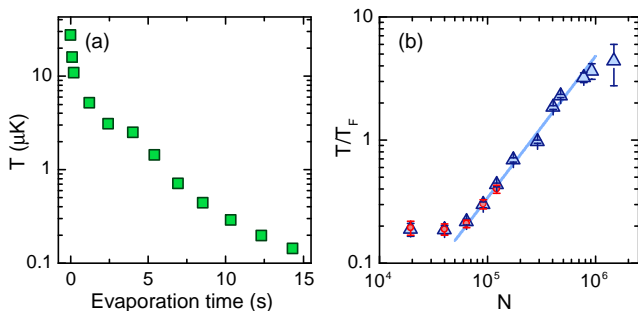pulation in spin states different from the $m_F = -19/2$ state. Figure 3 show the relevant portion of the TOF image, where atoms are observed. To identify unambiguously the spatial positions of the different spin components, we intentionally prepare a spin mixture by radio-frequency (rf) transfer; see Fig. 3. It is worth mentioning that we observe fast spin relaxation when a multicomponent mixture is prepared [40].

The effectiveness of our evaporative cooling scheme suggests a very favorable ratio of the elastic scattering rate to the inelastic one. We explore elastic scattering by measuring the elastic dipolar cross section σ_{el} in our spin-polarized fermionic sample via cross-dimensional thermalization experiments [33]. We compress the system in one spatial direction by increasing the power of the vertical beam by about a factor of 3. We then monitor the time evolution of the temperature in the other direction, as shown in the inset in Fig. 4. The time constant τ for cross-dimensional thermalization is directly connected to σ_{el} through the relation $\tau = \alpha/(\bar{n}\sigma_{\text{el}}v)$, where α is the number of collisions required to thermalize, $\bar{n}$ is the mean density, and $v = 4\sqrt{k_B T/(\pi m)}$ is the mean relative velocity. A delicate point of our analysis is the estimation of α, which depends on the underlying scattering mechanism. We employ $\alpha = 4.1$, which has been numerically calculated for nondipolar p-wave collisions and has been applied to KRb polar molecules [21]. Although p-wave collisions are expected to be the leading term in dipolar scattering of identical fermions, more detailed calculations of α might be needed to fully account for the mixing of partial waves resulting from the DDI [41].

In this way, we explore elastic scattering over a wide range of atom numbers from 3×10^4 to 1.1×10^5 and for various final temperatures ranging from 300 to 600 nK. Our findings at 0.59 G [42] are shown in Fig. 4. In the nondegenerate regime ($T \gtrsim T_F$), we obtain a constant elastic cross section with a mean value of $2.0(5) \times 10^{-12}$ cm^2, corresponding to $[2.7(3) \times 10^2 a_0]^2$,

FIG. 2 (color online). Evaporation trajectory to Fermi degeneracy. (a) Temperature evolution during the evaporation ramp and (b) corresponding T/T_F versus N. The ratio T/T_F is obtained from the width σ of the distribution (triangles) and from the fugacity (circles); see the text. The error bars originate from statistical uncertainties in temperature, number of atoms, and trap frequencies for the width measurements and the standard deviations obtained from several independent measurements for the fugacity. The solid line is a linear fit to the data for $0.2 < T/T_F < 4$.

FIG. 3 (color online). Absorption images of the atomic cloud with a Stern-Gerlach separation of the spin components. A magnetic field gradient of about 40 G/cm is applied during the expansion for about 7 ms. (a)–(e) Along the entire evaporative cooling sequence, atoms are always spin-polarized in the lowest hyperfine sublevel $|F = 19/2, m_F = -19/2\rangle$. T/T_F of the atomic samples are indicated in each panel. In (f), the image is obtained right after rf mixing of the spin states for the sample at $T/T_F = 0.33(1)$. The three clouds correspond to the magnetic sublevels $m_F = -19/2, -17/2$, and $-15/2$ from bottom to top.
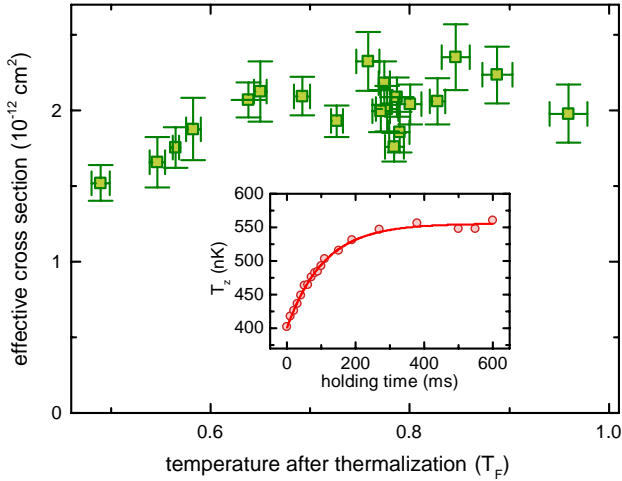
FIG. 4 (color online).   Effective elastic cross section as a function of T/T_F after thermalization. In the nondegenerate regime, the effective cross section is constant and gives a mean value of $2.0(5) \times 10^{-12}$ cm^2. The error bars for each point contain the statistical uncertainties of the time constant for cross-dimensional thermalization, of the trap frequencies, and of the temperature. A typical cross-dimensional thermalization measurement with an exponential fit to the data is shown in the inset. T_z is the temperature along the z direction.

where a_0 is the Bohr radius. The error bar is mainly due to systematic uncertainties in trap frequencies, temperature, and number of atoms. Below T_F, the effect of quantum degeneracy becomes visible through a suppression of scattering events caused by Pauli blocking. In this regime, we can interpret our measurements in terms of an effective elastic cross section, which also includes the Pauli suppression factor. As expected, we observe a substantial decrease of the effective σ_{el} for decreasing T/T_F, similarly to the case of s-wave collisions between fermions in different spin states [44].

Dipolar scattering theories predict an energy-independent elastic cross section for identical fermions in the low-energy regime [18–20]. The cross section is predicted to follow a universal scaling law that is fully determined by a single parameter—the dipolar length D [30]—and it reads as

$$\sigma_{el} = 6.702 \times D^2, \qquad (1)$$

where $D = 2\pi^2 d^2 m/h^2$ with $d^2 = \mu_0 \mu^2/(4\pi)$ and μ_0 being the vacuum permeability. This equation shows a clear analogy to the ordinary s-wave scattering, where D plays the role of the scattering length. For the Er parameters, the universal theory predicts $\sigma_{el} = 1.8 \times 10^{-12}$ cm^2, which is in reasonable agreement with the measured value. The small deviation might be due to the chosen value for α, to systematic errors, or to a residual effect of the short-range physics, which is not included in the theory.

Our observations suggest that inelastic losses are very weak. Since the atoms are fully polarized in the lowest spin state, inelastic losses can be caused only by collisions with the background gas and by three-body decay. To investigate this more quantitatively, we carry out atom-decay measurements by recording the number of atoms as a function of the hold time in an ODT initially loaded with $N \simeq 1 \times 10^5$ atoms at $T/T_F \simeq 0.47$. In spite of the very high peak density of 3×10^{14} cm^{-3}, we find the atom number to decay in a purely exponential manner (time constant 40 s) without showing any signature of three-body processes. From this observation we can derive an upper limit for the three-body recombination rate constant as low as $L_3 \leq 3 \times 10^{-30}$ cm^6/s.

The remarkable efficiency of evaporative cooling in a single-component Fermi gas of Er and the exceptionally high densities together with low inelastic collision rates can be understood in terms of a very favorable combination of the DDI with the p-wave barrier. While DDI is strong enough to provide us with a sufficient cross section for elastic collisions, it is weak enough to preserve a substantial repulsive barrier for any alignment of the colliding dipoles. Even for the case of maximum dipolar attraction (head-to-tail configuration), the effective potential, given by the interplay between the p-wave barrier and the DDI, features a repulsive barrier with a maximum height $V(r_{max}) = 2\hbar^2/(27mD^2)$ at $r_{max} = 3D$. For Er, the barrier height still exceeds $k_B \times 7$ μK, which is much larger than all collision energies in the final evaporation stage. This prevents atoms from getting close to each other, and three-body decay, which requires short-range interactions, is strongly suppressed.

In conclusion, we produce a degenerate dipolar Fermi gas of ^{167}Er atoms. We demonstrate direct evaporative cooling of identical fermions via universal dipolar scattering. Our method provides two key advantages: feeble inelastic losses and exceptionally high attainable densities. The former aspect is favorable for reaching low values of T/T_F, which are ultimately limited by the so-called hole-heating mechanism caused by inelastic losses [45,46]. The latter aspect has important consequences for dipolar physics. The relevant energy scale for dipolar phenomena at the many-body level is given by $n_0 d^2$ [20,34]. Given the high densities achieved here, our degenerate Fermi gas of Er currently is the most dipolar quantum gas available in experiments, with $n_0 d^2$ being 0.92% of the Fermi energy. We speculate that even much higher densities than the ones here attained may be achieved, since we do not see any limiting process. This may open a way for observing p-wave pairing in dipolar gases and for the creation of an anisotropic Fermi superfluid [47,48].

[1] S. Giorgini, L. P. Pitaevskii, and S. Stringari, Rev. Mod. Phys. **80**, 1215 (2008).

[2] G. Roati, E. de Mirandes, F. Ferlaino, H. Ott, G. Modugno, and M. Inguscio, Phys. Rev. Lett. **92**, 230402 (2004).

[3] T. Nicholson, M. Martin, J. Williams, B. Bloom, M. Bishof, M. Swallows, S. Campbell, and J. Ye, Phys. Rev. Lett. **109**, 230801 (2012).

[4] B. DeMarco and D. S. Jin, Science **285**, 1703 (1999).

[5] S. R. Granade, M. E. Gehm, K. M. O'Hara, and J. E. Thomas, Phys. Rev. Lett. **88**, 120405 (2002).

[6] T. Fukuhara, Y. Takasu, M. Kumakura, and Y. Takahashi, Phys. Rev. Lett. **98**, 030401 (2007).

[7] B. DeSalvo, M. Yan, P. Mickelson, Y. N. Martinez De Escobar, and T. Killian, Phys. Rev. Lett. **105**, 030402 (2010).

[8] S. Taie, Y. Takasu, S. Sugawa, R. Yamazaki, T. Tsujimoto, R. Murakami, and Y. Takahashi, Phys. Rev. Lett. **105**, 190401 (2010).

[9] M. K. Tey, S. Stellmer, R. Grimm, and F. Schreck, Phys. Rev. A **82**, 011608 (2010).

[10] A. G. Truscott, K. E. Strecker, W. I. McAlexander, G. B. Partridge, and R. G. Hulet, Science **291**, 2570 (2001).

[11] F. Schreck, L. Khaykovich, K. L. Corwin, G. Ferrari, T. Bourdel, J. Cubizolles, and C. Salomon, Phys. Rev. Lett. **87**, 080403 (2001).

[12] J. M. McNamara, T. Jeltes, A. S. Tychkov, W. Hogervorst, and W. Vassen, Phys. Rev. Lett. **97**, 080404 (2006).

[13] M. Lu, N. Q. Burdick, and B. L. Lev, Phys. Rev. Lett. **108**, 215301 (2012).

[14] G. Roati, F. Riboli, G. Modugno, and M. Inguscio, Phys. Rev. Lett. **89**, 150403 (2002).

[15] Z. Hadzibabic, C. A. Stan, K. Dieckmann, S. Gupta, M. W. Zwierlein, A. Gorlitz, and W. Ketterle, Phys. Rev. Lett. **88**, 160401 (2002).

[16] C. Silber, S. Gunther, C. Marzok, B. Deh, P. W. Courteille, and C. Zimmermann, Phys. Rev. Lett. **95**, 170408 (2005).

[17] F. M. Spiegelhalder, A. Trenkwalder, D. Naik, G. Hendl, F. Schreck, and R. Grimm, Phys. Rev. Lett. **103**, 223203 (2009).

[18] L. D. Landau and E. M. Lifshitz, *Quantum Mechanics*, Course of Theoretical Physics Vol. 3 (Butterworth-Heinemann, Oxford, 1977).

[19] H. Sadeghpour, J. Bohn, M. Cavagnero, B. Esry, I. Fabrikant, J. Macek, and A. Rau, J. Phys. B **33**, R93 (2000).

[20] M. A. Baranov, Phys. Rep. **464**, 71 (2008).

[21] K. K. Ni, S. Ospelkaus, D. Wang, G. Quemener, B. Neyenhuis, M. H. G. de Miranda, J. L. Bohn, J. Ye, and D. S. Jin, Nature (London) **464**, 1324 (2010).

[22] M. H. G. de Miranda, A. Chotia, B. Neyenhuis, D. Wang, G. Quéméner, S. Ospelkaus, J. L. Bohn, J. Ye, and D. S. Jin, Nat. Phys. **7**, 502 (2011).

[23] M. Lu, N. Q. Burdick, S. H. Youn, and B. L. Lev, Phys. Rev. Lett. **107**, 190401 (2011).

[24] K. Aikawa, A. Frisch, M. Mark, S. Baier, A. Rietzler, R. Grimm, and F. Ferlaino, Phys. Rev. Lett. **108**, 210401 (2012).

[25] J. M. V. A. Koelman, H. T. C. Stoof, B. J. Verhaar, and J. T. M. Walraven, Phys. Rev. Lett. **59**, 676 (1987).

[26] J. M. V. A. Koelman, H. T. C. Stoof, B. J. Verhaar, and J. T. M. Walraven, Phys. Rev. B **38**, 9319 (1988).

[27] M. Marinescu and L. You, Phys. Rev. Lett. **81**, 4596 (1998).

[28] W. Geist, A. Idrizbegovic, M. Marinescu, T. Kennedy, and L. You, Phys. Rev. A **61**, 013406 (1999).

[29] C. Ticknor, Phys. Rev. Lett. **100**, 133202 (2008).

[30] J. L. Bohn, M. Cavagnero, and C. Ticknor, New J. Phys. **11**, 055039 (2009).

[31] Z. Idziaszek and P. S. Julienne, Phys. Rev. Lett. **104**, 113202 (2010).

[32] J. Ye (private communication).

[33] C. R. Monroe, E. A. Cornell, C. A. Sackett, C. J. Myatt, and C. E. Wieman, Phys. Rev. Lett. **70**, 414 (1993).

[34] M. A. Baranov, M. Dalmonte, G. Pupillo, and P. Zoller, Chem. Rev. **112**, 5012 (2012).

[35] A. Frisch, K. Aikawa, M. Mark, F. Ferlaino, E. Berseneva, and S. Kotochigova, Phys. Rev. A **88**, 032508 (2013).

[36] A. Frisch, K. Aikawa, M. Mark, A. Rietzler, J. Schindler, E. Zupanic, R. Grimm, and F. Ferlaino, Phys. Rev. A **85**, 051401 (2012).

[37] Proceedings of the International School of Physics "Enrico Fermi," Course CLXIV, edited by M. Inguscio, W. Ketterle, and C. Salomon (IOS Press, Amsterdam, 2008).

[38] M. Bartenstein, A. Altmeyer, S. Riedl, S. Jochim, C. Chin, J. H. Denschlag, and R. Grimm, Phys. Rev. Lett. **92**, 120401 (2004).

[39] M. W. Zwierlein, C. A. Stan, C. H. Schunck, S. M. F. Raupach, A. J. Kerman, and W. Ketterle, Phys. Rev. Lett. **92**, 120403 (2004).

[40] K. Aikawa, A. Frisch, M. Mark, S. Baier, R. Grimm, and F. Ferlaino (to be published).

[41] J. Bohn and D. Jin (private communication).

[42] The magnetic fields are chosen to avoid Er Feshbach resonances [43].

[43] A. Frisch, M. Mark, K. Aikawa, F. Ferlaino, J. L. Bohn, C. Makrides, A. Petrov, and S. Kotochigova, arXiv:1312.1972.

[44] B. DeMarco, S. B. Papp, and D. S. Jin, Phys. Rev. Lett. **86**, 5409 (2001).

[45] E. Timmermans, Phys. Rev. Lett. **87**, 240403 (2001).

[46] L. D. Carr, T. Bourdel, and Y. Castin, Phys. Rev. A **69**, 033603 (2004).

[47] L. You and M. Marinescu, Phys. Rev. A **60**, 2324 (1999).

[48] M. A. Baranov, M. S. Mar'enko, V. S. Rychkov, and G. V. Shlyapnikov, Phys. Rev. A **66**, 013606 (2002).

Chapter 10

Publication: Quantum chaos in ultracold erbium

10.1. Introduction

In the presented publication the correlation and distribution of Feshbach resonances (FR) in the collision of atomic erbium were studied by performing high-resolution Feshbach spectroscopy. A total of 190 FRs were found for each of the two bosonic isotopes ^{168}Er and ^{166}Er in the magnetic field range from 0 to 70 G. This corresponds to a density of about three resonances per Gauss. For the fermionic isotope ^{167}Er 115 resonances have been observed up to 4.5 G, resulting in a density of about 25 resonances per Gauss. Compared to alkali atoms, which typically have one resonance each ten Gauss, the density of FRs in erbium is tremendously high.

Feshbach spectroscopy is a commonly used technique to study collisional properties of various atomic species at ultracold temperatures, as outlined in Sec. 4.3. The level of control over the particle interaction and the energy resolution of the collision energy are unprecedentedly high compared to other spectroscopic techniques, e.g. neutron scattering experiments. Ultracold physics is currently about to enter a new regime where far more complex atomic species like magnetic lanthanide atoms or even molecules are being studied.

Instead of following a microscopic approach based on coupled-channel calculations, as is routinely done with alkali atoms, we analyzed the Feshbach spectrum using statistical tools. Coupled-channel calculations are not easy to carry out in case of erbium because of the large number of scattering parameters of the 49 gerade Born-Oppenheimer potentials and the anisotropic interaction potential, see Sec. 4.1.2. The statistical analysis of FRs is a novel approach in ultracold atom experiments. The characteristic measures provided by the random matrix theory could be confirmed within this analysis of the Feshbach spectrum of erbium. This suggests that *quantum chaotic scattering* controls the supposedly 'simple' collision process of two erbium atoms. Consequently, a strong coupling between individual molecular states is expected as outlined in Sec. 10.3 and Ref. [Kot].

10.1.1. High-resolution Feshbach spectroscopy

Feshbach resonances are an important tool for understanding the scattering properties of a system. The first observation of FRs in a sample of lanthanide atoms had been made by our group, see Chapter 7. Already in these early experiments we observed an unusually large density of resonances. In the present publication we extended the magnetic field scanning range from 0 to 70 G. Compared to the density of FRs of other atomic samples, like alkali atoms as ^{133}Cs [Chi04], dipolar atoms as ^{52}Cr [Wer05] or mixtures of alkali atoms as K+Rb [Ino04, Fer06] and Rb+Cs [Pil09], the density of resonances in the case of erbium is one to two orders of magnitude larger.

For the high-resolution Feshbach scan we have chosen a magnetic-field resolution of 20 mG. The experimental procedure consisted of preparing an ultracold sample of ^{168}Er or ^{166}Er in the energetically lowest Zeeman sublevel $m_J = -6$ at a temperature of 330 nK, which was just before the onset of condensation. We then changed the magnetic field to a target value and kept the atoms at this field for 400 ms. After switching of the trap and recording the atom number the procedure was repeated for the next value off the magnetic field. For a high reproducibility the electric current for creating the magnetic field was actively stabilized by a feedback loop at the same time ensuring a fast but smooth change of the current to the target value within a few ms. The maximum ramp speed of the magnetic field was limited by eddy currents in the vacuum chamber. The trap-loss spectroscopy scan was performed successively with a step size of 20 mG for ranges of 1 G. If a trap-loss feature was found in this range it was rescanned with a smaller step size down to 5 mG. Before continuing the scan for the next region the stability of the atom number was confirmed by repeating the measurement for several previously measured magnetic field values. Scanning the magnetic field from 0 to 70 G for both isotopes required 13,200 individual measurements lasting for about 20 s each.

Recently a Feshbach scan of four different isotopes of dysprosium was reported in Ref. [Bau14]. A similar density of roughly 3.5 resonances per Gauss was observed in the atom-loss spectra of bosons in the range from 0 to 6 G at similar temperatures as in the erbium case. For this set of measurements the total number of resonances was not large enough to perform a statistical analysis of the resonance spacings and correlations for dysprosium.

10.1.2. Statistical analysis of Feshbach resonances

We analyzed the distribution of FRs using the statistical methods introduced by random matrix theory, see Chapter 5. First, the position of maximum atom loss was determined. For simplicity this was done by fitting a Gaussian to the loss maxima. Then the staircase function of Feshbach resonances was created, see Sec. 5.1.4. The staircase function has a similar dependence on the magnetic field for ^{168}Er, ^{166}Er, and ^{167}Er. After a non-linear increase at low magnetic field values up to about 20 G follows a linear increase up to the maximum measured field. For the fermionic isotope ^{167}Er the linear dependence already sets in at about 1.5 G and the density of resonances is about a factor of five higher than for the bosons.

The density of resonances, $\rho(B)$, is derived by calculating the slope of the staircase function. The mean density of resonances, $\bar{\rho}$, and the mean width, $\overline{\Gamma}$, are important statistical values for comparisons with theoretical coupled-channel calculations. In the presented trap-loss spectroscopy the width of the resonances can be derived either by locating the zero crossing of the scattering length or by determining the width of a Gaussian fit to the loss feature. The former method is very reliable, but is only possible if a local maximum of the atomic cloud size can be observed, whereas the second method is only to be taken as a rough estimate of the resonance width. A complete set of extracted resonance positions and widths for ^{168}Er and ^{166}Er is given in Appendix D.

10.2. Publication:
Quantum chaos in ultracold collisions of gas-phase erbium atoms[†‡]

Albert Frisch,[1] Michael Mark,[1] Kiyotaka Aikawa,[1] Francesca Ferlaino,[1] John L. Bohn,[2] Constantinos Makrides,[3] Alexander Petrov,[3,4,5] Svetlana Kotochigova[3]

[1] *Institut für Experimentalphysik, Universität Innsbruck, 6020 Innsbruck, Austria*
[2] *JILA, University of Colorado and National Institute of Standards and Technology, Boulder, Colorado 80309-0440, USA*
[3] *Department of Physics, Temple University, Philadelphia, Pennsylvania 19122, USA*
[4] *St. Petersburg Nuclear Physics Institute, Gatchina 188300, Russia*
[5] *Division of Quantum Mechanics, St. Petersburg State University, 198904, Russia*

[†] The author of the present thesis developed the experimental procedures, performed the measurements, analyzed the data, and strongly contributed in writing the manuscript. The theoretical calculations of this publication were contributed by C. M., A. P., and S. K.

[‡] The preprint version of the publication is attached for online access of this thesis.

Quantum Chaos in Ultracold Collisions of Erbium

Albert Frisch, Michael Mark, Kiyotaka Aikawa, and Francesca Ferlaino*
Institut für Experimentalphysik, Universität Innsbruck, Technikerstraße 25, 6020 Innsbruck, Austria

John L. Bohn
JILA, University of Colorado and National Institute of Standards and Technology, Boulder, Colorado 80309-0440, USA

Constantinos Makrides, Alexander Petrov,† and Svetlana Kotochigova
Department of Physics, Temple University, Philadelphia, Pennsylvania 19122, USA
(Dated: December 6, 2013)

Atomic and molecular samples reduced to temperatures below 1 microkelvin, yet still in the gas phase, afford unprecedented energy resolution in probing and manipulating how their constituent particles interact with one another. As a result of this resolution, atoms can be made to scatter resonantly at the experimenter's whim, by precisely controlling the value of a magnetic field [1]. For simple atoms, such as alkalis, scattering resonances are extremely well-characterized [2]. However, ultracold physics is now poised to enter a new regime, where far more complex species can be cooled and studied, including magnetic lanthanide atoms and even molecules. For molecules, it has been speculated [3, 4] that a dense forest of resonances in ultracold collision cross sections will likely express essentially random fluctuations, much as the observed energy spectra of nuclear scattering do [5]. According to the Bohigas-Giannoni-Schmit conjecture, these fluctuations would imply chaotic dynamics of the underlying classical motion driving the collision [6, 7]. This would provide a paradigm shift in ultracold atomic and molecular physics, necessitating new ways of looking at the fundamental interactions of atoms in this regime, as well as perhaps new chaos-driven states of ultracold matter.

In this report we provide the first experimental demonstration that random spectra are indeed found at ultralow temperatures. In the experiment, an ultracold gas of erbium atoms is shown to exhibit many Fano-Feshbach resonances, for bosons on the order of 3 per gauss. Analysis of their statistics verifies that their distribution of nearest-neighbor spacings is what one would expect from random matrix theory [8]. The density and statistics of these resonances are explained by fully-quantum mechanical scattering calculations that locate their origin in the anisotropy of the atoms' potential energy surface. Our results therefore reveal for the first time chaotic behavior in the native interaction between ultracold atoms.

In the common perception, atoms are regarded as *simple* systems in sharp contrast to *complex* molecules, whose behavior is dictated by many (rotational and vibrational)

degrees of freedom. The recent realization of dipolar Bose-Einstein condensates and Fermi gases of magnetic lanthanides [9–12] made available a novel class of atoms in the ultracold regime. These exotic species, such as erbium (Er), allow to bridge the enormous conceptual gap between *simple* atoms and molecules, potentially providing a natural testbed to explore complex scattering dynamics in a controlled environment. The rich scattering behavior of lanthanides has been pointed out in pioneering experiments at millikelvin temperatures [13, 14] and theoretical work on cold collisions of atoms with non-zero angular momenta [15, 16].

A wealth of intriguing properties in Er, which is the focus of this paper, originates from its exotic electronic configuration. Er is a submerged-shell atom with electron vacancies in the inner anisotropic $4f^{12}$ shell, which lies beneath a filled $6s^2$ shell. As a consequence, it not only has a large magnetic moment of 7 Bohr magnetons (μ_B) but also has a large electronic orbital (total) angular momentum quantum number of $L = 5$ ($J = 6$); note that for bosonic (fermionic) isotope the nuclear angular quantum number is $I = 0$ ($I = 7/2$). Large values for L and J are sources of anisotropy in the interatomic interaction. Moreover, the two-body scattering is controlled by as many as 91 electronic Born-Oppenheimer (BO) interaction potentials, each potential accounting for a specific orientation of J with respect to the internuclear axis. All BO potentials are anisotropic and include at large internuclear separations a strong dipole-dipole interaction (DDI) and anisotropic van der Waals dispersion potentials. This situation is in contrast to that of conventional ultracold atoms, such as alkali-metal atoms, where the scattering is determined mainly by the isotropic singlet and triplet BO potentials [2]. Recent theoretical work predicted the existence of anisotropy-induced Fano-Feshbach resonances in magnetic lanthanides [17]. This greater complexity brings significant new challenges in understanding and exploiting scattering processes.

Our experimental study is based on high-resolution trap-loss spectroscopy of Fano-Feshbach resonances in an optically-trapped ultracold sample of Er atoms in the energetically lowest magnetic Zeeman sublevel. We prepare the ultracold sample by following a similar cooling and trapping approach to that described in Ref. [11] for bosons and Ref. [12] for fermions (Method Summary).
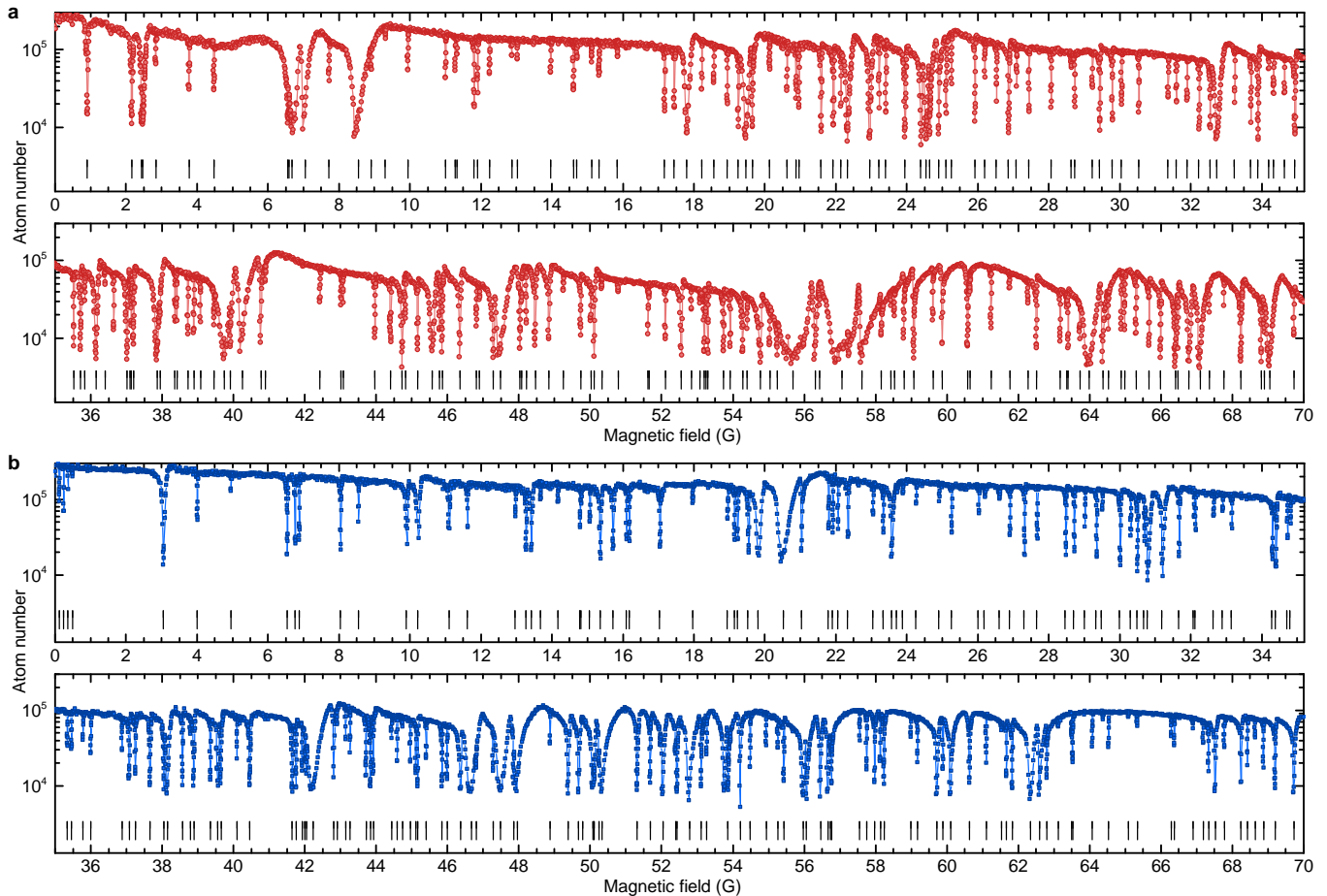
Figure 1 | Fano-Feshbach spectrum of ^{168}Er and ^{166}Er from 0 to 70 G. The trap-loss spectroscopy is performed in an optically trapped sample of Er atoms in the energetically lowest Zeeman sublevel $m_J = -6$ at a temperature of 330 nK. The atom number is measured after a holding time of 400 ms. **a,** We observe 190 Fano-Feshbach resonances for ^{168}Er and **b,** 189 resonances for ^{166}Er. Resonance positions are extracted by fitting a Gaussian shape to individual loss features; a full list is given in the Supplementary Information.

After the preparation procedure, the ultracold sample typically contains about 10^5 atoms at a temperature around 400 nK. High-resolution trap-loss spectroscopy consists of many experimental cycles. In each cycle, we ramp the magnetic field to a target value B and hold the atoms for 400 ms in the optical dipole trap, during which they undergo elastic and inelastic collisions. To probe the loss of atoms from the trap, we record the atom number by applying standard time-of-flight absorption imaging at zero magnetic field. In the next experimental cycle, we vary the magnetic field value from 0 to 70 G with step sizes of a few mG and repeat the measurement. Figure 1 shows the loss spectra for ^{168}Er and ^{166}Er. For both isotopes, we observe an enormous number of resonant loss features, which we interpret as being caused by Fano-Feshbach resonances [2]. We identify 190 resonances for ^{168}Er and 189 resonances for ^{166}Er, meaning that we observe about 3 resonances per gauss. We performed similar spectroscopic measurements with the

fermionic isotope ^{167}Er, revealing a much higher density of resonances that exceeds 20 resonances per gauss (Extended Data Fig. 1). The fermionic case is complicated by its additional hyperfine structure and detailed studies will be subject of future work.

The immense density of resonances in Er is without precedent in ultracold quantum gases. For comparison, the density of resonances observed in experiments with ultracold alkali-metal atoms or even mixtures is about two orders of magnitude lower than Er (c.f. Ref. [18, 19]). In Er, it is unclear whether a quantitative mapping of the observed resonances is possible at all. In principle there are at least 91 unknown parameters, corresponding to the phase shifts introduced by the BO potentials [17]. Instead, we focus our theoretical analysis on fundamental questions, such as: Can the observed density of resonances be reproduced by microscopic calculations? Do our results imply the presence of highly anisotropic interactions, which call into play resonant states of high

orbital momentum? We answer these questions in the affirmative using full coupled-channel (CC) calculations, supported by an analytical model.

We construct a first-principle CC model for Er+Er scattering to calculate the spectrum of Fano-Feshbach resonances for the experimental conditions. Following Ref. [17], our model uses the atomic basis set and Hamiltonian (Methods) that includes the radial kinetic and rotational energy operators, the Zeeman interaction, and the 91 anisotropic BO potentials. For small interatomic separations R, the BO potentials are calculated using the *ab initio* relativistic multi-reference configuration-interaction method [20]. At intermediate to large R, the BO potentials are expressed as a sum of multipolar interaction terms. The van der Waals dispersion interaction potentials ($\propto 1/R^6$) are determined from experimental data on atomic transition frequencies and oscillator strengths [21, 22]. An important point is that the dispersion potentials have both isotropic and anisotropic contributions. The latter comes from the non-S state character of the Er electronic ground state. The BO potentials induce thus either isotropic (ℓ and m_ℓ conserving) or anisotropic (ℓ or m_ℓ changing) couplings. Here, ℓ and m_ℓ are the partial wave quantum number and its projection on the magnetic-field quantization axis.

We perform CC calculations for bosonic ^{168}Er, considering s-wave ($\ell = 0$) collisions and couplings to molecular states with even ℓ up to $L_{\max} = 20$. We calculate the elastic collisional rate coefficient as a function of magnetic field to obtain the Fano-Feshbach resonance spectrum. For $L_{\max} = 20$, we observe a very dense resonance spectrum with about 1.5 resonances per gauss, which qualitatively reproduces our experimental observation (Extended Data Fig. 2). To get deeper insight into the role of the anisotropy of the potentials, we calculate the mean density of resonances $\overline{\rho}$ from our CC calculations for different values of the maximum partial wave $L_{\max}$ (Fig. 2). For $L_{\max}$ up to 20, we observe that $\overline{\rho}$ increases with $L_{\max}$ in a quadratic manner. This dependence stands in stark contrast to alkali-metal atoms, where high-partial-wave resonances tend to be too narrow to be observed.

Since our limited computational resources do not allow us to perform calculations for $L_{\max} > 20$, it is worth estimating the density of resonances in a simpler way, based on the separated atom quantum numbers [3]. The key ideas of our model are the following. For each channel $|j_1 m_{J,1}, j_2 m_{J,2}, \ell m_\ell\rangle$ we define the long-range potential $-C_6/R^6 + \hbar^2\ell(\ell+1)/(2\mu R^2) + g\mu_B(m_{J,1} + m_{J,2})B$, with the isotropic van der Waals C_6 coefficient of the BO potentials. Here μ is the reduced mass, g is the atomic g-factor, and for ground state Er $C_6 = 1723$ a.u.. Fano-Feshbach resonances in our open ($m_{J,1} = -6$) + ($m_{J,2} = -6$) channel are due to couplings to the most-weakly bound rovibrational level of closed channels. For a van der Waals potential [2, 23] this bound state has a binding energy that must fall within the ℓ-dependent energy window $[-\Delta_\ell, 0]$ with $\Delta_\ell > 0$. The short range potentials are not accurately known and,
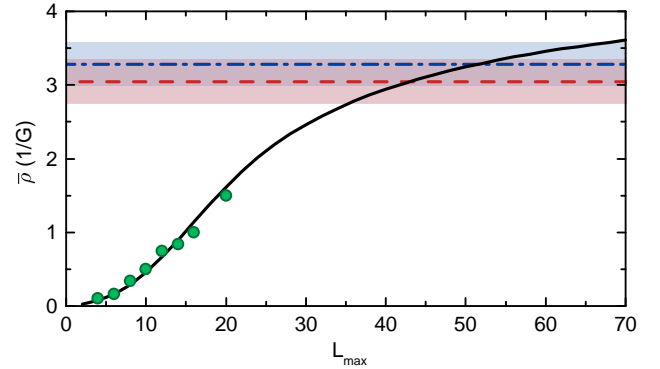
Figure 2 | Mean resonance density for bosonic Er as a function of largest included partial wave $L_{\max}$. CC calculations for $L_{\max}$ up to 20 (circles) and RQDT calculation (solid line) for a magnetic-field region from 0 G to 70 G. For calculations a collision energy of $E/k_B = 360$ nK is assumed. The mean densities of resonances measured in the experiment are shown for ^{168}Er (dashed line) and for ^{166}Er (dash-dotted line) with one-sigma confidence bands (shaded areas).

for each closed channel, there is a probability dE_b/Δ_ℓ of finding a bound state with a binding energy between E_b and $E_b + dE_b$. From Ref. [23] and numerical simulations we find $\Delta_\ell/E_{\text{vdW}} \approx 38.7 + 25.5\ell + 3.17\ell^2$, where $E_{\text{vdW}} = \hbar^2/(2\mu x_{\text{vdW}}^2)$ and $x_{\text{vdW}} = \sqrt[4]{2\mu C_6/\hbar^2}/2$. Each closed channel contributes $g\mu_B\delta m/\Delta_\ell$ to the mean resonance density, where $g\mu_B\delta m > 0$ is the magnetic-moment difference of the closed and open channels and δm is their difference in molecular projection quantum numbers. Adding the contributions for the closed channels gives $\overline{\rho}$. This counting technique, which we here name random quantum defect theory (RQDT), yields the mean density of states shown in Fig. 2. For $L_{\max} \leqslant 20$, the results of our analytic RQDT agrees very well with the exact CC calculations. For larger $L_{\max}$, the density of resonances keeps growing and eventually saturates to a value comparable to the one observed in the experiment. RQDT shows that at least 40 partial waves need to be considered to reproduce the experimental observations.

Our microscopic models reproduce well the qualitative behavior of the system. However, given the complexity of the scattering, the analysis of ultracold collision data can not and should not aim anymore at the assignment of individual resonances and the fundamental question of how to tackle complex scattering naturally arises. Historically, spectra of great complexity have been understood within the framework of random matrix theory (RMT), as originally developed by Wigner to describe heavy nuclei containing a very large number of degrees of freedom [24]. This is an alternative view of the quantum mechanics of complex systems, where individual energy levels and resonances are not theoretically reproduced one-by-one, yet their statistics can be described [25]. RMT characterizes spectra by fluctuations of their energy levels and

classifies their statistical behavior in terms of symmetry classes, e. g. the Gaussian-orthogonal ensemble (GOE) in the case of a system with time-reversal symmetry, such as neutral atoms.

Following RMT, the distribution of spacings between neighboring levels (or resonances) characterizes the spectral fluctuations of the system and reflects the absence or the presence of level correlations in terms of a dimensionless parameter, s, i. e. the actual spacing between neighboring levels in units of the mean spacing, $\bar{d} = 1/\bar{\rho}$. Whereas the nearest-neighbor spacing (NNS) distribution $P(s)$ of non-interacting levels is Poissonian, $P_{\mathrm{P}} = \exp(-s)$, strongly interacting levels obey a totally different distribution which, in the case of GOE statistics, is known as the Wigner-Dyson (WD) distribution or *Wigner surmise* [25]

$$P_{\mathrm{WD}} = \frac{\pi}{2} s \exp(-\pi s^2/4), \qquad (1)$$

which shows a strong level repulsion for small s, $P_{\mathrm{WD}}(0) = 0$. The field of application of the WD distribution is so vast as to make it a universal feature of very complex systems, such as heavy nuclei, disordered conductors, zeros of the Riemann function in number theory, and even risk management models in finance [5]. Remarkably, the Bohigas-Giannoni-Schmit conjecture further enriched the field of applications of GOE statistics [6], showing that it applies generally to chaotic systems, such as Rydberg atoms in strong magnetic fields or Sinai billiards, where only few degrees of freedom are relevant, but where motion in these degrees of freedom occurs on a highly anisotropic potential energy surface [7]. Recently, it has been speculated that even cold and ultracold atom-molecule collisions will show essential features of GOE statistics [3, 4].

Inspired by these works, we statistically analyze both the experimental and calculated Fano-Feshbach spectrum according to RMT. To obtain the NNS distribution of resonances, we first derive $\bar{\rho}$ and the mean spacing between resonances, $\bar{d}$, by constructing the so-called *staircase function* [7]. This step-like function counts the number of resonances below a magnetic field value B and is defined as $\mathcal{N}(B) = \int_0^B dB' \sum_i \delta(B' - B_i)$, with δ being the delta function and B_i the position of the i-th resonance. For our experimental data (Fig. 3a) the staircase function shows an increase of the number of resonances with B, which proceeds linearly at large B and flattens out towards lower magnetic-field values (Fig. 3b). The density of resonances is given by the derivative of the staircase function. We evaluate $\bar{\rho}$ in the region above 30 G, where the staircase function shows a linear progression (Supplementary Information) and we obtain $\bar{\rho} = 3.0(3)\,\mathrm{G}^{-1}$ and $\bar{d} = 0.33(3)\,\mathrm{G}$. We perform a similar analysis with ^{166}Er and find $\bar{\rho} = 3.3(3)\,\mathrm{G}^{-1}$ and $\bar{d} = 0.31(3)\,\mathrm{G}$ (Extended Data Fig. 3). For CC-calculation data, we find $\bar{\rho} = 3.3(3)\,\mathrm{G}^{-1}$ for $L_{\max} = 20$ (Fig. 2). We finally derive the NNS distribution for the experimental and CC-
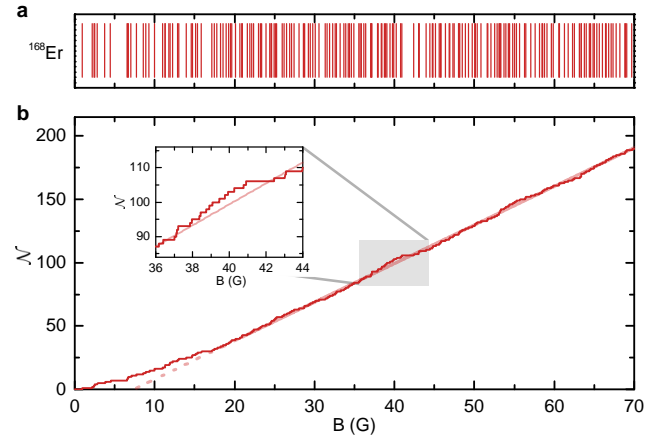
Figure 3 | Loss-maxima position and staircase function for ^{168}Er. a, Positions of the measured loss maxima of Fig. 1 are shown as vertical lines. **b**, The staircase function shows a linear dependence on the magnetic field at large values. A linear fit to the data above 30 G is plotted in light colors. The inset shows a magnification of the data to emphasize the step-like nature of the staircase function.

calculated data by constructing a histogram of resonance spacings. We choose a number of bins on the order of $\sqrt{N}$, with N being the number of Fano-Feshbach resonances used for analysis [26]. We then rescale the histogram in terms of the dimensionless quantity $s = B/\bar{d}$ and normalize the distribution in order to obtain $P(s)$.

Figure 4 is the main result of our statistical analysis for ^{168}Er. The plot shows the NNS distribution of the experimental and the CC-calculated Fano-Feshbach resonances together with the parameter-free Poisson and Wigner-Dyson distributions (Eq. 1). We see an impressive agreement between the experimental result and the CC calculations. Remarkably, both follow a distribution much closer to the WD than to the Poissonian one. To quantify the agreement with the GOE statistics, we evaluate the reduced chi squared, $\tilde{\chi}^2$, between our data and the Poisson and WD distribution. We find $\tilde{\chi}^2_{\mathrm{WD}} = 0.9$ and $\tilde{\chi}^2_{\mathrm{P}} = 2.3$ for our experimental data and $\tilde{\chi}^2_{\mathrm{WD}} = 0.8$ and $\tilde{\chi}^2_{\mathrm{P}} = 3.0$ for the data of the CC calculations. The fact that $\tilde{\chi}^2_{\mathrm{WD}} \leqslant 1$ confirms that our data are well described by a WD distribution. Similar results are found for ^{166}Er (Extended Data Fig. 4).

To further investigate the spectral correlations, we analyze our data in terms of other statistical quantities, such as the number variance and the two-gap distribution function (Supplementary Information) [27]. The number variance $\Sigma^2(\Delta B)$ measures the fluctuations of the number of resonances in a magnetic-field interval ΔB (Methods) [7] . For non-correlated (Poissonian-distributed) levels, $\Sigma^2 = \Delta B$, indicating large fluctuations around a mean value. For quantum chaotic systems, the correlations are strong and the fluctuations are thus less spread out. In this case, $\Sigma^2 \propto \ln(\Delta B)$. This slower increase

Figure 4 | NNS distribution and number variance. a, ^{168}Er NNS distribution above 30 G with a bin size of 160 mG. The plot shows the experimental data (circles) with the corresponding Brody distribution (solid line), the Brody distribution for the CC calculation with $L_{max} = 20$ (dotted line), and the parameter free distributions P_P (dashed line) and P_{WD} (short-dashed line). The Brody distribution is given in the Methods section. For the error bars in the experimental d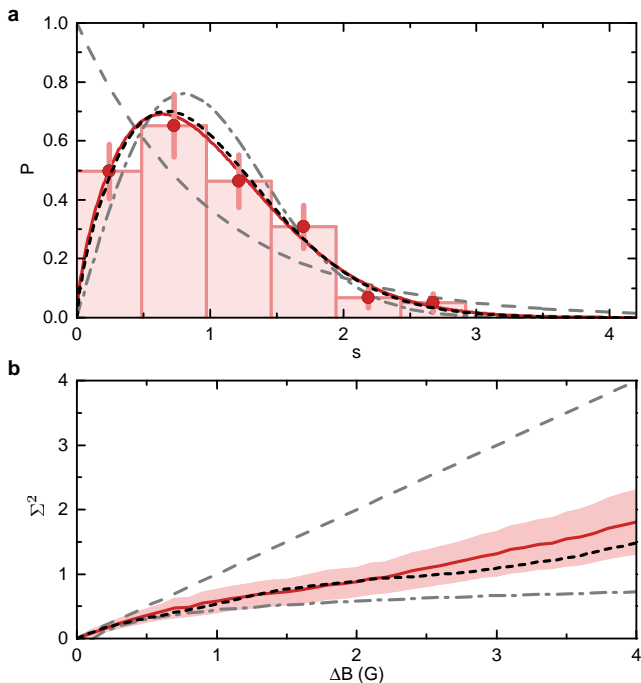ata, we assume a Poisson counting error. **b,** Number variance for the experimental data (solid line) with a two-sigma confidence band (shaded area), the CC-calculation data (dotted line), P_P (dashed line), and P_{WD} (short-dashed line).

of the number variance is regarded as a strong *spectral rigidity* of the system [7]. Our observations clearly deviate from the Poissonian behavior showing that Σ^2 tends to the WD case (Fig. 4b) and confirm the presence of correlations in our system.

To conclude, our observations reproduce the salient features predicted by GOE statistics for chaotic systems, the level repulsion and the spectral rigidity. This implies a degree of complexity in Er+Er cold collisions unprecedented in any previous ultracold scattering system. Our results bring the powerful analytical tools of quantum chaos to bear [7]. In particular, these approaches connect the large-scale structure of the spectra to simple features such as the shortest closed classical orbits in the potential energy surface, where these connections are made by the Gutzwiller trace formula [28]. Identifying the most important closed orbits will then shed light on the potential energy surface itself, providing a route to describing ultracold collisions that is complementary to the elaborate close-coupling calculations that will be difficult to connect in detail with the data.

Erbium represents the first occasion where statistical analyses and chaotic behavior are important to ultracold collisions, but they will not be the last. Specifically, much experimental effort is being exerted toward producing ultracold molecular samples, which also enjoy highly anisotropic potential energy surfaces. Learning to read complex spectra, by acknowledging their essentially chaotic nature, represents a turning point in how the field will consider ultracold collisions in the future and provide new inroads into ultracold chemistry.

METHODS SUMMARY

Sample preparation. For bosonic sample preparation we follow the approach of Ref. [11]. We obtain about 3×10^5 optically-trapped atoms at a density of 3×10^{13} cm^{-3}. The trap-loss spectroscopy is performed in a trap with frequencies of $(\nu_x, \nu_y, \nu_z) = (65, 26, 270)$ Hz. The temperature of the cloud is measured by time-of-flight imaging at 0.4 G and gives $T_{168} = 326(4)$ nK and $T_{166} = 415(4)$ nK, respectively. We ramp the magnetic field within 10 ms to a probe value between 0 and 70 G, and hold the atomic cloud for 400 ms in the optical dipole trap. We observe an increase of the temperature up to 560 nK at a magnetic field of about 50 G due to the ramping over many Fano-Feshbach resonances. For fermionic sample preparation we follow the approach of Ref. [12]. We obtain about 1.2×10^5 fermionic atoms at a density of 2×10^{14} cm^{-3} and at a temperature of $0.4\,T_F$, where $T_F = 1.0(1)\,\mu$K is the Fermi temperature. The trap frequencies are $(427, 66, 457)$ Hz.

* francesca.ferlaino@uibk.ac.at; corresponding author
† Alternative address: St. Petersburg Nuclear Physics Institute, Gatchina, 188300; Division of Quantum Mechanics, St. Petersburg State University, 198904, Russia.
[1] S. Inouye, M. R. Andrews, J. Stenger, H.-J. Miesner, D. M. Stamper-Kurn, and W. Ketterle, "Observation of Feshbach resonances in a Bose-Einstein condensate." Nature **392**, 151 (1998).
[2] C. Chin, R. Grimm, P. S. Julienne, and E. Tiesinga, "Feshbach resonances in ultracold gases." Rev. Mod. Phys. **82**, 1225 (2010).

[3] M. Mayle, B. P. Ruzic, and J. L. Bohn, "Statistical aspects of ultracold resonant scattering." Phys. Rev. A **85**, 062712 (2012).
[4] M. Mayle, G. Quéméner, B. P. Ruzic, and J. L. Bohn, "Scattering of ultracold molecules in the highly resonant regime." Phys. Rev. A **87**, 012709 (2013).
[5] T. Guhr, A. Müller-Groeling, and H. A. Weidenmüller, "Random-matrix theories in quantum physics: common concepts." Physics Reports **299**, 189 (1998).
[6] O. Bohigas, M. J. Giannoni, and C. Schmit, "Characterization of chaotic quantum spectra and universality of

level fluctuation laws." Phys. Rev. Lett. **52**, 1 (1984).

[7] H. A. Weidenmüller and G. E. Mitchell, "Random matrices and chaos in nuclear physics: Nuclear structure." Rev. Mod. Phys. **81**, 539 (2009).

[8] T. A. Brody, "A statistical measure for the repulsion of energy levels." Lettere Al Nuovo Cimento Series 2 **7**, 482 (1973).

[9] M. Lu, N. Q. Burdick, S. H. Youn, and B. L. Lev, "Strongly dipolar Bose-Einstein condensate of dysprosium." Phys. Rev. Lett. **107**, 190401 (2011).

[10] M. Lu, N. Q. Burdick, and B. L. Lev, "Quantum degenerate dipolar Fermi gas." Phys. Rev. Lett. **108** (2012).

[11] K. Aikawa, A. Frisch, M. Mark, S. Baier, A. Rietzler, R. Grimm, and F. Ferlaino, "Bose-Einstein condensation of erbium." Phys. Rev. Lett. **108**, 210401 (2012).

[12] K. Aikawa, A. Frisch, M. Mark, S. Baier, R. Grimm, and F. Ferlaino, "Reaching Fermi degeneracy via universal dipolar scattering." ArXiv e-prints (2013), arXiv:1310.5676.

[13] C. I. Hancox, S. C. Doret, M. T. Hummon, L. Luo, and J. M. Doyle, "Magnetic trapping of rare-earth atoms at millikelvin temperatures." Nature **431**, 281 (2004).

[14] C. B. Connolly, Y. S. Au, S. C. Doret, W. Ketterle, and J. M. Doyle, "Large spin relaxation rates in trapped submerged-shell atoms." Phys. Rev. A **81**, 010702 (2010).

[15] V. Kokoouline, R. Santra, and C. H. Greene, "Multichannel cold collisions between metastable Sr atoms." Phys. Rev. Lett. **90**, 253201 (2003).

[16] R. V. Krems, G. C. Groenenboom, and A. Dalgarno, "Electronic interaction anisotropy between atoms in arbitrary angular momentum states." J. Phys. Chem. A **108**, 8941 (2004).

[17] A. Petrov, E. Tiesinga, and S. Kotochigova, "Anisotropy-induced Feshbach resonances in a quantum dipolar gas of highly magnetic atoms." Phys. Rev. Lett. **109**, 103002 (2012).

[18] M. Berninger, A. Zenesini, B. Huang, W. Harm, H.-C. Nägerl, F. Ferlaino, R. Grimm, P. S. Julienne, and J. M. Hutson, "Feshbach resonances, weakly bound molecular states, and coupled-channel potentials for cesium at high magnetic fields." Phys. Rev. A **87**, 032517 (2013).

[19] T. Takekoshi, M. Debatin, R. Rameshan, F. Ferlaino, R. Grimm, H.-C. Nägerl, C. R. Le Sueur, J. M. Hutson, P. S. Julienne, S. Kotochigova, and E. Tiemann, "Towards the production of ultracold ground-state RbCs molecules: Feshbach resonances, weakly bound states, and the coupled-channel model." Phys. Rev. A **85**, 032506 (2012).

[20] S. Kotochigova, H. Levine, and I. Tupitsyn, "Correlated relativistic calculation of the giant resonance in the Gd^{3+} absorption spectrum." Int. J. Quant. Chem. **65**, 575 (1998).

[21] A. Kramida, Y. Ralchenko, and J. Reader, "NIST atomic spectra database (ver. 5.0)." (2013).

[22] J. E. Lawler, J. Wyart, and E. A. D. Hartog, "Atomic transition probabilities of Er I." J. Phys. B: At. Mol. Opt. Phys. **43**, 235001 (2010).

[23] B. Gao, "Zero-energy bound or quasibound states and their implications for diatomic systems with an asymptotic van der Waals interaction." Phys. Rev. A **62**, 050702(R) (2000).

[24] E. P. Wigner, "On a class of analytic functions from the quantum theory of collisions." Annals of Mathematics Second Series, **53**, 36 (1951).

[25] F. J. Dyson and M. L. Mehta, "Statistical theory of the energy levels of complex systems. IV." Journal of Mathematical Physics **4**, 701 (1963).

[26] J. Taylor, *An Introduction to Error Analysis: The Study of Uncertainties in Physical Measurements*, A series of books in physics (University Science Books, 1997).

[27] T. A. Brody, J. Flores, J. B. French, P. A. Mello, A. Pandey, and S. S. M. Wong, "Random-matrix physics: Spectrum and strength fluctuations." Rev. Mod. Phys. **53**, 385 (1981).

[28] M. Gutzwiller, *Chaos in Classical and Quantum Mechanics* (Springer, 1990).

[29] A. Frisch, K. Aikawa, M. Mark, A. Rietzler, J. Schindler, E. Zupanič, R. Grimm, and F. Ferlaino, "Narrow-line magneto-optical trap for erbium." Phys. Rev. A **85**, 051401 (2012).

[30] J. D. Watts, J. Gauss, and R. J. Bartlett, "Coupled-cluster methods with noniterative triple excitations for restricted open-shell Hartree-Fock and other general single determinant reference functions: Energies and analytical gradients." J. Chem. Phys. **98**, 8718 (1993).

METHODS

Experimental procedures. For bosonic sample preparation we follow the approach of Ref. [11]. In brief, after the magneto-optical trap [29], we load the atoms in an optical dipole trap composed of two laser beams in horizontal (1,064 nm, 0.4 W, single-mode) and vertical direction (1,064 nm, 4.0 W, broadband Yb fiber-laser). In the trap, we force evaporation by ramping down the power of both trapping laser beams within 6.2 s, in the presence of a homogeneous magnetic field of 0.4 G to prevent spin-flips to other Zeeman states. We stop evaporative cooling before the onset of Bose-Einstein condensation. Our final trap has frequencies of $(\nu_x, \nu_y, \nu_z) = (65, 26, 270)$ Hz and contains about 3×10^5 atoms at a density of 3×10^{13} cm^{-3}. The temperature of the atomic cloud is measured by time-of-flight imaging for both isotopes at 0.4 G and gives $T_{168} = 326(4)$ nK and $T_{166} = 415(4)$ nK. We ramp the homogeneous magnetic probe field up to 70 G within 10 ms and hold the atomic cloud for 400 ms in the optical dipole trap. The magnetic field is suddenly (< 5 ms, limited by eddy currents) switched off and the atom number and size of the cloud is measured via absorption imaging after a time of flight of 15 ms. We observe an increase of the temperature up to 560 nK at a magnetic field of about 50 G due to ramping over many Fano-Feshbach resonances. For fermionic sample preparation we follow the approach of Ref. [12]. We obtain about 1.2×10^5 fermionic atoms at a density of 2×10^{14} cm^{-3} and at a temperature of $0.4\,T_\mathrm{F}$, where $T_\mathrm{F} = 1.0(1)\,\mu$K is the Fermi temperature. The trap frequencies are $(427, 66, 457)$ Hz.

Magnetic-field control. An analog feedback loop stabilizes the current for the homogeneous magnetic-field coils with a relative short-term stability of better than 2×10^{-4}. Calibration of the magnetic field is done by driving a radio-frequency transition between Zeeman states $m_J = -6$ and $m_J = -5$. Trap-loss spectroscopy is carried out in steps of 20 mG (out of resonance) and 5 mG (on resonance). The long-term offset stability of the magnetic field was observed during the data recording period to be better than 4 mG within one week.

Coupled-channel calculations. We perform exact CC calculations for Er+Er scattering in the basis $|j_1 m_{J,1}, j_2 m_{J,2}, \ell m_\ell\rangle \equiv Y_{\ell m_\ell}(\theta, \phi)|j_1 m_{J,1}\rangle|j_2 m_{J,2}\rangle$, where $\vec{j}_{a=1,2}$ are the atomic angular momenta with space-fixed projection $m_{J,a=1,2}$ along the magnetic-field direction, the spherical harmonics $Y_{\ell m_\ell}(\theta, \phi)$ describe molecular rotation with partial wave $\vec{\ell}$, and where the angles θ and ϕ orient the internuclear axis relative to the magnetic field.

For a closed-coupling calculation of the rovibrational motion and of the scattering of the atoms we need all electronic potentials dissociating to two ground-state atoms. There are 91 BO potentials for Er$_2$, of which 49 are gerade and 42 are ungerade potentials. For collisions of bosons in the same Zeeman state only gerade states matter. These potential surfaces have been obtained using an *ab initio* relativistic multi-reference configuration-interaction method (RMRCI) [20], and converted into a tensor operator form with R-dependent coefficients. Examples of tensor operators are the exchange interaction $V_\mathrm{ex}(R)\vec{j}_1 \cdot \vec{j}_2$ and the anisotropic quadrupole-rotation operator $V_\mathrm{Q}(R)Y_2(\hat{R}) \cdot [\vec{j}_1 \otimes \vec{j}_1]_2$ coupling the quadrupole operator $[\vec{j}_1 \otimes \vec{j}_1]_2$ of one atom with angular momentum j_1 to the rotation of the molecule. See [17] for other operators.

Collisions of submerged 4f-shell atoms at low temperatures also depend on the intermediate to long-range isotropic and anisotropic dispersion, magnetic dipole-dipole and quadrupole-quadrupole interatomic interactions. The van der Waals dispersion potentials for two ground-state atoms are obtained using the transition frequencies and oscillator strengths [21, 22]. The quadrupole moment of Er is calculated using an unrestricted atomic coupled-cluster method with single, double, and perturbative triple excitations uccsd(t) [30] and shown to be small at $Q = 0.029$ a.u..

We use a first-principle coupled-channel model to calculate anisotropy-induced magnetic Fano-Feshbach-resonance spectra of bosonic Erbium. The model treats the Zeeman, magnetic dipole-dipole, and isotropic and anisotropic dispersion interactions on equal footing. The Hamiltonian includes

$$H = -\frac{\hbar^2}{2\mu}\frac{d^2}{dR^2} + \frac{\vec{\ell}^2}{2\mu R^2} + H_\mathrm{Z} + V(\vec{R}, \tau),$$

where $\vec{R}$ describes the orientation of and separation between the two atoms. The first two terms are the radial kinetic and rotational energy operators, respectively. The Zeeman interaction is $H_\mathrm{Z} = g\mu_\mathrm{B}(j_{1z} + j_{2z})B$, where g is an atomic g-factor and j_{iz} is the z component of the angular momentum operator $\vec{j}_i$ of atom $i = 1, 2$. The interaction, $V(\vec{R}, \tau)$, includes the Born-Oppenheimer and the magnetic dipole-dipole interaction potentials, which are anisotropic, and τ labels the electronic variables. Finally, μ is the reduced mass and for $R \to \infty$ the interaction $V(\vec{R}, \tau) \to 0$. Coupling between the basis states is due to $V(\vec{R}, \tau)$, inducing either isotropic (ℓ and m_ℓ conserving) or anisotropic (ℓ or m_ℓ changing) couplings. The Hamiltonian conserves $M_\mathrm{tot} = m_{J,1} + m_{J,2} + m_\ell$ and is invariant under the parity operation so that only even (odd) ℓ are coupled. In the atomic basis set, the Zeeman and rotational interaction are diagonal.

NNS probability distribution. As the density of resonances is not constant below 30 G we restrict our analysis to resonances appearing from 30 to 70 G. We plot a histogram of spacings between adjacent resonances given by $d_i = B_{i+1} - B_i$. For this an appropriate number of bins is chosen on the order of $\sqrt{N}$, with N being the total number of Fano-Feshbach resonances observed up to 70 G. This ensures a bin size at least an order of magnitude larger than the mean resolution of the trap-loss spectroscopy scan. For every bin a statistical counting error according to a Poisson distribu-

tion is assigned. Next, the magnetic-field axis of the histogram is divided by the mean spacing of resonances to get the dimensionless quantity $s = B/\bar{d}$. To calculate the NNS probability distribution $P(s)$ the histogram has to be normalized such that $\int_0^\infty ds\, P(s) = 1$. As shown in Ref. [27], the probability distribution of uncorrelated random numbers is simply given by the Poisson distribution $P_{\mathrm{P}}(s) = \exp(-s)$. A theoretical spacing distribution of random matrices can not be written in a simple form but, according to the Wigner surmise, an excellent approximation is given by the Wigner-Dyson distribution $P_{\mathrm{WD}}(s) = \frac{\pi}{2} s \exp(-\pi s^2/4)$. A way of discriminating between these two distributions is to fit the so-called *Brody distribution* to the NNS distribution [8]. It is an empirical function with a single fitting parameter η, which interpolates between P_{WD} and P_{P} and quantifies the tendency (and not the degree of chaoticty) of the observed distribution to be more Poisson-like ($\eta = 0$) or more Wigner-Dyson-like ($\eta = 1$). It is defined by

$$P_{\mathrm{B}}(s) = A s^\eta \exp(-\alpha s^{\eta+1})$$
$$A = (\eta + 1)\alpha$$
$$\alpha = \left[\Gamma\left(\frac{\eta+2}{\eta+1}\right)\right]^{\eta+1},$$

where Γ denotes the Gamma function. From a least-squares fit to the experimental data, we obtain $\eta_{168} = 0.66(10)$ for ^{168}Er and $\eta_{166} = 0.73(18)$ for ^{166}Er, and a fit to the CC-calculation data gives $\eta_{\mathrm{CC}} = 0.72(18)$.

Number variance. The number variance Σ^2 is a quantity that depends on long-range correlations between resonance spacings within an interval ΔB. It is defined by

$$\Sigma^2(\Delta B) = \overline{n^2(B_0, \Delta B)} - (\overline{n(B_0, \Delta B)})^2 ,$$

with $n(B_0, \Delta B) = \mathcal{N}(B_0 + \Delta B) - \mathcal{N}(B_0)$ giving the number of resonances in the interval $[B_0, B_0 + \Delta B]$ and the bar denotes the mean value over all B_0. For a Poisson distribution, $\Sigma^2 = \Delta B$. By contrast, for a spectrum according to RMT one expects $\Sigma^2 = 1/\pi^2 \left(\ln(2\pi\Delta B) + \gamma + 1 - \pi^2/8\right)$, for large ΔB and where $\gamma = 0.5772...$ is Euler's constant [25]. This behavior reflects that there are only very small fluctuations around an average number of resonances within a given interval of size ΔB (spectral rigidity). Compared to the NNS distribution the number variance is more suitable to probe long distances in the spectrum. A clear signature of level repulsion on the one hand and a large spectral rigidity on the other are central properties of strong correlations between levels according to RMT [27].
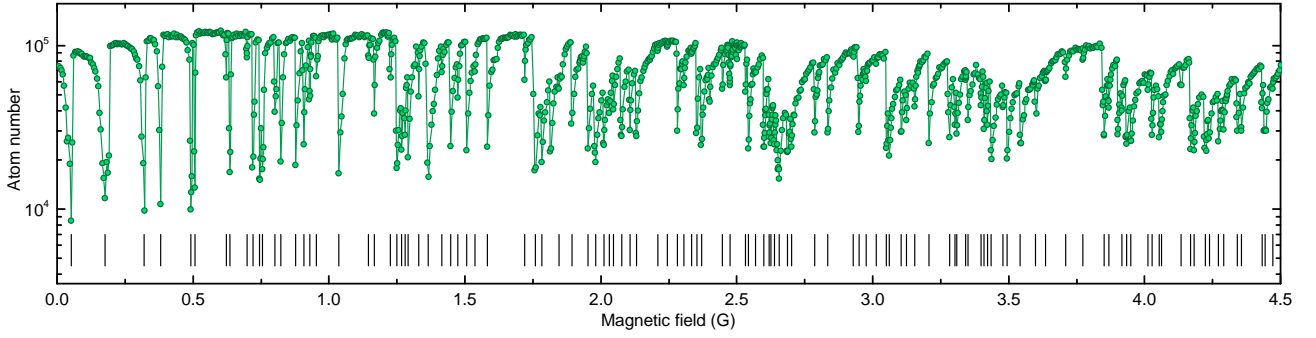
Extended Data Figure 1 | Fano-Feshbach spectrum of fermionic ^{167}Er from 0 to 4.5 G. The trap-loss spectroscopy is performed in an optically trapped sample of fermionic Er atoms at a temperature of $0.4\,T_\mathrm{F}$, where $T_\mathrm{F} = 1.0(1)\,\mu\mathrm{K}$ is the Fermi temperature. The atoms are spin-polarized in the lowest Zeeman sublevel, $m_F = -19/2$. We keep the atomic sample at the magnetic probing field for a holding time of 100 ms. We observe 115 resonances up to 4.5 G, which we attribute to be Fano-Feshbach resonances between identical fermions. The corresponding mean density is about 26 resonances per gauss.
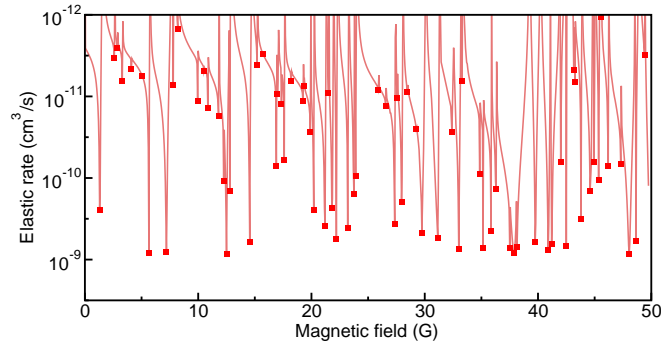
Extended Data Figure 2 | Elastic rate coefficient of $m_J = -6$ ^{168}Er collisions. The s-wave elastic rate coefficient as a function of magnetic field assuming a collision energy of $E/k_\mathrm{B} = 360$ nK. Partial waves ℓ up to 20 are included. A divergence of the elastic rate coefficient, i.e. the position of a Fano-Feshbach resonance, is marked with squares.
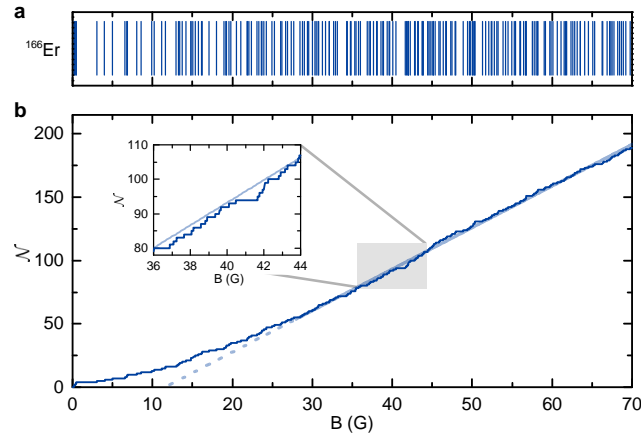
Extended Data Figure 3 | Statistical analysis of high-density Fano-Feshbach resonances of isotope ^{166}**Er. a,** Position of the resonances are marked with vertical lines. **b,** The staircase function shows a similar behavior to ^{168}Er (Fig. 3). A linear fit to the data above 30 G is plotted in light colors. From the staircase function we calculate a mean density of resonances of $\bar{\rho} = 3.3(3)\,\mathrm{G}^{-1}$, which corresponds to a mean distance between resonances of $\bar{d} = 0.31(3)\,\mathrm{G}$.
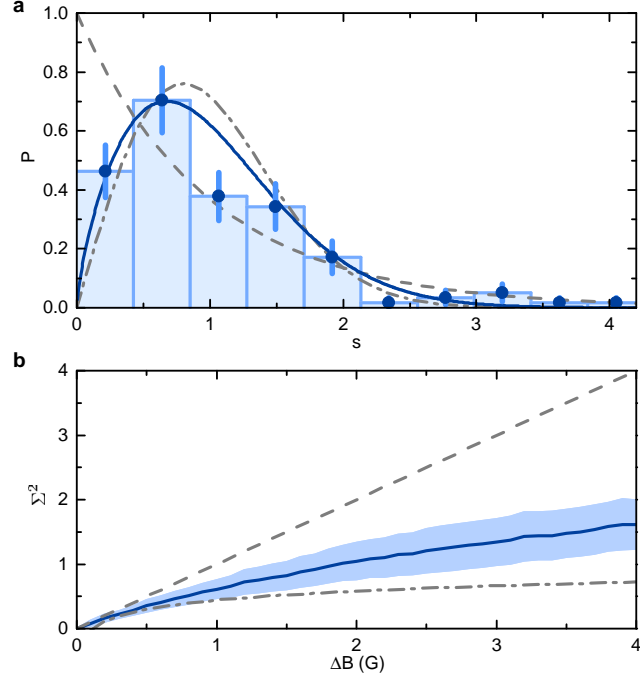
Extended Data Figure 4 | NNS distribution and number variance. a, ^{168}Er NNS distribution above 30 G with a bin size of 140 mG. For the error bars we assume a Poisson counting error. The plot shows the experimental data (circles) with the corresponding Brody distribution (solid line). The parameter free distributions P_{P} (short-dashed line) and P_{WD} are shown and reduced chi-squared values are $\tilde{\chi}^2_{\mathrm{P}} = 2.32$ for the Poisson and $\tilde{\chi}^2_{\mathrm{WD}} = 1.85$ for the Wigner-Dyson distribution. **b,** Number variance Σ^2 for the same experimental data (solid line) with a two-sigma confidence band (shaded area). The number variance from experimental data shows a clear deviation from the number variance of a Poisson distribution.

10.3. Further work

10.3.1. RMT and Feshbach spectroscopy

To gain a deeper insight into the coupling between molecular states we developed a toy model, which allows to calculate the binding energy of a random set of coupled molecular states dependent on the magnetic field. Utilizing this model we can then determine the position, at which the states cross the threshold at zero energy and derive a 'simulated Feshbach spectrum'. We analyze the NNS distribution of these artificial Feshbach resonances for different coupling strengths and observe a Wigner-Dyson distribution only for strong coupling strengths. The energy dependence was derived by diagonalizing the model's Hamiltonian

$$H = H_0 + H_{\mathrm{cpl}} - \mu_{\mathrm{mol}} B \ , \tag{10.1}$$

where H_0 gives the energy of the states at zero magnetic field B, H_{cpl} contains the coupling strengths between different states in the off-diagonal elements, and the last term gives the Zeeman shift of the states. For simplicity, the magnetic moment of the simulated molecular states, μ_{mol}, is chosen randomly from all possible combinations of m_J states of two erbium atoms. Furthermore, a representative density of resonances of about three per Gauss, like observed in the experiment, was assumed. The coupling strength between two molecular levels are randomly chosen from a Gaussian distribution with a given variance of ν_a^2, see Fig. 10.1.

Figure 10.2 shows the magnetic-field dependence of the simulated binding energy of coupled molecular states for different values of ν_a^2. For larger values of the coupling avoided crossings of states become visible. As the slope of the state changes with the magnetic field when moving over an avoided crossing, its magnetic moment changes accordingly. For stronger coupling strengths this effect leads to a more homogeneous distribution of magnetic moments of states, as seen in Fig. 10.2(c-d).
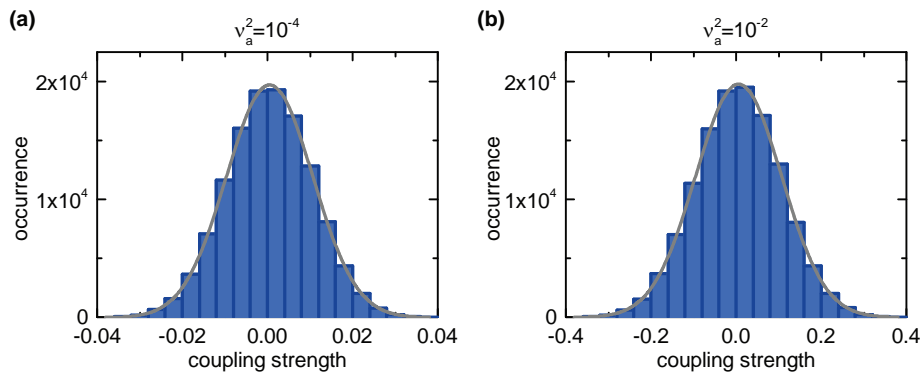
Figure 10.1.: Random Gaussian-distributed coupling strength for the molecular state coupling simulation shown in Fig. 10.2. The histogram (blue) plots the occurrence of coupling matrix elements with zero mean and a variance of (a) $\nu_a^2 = 10^{-4}$ and (b) $\nu_a^2 = 10^{-2}$, respectively. Each histogram contains 124,750 matrix elements, which are needed for a coupling matrix H_{cpl} of size 500×500. The solid line (gray) shows a Gaussian fit to the histogram.
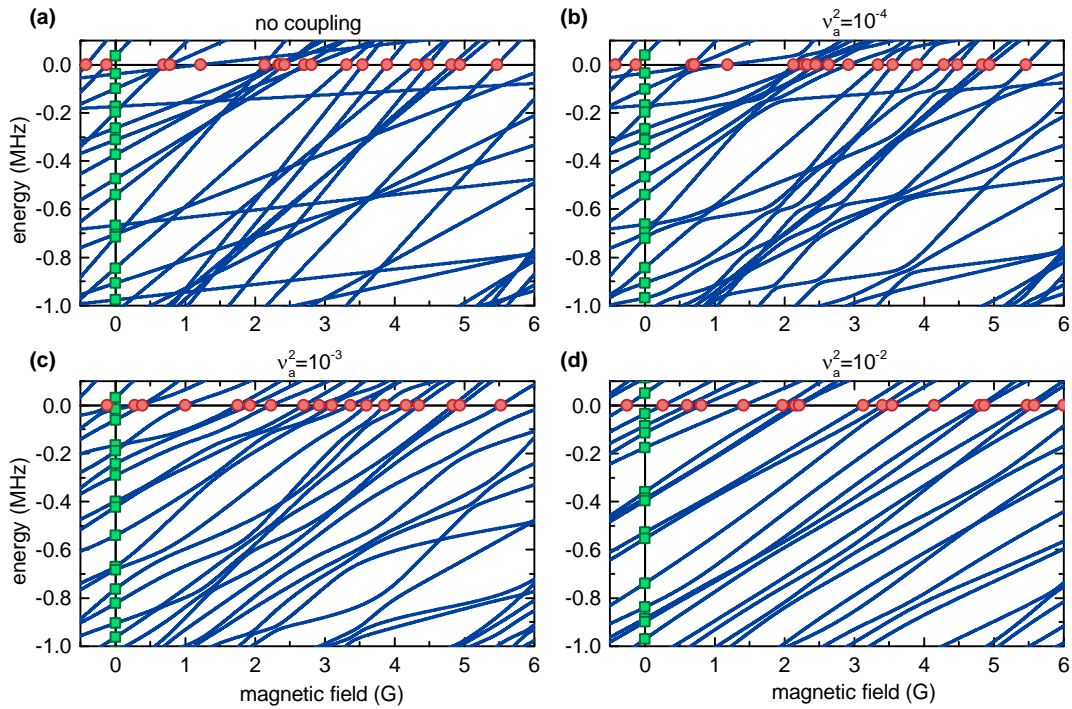
Figure 10.2.: Magnetic field dependence of the energy of simulated molecular states (blue) with random magnetic moments assuming (a) no coupling between molecular states and randomly chosen Gaussian distributed coupling strengths with (b) $\nu_a^2 = 10^{-4}$, (c) $\nu_a^2 = 10^{-3}$, and (d) $\nu_a^2 = 10^{-2}$. The slope of the states equals their magnetic moment. Additionally, the crossing of a state with the threshold, i. e. the position of a Feshbach resonance, ($E = 0$) is marked with red circles and the energy of the state at zero magnetic field ($B = 0$) is shown by green squares. Avoided crossings appear when a coupling between states is present.

The strong coupling between molecular states leads to a significant change of the distribution of FR positions, as shown in Fig. 10.3. The molecular states are assumed to be distributed according to a Wigner-Dyson distribution with respect to energy. The distribution of FRs changes from uncorrelated resonances (without coupling) to strongly correlated resonances (for coupled molecular states) following a Wigner-Dyson distribution.

Contrary to a simple system of, e. g. alkali-metal atoms, where coupled-channel calculations can be easily performed and the Feshbach spectrum fully assigned [Chi10], lanthanide atoms are challenging for theorists. Due to the unprecedented high density of FRs and strongly coupled molecular states, the way of describing a Feshbach spectrum by employing random matrix theory seems to be the most fruitful at the moment.
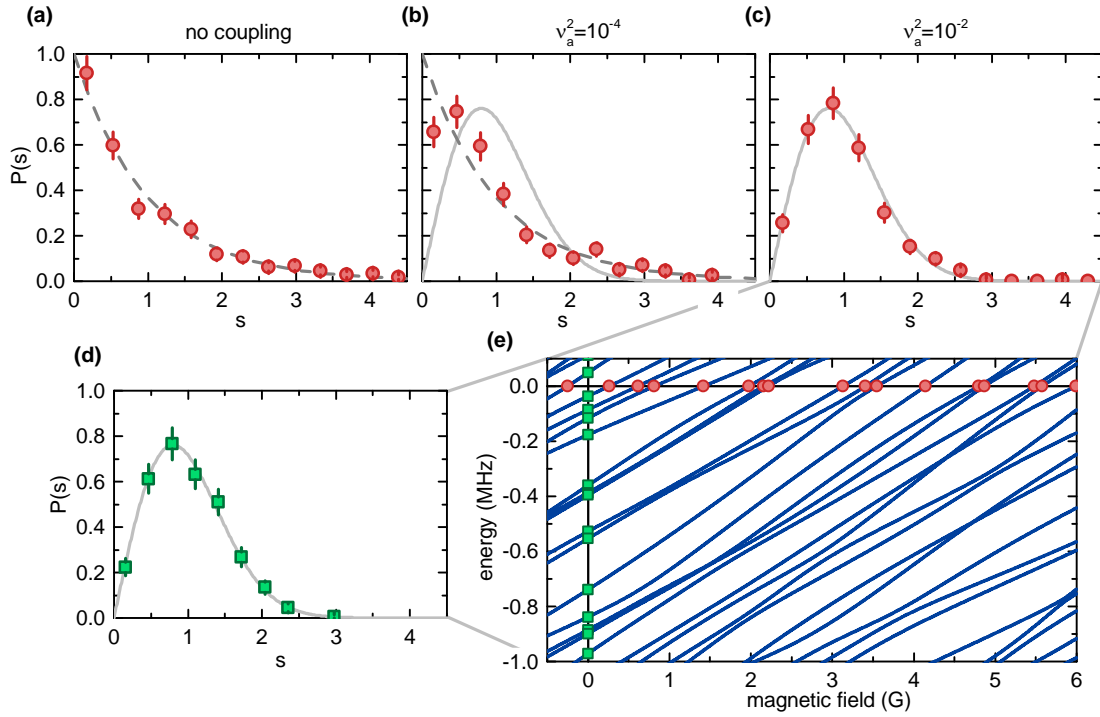
Figure 10.3.: NNS distribution $P(s)$ of molecular states (a-c) along the magnetic field axis and (d) along the energy axis. $P(s)$ dependent on the magnetic field is shown for non-coupled states (a) and Gaussian-distributed coupling strengths with (b) a variance of $\nu_a^2 = 10^{-4}$ and (c) with $\nu_a^2 = 10^{-2}$. (d) In all three cases the energy of the states at zero magnetic field are assumed to be randomly distributed according to a Wigner-Dyson distribution. The solid line shows a Wigner-Dyson distribution and the dashed line a Poisson distribution. A total of 500 states was used to derive the NNS distributions. Panel (e) shows only a small region of the magnetic field dependence of states as in Fig. 10.2 for a coupling strength of $\nu_a^2 = 10^{-2}$.

10.3.2. Feshbach resonance width distribution

It was shown in Ref. [Por56] that widths from nuclear reactions can be described by a chi-squared (χ^2) distribution. This distribution is defined as

$$P_{\chi^2}(s) = \frac{1}{\Gamma(n)}(ns)^{n-1}e^{-ns}n \ , \qquad\qquad 10.2$$

where Γ is the Gamma function and $\nu = 2n$ is the so-called *degree of freedom*. For $\nu = 2$ this gives $P_{\chi^2}(s) = \exp(-s)$, being an exponential distribution.

Widths of resonances in nuclear spectra were best fitted by a distribution with one degree of freedom. Figure 10.4 shows the distribution, $P(s)$, of erbium Feshbach resonance widths. The histogram was created by binning the width data from trap-loss spectroscopy into a histogram with a bin size of $25\,\mathrm{mG}$. Normalizing the width is done by $s = \Gamma_{\mathrm{red}}/\overline{\Gamma}_{\mathrm{red}}$, with $\overline{\Gamma}$ being the arithmetic mean of widths. This results in $P(s)$, which is compared with chi-squared distributions of different degrees of freedom. We observe that it fits best by a χ^2-distribution with one degree of freedom. Following Ref. [Por56] this corresponds to a
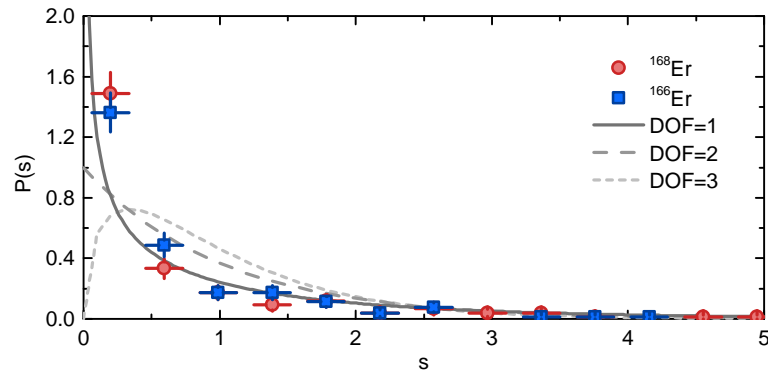
Figure 10.4.: Normalized width distribution of Feshbach resonances in ^{168}Er (red circles) and ^{166}Er (blue squares) above $30\,$G. The χ^2-distributions with degrees of freedom (DOF) of one, two, and three are plotted in gray colors for comparison. The data points agree best with the χ^2-distribution with DOF $= 1$. Error bars result from statistical uncertainties from creating the histogram. The error is taken to be $\sqrt{N}$ with N the number of counts per bin.

single outgoing channel N_o, which is as expected by the preparation of erbium atoms in their energetically lowest Zeeman state.

11

Publication: Fermi surface deformation

11.1. Introduction

Dipolar many-body effects in atomic Fermi gases are a rather unexplored field. This is due to the fact that only recently suitable fermionic systems have become available. The magnitude of dipolar effects is given by the ratio $\frac{nd^2}{E_F}$, which is typically much smaller than unity. Here, E_F is the Fermi energy, n the peak number density, and d^2 the coupling constant of the dipole-dipole interaction (DDI), being for magnetic dipoles $\frac{\mu_0\mu^2}{4\pi}$.

A first dipolar many-body effect should be noticeable in a deformation of the Fermi surface. The Fermi surface deformation (FSD) is predicted in many theoretical works, see Refs. [Miy08, Fre09, Bai12b], but has not been experimentally observed before. In the presented publication we confirm the deformation of the Fermi surface in a degenerate Fermi gas of erbium atoms. Furthermore, we demonstrate that it is indeed a many-body effect. The FSD in the erbium system is caused by the anisotropy of the magnetic DDI. The DDI induces two additional contributions in the total energy of the system. The first one is the Hartree direct term and the second one is the Fock exchange term, see Ref. [Miy08]. In case of isotropic contact interaction these two terms cancel each other and the Fermi surface is always isotropic.

The amount of deformation for the parameters of our experiment is expected to be very small, just on the order of a few percent, which makes the detection of the FSD very difficult. We have shown that the amount of deformation depends on the Fermi energy of the system as it increases for higher Fermi energies, clearly showing the quantum many-body nature of the FSD. Furthermore, the direction of the FSD follows the orientation of the polarizing magnetic field. In time-of-flight images, revealing the momentum distribution of the cloud, it was possible to visualize the FSD by an anisotropic shape of the atom cloud.

This first experimental verification of the FSD might lead to further investigations on collective excitations and anisotropic superfluid pairing, see Ref. [Bar02b].

11.2. Publication:
Observation of Fermi surface deformation in a dipolar quantum gas[†][‡]

Kiyotaka Aikawa,[1] Simon Baier,[1] Albert Frisch,[1] Michael Mark,[1] Cornelis Ravensbergen,[1,2] and Francesca Ferlaino[1,2]

[1] *Institut für Experimentalphysik and Zentrum für Quantenphysik, Universität Innsbruck, Technikerstraße 25, 6020 Innsbruck, Austria*
[2] *Institut für Quantenoptik und Quanteninformation, Österreichische Akademie der Wissenschaften, 6020 Innsbruck, Austria*

[†]   The author of the present thesis helped in taking the data and contributed in writing the manuscript.
[‡]   The preprint version of the publication is attached for online access of this thesis.

Observation of Fermi surface deformation in a dipolar gas: a quantum nematic phase in the ultracold regime

K. Aikawa,[1] S. Baier,[1] A. Frisch,[1] M. Mark,[1] C. Ravensbergen,[1, 2] and F. Ferlaino[1]

[1]*Institut für Experimentalphysik and Zentrum für Quantenphysik,*
Universität Innsbruck, Technikerstraße 25, 6020 Innsbruck, Austria
[2]*Institut für Quantenoptik und Quanteninformation,Österreichische Akademie der Wissenschaften, 6020 Innsbruck, Austria*
(Dated: May 8, 2014)

The deformation of a Fermi surface is a fundamental phenomenon leading to a plethora of exotic quantum phases with broken symmetries. Understanding these phases, which play crucial roles in a wealth of systems, is a major challenge in condensed matter physics. Here, we report on the observation of a Fermi surface deformation in a quantum gas of erbium atoms. The deformation is triggered by the strong magnetic dipole-dipole interaction among erbium atoms. We demonstrate that the Fermi surface deformation is tunable via an external trapping potential. Our work shows that the ground state of a dipolar Fermi gas is a nematic phase and that a dipolar Fermi gas provides an ideal clean system for exploring a nematic phase in a highly controlled manner.

PACS numbers: 03.75.Ss, 37.10.De, 51.60.+a, 67.85.Lm

The Fermi-liquid theory, formulated by Landau in the late 50's, is one of the most powerful tools in modern condensed matter physics [1]. It captures the behavior of interacting Fermi systems in the normal phase, such as electrons in metals and liquid ^{3}He [2], and provides the basis for understanding Cooper pairing in conventional superconductors. Within this theory, the interaction is accounted by *dressing* the fermions as quasi-particles with effective mass and effective interaction, and with an isotropic Fermi surface (FS) in momentum space. In strongly correlated electron systems, however, the electron-electron (Coulomb) interaction can violate the Fermi-liquid picture and give rise to a deformed FS, which breaks the symmetry of the system. The deformation of a FS is often referred to as a Pomeranchuk instability of a normal Fermi liquid [3]. The simplest realization of such a situation, where the rotational symmetry of the FS is broken, is a quantum nematic phase, which is named in analogy with liquid crystal phases [4]. Symmetry-breaking FSs in solids have attracted enormous attention for their potential impact on pseudogap phases in high-transition-temperature superconductors and quantum criticality [5–7]. Recent experimental work reported on signatures of such a phenomenon in transport, mechanical, and surface properties of various materials, including superconductors such as cuprates [8–11] and iron pnictides [12–14]. However, the direct observation of spontaneously deformed Fermi surfaces in solids remains an elusive goal since a FS is strongly affected by disorders, impurities, and underlying crystalline structures [15, 16].

A completely distinct approach to quantum nematic phases is to explore ultracold Fermi gases with strong dipole-dipole interaction (DDI) [17–20], as realized with ultracold polar molecules and magnetic atoms [21–23]. Differently from *s*-wave interaction that can entail an isotropic broadening of the always-spherical FS [24, 25], the anisotropic DDI is predicted to impact the momentum distribution of fermions in a profound and subtle way, giving rise to a permanent deformation of the FS [19, 20, 26–28]. The realization of such a quantum nematic phase in experiments would strengthen the role of ul-
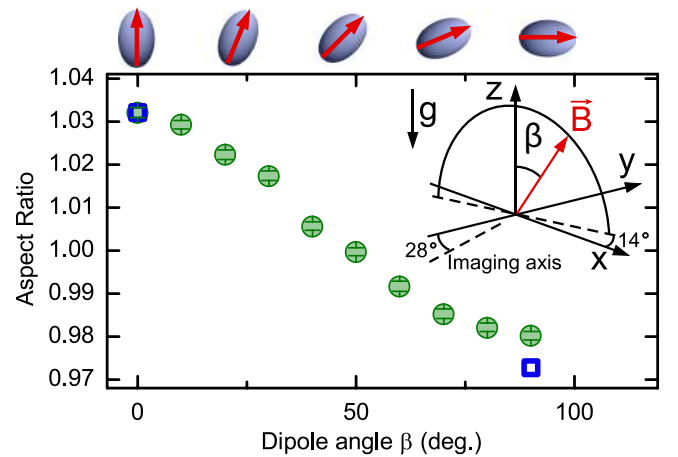
FIG. 1: (color online) AR of an expanding dipolar Fermi gas as a function of the angle β. The sample contains 7×10^4 atoms at a typical temperature of $T/T_F = 0.18$. In this measurement, the trap frequencies in three directions are $(f_x, f_y, f_z) = (579, 91, 611)$ Hz. The data are taken at $t_{\text{TOF}} = 12$ ms. The error bars are standard errors of more than 20 independent measurements. For comparison, the calculated values are also shown for $0°$ and $90°$ (squares). The inset schematically illustrates the geometry of the system. Gravity is along the z direction. The atomic cloud is imaged with an angle of $28°$ with respect to the y axis. The magnetic field orientation is rotated on the plane with an angle of $14°$ with respect to the xz plane. Schematic illustrations of the imaged atomic cloud emphasizing the anisotropy are also shown above the panel.

tracold matters as an excellent quantum simulator for exotic condensed matter phenomena.

In this paper, we report on the direct observation of a Fermi surface deformation (FSD) in a dipolar quantum gas of fermionic ^{167}Er atoms. The large DDI among the fermions results from the large Er magnetic moment μ of 7 Bohr magneton. We demonstrate that the magnitude and the orientation of the FSD can be controlled with external fields. The deformation vanishes at high temperatures of around T_F, where T_F
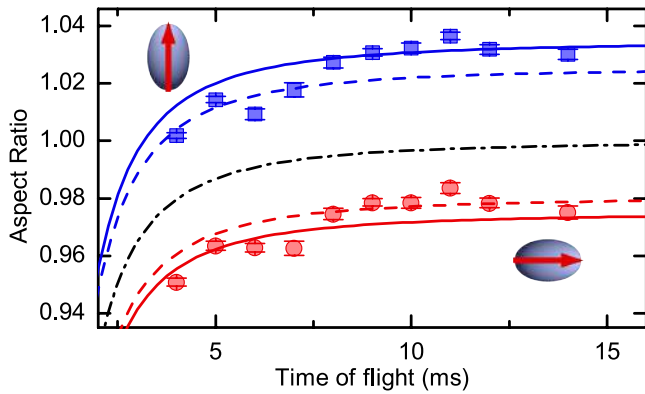
FIG. 2: (color online) Time evolution of the AR of the atomic cloud during the expansion. Measurements are performed for two dipole angles, $\beta = 0°$ (squares) and $\beta = 90°$ (circles) under the same conditions as in Fig. 1. The error bars are standard errors of more than 20 independent measurements. The theoretical curves show the full numerical calculations (solid lines), which include both the FSD and the NBE effects, and the calculation in the case of ballistic expansions (dashed lines), i.e. in the absence of the NBE effect. For comparison, the calculation for a non-interacting Fermi gas is also shown (dot-dashed line).

is the Fermi temperature, pointing to the quantum-mechanical nature of the observed effect. Our observations are in very good agreement with calculations based on Refs. [26–28]. This work constitutes the first observation of a many-body quantum effect in a dipolar Fermi gas in three-dimensions and provides direct evidence that the ground state of a dipolar Fermi gas is a nematic phase.

Our starting point is a single-component quantum degenerate dipolar Fermi gas of ^{167}Er atoms [23] (Supplementary Materials). The ultracold sample is confined in a three-dimensional harmonic trap consisting of two laser beams in a crossed-beam configuration. We control the orientation of the atoms' dipole moment with an external polarizing magnetic field; see inset Fig. 1.

To explore the impact of the DDI on the momentum distribution, we study the expansion dynamics of the gas when released from the trap. Such a time-of-flight (TOF) experiment is extremely powerful to probe properties of trapped gases and many-body phenomena [24, 25], providing, for instance, the early "smoking-gun" evidence for Bose-Einstein condensation [29, 30]. The crucial point of this method is that for a long expansion time, the size of the atomic cloud is dominated by the velocity dispersion and, in the case of ballistic (*free*) expansions, the TOF images purely reflect the momentum distribution in the trap. In our experiment, we release the degenerate Fermi gas from an optical dipole trap (ODT) and image the sample after a long expansion time t_{TOF}. We then analyze the aspect ratio (AR) of the cloud, i.e. the vertical-to-horizontal ratio of the observed radii (Supplementary Materials).

Figure 1 shows the AR of the Fermi gas for various dipole orientations β, where β is defined as the angle of the magnetic
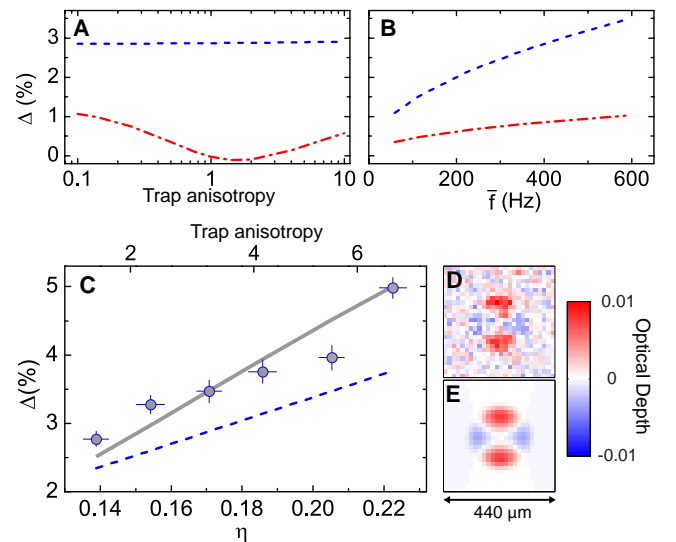
FIG. 3: (color online) Deformation Δ for various trap geometries. The calculations consider a cigar-shaped trap with $f_x = f_z$ and show separately the behavior of the FSD (dashed lines) and the NBE (dotted lines) as a function of the trap anisotropy $\sqrt{f_x f_y}/f_z$ at $\bar{f} = 400\,\text{Hz}$ (A) and as a function of $\bar{f}$ at $\sqrt{f_x f_y}/f_z = 5$ (B). (C) Experimentally observed deformations at $t_{TOF} = 12\,\text{ms}$ are plotted as a function of η, together with the full calculation (solid line) and the calculation considering only FSD (dashed line). The sample contains 6×10^4 atoms at a typical temperature of $T/T_F = 0.15$. The error bars represents standard errors of about 15 independent measurements. The variation of the trap anisotropy in the experiment is indicated in the top axis. (D) Visualized FSD for the observed TOF image at $\eta = 0.14$. (E) Visualized FSD for the fitted image at $\eta = 0.14$.

field orientation with respect to the z axis (see inset Fig. 1). We observe a clear deviation of the AR from unity, corresponding to an ellipsoidal distribution with cloud elongation along the orientation of the polarizing magnetic field. For vertical polarization, we estimate a cloud anisotropy of about 3%. Remarkably, we observe that the ellipticity of the Fermi gas rotates with the magnetic field orientation, keeping the major axis of the ellipse always aligned with the dipole orientation. This behavior clearly shows that the DDI is the origin of the observed anisotropy and stretches the FS along the orientation of the dipoles. Subsequently, we investigate the expansion dynamics for two dipole orientations by following the time evolution of the AR (Fig. 2). At short t_{TOF}, AR rapidly changes as a consequence of the radial expansion (acceleration). Eventually, for $t_{TOF} > 10\,\text{ms}$, it plateaus for both angles, revealing the momentum distribution of the sample.

The one-to-one mapping between the initial momentum distribution of the trapped Fermi gas and the position distribution of the expanding cloud after long t_{TOF} strictly holds only in the case of pure ballistic (i.e. free) expansions. In our experiments, the DDI is acting even during the expansion and could potentially mask the observation of the FSD. To evaluate the effect of the non-ballistic expansion (NBE), we perform numerical calculations based on a Hartree-Fock mean-

field theory in the zero temperature limit [26–28] (Supplementary Materials). In Fig. 2, we compare the experimental data with the parameter-free theoretical curves, which include both the FSD and the NBE effects. We observe an excellent overall agreement between the experiment and the theory, showing that our model accurately describes the behavior of our system. In addition, we plot the numerical simulations in the case of pure ballistic expansions. The comparison between the ballistic and non-ballistic expansion reveals that the latter plays a minor role in the final AR, showing that the observed anisotropy dominantly originates from the FSD. For the sake of completeness, Fig. 2 also shows the calculation for a non-interacting Fermi gas, whose FS is spheric.

The FSD is a quantum phenomena that comes from the antisymmetrization of many-body fermion wavefunctions. It has been predicted that its magnitude increases with the Fermi energy and the dipole moment and that. In the limit of weak DDI, the magnitude of the FSD is linearly proportional to a dimensionless parameter [26, 27]

$$\eta = AC_{dd}\sqrt{E_F} \tag{1}$$

Here, $A = c_0 m^{3/2}/h^3$ is a numerical factor with $c_0 = 8\pi^3 6^{-1/6} \simeq 184$, m the mass of ^{167}Er, and h the Planck constant, $C_{dd} = \mu_0\mu^2/(4\pi)$ denotes the dipolar coupling constant with μ_0 vacuum permeability, and $E_F = k_B T_F = h\bar{f}(6N)^{1/3}$ is the Fermi energy for a non-interacting Fermi gas in a harmonic trap with k_B the Boltzmann constant, $\bar{f} = (f_x f_y f_z)^{1/3}$ the mean trap frequency, and N the number of atoms. Intuitively, this scaling is interpreted as follows: a larger E_F, resulting in a higher number density and thus in a smaller interparticle spacing, gives rise to larger DDI in a Fermi gas. These arguments open up the possibility of tuning the FSD by changing E_F, i.e. the external trapping potential and the number density.

We explore the dependence on the external trapping potential in experiment and substantiate the experimental results by calculations. For convenience, we define the deformation factor, Δ, as $\Delta = 1 - AR$. We first simulate how Δ varies when the trap anisotropy, $\sqrt{f_x f_z}/f_y$, (Fig. 3A) and/or $\bar{f}$ (Fig. 3B) are varied. In the calculations, we keep the FSD and the NBE contributions separated. Our theoretical results clearly convey the following information: (i) the FSD gives the major contribution to Δ and is truly independent from the trap anisotropy, while it increases with $\bar{f}$, (ii) the NBE effect is reminiscent of the trap anisotropy and vanishes for a spherical trap [27].

In the experiment, we explore the dependence of Δ on the trap geometry for $\beta = 0°$ by keeping the axial frequency (f_y) constant and vary the radial frequencies ($f_x = f_z$ within 5 %) (Fig. 3C). This leads to a variation in the trap anisotropy, in $\bar{f}$, and thus in η. We observe a linear dependence of Δ on η in agreement with Refs. [26, 27] and our numerical calculations. The excellent agreement between experiments and theory shows that our system is a clean sample allowing us to investigate a nematic phase under a highly controlled environment.
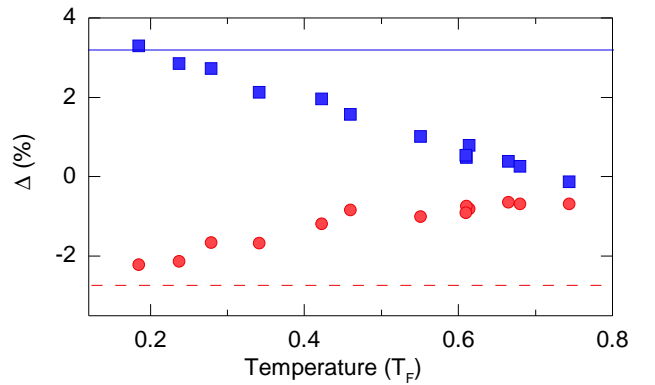
FIG. 4: (color online) Deformation as a function of the temperature of the cloud. Measurements are performed for two dipole angles, $\beta = 0°$ (squares) and $\beta = 90°$ (circles) under the same conditions as in Fig. 2. The experimental data are taken at $t_{TOF} = 12\,\text{ms}$. The plot shows the numerically calculated values at zero temperature for $\beta = 0°$ (solid line) and $\beta = 90°$ (dashed line).

In analogy with a study on nematicity in a superconducting material [31], we graphically emphasize the FSD in the measurements at $\eta = 0.14$ by subtracting the TOF absorption image taken at $\beta = 90°$ from the one at $\beta = 0°$ (Fig. 3D). The resulting image shows a clover-leaf-like pattern, visualizing that the momentum spread in the orientation of the dipoles is larger than in the other direction. For comparison, the same procedure is applied for images obtained by a fit to the observed cloud (Fig. 3E). At $\eta = 0.14$, the trap anisotropy is so small that the NBE effect is negligibly small. Therefore, the deformation visualized here is almost purely the FSD.

Finally, we investigate the temperature dependence of Δ (Fig. 4). We prepare samples at various temperatures by stopping the evaporative cooling procedure at arbitrary points [32]. The final trap geometry is kept constant. By reducing the temperature of the Fermi gas, we observe the emergence of the FSD which becomes more and more pronounced at low temperature and eventually approaches the zero-temperature limit. The observed temperature dependence qualitatively agrees with a theoretical result at finite temperatures [33]. Our observation clearly shows the quantum many-body nature of the FSD.

The observation of a deformed Fermi surface sets the basis for future investigations on quantum many-body dipolar phenomena, including dipolar collective excitations [27, 28, 34, 35], and exotic phases in strongly correlated dipolar gases [18, 19]. Taking advantage of the wide tunability of cold atom experiments, dipolar Fermi gases are ideally clean system for exploring an exotic and topological phases in a highly controlled manner.

Supplementary Materials

Experimental setup

We obtain a quantum gas of fermionic ^{167}Er atoms via laser cooling in a narrow-line magneto-optical trap [36] followed by evaporative cooling in an ODT [23]. During the entire experimental procedure, the fermions are fully polarized into the lowest hyperfine sublevel $|F = 19/2, m_F = -19/2\rangle$, where F is the total angular momentum quantum number and m_F is its projection along the quantization axis. The sample is trapped in a crossed ODT consisting of a horizontally (y axis) and a vertically (z axis) propagating beam at 1570 nm. The beam waist of the horizontal beam is kept constant to be $15\,\mu$m, while that of the vertical beam can be tuned from $20\,\mu$m to $90\,\mu$m. By controlling the power of the two beams and the beam waist of the vertical beam, we are able to vary the trap geometry from a nearly spherical shape to a cigar shape. The magnetic field amplitude is always kept constant to be 0.58 G where we do not see any influence of Feshbach resonances [37]. The magnetic field orientation is controlled with two sets of coils. During evaporative cooling, the magnetic field is vertically oriented ($\beta = 0°$).

Imaging and fitting procedure

We measure the deformation of the cloud shape in the TOF absorption image by applying the conventional polylogarithmic fit for an ideal Fermi gas [38–40]. The fit has six free parameters: the positions and sizes in two directions, the fugacity, and the optical depth. The fugacity ζ is directly connected to T/T_F through the relation $T/T_F = [-6 \times \text{Li}_3(-\zeta)]^{-1/3}$, with Li_n being the n-th order polylogarithmic function. The optical depth is proportional to N. Although the optical depth is related to ζ through N and T_F by $T_F = h\bar{f}(6N)^{1/3}/k_B$, we leave both free in the fitting procedure and confirm that they are consistent with each other. Here, we assume that the cloud has a constant fugacity over the entire cloud because the momentum deformation is small. Rigorously speaking, T_F is anisotropic and T is constant over the cloud, and thus ζ should be anisotropic. Dealing with such a distribution is beyond the scope of the present work.

Errors in AR

By taking the average of more than 20 independent measurements, we are able to determine the AR with a typical precision of 0.1 %, corresponding to the standard error of multiple measurements. In addition, there are five possible sources of systematic errors in the measured AR. (a) Variation in the pixel sizes. The variation in pixel sizes over the area of the cloud can introduce a systematic error in deformation. There is no measured data available for our CCD camera (Andor, iXon3). (b) Residual interference fringes. Interference fringes, arising from dusts on the imaging optics, can produce a fixed background pattern on the image. From the TOF measurements shown in Fig. 2, where the position of the atomic cloud varies with TOF by a free fall, we estimate the combined effect of (a) and (b) to be within ± 0.5 %. (c) Error in the fitting procedure. Although our fitting procedure assuming a constant fugacity may give rise to a systematic error in deriving the AR, it is difficult to quantitatively estimate it owing to the lack of an appropriate model. Investigating this effect will be an important future work. (d) Fluctuations in the magnetic field. The effect of the fluctuation in magnetic field, which results in a fluctuation in the dipole orientation, is negligibly small at $\beta = 0°$ and $\beta = 90°$ (< 0.05 % in deformation). (e) Tilt of the camera. Assuming that the camera is aligned perpendicular to the imaging beam path within $1°$, we infer that the influence of the tilt of the camera on the AR is negligible (< 0.02 %).

Calculation of the deformation

In the present work, the collision rate associated with universal dipolar scattering [23, 41] is lower than the lowest trap frequency. Therefore, our sample is in the collisionless regime, where the mean free path is longer than the size of the cloud [42]. We describe the trapped dipolar Fermi gas in the collisionless regime in the zero temperature limit with an ansatz that the Wigner distribution function is given as an ellipse

$$g(\mathbf{r},\mathbf{k},t) = \Theta\left(1 - \sum_{j=1}^{3}\frac{r_j^2}{R_j^2} - \sum_{j=1}^{3}\frac{k_j^2}{K_j^2}\right) \qquad (2)$$

where Θ denotes the Heaviside's step function, and $\mathbf{r}$, $\mathbf{k}$, and t denote coordinate, wave vector, and time, respectively. The parameters R_j and K_j represent the Thomas-Fermi radius and the Fermi momentum in the jth direction. These parameters are numerically determined by minimizing the total energy in the presence of the DDI. The validity of this approach was numerically confirmed [43]. At equilibrium, the parameters K_j include the information of the anisotropic FS.

The expansion dynamics is calculated using the Botzmann-Vlasov equation for the Wigner distribution function under the scaling ansatz [44–46]. The scaling parameters, representing variations from the equilibrium condition, are described by a set of coupled time-dependent differential equations. The NBE effect is naturally included in this framework. We numerically solve the equations for the general triaxial geometry, where the trap frequencies in three directions are different and the dipoles are oriented in the direction of one of the trap axes. This reflects our experimental situation at $\beta = 0°$ and $\beta = 90°$.

We calculate the sizes of the cloud on the image plane, taking into account the angle of $28°$ between the imaging axis and the y axis (see inset Fig. 1). In all our measurements, we observe an asymmetry between $\beta = 0°$ and $\beta = 90°$, i.e. $|\Delta|$ is larger at $\beta = 0°$ than at $\beta = 90°$. We observe this asymmetry also in the subtracted images in Fig. 3D and Fig. 3E as a higher contrast in the vertical direction than in the horizontal direction. This asymmetry is well reproduced by our calculation and is understood as follows. At $\beta = 0°$, the major axis (x) of the ellipse is oriented to the z direction and is fully imaged. By contrast, at $\beta = 90°$, the major axis is not perpendicular to the imaging plane and we observe a combined size between the major and minor (y) axis of the ellipse. Therefore, the observed deformation at $\beta = 90°$ is always smaller than that at $\beta = 0°$.

Image subtraction for Fig. 3D,E

The image shown in Fig. 3D is obtained in the following procedure. The TOF absorption images from 18 independent measurements are averaged and binned by 2×2 pixels to reduce background noise. This procedure is applied for the measurements at $\beta = 0°$ and $\beta = 90°$, yielding two images. We subtract the image at $\beta = 90°$ from the one at $\beta = 0°$. This image subtraction is very sensitive to the relative position of the clouds on the two images down to a sub-pixel level. We obtain accurate positions of the center of the cloud from the fit and shift the coordinate of the image at $\beta = 90°$ such that the center positions of two images exactly agree. We then apply spline interpolation for the image at $\beta = 90°$ to estimate the optical depth of the cloud at each pixel position in the image $\beta = 0°$. Unlike the procedure used in Ref. [31], where the anisotropy is extracted by rotating a single image by $90°$ and subtracting it from the original image, our procedure with two images at two dipole orientations allows us to extract only the anisotropy originating from the DDI.

[1] L. D. Landau and E. M. Lifshitz, *Statistical Physics, Part 2* (Pergamon, Oxford, 1980).
[2] A. J. Leggett, Rev. Mod. Phys. **47**, 331 (1975).
[3] I. I. Pomeranchuk, Sov. Phys. JETP-USSR **8**, 361 (1959).
[4] S. A. Kivelson, E. Fradkin, and V. J. Emery, Nature **393**, 550 (1998).
[5] E. Fradkin, S. A. Kivelson, M. J. Lawler, J. P. Eisenstein, and A. P. Mackenzie, Annu. Rev. Condens. Matter Phys. **1**, 153 (2010).
[6] M. Vojta, Adv. Phys. **58**, 699 (2009).
[7] S. A. Kivelson, I. Bindloss, E. Fradkin, V. Oganesyan, J. Tranquada, A. Kapitulnik, and C. Howald, Rev. Mod. Phys. **75**, 1201 (2003).
[8] Y. Ando, K. Segawa, S. Komiya, and A. Lavrov, Phys. Rev. Lett. **88**, 137005 (2002).
[9] V. Hinkov, D. Haug, B. Fauqué, P. Bourges, Y. Sidis, A. Ivanov, C. Bernhard, C. Lin, and B. Keimer, Science **319**, 597 (2008).
[10] R. Daou, J. Chang, D. LeBoeuf, O. Cyr-Choiniere, F. Laliberté, N. Doiron-Leyraud, B. Ramshaw, R. Liang, D. Bonn, W. Hardy, et al., Nature **463**, 519 (2010).
[11] M. Lawler, K. Fujita, J. Lee, A. Schmidt, Y. Kohsaka, C. K. Kim, H. Eisaki, S. Uchida, J. Davis, J. Sethna, et al., Nature **466**, 347 (2010).
[12] T.-M. Chuang, M. Allan, J. Lee, Y. Xie, N. Ni, S. Bud'ko, G. Boebinger, P. Canfield, and J. Davis, Science **327**, 181 (2010).
[13] J.-H. Chu, J. G. Analytis, K. De Greve, P. L. McMahon, Z. Islam, Y. Yamamoto, and I. R. Fisher, Science **329**, 824 (2010).
[14] R. M. Fernandes, L. H. VanBebber, S. Bhattacharya, P. Chandra, V. Keppens, D. Mandrus, M. A. McGuire, B. C. Sales, A. S. Sefat, and J. Schmalian, Phys. Rev. Lett. **105**, 157003 (2010).
[15] M. Yi, D. Lu, J.-H. Chu, J. G. Analytis, A. P. Sorini, A. F. Kemper, B. Moritz, S.-K. Mo, R. G. Moore, M. Hashimoto, et al., Proc. Natl. Acad. Sci. U.S.A **108**, 6878 (2011).
[16] A. Damascelli, Z. Hussain, and Z.-X. Shen, Rev. Mod. Phys. **75**, 473 (2003).
[17] T. Lahaye, C. Menotti, L. Santos, M. Lewenstein, and T. Pfau, Rep. Prog. Phys. **72**, 126401 (2009).
[18] M. A. Baranov, M. Dalmonte, G. Pupillo, and P. Zoller, Chem. Rev. **112**, 5012 (2012).
[19] B. M. Fregoso, K. Sun, E. Fradkin, and B. L. Lev, New J. Phys. **11**, 103003 (2009).
[20] C.-K. Chan, C. Wu, W.-C. Lee, and S. Das Sarma, Phys. Rev. A **81**, 023602 (2010).
[21] K. K. Ni, S. Ospelkaus, M. H. G. de Miranda, A. Pe'er, B. Neyenhuis, J. J. Zirbel, S. Kotochigova, P. S. Julienne, D. S. Jin, and J. Ye, Science **322**, 231 (2008).
[22] M. Lu, N. Q. Burdick, and B. L. Lev, Phys. Rev. Lett. **108**, 215301 (2012).
[23] K. Aikawa, A. Frisch, M. Mark, S. Baier, R. Grimm, and F. Ferlaino, Phys. Rev. Lett. **112**, 010404 (2014).
[24] I. Bloch, J. Dalibard, and W. Zwerger, Rev. Mod. Phys. **80**, 885 (2008).
[25] S. Giorgini, L. P. Pitaevskii, and S. Stringari, Rev. Mod. Phys. **80**, 1215 (2008).
[26] T. Miyakawa, T. Sogo, and H. Pu, Phys. Rev. A **77**, 061603 (2008).
[27] T. Sogo, L. He, T. Miyakawa, S. Yi, H. Lu, and H. Pu, New J. Phys. **11**, 055017 (2009).
[28] F. Wächtler, A. R. Lima, and A. Pelster, arXiv preprint arXiv:1311.5100 (2013).
[29] M. H. Anderson, J. R. Ensher, M. R. Matthews, C. E. Wieman, and E. A. Cornell, Science **269**, 198 (1995).
[30] K. Davis, M. Mewes, M. Andrews, N. Van Druten, D. Durfee, D. Kurn, and W. Ketterle, Phys. Rev. Lett. **75**, 3969 (1995).
[31] E. Rosenthal, E. Andrade, C. Arguello, R. Fernandes, L. Xing, X. Wang, C. Jin, A. Millis, and A. Pasupathy, Nat. Phys. **10**, 225 (2014).
[32] Although N is larger at higher temperatures by up to a factor of 2.5 as compared to the lowest temperature, this variation is expected to give a minor increase in Δ at high temperatures ($\leq$ 30% as compared to Δ at the lowest temperature) because of its weak dependence on N given in Eq.(1).
[33] D. Baillie and P. Blakie, Phys. Rev. A **82**, 033605 (2010).
[34] M. Babadi and E. Demler, Phys. Rev. A **86**, 063638 (2012).
[35] Z.-K. Lu, S. Matveenko, and G. Shlyapnikov, Phys. Rev. A **88**, 033625 (2013).
[36] A. Frisch, K. Aikawa, M. Mark, A. Rietzler, J. Schindler, E. Zupanic, R. Grimm, and F. Ferlaino, Phys. Rev. A **85**, 051401 (2012).
[37] A. Frisch, M. Mark, K. Aikawa, F. Ferlaino, J. L. Bohn,

C. Makrides, A. Petrov, and S. Kotochigova, Nature **507**, 475 (2014).

[38] M. Inguscio, W. Ketterle, and C. Salomon, eds., *Ultra-cold Fermi Gases* (IOS Press, Amsterdam, 2008), Proceedings of the International School of Physics "Enrico Fermi", Course CLXIV, Varenna, 20-30 June 2006.

[39] B. DeSalvo, M. Yan, P. Mickelson, Y. M. De Escobar, and T. Killian, Physi. Rev. Lett. **105**, 030402 (2010).

[40] M. K. Tey, S. Stellmer, R. Grimm, and F. Schreck, Phys. Rev. A **82**, 011608 (2010).

[41] J. L. Bohn, M. Cavagnero, and C. Ticknor, New J. Phys. **11**, 055039 (2009).

[42] C. J. Pethick and H. Smith, *Bose-Einstein condensation in dilute gases* (Cambridge University Press, 2002).

[43] S. Ronen and J. L. Bohn, Phys. Rev. A **81**, 033601 (2010).

[44] D. Guéry-Odelin, Phys. Rev. A **66**, 033613 (2002).

[45] C. Menotti, P. Pedri, and S. Stringari, Phys. Rev. Lett. **89**, 250402 (2002).

[46] H. Hu, X.-J. Liu, and M. Modugno, Phys. Rev. A **67**, 063614 (2003).

Chapter

12

Conclusion and outlook

This thesis describes the creation and study of bosonic and fermionic degenerate quantum gases of erbium atoms. It documents setting up the experimental apparatus from a completely empty lab to a fully working experiment. We had to face the challenge of designing an apparatus for an atomic species, which was unknown to quantum gas experiments and not well characterized in its relevant atomic properties. In the planning phase, our greatest concerns included, whether the chosen narrow-line laser-cooling approach using erbium would turn out to work as good as expected, where Feshbach resonances would be located, and whether the lifetime of the atomic sample in the optical dipole trap would be long enough, i. e. not limited by light-assisted collisions or off-resonant absorption. The reported results after the successful demonstration of the narrow-line magneto-optical trap of erbium were beyond our expectations. Not only that this experiment allowed for the first production of degenerate gases of erbium, but also the number of further investigations is vast.

The slow transformation from an idea to a room-filling experiment took place in many small steps, each of which brought us closer to exploring interesting physics. Many more steps will be made using the erbium machine to continue studying ultracold dipolar gases. Some of these steps are under preparation and undertaken right now or will be done in the near future. These further developments will be briefly listed in the following section. Other steps lie in the more distant future and are difficult to predict as they strongly depend on the direction in which the experiment will go. Nevertheless, some of the long term goals for the erbium experiment are presented in Sec. 12.2.

12.1. Further investigations

Weakly-bound molecules   Weakly-bound molecules can be created using the magneto-association technique across by ramping over a Feshbach resonance, see Ref. [Chi10]. This standard technique can also be applied to erbium associating two atoms to a Er_2 molecule. Dependent on how the individual total angular moments of both atoms add up, the molecule can have a magnetic moment of up to about $14\,\mu_B$. The combination of such a large magnetic moment and the large mass of Er_2 makes this system regarding its dipolarity competitive to current experiments using polar heteronuclear molecules, like KRb [Ni08] or RbCs [Tak14].

We have conducted preliminary measurements with ^{168}Er, in which we utilized a Feshbach resonance at $912(1)\,$mG with a width of $39(2)\,$mG to prepare up to 2×10^4 Er$_2$ molecules at a temperature of $300\,$nK and a molecule density of $8 \times 10^{11}\,$cm^{-3}. The simple preparation of weakly-bound molecules is the first step towards experiments with deeply-bound molecules possessing an exceptionally large magnetic dipole moment.

Molecular binding energy The binding energy of a weakly-bound molecule depends on the magnetic field. A sinusoidal modulation of the constant magnetic field in the vicinity of a Feshbach resonance drives a resonant conversion of atoms into a weakly-bound molecule, only if the modulation frequency equals the binding energy of the molecule, see Ref. [Tho05]. This so-called *wiggling technique* is often used to measure the binding energy at different values of the magnetic field. Very close to the Feshbach resonance the binding energy changes quadratically with the magnetic field, whereas further away from the resonance a linear dependence is given, see Sec. 4.3. From the linear dependency the magnetic moment of the molecular state with respect to the magnetic moment of two free atoms can be derived. In the erbium experiment this technique was recently used to measure the magnetic moment of five different molecular states at Feshbach resonances below $2.5\,$G. The values of the magnetic moments range from $\mu = 7.96\,\mu_{\mathrm{B}}$ to $11.8\,\mu_{\mathrm{B}}$, see Ref. [Aik14a]. In the near future wiggling measurements at Feshbach resonances above $3\,$G are important to characterize the spectrum of molecular states in more detail. First theoretical efforts show that in contrast to alkali atoms one single molecular state of lanthanide atoms turns out to posses a magnetic moment, which is a linear combination of magnetic moments of different Zeeman sublevels.

Observation of the roton minimum It has been theoretically shown that a so-called *roton minimum* should emerge in the excitation spectrum of an ultracold Bose gas with short-range two-body interaction. This roton minimum can be observed as a local minimum in a non-trivial energy dispersion relation and is known from condensed matter systems, like superfluid helium, where the roton resembles an elementary excitation of rotation. More recently, the roton spectrum of a quasi-two-dimensional dipolar Bose-Einstein condensate has been theoretically studied in Ref. [San03a]. Dipolar atoms like ^{52}Cr, ^{164}Dy, or ^{168}Er in current experiments are expected to reveal the roton spectrum when the atom cloud is tightly confined in the polarization direction of the dipoles, see Ref. [Bla12]. The roton minimum can then be measured in the ultracold gas using Bragg spectroscopy. We plan to pursue this route towards the roton minimum with erbium atoms in an array of two-dimensional trapping potentials. We will carry out Bragg spectroscopy with both $1064\,$nm and $532\,$nm light, which enables us to measure the excitation spectrum and observe signatures of the roton minimum.

Exotic optical potentials By carefully engineering optical potentials of larger complexity, like honeycomb, triangular, or dimer potentials, it is possible to explore condensed-matter phenomena in a highly flexible way using ultracold atoms. For example, it has been experimentally demonstrated in Ref. [Tar12] that so-called *Dirac points* can be created using a Fermi gas in a honeycomb lattice. As in this experiment the massless electrons of graphene

are mimicked, it is often referred to as artificial graphene. What makes an important difference to experiments in condensed-matter physics is the high degree of tunability in ultracold atomic systems. Adding long-range interactions between atoms in such a honeycomb potential would open the opportunity to study strong correlation effects, which are not accessible in the field of condensed-matter physics. As a first approach we are working on creating a three-dimensional optical lattice using standing waves of 532-nm light in two directions and 1064-nm light in the third direction. This gives a twice as large lattice constant in one direction than in the other two. It is speculated, that in a dipolar system the superfluid to Mott-insulator transition will be modified dependent on the orientation direction of the dipoles with respect to the optical lattice. Theoretical calculations also predict a modification of the Mott lobes by the dipole-dipole interaction, see Ref. [CS10]. We are in close collaboration with the group of P. Zoller from Innsbruck to investigate the parameter range, which will be accessible with this lattice setup in the current erbium experiment.

12.2. Our vision

LiEr molecules From the beginning the erbium experiment has been designed such that lithium can be added as a second species in the distant future. A lithium oven can be mounted between the erbium transversal cooling stage and the atom beam shutter, which will form a combined Er/Li atom beam. The Zeeman slower was designed to operate with both species simultaneously and should allow an efficient loading of an erbium and a lithium magneto-optical trap during a single experimental cycle. After cooling both elements to ultracold temperatures via forced evaporation one can think of many interesting experiments and measurements with such a heteronuclear mixture. For example, three-body bound states, so-called *Efimov states* could be investigated, or a two-species superfluid mixture of fermions could be created. In both cases the extreme mass imbalance between erbium and lithium and the magnetic moment of erbium makes this combination favorable compared to mixtures of alkali atoms. One could further think of associating a lithium and erbium atom to a weakly-bound LiEr molecule via the magneto-association technique. Then, in principle, a STIRAP (Stimulated Raman adiabatic passage) process could transfer the molecule into its ground state, where the two atoms will be strongly bound. This process creates a stable polar molecule with both large magnetic and electric dipole moments. The electric dipole moment is tunable via an external electric field and allows for the full control of the electric dipole-dipole interaction strength. This might open the field of so-called *ultracold chemistry*, which focuses on studying reaction dynamics and was mentioned in Ref. [Hut10]. With the erbium experiment the reaction dynamics between molecules and atoms or molecules and molecules in three or lower dimensions can then be explored. An early experimental study was done by letting KRb molecules collide with K or Rb atoms, respectively, see Ref. [Osp10]. Very recently, it was theoretically found that quantum entanglement plays an important role for activating and driving an ultracold chemical reaction towards its dynamical equilibrium, see Ref. [Ric14].

Spin-orbit coupling Atoms with large magnetic moments are promising to study the physics of spin-orbit (SO) coupling in ultracold gases, which was first demonstrated in a BEC of ru-

bidium atoms, see Ref. [Lin11]. SO coupling, i. e. an interaction between a particle's spin and its angular momentum, is important in condensed-matter systems for elucidating the spin-Hall effect in semi conductors [Kat04], topological insulators [Has10], and Majorana fermions [Sau10]. Furthermore, SO coupling can be accomplished with non-dipolar gases using artificial gauge fields, which have been realized within optical lattices, see Ref. [Aid11]. Dipolar atoms with a large magnetic dipole moment are favorable for these kind of experiments due to their intrinsic SO coupling induced by anisotropic interaction. This manifests itself in expected large dipolar relaxation rates, see Ref. [Nas13].

Topological superfluids   Utilizing strong spin-orbit coupling in a dipolar system one might be able to prepare topological superfluids. They are considered to be exotic states of matter and are of major interest since the discovery of topological insulators and superconductors, see Refs. [Has10, Qi11]. The fascinating thing about topological superfluids is the fact that their fundamental properties can only change if the system passes through a quantum phase transition, i. e. the properties are 'topologically protected'. In Ref. [Nas13] the implementation of a topological superfluid using lanthanide atoms is proposed. Here, the experimental setup consists of a one-dimensional Fermi gas, which is placed in the proximity of a two-dimensional superfluid made of condensed Feshbach molecules. For creating a topological superfluid the Fermi gas has to be trapped in a spin-dependent optical dipole potential, which is difficult to create for fermionic alkali atoms due to large heating rates induced by spontaneous emission. The reason for this heating is because of the small fine-splitting of the excited P-state of alkali atoms in comparison to the large linewidth of the laser-cooling transition. This problem should be overcome by using optical lattices with wavelengths closely tuned to the narrow-line transitions in ^{161}Dy or ^{168}Er, which makes it possible to create strong spin-dependent potentials with small heating rates. According to the proposal, lanthanide atoms should enable the study of topological superfluids. We do not know yet, whether these will be realistic experiments in our setup. However, topological superfluids represent an interesting research direction, which deserve further investigation.

A

Measurement of the natural linewidth of the 401-nm transition

The natural linewidth of the 401-nm transition was measured by absorption imaging of an atomic sample in a magneto-optical trap (MOT) for three different isotopes of erbium. Figure A.1 shows the results of this measurement. A comparison between values of the linewidth found in literature and the result of the present work is found in Table A.1. The temperature of the atomic sample was determined by time-of-flight absorption imaging to be $11.1\,\mu$K for ^{166}Er, $13.9\,\mu$K for ^{168}Er, and $14.6\,\mu$K for ^{170}Er. Typical atom numbers ranged between 1 and 2.5×10^7. Due to the low temperature of the atomic sample the thermal Doppler broadening is as small as 60 kHz. Collisional broadening of the natural linewidth is estimated to be about 52 kHz for a peak number density of $8 \times 10^9\,\mathrm{cm}^{-3}$. Both broadening effects are one order of magnitude smaller than the systematic and statistic error and are thus neglected.
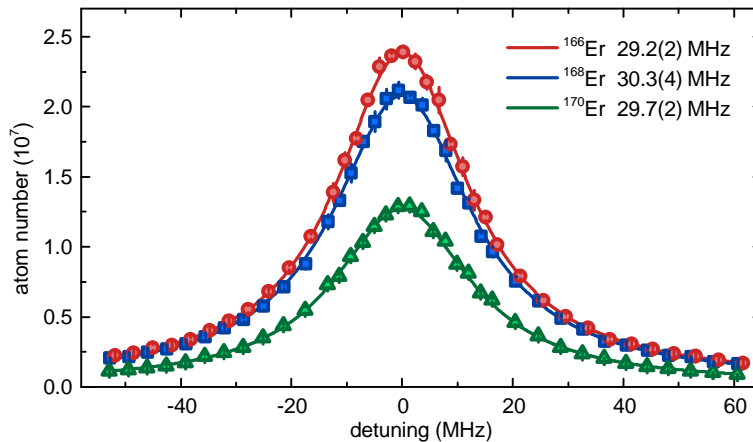
Figure A.1.: Linewidth measurement of the 401-nm transition for three different bosonic isotopes ^{166}Er, ^{168}Er, and ^{170}Er. A Lorentzian fit is applied to the data points and the natural linewidth is given for each isotope with a statistical error. Averaging these three values and considering the systematic error (see text) the value for the natural linewidth is $\Delta\nu = 29.7(6)$ MHz, which is in very good agreement with a lifetime measurement of the excited state in Ref. [Har10].

167

linewidth (MHz)	measurement method	Ref.
27.5(2.8)	lifetime of excited state	[Mar80, Ral11]
35.6(1.2)	laser-induced fluorescence	[McC06a]
29.5(1.5)	lifetime of excited state	[Har10, Law10]
29.7(6)	absorption measurement	this work

Table A.1.: Comparison of natural linewidth measurements of the erbium 401-nm transition using various methods found in literature and the one presented in this work.

After preparing the atomic sample in the MOT absorption imaging was applied using 401-nm laser light with variable detuning from -60 to $+60$ MHz with respect to the atomic transition frequency. Absorption imaging gives a two-dimensional image of the optical density of the atomic cloud. The total atom number is then found by separately integrating the optical density along both image axes, fitting a Gaussian-shaped curve to the one-dimensional density distribution, and integrating this Gaussian fit. The assumption of a Gaussian density distribution is valid for a purely thermal atom cloud, which is the case in the present measurement. This imaging procedure is commonly used as a standard absorption imaging technique.

Deriving the optical density from an absorption image needs knowledge of the detuning of the imaging light and of the natural linewidth of the transition. If the linewidth is unknown, it can be measured by setting the detuning to zero in the calculation of the optical density. Measuring the total atom number dependent on the detuning reveals the natural linewidth, see Fig. A.1. Note, that this method can only be applied if at least a small amount of atoms can be detected, otherwise determining the atom number from the absorption image will not work properly. In spite of this restriction, the measurable range is sufficiently large to apply a Lorentzian fit to the data points and determine the linewidth.

The imaging laser light was detuned using an accusto-optical modulator (AOM) in double-pass configuration. It is driven by a radio frequency produced by a voltage controlled oscillator (VCO). The nonlinearity of the VCO gives a systematic error of the detuning of about 0.6 MHz over the full range of detuning.

Considering this systematic error and measuring the linewidth for three bosonic isotopes, see Fig. A.1, we determine the natural linewidth of the 401-nm transition of erbium to be $\Delta\nu = \frac{\Gamma}{2\pi} = 29.7(6)$ MHz. This agrees with some of the most recent measurements found in literature, see Table A.1.

B

Erbium high-temperature oven

The erbium high-temperature oven[1] creates a roughly collimated atom beam by evaporating solid pieces of erbium. It consists of two separate heating filaments. The first filament heats the erbium source material contained in a tantalum crucible, in the so-called *effusion cell*, and the second filament heats the aperture setup used for collimation in the *hot lip* section. The temperature of both filaments can be independently controlled, but due to heat radiation and heat conduction by the crucible itself, the temperature difference can not be larger than about 250 °C. Usually the temperature of the aperture setup is 100 °C higher than the temperature of the effusion cell to prevent a blockage of the apertures by excessive source material. Typical operating temperatures are 1100 °C for the effusion cell and 1200 °C for the aperture setup.

The heating filaments are made of tantalum wires. The wires are held in place by boron nitride (PBN) ceramic insulator disks. The insulator disks have a thickness of about 2 mm and are very fragile. Furthermore, they support the crucible setup in the center of the oven. Close to each filament a thermoelectric temperature sensor[2] is placed for temperature measurements and stabilization via a PID controller[3]. The controller allows for a temperature stability[4] of about ±0.1 °C. The filaments are connected to two independent power supplies delivering up to a power of 700 W each with a maximum output current of 13 A. According to the manufacturer the maximum achievable temperature of the crucible is 1600 °C. For erbium a temperature of not more than 1500 °C is advisable to prevent melting the source material. The current of the heating filaments should not exceed 3.5 A for the effusion cell and 6.1 A for the hot lip.

To prevent excessive heating of the vacuum chamber, several temperature shields are implemented within the high-temperature oven. First, three layers of tantalum foil provide a passive shielding of heat radiation. Second, an outer tube enclosing the oven provides water cooling. A flow rate of at least 2 l/min must be guaranteed during oven operation. If this is not the case, the power supplies of the oven will be switched off automatically by a

---

[1] dual-filament effusion cell, model DFC-40-10-WK-2B with control unit CU-3504-S2-DC
     from CreaTec Fischer & Co. GmbH
     Effusion cells are commonly used for molecular beam epitaxy systems.
[2] thermocouple type C, usable up to 2300 °C
[3] model 3504, from Invensys Eurotherm Ltd
[4] at temperatures below 500 °C the PID regulator tends to oscillate within ±20 °C
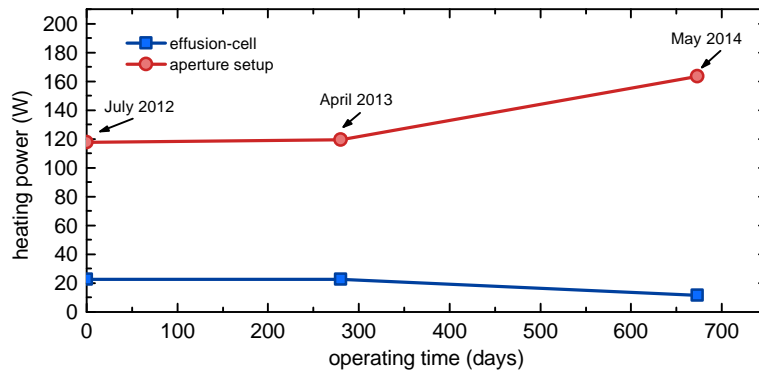
Figure B.1.: Heating power needed for operating the high-temperature oven over the timespan of about two years. The temperature of the effusion cell and aperture setup is $1100\,°C$ and $1200\,°C$, respectively. Lines are shown as a guide to the eye.

water watch dog. Furthermore, the cooling water circuit must not be tightly switched-off to prevent any high pressure from building up, in case the residual cooling water starts to boil and steam needs to escape. This is achieved by a one-way gate valve in the back-flow of the cooling water circuit. Due to the multi-stage temperature shielding the vacuum tube containing the oven usually has a temperature of $40\,°C$ on the outer side. Strong heat radiation in front of the oven, which is not effectively shielded, heats those parts of the vacuum chamber to about $120\,°C$.

The oven must not be operated at pressures larger than $10^{-5}\,mbar$, otherwise the heating filaments can be damaged easily. Temperature ramps for heating and cooling from 5 to $30\,°C/min$ are standard. If the temperature is ramped up too fast, thermal stress can break the ceramic insulators. When the experiment is out of operation, the oven is ramped down to a standby temperature of typically $700\,°C$ for the effusion cell and $800\,°C$ for the hot lip. This increases the lifetime of the source material significantly. Lower standby-temperatures are not advisable, as the crucible might slightly deform over many ramping cycles due to thermal stress. In case of strong deformation, the crucible can't be extracted from the oven easily any more, which might cause some of the ceramic insulator disks to break[5].

The crucible has a total length of $150\,mm$ and an inner diameter of $12\,mm$, see Fig. 3.2 for further dimensions. This corresponds to a volume capacity of $17\,cm^3$. After the aperture inset is mounted inside the crucible, a volume of about $7\,cm^3$ remains for the source material. The crucible is usually filled with up to $10\,g$ of erbium, which turns out to be enough for more than 5200 hours of operation[6] and continuing, at an effusion-cell temperature of $1100\,°C$.

---

[5]   In the case of oven damage, the manufacturer offers a full refurbishment of the oven.

[6]   The source material in the crucible was not yet emptied at the time this thesis was written.
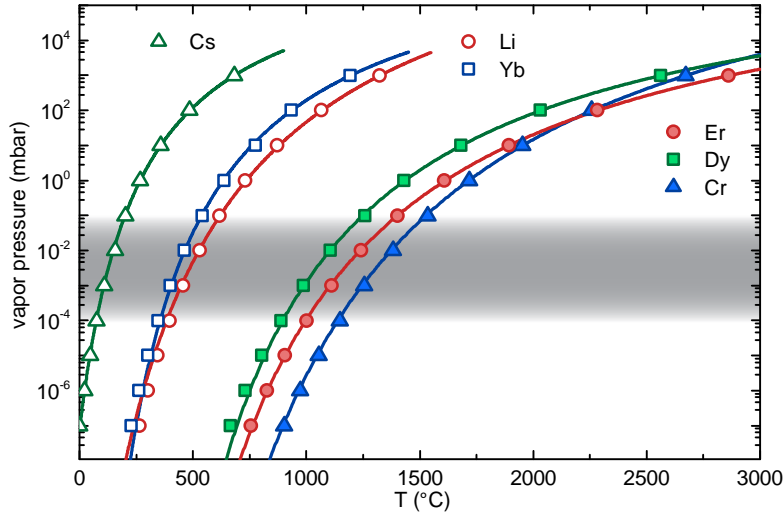
Figure B.2.: Vapor pressure for various elements. Chromium, dysprosium and erbium have a similar vapor pressure and require a high-temperature oven. Cesium is shown for comparison as an element with a low melting point of only 28 °C, whereas lithium and ytterbium have an intermediate vapor pressure. The region of a suitable vapor pressure for ultracold gas experiments is indicated by the gray shaded area.

B.2. Erbium vapor pressure

The high melting point of erbium at a temperature of 1529 °C makes the construction of an oven for evaporating atoms technically difficult. In general, the saturated vapor pressure of an element, p_{vap}, is the figure of merit for choosing a suitable type of oven for the experimental setup. By the precise knowledge of its temperature dependence one can estimate the flux of an atom beam and thus the loading time of the magneto-optical trap in the further experiment, see Chapter 6. The temperature dependence of p_{vap} is accurately described by the Antoine equation

$$p_{\text{vap}}(T) = 10^{A - \frac{B}{C+T}} \ , \qquad \text{B.1}$$

with A, B, and C being empirical material constants without any units. A full set of vapor pressure data for various elements and chemical compounds can be found in Ref. [Gra72]. A nonlinear least-squares fit to the vapor pressure data of erbium using Eq. B.1 gives $A_{\text{Er}} = 7.103(4)$, $B_{\text{Er}} = 12170(20)$, and $C_{\text{Er}} = 100(2)$ for T in units of °C and p in units of mbar. Figure B.2 shows the vapor pressure p_{vap} for a broad selection of elements commonly used in ultracold gas experiments.

Having an expression for p_{vap} we can roughly estimate the atom flux in dependence on the temperature of the oven. For this the longitudinal velocity distribution, f_{em}, of atoms with mass m is calculated from the Maxwell-Boltzmann distribution by

$$f_{\text{em}}(v, T) = \left(\frac{\pi D_{\text{em}}}{2} \right)^2 \frac{p_{\text{vap}}(T)}{k_{\text{B}}T} \left(\frac{m}{2\pi k_{\text{B}}T} \right)^{\frac{3}{2}} v^3 \exp\left(-\frac{mv^2}{2k_{\text{B}}T} \right) \sin^2(\theta_{\text{em}}) \ , \qquad \text{B.2}$$

see also Refs. [Ram05, Chi07]. Here, atoms are assumed to escape the oven through a disk-shaped aperture of diameter D_{em} under a solid angle θ_{em} and k_{B} is the Boltzmann constant.
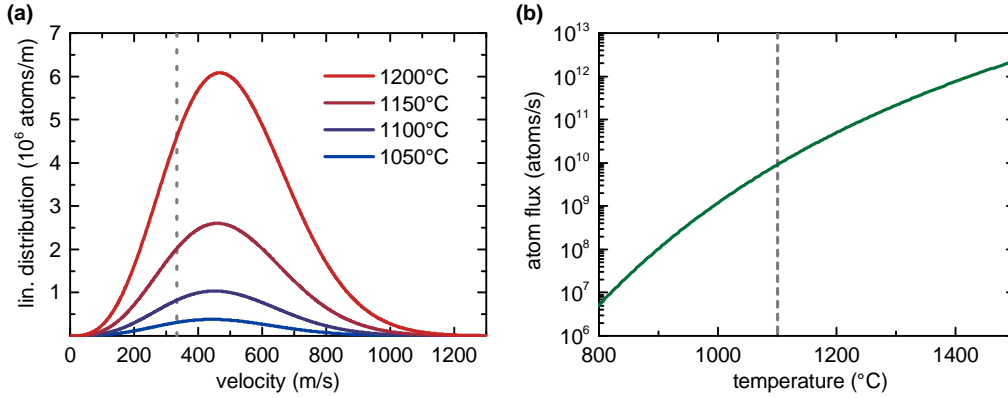
Figure B.3.: (a) Velocity distribution for four different oven temperatures typically used in the experiment. The position of the maximum shifts only a small amount from $443\,\mathrm{m/s}$ for a temperature of $1050\,^{\circ}\mathrm{C}$ to $468\,\mathrm{m/s}$ for $1200\,^{\circ}\mathrm{C}$. The maximum Zeeman slower capture velocity of $400\,\mathrm{m/s}$ is shown as a dotted line. (b) Estimated atom flux into the main chamber for an oven aperture with $D_{\mathrm{em}} = 3\,\mathrm{mm}$, $\theta_{\mathrm{em}} = 0.03$, and a Zeeman slower capture velocity of $400\,\mathrm{m/s}$. A typical oven temperature of $1100\,^{\circ}\mathrm{C}$ is highlighted by the dashed line.

The velocity distribution has its maximum located at $v_{\mathrm{max}} = \sqrt{\frac{3k_{\mathrm{B}}T}{m}} \approx 450\,\mathrm{m/s}$ for a typical temperature of $1100\,^{\circ}\mathrm{C}$ in the case of erbium, see Fig. B.3(a). By integrating f_{em} up to the Zeeman slower capture velocity, v_c, the atom flux, Φ, which will be available after the Zeeman slower, can be estimated as

$$\Phi(T) = \int\limits_{0}^{v_c} f_{\mathrm{em}}(v, T)dv \propto \frac{p_{\mathrm{vap}}(T)}{\sqrt{T}} \ . \tag{B.3}$$

Figure B.3(b) shows the atom flux into the main chamber, which increases more than five orders of magnitude when the oven temperature is raised from $800\,^{\circ}\mathrm{C}$ to $1400\,^{\circ}\mathrm{C}$.

B.3. Oven refilling procedure

A depletion of the source material in the erbium oven can be detected easily by a rapid decrease of the atom number in the magneto-optical trap (MOT) within the timespan of a few days. During this time, the MOT loading rate shows the following characteristic signature. After reaching operational temperature of the oven, the atom number in the MOT first seems to be as usual but after one to two hours of operation it drops significantly to less than half of its original value. Furthermore, the fluorescence of erbium atoms in the transversal cooling section gets weaker. In such a case the oven crucible has to be refilled. The refilling procedure is described in the following and takes at least ten days until the experiment can be continued.

Erbium source material can be purchased in various shapes from different suppliers[7]. We have made good experiences with erbium pieces, which are distilled dendritic, although the

---

[7] usually $25\,\mathrm{g}$ of $99.9\,\%$ pure erbium, distilled dendritic, purchased from Alfa Aesar
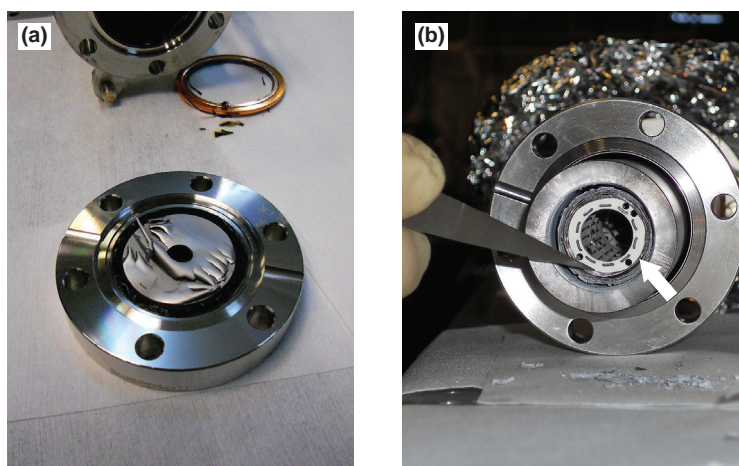
Figure B.4.: Cleaning the high-temperature oven from old source material. (a) A thin erbium foil is deposited on the aperture before the transversal cooling section. Peeling off foils under air can lead to a spontaneous ignition of the erbium foil. (b) Heating filaments are kept in place by ceramic spacers (arrow). After a long time of operation the degraded heat shield of the oven has to be cleaned to avoid direct contact with the crucible.

price per gram is twice as large as compared to normal pieces. Dendritic pieces have the advantage that they can be easily cut into smaller pieces fitting better into the crucible. Normal, solid pieces of erbium would need much rougher handling.

Refilling the high-temperature oven consists of two major tasks. First, the oven has to be dismounted from the vacuum chamber and old source material has to be removed. In case of a damage of the oven, it has to be repaired or even replaced. Because of excessive erbium material deposited in the aperture setup, the crucible can usually not be dismounted. A new crucible setup has to be ordered and prepared beforehand. Then follows the second task, which consists of filling the crucible with new source material, mounting the oven, and restoring the vacuum again.

Removing old source material

This task includes flooding the oven chamber with argon gas, dismounting the oven from the vacuum chamber, removing the crucible, and cleaning the crucible and oven. The task will be presented in the following steps.

1. Tightly close the gate valve between the UHV section and the oven section.
2. Switch off the oven power supply and close the cooling water cycle.
3. Prepare a needle valve with a pressure monitor mounted on a CF40 T-piece for flooding the oven chamber with argon gas. A simple latex glove acting as a balloon suits perfectly as a pressure monitor.
4. Mount the T-piece to the angled valve of the oven chamber.
5. Connect a scroll pump to the third flange of the T-piece.

6. Clean the T-piece by repeatedly pumping off and slowly flooding with argon through the needle valve.

7. Disconnect the pumping station and close the T-piece with a blind flange.

8. Switch off the ion getter pump and pressure gauge mounted on the high vacuum part of the vacuum chamber.

9. Carefully open the angled valve, while keeping the T-piece filled with argon at a pressure slightly above ambient pressure. The glove should always be filled like a small balloon.

10. As the angled valve is *very slowly* opened, adjust the needle valve to keep the T-piece and the balloon slightly over-pressurized at all times.

11. When the oven chamber is fully flooded with argon, the high-temperature oven can be unmounted between the CF40 port aligner and the oven vacuum tube. Remove also the port aligner and the additional aperture disk from the transversal cooling vacuum chamber. Close the transversal cooling section with a CF40 blind flange again to prevent argon gas from leaking out.

12. During operation of the oven thin foils of erbium are deposited inside the port aligner, see Fig. B.4. Take care as they can spontaneously ignite and burn when brought from the inert argon atmosphere into air. *DO NOT* put burning pieces of erbium into water! Erbium produces hydrogen gas when put in water! Erbium foil and other small pieces can be safely contained in paraffin oil, which reduces the risk of ignition.

13. Clean the aperture and the port aligner from deposited erbium material.

14. Carefully take out the crucible from the oven tube. Due to slight expansion of the crucible it might get stuck easily. Try to carefully rotate the crucible setup before pulling it out slowly.

15. Inspect the ceramic isolators inside the oven. They might easily break during handling of the crucible. If the heating filaments can not be kept safely in place anymore, the oven has to be refurbished by the manufacturer.

16. Try to disassemble the crucible. Erbium deposited in the aperture setup makes this step difficult or even impossible. If it can not be disassembled a new crucible setup has to be used for refilling.

17. Make sure the oven is clean. Remove any loose pieces of the heat shield as it might get dissolved at high temperatures over longer times, see Fig. B.4(b).

Filling with new source material

Filling the oven is done in the following steps including preparing erbium pieces, assembling the crucible setup, mounting the oven on the vacuum chamber, and pumping off the oven chamber.

1. An accurate scale is needed to measure the amount of erbium filled into the crucible. Properly clean all tools needed with isopropyl alcohol before continuing.

2. Prepare all necessary parts for the crucible setup. Clean the parts in an ultrasonic
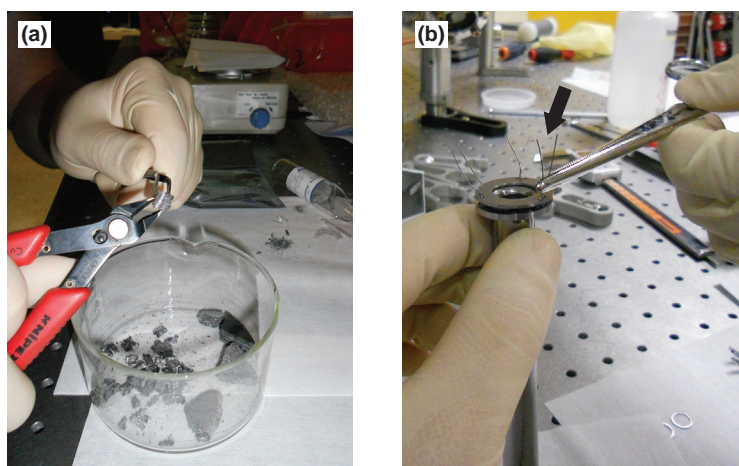
Figure B.5.: Refilling the crucible with source material. (a) Preparing small pieces of erbium. Distilled dendritic pieces of erbium can be easily cut using cutting pliers. (b) The crucible setup is assembled. Tantalum wires (arrow) fix the aperture setup on the crucible tube.

    bath, first using acetone, then isopropyl alcohol, about 15 min each is sufficient.

3. Dendritic erbium is usually shipped in 5 mm thick disks. Remove small pieces from the disk using cutting pliers, see Fig. B.5(a). The pieces should not be larger than 5 mm to easily fit into the crucible.

4. Fill about 10 g of erbium pieces into the crucible. Slightly compress the erbium pieces to the back part of the crucible by tapping the crucible carefully on the table.

5. Assemble the crucible setup according to the oven's manual, see also Fig. B.5(b).

6. Slide the crucible setup into the oven and ensure a snug fit.

7. First mount the additional aperture and the port aligner on the transversal cooling vacuum chamber.

8. Mount the oven onto the port aligner on the vacuum chamber.

9. Start pumping off the vacuum chamber.

10. After reaching less than 10^{-7} mbar switch on the ion getter pumps of the oven chamber.

11. Switch on the oven power supply and cooling water.

12. When the pressure is below 10^{-8} mbar the oven can be heated slowly up to 200 °C using a ramp of 10 °C/min.

13. Observe the vacuum pressure during the heat up. When the pressure again drops below 10^{-7} mbar, continue heating up the oven to standby temperature in steps of 100 °C.

14. Heat the oven to operating temperature and try to observe a fluorescence signal in the transversal cooling stage using the TC laser light.

15. Ramp the oven back to room temperature and switch it off.

16. Flash the titanium sublimation pump in the oven chamber for 180 s with 42 A.

17. If the total pressure reaches less than 10^{-8} mbar, close the angled valve, switch off the pumping station. Disconnect the pumping station.

18. Open the gate valve between the UHV section and the oven section.

19. Continue with the experiment.

Note, that no extra baking of the oven vacuum chamber is necessary to achieve a pressure suitable for the experiment due to the getter properties of erbium, see Ref. [Mül72]. After a few heat-up cycles of the oven to operating temperatures the pressure should be low enough for continuing with the experiment. Typical values for the total pressure are 6×10^{-9} mbar when the oven is at room temperature and 2×10^{-8} mbar when it is at an operating temperature of $1100\,°C$ one day after the refilling has been completed. The pressure at high temperature of the oven should drop to a value of 1×10^{-9} mbar after some days of operation and the experiment can be continued.

C
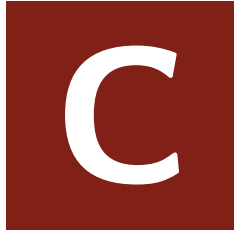
Notes on the blue master laser system

The blue laser system, which is presented in Sec. 3.5.1, ultimately relies on the stable operation of the blue master laser[1]. Its working principle and the most important operating parameters will be described in the following. For further details, please refer to the guidelines and datasheets provided by the manufacturer.

The master laser works as follows. It amplifies the light coming from a diode laser by a tapered amplifier (TA) and then doubles its frequency by second harmonic generation (SHG). The diode laser comprises of an external-cavity diode laser (ECDL), which operates at 802 nm and delivers about 44 mW output power. The laser-diode current is actively stabilized by a PID control loop to 92 mA and the temperature is set to 22.3 °C. About 10 mW of the laser power exits the system at this point and is used for monitoring on a wavelength meter[2] as reference. The remaining power is then amplified by the TA to about 635 mW. The TA-chip is usually operated with a current of 1780 mA at a temperature of 20.3 °C. After passing some mode-matching lenses the light enters the SHG cavity, which is locked to the wavelength of the master laser using the Pound-Drever-Hall (PDH) technique. The required sidebands for this locking technique are generated by modulating the laser-diode current with a radio-frequency signal at a frequency of about 20 MHz.

The laser light frequency is doubled in the SHG cavity by a non-linear crystal. The temperature of the crystal has to be precisely controlled to 39.4 °C for optimal phase matching between the fundamental light and the frequency-doubled light. The temperature is chosen high to prevent dust from sticking to the surfaces of the crystal. The maximum doubling efficiency is about 33 %. In this setup a lithium triborate (LBO) crystal is used for frequency-doubling. An early version of this SHG cavity suffered from strong degradation of the crystal due to large light intensities over a timespan of a few weeks. The output power dropped by about 25 % within one week. Shifting the crystal by a few 10 μm recovered the doubling efficiency. This optimization had to be done every few weeks. Finally, the doubling cavity was refurbished by the manufacturer and the crystal was replaced. The new cavity shows a loss of output power of less than 1 % over the timespan of a week. After the frequency-doubling

---

[1] TA-SHG-pro system, from Toptica Photonics AG
[2] model WS7-R MC, from HighFinesse GmbH

stage a total of 209 mW of light at 401 nm is available at optimum conditions in the new setup. An output power of at least 80 mW is necessary for the experiment.

D

Feshbach resonances data tables of bosonic erbium

The Feshbach resonance positions, B_{res}, and widths, Δ, are determined from high-resolution Feshbach spectroscopy as described in Chapter 10. For convenience, the loss features are reported in ascending order with respect to their positions and labeled with index i. The error in brackets gives one standard deviation. Δ is determined either from a Gaussian fit as the half-width at $1/e^2$ (method G) or by measuring the zero crossing of the resonance, B_{zero}, being $\Delta = |B_{\mathrm{res}} - B_{\mathrm{zero}}|$ (method Z). Feshbach resonance data for isotope ^{168}Er can be found in Table D.1 and for isotope ^{166}Er in Table D.2.

Table D.1.: Feshbach resonance data for isotope [168]Er.

i	B_{res} (G)	Δ (mG)	meth.	i	B_{res} (G)	Δ (mG)	meth.	i	B_{res} (G)	Δ (mG)	meth.
1	0.912(1)	39(2)	Z	65	28.643(1)	21(3)	G	129	49.735(1)	31(1)	Z
2	2.167(1)	36(1)	Z	66	28.737(1)	19(1)	G	130	50.019(1)	15(3)	G
3	2.436(3)	14(9)	G	67	29.233(1)	17(1)	G	131	50.113(1)	104(4)	Z
4	2.476(1)	153(6)	G	68	29.448(1)	32(2)	Z	132	50.325(1)	18(2)	G
5	2.838(9)	16(2)	G	69	29.797(1)	25(2)	Z	133	50.788(1)	15(2)	G
6	3.778(1)	22(2)	G	70	30.057(1)	26(2)	G	134	51.624(1)	15(1)	G
7	4.481(1)	23(2)	G	71	30.541(1)	15(1)	Z	135	51.651(1)	12(2)	G
8	6.558(1)	29(5)	G	72	31.369(1)	19(2)	G	136	52.110(1)	18(1)	G
9	6.594(1)	22(9)	G	73	31.602(1)	18(1)	G	137	52.552(2)	66(3)	Z
10	6.674(5)	217(10)	Z	74	31.903(1)	16(2)	G	138	52.835(1)	14(1)	G
11	7.048(5)	343(8)	Z	75	32.243(1)	25(2)	Z	139	53.082(1)	13(2)	G
12	7.725(1)	15(2)	G	76	32.556(1)	25(2)	G	140	53.195(1)	33(5)	G
13	8.549(7)	900(16)	Z	77	32.753(2)	283(5)	Z	141	53.245(1)	14(3)	G
14	8.909(1)	18(2)	G	78	33.245(1)	17(1)	G	142	53.299(1)	33(4)	Z
15	9.311(1)	13(2)	G	79	33.703(1)	21(1)	G	143	53.738(1)	31(3)	G
16	9.946(1)	18(2)	G	80	33.903(1)	61(2)	Z	144	53.925(1)	19(1)	G
17	11.004(1)	17(1)	G	81	34.206(1)	13(1)	G	145	54.272(2)	20(5)	Z
18	11.274(1)	17(1)	G	82	34.340(1)	21(1)	G	146	54.404(1)	12(1)	G
19	11.329(1)	11(1)	G	83	34.647(1)	16(1)	G	147	54.763(4)	57(4)	Z
20	11.807(1)	22(1)	G	84	34.939(1)	53(1)	Z	148	55.035(1)	18(2)	G
21	11.913(1)	18(1)	G	85	35.524(1)	17(2)	Z	149	55.239(1)	18(3)	G
22	12.250(1)	18(1)	G	86	35.713(1)	45(1)	Z	150	55.692(1)	300	G
23	12.873(1)	11(1)	G	87	35.836(1)	15(1)	G	151	56.314(1)	109(3)	Z
24	13.029(1)	15(1)	G	88	36.148(1)	132(4)	Z	152	56.436(1)	15(3)	G
25	13.968(1)	16(1)	G	89	36.399(1)	13(3)	G	153	57.06(2)	3531	Z
26	14.614(1)	20(1)	G	90	37.015(1)	83(1)	Z	154	57.612	89(1)	Z
27	14.711(1)	14(1)	G	91	37.105(1)	4(1)	G	155	58.167(2)	13(2)	Z
28	15.126(1)	14(1)	G	92	37.137(1)	17(2)	G	156	58.426(1)	14(2)	G
29	15.336(1)	19(1)	G	93	37.198(1)	54(2)	Z	157	58.528(1)	7(1)	Z
30	15.851(1)	11(1)	G	94	37.856(1)	178(24)	G	158	58.795(2)	27(4)	Z
31	17.180(1)	23(1)	G	95	37.944(1)	152(1)	Z	159	59.078(1)	55(2)	Z
32	17.450(1)	21(2)	G	96	38.362(1)	17(2)	G	160	59.609(1)	16(2)	G
33	17.808(3)	207(4)	Z	97	38.416(1)	18(2)	G	161	59.875(3)	85(10)	Z
34	18.229(1)	18(1)	G	98	38.728(1)	19(2)	G	162	60.585(1)	51(3)	G
35	18.566(1)	19(2)	G	99	38.895(1)	23(2)	G	163	60.646(1)	8(2)	G
36	18.948(1)	20(1)	G	100	39.075(1)	16(1)	G	164	61.241(1)	22(1)	G
37	19.258(1)	21(2)	G	101	39.458(1)	16(3)	G	165	61.759(1)	13(1)	G
38	19.469(1)	145(1)	Z	102	39.739(8)	1722	Z	166	62.271(1)	15(1)	G
39	19.66(1)	171(13)	Z	103	39.919(1)	16(3)	G	167	62.510(1)	52(3)	Z
40	20.138(1)	16(1)	G	104	40.252(6)	202(7)	Z	168	63.174(1)	9(2)	Z
41	20.627(1)	18(2)	G	105	40.772(2)	106(4)	Z	169	63.367(1)	6(2)	G
42	20.884(1)	20(2)	G	106	40.901(1)	17(2)	G	170	63.398(1)	18(3)	Z
43	20.965(1)	25(2)	Z	107	42.429(1)	20(1)	G	171	63.727(1)	17(3)	G
44	21.588(1)	47(2)	Z	108	43.019(1)	20(2)	G	172	63.985(3)	348(7)	Z
45	21.934(1)	43(2)	Z	109	43.078(1)	13(1)	G	173	64.374(4)	76(5)	Z
46	22.146(1)	16(1)	G	110	43.969(1)	23(1)	Z	174	64.522(1)	16(1)	G
47	22.34(1)	190(13)	Z	111	44.404(1)	44(4)	Z	175	64.889(1)	17(1)	G
48	22.960(1)	159(2)	Z	112	44.731(1)	109(7)	Z	176	64.985(1)	20(1)	G
49	23.224(1)	21(1)	G	113	44.823(1)	18(2)	G	177	65.302(1)	37(1)	Z
50	23.413(1)	21(2)	G	114	45.165(1)	27(4)	G	178	65.671(1)	33(3)	Z
51	23.953(1)	67(3)	Z	115	45.571(1)	156(8)	Z	179	65.989(1)	46(2)	Z
52	24.40(2)	48(15)	Z	116	45.772(1)	19(3)	G	180	66.401(1)	58(2)	Z
53	24.549(1)	73(3)	Z	117	45.851(1)	88(4)	Z	181	66.475(1)	51(1)	Z
54	24.649(1)	14(3)	G	118	46.343(1)	89(3)	Z	182	66.790(1)	118(3)	Z
55	24.908(2)	100(5)	Z	119	46.815(1)	20(2)	G	183	67.103(1)	497	Z
56	25.117(1)	42(3)	Z	120	46.900(1)	12(3)	G	184	67.354(1)	18(2)	G
57	25.265(1)	17(2)	G	121	47.284(3)	58(10)	G	185	67.767(1)	12(1)	G
58	25.925(1)	26(3)	G	122	47.485(7)	1193	Z	186	68.240(1)	113(3)	Z
59	26.202(1)	12(1)	G	123	48.035(1)	141(7)	Z	187	68.810(1)	26(1)	Z
60	26.534(1)	19(1)	G	124	48.082(1)	7(2)	G	188	68.895(1)	16(4)	G
61	26.877(1)	99(4)	Z	125	48.207(1)	21(2)	G	189	69.046(1)	347(3)	Z
62	27.098(1)	18(1)	G	126	48.473(1)	98(3)	Z	190	69.727(1)	19(2)	G
63	27.447(1)	20(1)	G	127	48.842(2)	138(5)	Z				
64	28.070(1)	23(1)	G	128	49.251(1)	14(2)	G				

Table D.2.: Feshbach resonance data for isotope ^{166}Er. Four loss features, at positions $121\,\mathrm{mG}$, $244\,\mathrm{mG}$, $366\,\mathrm{mG}$, and $490\,\mathrm{mG}$, which have been reported in the extended data of Ref. [Fri14], have been caused by a technical problem and are not due to Feshbach resonances.

i	B_res (G)	Δ (mG)	meth.	i	B_res (G)	Δ (mG)	meth.	i	B_res (G)	Δ (mG)	meth.
1	3.056(2)	124(4)	Z	63	31.683(1)	33(2)	G	125	50.119(1)	56(10)	G
2	4.012(5)	23(1)	G	64	32.106(1)	16(2)	G	126	50.249(1)	24(4)	G
3	4.955(1)	9(2)	G	65	32.145(1)	13(2)	G	127	50.32(1)	483(30)	G
4	6.546(1)	38(2)	Z	66	32.656(1)	17(2)	G	128	51.321(1)	65(3)	G
5	6.768(1)	23(2)	G	67	32.909(1)	14(2)	G	129	51.684(1)	48(3)	Z
6	6.884(1)	26(2)	G	68	33.166(1)	13(2)	G	130	52.04(1)	161(11)	Z
7	8.053(1)	29(2)	G	69	34.309(1)	15(1)	Z	131	52.395(1)	27(4)	G
8	8.553(1)	20(2)	G	70	34.408(1)	77(4)	Z	132	52.435(1)	76(2)	Z
9	9.910(1)	47(5)	Z	71	34.734(1)	19(1)	G	133	52.795(1)	235(15)	G
10	10.228(3)	116(6)	Z	72	34.824(1)	13(1)	G	134	53.114(2)	55(5)	Z
11	11.108(1)	52(6)	Z	73	35.345(1)	15(1)	G	135	53.267(1)	19(1)	G
12	11.623(1)	27(1)	Z	74	35.463(1)	18(1)	G	136	53.863(4)	88(10)	G
13	12.978(1)	14(2)	G	75	35.784(1)	14(1)	G	137	54.207(2)	101(5)	Z
14	13.278(1)	34(1)	Z	76	36.006(1)	18(1)	G	138	54.488(1)	19(2)	G
15	13.426(2)	92(7)	Z	77	36.876(1)	14(2)	G	139	54.932(1)	17(1)	G
16	13.686(1)	16(2)	G	78	37.077(1)	49(5)	Z	140	55.263(1)	17(2)	G
17	14.177(1)	19(2)	G	79	37.253(1)	17(2)	Z	141	55.431(1)	35(2)	Z
18	14.801(1)	17(2)	G	80	37.662(1)	45(3)	Z	142	55.974(1)	131(13)	G
19	14.835(1)	13(1)	G	81	38.048(1)	23(1)	G	143	56.062(1)	144(33)	G
20	15.077(1)	18(2)	G	82	38.145(1)	190(5)	Z	144	56.456(1)	149(4)	Z
21	15.371(1)	70(2)	Z	83	38.573(1)	39(3)	Z	145	56.668(1)	121(3)	Z
22	15.726(1)	68(2)	Z	84	38.788(1)	12(2)	G	146	56.740(3)	4(4)	Z
23	16.107(1)	19(2)	G	85	38.888(1)	84(5)	Z	147	56.768(1)	29(3)	G
24	16.187(1)	38(2)	Z	86	39.354(1)	11(2)	Z	148	57.556(1)	15(1)	G
25	17.053(1)	25(2)	G	87	39.563(2)	52(2)	Z	149	57.753(1)	21(1)	G
26	17.977(1)	17(3)	G	88	39.652(1)	110(5)	Z	150	57.978(1)	33(2)	G
27	18.961(1)	20(3)	G	89	40.099(1)	13(1)	G	151	58.135(1)	19(2)	G
28	19.152(1)	22(1)	G	90	40.459(1)	87(4)	Z	152	58.239(1)	31(2)	G
29	19.239	20(1)	G	91	41.649(1)	27(1)	Z	153	58.987(1)	13(1)	G
30	19.543(1)	21(3)	Z	92	41.756(1)	36(2)	Z	154	59.179(1)	18(1)	G
31	19.82(1)	158(12)	Z	93	41.926(1)	17(2)	G	155	59.718(2)	77(6)	G
32	20.539(4)	417(18)	G	94	42.003(1)	18(3)	G	156	59.890(1)	21(1)	G
33	21.047(2)	63(8)	Z	95	42.040(1)	14(1)	G	157	60.111(2)	97(7)	G
34	21.803(1)	21(2)	G	96	42.229(7)	473(29)	G	158	60.637(1)	45(2)	G
35	21.922(1)	22(2)	G	97	42.817(1)	53(4)	Z	159	61.104(1)	24(2)	G
36	22.068(1)	50(5)	Z	98	42.906(1)	19	G	160	61.522(1)	8(1)	G
37	22.350(1)	27(2)	G	99	43.146(1)	14(1)	G	161	61.667(1)	33(2)	Z
38	23.055(1)	17(2)	G	100	43.273(1)	14(1)	G	162	61.829(1)	53(5)	Z
39	23.345(1)	19(2)	Z	101	43.716(1)	26(1)	Z	163	62.348(3)	156(12)	G
40	23.585(1)	72(3)	G	102	43.844(1)	47(1)	Z	164	62.600(2)	97(33)	G
41	23.725(1)	15(4)	G	103	43.922(1)	23(1)	G	165	62.804(1)	16(2)	Z
42	23.898(1)	15(2)	G	104	44.436(1)	16(1)	G	166	63.126(1)	16(1)	G
43	24.272(1)	12(1)	G	105	44.589(1)	19(6)	G	167	63.500(1)	5(1)	Z
44	24.924(1)	14(2)	G	106	44.737(1)	12(1)	G	168	63.524(1)	21(1)	G
45	25.272(1)	19(1)	G	107	44.961(1)	15(1)	G	169	64.078(1)	18(1)	G
46	26.036(1)	17(1)	G	108	45.111(1)	20(2)	G	170	64.535(1)	17(2)	G
47	26.206(1)	13(2)	G	109	45.168(1)	40(2)	Z	171	65.089(1)	5(2)	G
48	26.621(1)	10(2)	G	110	45.405(1)	16(1)	G	172	65.334(1)	16(1)	G
49	26.915(1)	19(1)	G	111	45.850(1)	29(1)	Z	173	66.287(1)	14(2)	G
50	27.324(1)	30(1)	Z	112	45.989(1)	22(1)	G	174	66.375(1)	18(1)	G
51	27.681(1)	23(1)	G	113	46.359(2)	63(7)	G	175	66.898(1)	12(1)	G
52	28.488(1)	31(1)	Z	114	46.664(4)	311(5)	Z	176	67.186(1)	15(1)	G
53	28.726(1)	25(1)	Z	115	46.803(1)	10(4)	G	177	67.333(1)	20(2)	Z
54	29.024(1)	14(1)	G	116	47.282(1)	16(2)	G	178	67.519(2)	72(6)	G
55	29.357(1)	25(1)	Z	117	47.478(8)	366(36)	G	179	67.776(1)	6(3)	Z
56	29.515(1)	16(1)	G	118	47.851(1)	27	G	180	68.243(1)	38(4)	G
57	30.023(1)	44(2)	Z	119	47.962(6)	238(23)	G	181	68.426(1)	17(1)	G
58	30.319(1)	21(2)	G	120	48.873(1)	17(1)	G	182	68.642(1)	13(1)	G
59	30.508(1)	31(1)	Z	121	49.384(1)	90(3)	Z	183	68.875(1)	16(1)	G
60	30.703(1)	16(4)	G	122	49.676(2)	105(4)	Z	184	69.200(1)	35(2)	G
61	30.810(2)	154(4)	Z	123	49.793(1)	15(3)	G	185	69.728(2)	97(5)	G
62	31.220(2)	95(10)	G	124	50.072(1)	90(4)	G				

E

Full level diagram of erbium

Figure E.1 shows all known energy levels of neutral erbium (ErI) according to Ref. [Ral11], which uses [Mar78] as a primary data source. In total, 312 states with odd and 358 states with even parity are known up-to-date. Transition energies range from $5035.1\,\mathrm{cm}^{-1}$ to $46{,}970.8\,\mathrm{cm}^{-1}$ from the ground state. The ionization energy of erbium is, according to Refs. [Wor78, Mar78],

$$E = 49{,}262(5)\,\mathrm{cm}^{-1} = 6.1078(6)\,\mathrm{eV} \approx 203\,\mathrm{nm}\ . \qquad \mathrm{E.1}$$
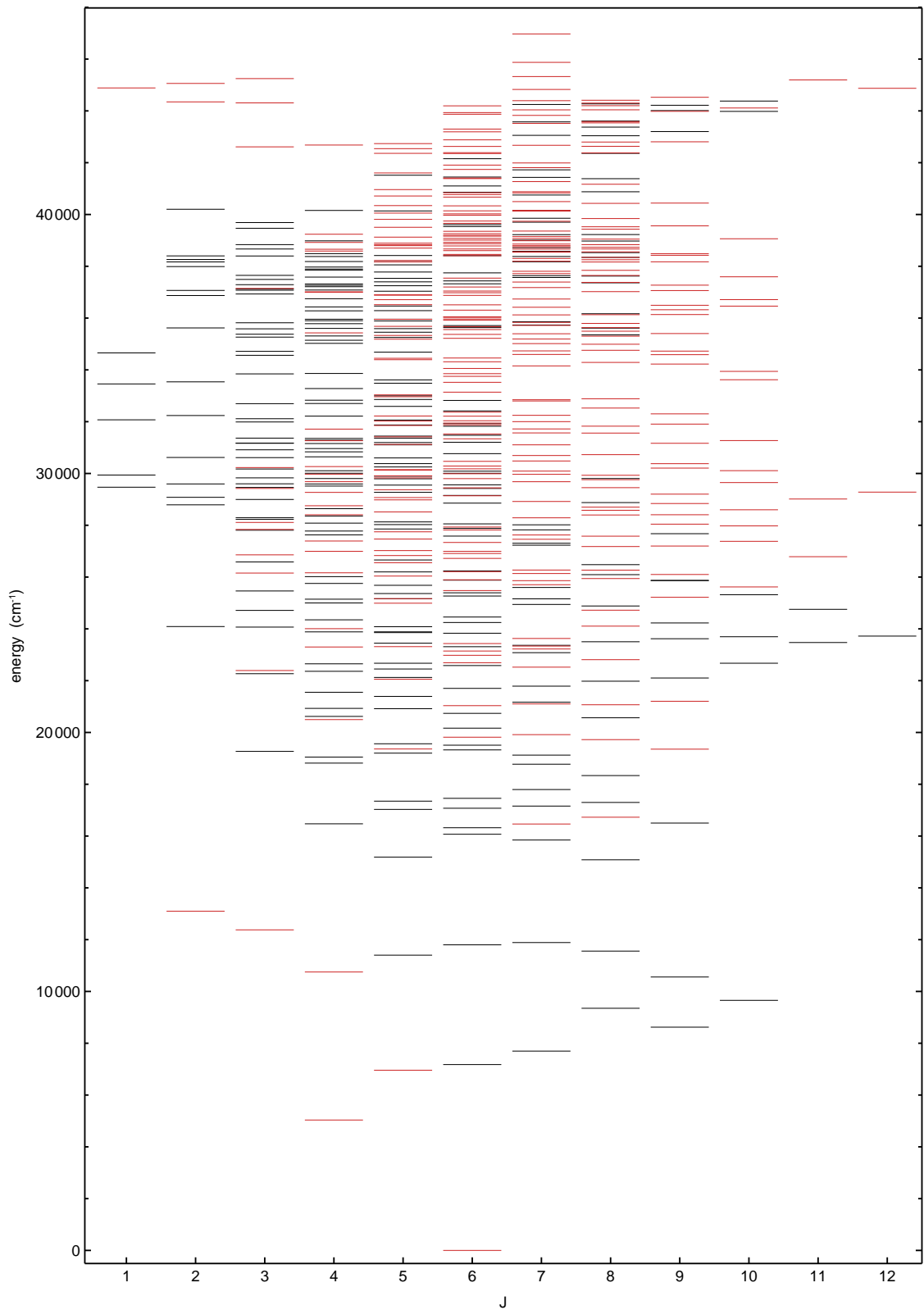
Figure E.1.: Full energy spectrum of erbium. Levels have a total angular momentum quantum number J ranging from one to twelve. States with even (odd) parity are shown in red (black). The data is taken from Ref. [Ral11].

Bibliography

[Aid11]   M. Aidelsburger, M. Atala, S. Nascimbène, S. Trotzky, Y.-A. Chen, and I. Bloch, *Experimental realization of strong effective magnetic fields in an optical lattice*, Phys. Rev. Lett. **107**, 255301 (2011).

[Aik12]   K. Aikawa, A. Frisch, M. Mark, S. Baier, A. Rietzler, R. Grimm, and F. Ferlaino, *Bose-Einstein condensation of erbium*, Phys. Rev. Lett. **108**, 210401 (2012).

[Aik14a] K. Aikawa et al., *Ultracold polar molecules near atomic threshold*, (2014), in preparation.

[Aik14b] K. Aikawa, A. Frisch, M. Mark, S. Baier, R. Grimm, J. L. Bohn, D. S. Jin, G. M. Bruun, and F. Ferlaino, *Anisotropic relaxation dynamics in a dipolar Fermi gas driven out of equilibrium*, ArXiv e-prints 1405.1537 (2014).

[Alt95]   H. Alt, H. D. Gräf, H. L. Harney, R. Hofferbert, H. Lengeler, A. Richter, P. Schardt, and H. A. Weidenmüller, *Gaussian orthogonal ensemble statistics in a microwave stadium billiard with chaotic dynamics: Porter-Thomas distribution and algebraic decay of time correlations*, Phys. Rev. Lett. **74**, 62 (1995).

[And95]   M. H. Anderson, J. R. Ensher, M. R. Matthews, C. E. Wieman, and E. A. Cornell, *Observation of Bose-Einstein condensation in a dilute atomic vapor*, Science **269**, 198 (1995).

[Ast08]   G. E. Astrakharchik and Y. E. Lozovik, *Super-Tonks-Girardeau regime in trapped one-dimensional dipolar gases*, Phys. Rev. A **77**, 013404 (2008).

[Bai12a] S. Baier, *An optical dipole trap for erbium with tunable geometry*, Master's thesis, Faculty of Mathematics, Computer Science and Physics; University of Innsbruck (2012).

[Bai12b] D. Baillie and P. B. Blakie, *Magnetostriction and exchange effects in trapped dipolar Bose and Fermi gases*, Phys. Rev. A **86**, 023605 (2012).

[Ban05]   H. Ban, M. Jacka, J. Hanssen, J. Reader, and J. McClelland, *Laser cooling transitions in atomic erbium*, Opt. Express **13**, 3185 (2005).

[Bar90]   B. Barbieri, N. Beverini, and A. Sasso, *Optogalvanic spectroscopy*, Rev. Mod. Phys. **62**, 603 (1990).

[Bar02a]   M. Baranov, Ł. Dobrek, K. Góral, L. Santos, and M. Lewenstein, *Ultracold dipolar gases - a challenge for experiments and theory*, Physica Scripta **2002**, 74 (2002).

[Bar02b]   M. A. Baranov, M. S. Marénko, V. S. Rychkov, and G. V. Shlyapnikov, *Superfluid pairing in a polarized dipolar Fermi gas*, Phys. Rev. A **66**, 013606 (2002).

[Bar04]   M. Bartenstein, A. Altmeyer, S. Riedl, S. Jochim, C. Chin, J. H. Denschlag, and R. Grimm, *Crossover from a molecular Bose-Einstein condensate to a degenerate Fermi gas*, Phys. Rev. Lett. **92**, 120401 (2004).

[Bar08]   M. Baranov, *Theoretical progress in many-body physics with ultracold dipolar gases*, Physics Reports **464**, 71 (2008).

[Bar14]   J. F. Barry, D. J. McCarron, E. B. Norrgard, M. H. Steinecker, and D. DeMille, *Magneto-optical trapping of a diatomic molecule*, Nature **512**, 286 (2014).

[Bau14]   K. Baumann, N. Q. Burdick, M. Lu, and B. L. Lev, *Observation of low-field Fano-Feshbach resonances in ultracold gases of dysprosium*, Phys. Rev. A **89**, 020701 (2014).

[Ber77]   M. V. Berry and M. Tabor, *Level clustering in the regular spectrum*, Proc. Roy. Soc. London Ser. A **356**, 375 (1977).

[Ber81]   M. Berry, *Quantizing a classically ergodic system: Sinai's billiard and the KKR method*, Ann. Phys. **131**, 163 (1981).

[Ber08]   A. J. Berglund, J. L. Hanssen, and J. J. McClelland, *Narrow-line magneto-optical cooling and trapping of strongly magnetic atoms*, Phys. Rev. Lett. **100**, 113002 (2008).

[Bil08]   J. Billy, V. Josse, Z. Zuo, A. Bernard, B. Hambrecht, P. Lugan, D. Clement, L. Sanchez-Palencia, P. Bouyer, and A. Aspect, *Direct observation of Anderson localization of matter waves in a controlled disorder*, Nature **453**, 891 (2008).

[Bit12]   S. Bittner, B. Dietz, M. Miski-Oglu, and A. Richter, *Extremal transmission through a microwave photonic crystal and the observation of edge states in a rectangular dirac billiard*, Phys. Rev. B **85**, 064301 (2012).

[Bla12]   P. B. Blakie, D. Baillie, and R. N. Bisset, *Roton spectroscopy in a harmonically trapped dipolar Bose-Einstein condensate*, Phys. Rev. A **86**, 021604 (2012).

[Blo08]   I. Bloch, J. Dalibard, and W. Zwerger, *Many-body physics with ultracold gases*, Rev. Mod. Phys. **80**, 885 (2008).

[Boh36]   N. Bohr, *Neutron capture and nuclear constitution*, Nature **137**, 344 (1936).

[Boh84a] O. Bohigas and M. J. Giannoni, *Mathematical and computational methods in nuclear physics*, Springer, 1984.

[Boh84b] O. Bohigas, M. J. Giannoni, and C. Schmit, *Characterization of chaotic quantum spectra and universality of level fluctuation laws*, Phys. Rev. Lett. **52**, 1 (1984).

[Boh09] J. L. Bohn, M. Cavagnero, and C. Ticknor, *Quasi-universal dipolar scattering in cold and ultracold gases*, New J. Phys. **11**, 055039 (2009).

[Boh14] J. L. Bohn and D. S. Jin, *Differential scattering and rethermalization in ultracold dipolar gases*, Phys. Rev. A **89**, 022702 (2014).

[Bou09] J. P. Bouchaud and M. Potters, *Financial applications of random matrix theory: A short review*, ArXiv e-prints 0910.1205 (2009).

[Bra95] C. C. Bradley, C. A. Sackett, J. J. Tollett, and R. G. Hulet, *Evidence of Bose-Einstein condensation in an atomic gas with attractive interactions*, Phys. Rev. Lett. **75**, 1687 (1995).

[Bra12] H. Brammer, J. Ulitzsch, R. Bourouis, and M. Weitz, *Doppler-free frequency-modulation spectroscopy of atomic erbium in a hollow-cathode discharge cell*, Applied Physics B **106**, 405 (2012).

[Bro73] T. A. Brody, *A statistical measure for the repulsion of energy levels*, Lettere Al Nuovo Cimento Series 2 **7**, 482 (1973).

[Bro81] T. A. Brody, J. Flores, J. B. French, P. A. Mello, A. Pandey, and S. S. M. Wong, *Random-matrix physics: Spectrum and strength fluctuations*, Rev. Mod. Phys. **53**, 385 (1981).

[Bur98] J. P. Burke, C. H. Greene, and J. L. Bohn, *Multichannel cold collisions: Simple dependences on energy and magnetic field*, Phys. Rev. Lett. **81**, 3355 (1998).

[Cab61] A. Y. Cabezas, I. Lindgren, and R. Marrus, *Atomic-beam investigations of electronic and nuclear ground states in the rare-earth region*, Phys. Rev. **122**, 1796 (1961).

[Cas01] Y. Castin, *Bose-Einstein condensates in atomic gases: Simple theoretical results*, Coherent atomic matter waves (R. Kaiser, C. Westbrook, and F. David, eds.), Springer, 2001.

[Chi83] W. J. Childs, L. S. Goodman, and V. Pfeufer, *Hyperfine structure of the $4f^{12}6s^2\ ^3h$ and ^3f terms of $^{167}Er\ I$ by atomic-beam, laser-rf double resonance*, Phys. Rev. A **28**, 3402 (1983).

[Chi04] C. Chin, V. Vuletić, A. J. Kerman, S. Chu, E. Tiesinga, P. J. Leo, and C. J. Williams, *Precision Feshbach spectroscopy of ultracold Cs_2*, Phys. Rev. A **70**, 032701 (2004).

[Chi07] R. Chicireanu, *Studies of cold chromium atoms in magnetic and optical traps*, Ph.D. thesis, Institut Galilée; Université Paris-Nord (2007).

[Chi09] C. Chin, V. V. Flambaum, and M. G. Kozlov, *Ultracold molecules: new probes on the variation of fundamental constants*, New J. Phys. **11**, 055048 (2009).

[Chi10] C. Chin, R. Grimm, P. Julienne, and E. Tiesinga, *Feshbach resonances in ultracold gases*, Rev. Mod. Phys. **82**, 1225 (2010).

[Chr09] P. Christian, *Stabilisierung eines Lasersystems zur Laserkühlung von Chromatomen*, Master's thesis, 5. Physikalisches Institut, University of Stuttgart (2009).

[Chu85] S. Chu, L. Hollberg, J. E. Bjorkholm, A. Cable, and A. Ashkin, *Three-dimensional viscous confinement and cooling of atoms by resonance radiation pressure*, Phys. Rev. Lett. **55**, 48 (1985).

[Con63] J. G. Conway and B. G. Wybourne, *Low-lying energy levels of lanthanide atoms and intermediate coupling*, Phys. Rev. **130**, 2325 (1963).

[Con97] J.-P. Connerade, *'Quantum chaos' and many-electron atoms*, J. Phys. B **30**, L31 (1997).

[Con10] C. B. Connolly, Y. S. Au, S. C. Doret, W. Ketterle, and J. M. Doyle, *Large spin relaxation rates in trapped submerged-shell atoms*, Phys. Rev. A **81**, 010702 (2010).

[Cou95] M. Courtney, N. Spellmeyer, H. Jiao, and D. Kleppner, *Classical, semiclassical, and quantum dynamics in the lithium Stark system*, Phys. Rev. A **51**, 3604 (1995).

[Cro14] J. F. E. Croft and J. L. Bohn, *Long-lived complexes and chaos in ultracold molecular collisions*, Phys. Rev. A **89**, 012714 (2014).

[CS10] B. Capogrosso-Sansone, C. Trefzger, M. Lewenstein, P. Zoller, and G. Pupillo, *Quantum phases of cold polar molecules in 2D optical lattices*, Phys. Rev. Lett. **104**, 125301 (2010).

[Dan08] J. G. Danzl, E. Haller, M. Gustavsson, M. J. Mark, R. Hart, N. Bouloufa, O. Dulieu, H. Ritsch, and H.-C. Nägerl, *Quantum gas of deeply bound ground state molecules*, Science **321**, 1062 (2008).

[Dav95] K. B. Davis, M. O. Mewes, M. R. Andrews, N. J. van Druten, D. S. Durfee, D. M. Kurn, and W. Ketterle, *Bose-Einstein condensation in a gas of sodium atoms*, Phys. Rev. Lett. **75**, 3969 (1995).

[Deb01] B. Deb and L. You, *Low-energy atomic collision with dipole interactions*, Phys. Rev. A **64**, 022717 (2001).

[Dei08] J. Deiglmayr, A. Grochola, M. Repp, K. Mörtlbauer, C. Glück, J. Lange, O. Dulieu, R. Wester, and M. Weidemüller, *Formation of ultracold polar molecules in the rovibrational ground state*, Phys. Rev. Lett. **101**, 133004 (2008).

[DeM99a] B. DeMarco, J. L. Bohn, J. P. Burke, M. Holland, and D. S. Jin, *Measurement of p-wave threshold law using evaporatively cooled fermionic atoms*, Phys. Rev. Lett. **82**, 4208 (1999).

[DeM99b] B. DeMarco and D. S. Jin, *Onset of Fermi degeneracy in a trapped atomic gas*, Science **285**, 1703 (1999).

[Den10] H. Deng, H. Haug, and Y. Yamamoto, *Exciton-polariton Bose-Einstein condensation*, Rev. Mod. Phys. **82**, 1489 (2010).

[Die08] B. Dietz, T. Friedrich, H. L. Harney, M. Miski-Oglu, A. Richter, F. Schäfer, and H. A. Weidenmüller, *Chaotic scattering in the regime of weakly overlapping resonances*, Phys. Rev. E **78**, 055204 (2008).

[Dys62a] F. J. Dyson, *Statistical theory of the energy levels of complex systems. I*, J. Math. Phys. **3**, 140 (1962).

[Dys62b] F. J. Dyson, *Statistical theory of the energy levels of complex systems. II*, J. Math. Phys. **3**, 157 (1962).

[Dys62c] F. J. Dyson, *Statistical theory of the energy levels of complex systems. III*, J. Math. Phys. **3**, 166 (1962).

[Dys63] F. J. Dyson and M. L. Mehta, *Statistical theory of the energy levels of complex systems. IV*, J. Math. Phys. **4**, 701 (1963).

[Ebl07] J. Eble and F. Schmidt-Kaler, *Optimization of frequency modulation transfer spectroscopy on the calcium 4^1S_0 to 4^1P_1 transition*, Appl. Phys. B **88**, 563 (2007).

[Eri60] T. Ericson, *Fluctuations of nuclear cross sections in the "continuum" region*, Phys. Rev. Lett. **5**, 430 (1960).

[Fat06] M. Fattori, T. Koch, S. Goetz, A. Griesmaier, S. Hensler, J. Stuhler, and T. Pfau, *Demagnetization cooling of a gas*, Nature Phys. **2**, 765 (2006).

[Fer34] E. Fermi, E. Amaldi, O. D'Agostino, F. Rasetti, and E. Segre, *Artificial radioactivity produced by neutron bombardment*, Proceedings of the Royal Society of London. Series A **146**, 483 (1934).

[Fer06]   F. Ferlaino, C. D'Errico, G. Roati, M. Zaccanti, M. Inguscio, G. Modugno, and A. Simoni, *Feshbach spectroscopy of a K-Rb atomic mixture*, Phys. Rev. A **73**, 040702 (2006).

[Fer11]   F. Ferlaino, A. Zenesini, M. Berninger, B. Huang, H.-C. Nägerl, and R. Grimm, *Efimov resonances in ultracold quantum gases*, Few-Body Systems **51**, 113 (2011).

[Fla99]   V. V. Flambaum, G. F. Gribakin, and C. Harabati, *Analytical calculation of cold-atom scattering*, Phys. Rev. A **59**, 1998 (1999).

[Fre09]   B. M. Fregoso and E. Fradkin, *Ferronematic ground state of the dilute dipolar Fermi gas*, Phys. Rev. Lett. **103**, 205301 (2009).

[Fri36]   O. R. Frisch and G. Placzek, *Capture of slow neutrons*, Nature **137**, 357 (1936).

[Fri98]   D. G. Fried, T. C. Killian, L. Willmann, D. Landhuis, S. C. Moss, D. Kleppner, and T. J. Greytak, *Bose-Einstein condensation of atomic hydrogen*, Phys. Rev. Lett. **81**, 3811 (1998).

[Fri14]   A. Frisch, M. Mark, K. Aikawa, F. Ferlaino, J. L. Bohn, C. Makrides, A. Petrov, and S. Kotochigova, *Quantum chaos in ultracold collisions of gas-phase erbium atoms*, Nature **507**, 475 (2014).

[Gao99]   B. Gao, *Repulsive $1/r^3$ interaction*, Phys. Rev. A **59**, 2778 (1999).

[Gao05]   B. Gao, E. Tiesinga, C. J. Williams, and P. S. Julienne, *Multichannel quantum-defect theory for slow atomic collisions*, Phys. Rev. A **72**, 042719 (2005).

[Gao08]   B. Gao, *General form of the quantum-defect theory for theory for $-1/r^\alpha$ type of potentials with $\alpha > 2$*, Phys. Rev. A **78**, 012702 (2008).

[Gio02]   S. Giovanazzi, A. Görlitz, and T. Pfau, *Tuning the dipolar interaction in quantum gases*, Phys. Rev. Lett. **89**, 130401 (2002).

[Gio08]   S. Giorgini, L. P. Pitaevskii, and S. Stringari, *Theory of ultracold atomic Fermi gases*, Rev. Mod. Phys. **80**, 1215 (2008).

[Gra72]   D. E. Gray, *American institute of physics handbook*, 3rd ed., pp. 4-298–4-300, McGraw-Hill New York, 1972.

[Grä92]   H.-D. Gräf, H. L. Harney, H. Lengeler, C. H. Lewenkopf, C. Rangacharyulu, A. Richter, P. Schardt, and H. A. Weidenmüller, *Distribution of eigenmodes in a superconducting stadium billiard with chaotic dynamics*, Phys. Rev. Lett. **69**, 1296 (1992).

[Gre02]   M. Greiner, O. Mandel, T. Esslinger, T. W. Hänsch, and I. Bloch, *Quantum phase transition from a superfluid to a Mott insulator in a gas of ultracold atoms*, Nature **415**, 39 (2002).

[Gri05]   A. Griesmaier, J. Werner, S. Hensler, J. Stuhler, and T. Pfau, *Bose-Einstein condensation of chromium*, Phys. Rev. Lett. **94**, 160401 (2005).

[Guh98]   T. Guhr, A. Müller-Groeling, and H. Weidenmüller, *Random-matrix theories in quantum physics: common concepts*, Physics Reports **299**, 189 (1998).

[Gün04]   K. J. Günter, *Design and implementation of a Zeeman slower for ^{87}Rb*, Master's thesis, École Normale Supérieure, Paris (2004).

[Gut90]   M. Gutzwiller, *Chaos in classical and quantum mechanics*, Springer, 1990.

[Han05]   D. Hansen and A. Hemmerich, *Doppler-free spectroscopy of metastable calcium in a discharge heat pipe*, Phys. Rev. A **72**, 022502 (2005).

[Haq82]   R. U. Haq, A. Pandey, and O. Bohigas, *Fluctuation properties of nuclear energy levels: Do theory and experiment agree?*, Phys. Rev. Lett. **48**, 1086 (1982).

[Har03]   M. L. Harris, *Design and construction of an improved Zeeman slower*, Ph.D. thesis, Department of Physics, Trinity College, Duke University (2003).

[Har10]   E. A. D. Hartog, J. P. Chisholm, and J. E. Lawler, *Radiative lifetimes of neutral erbium*, J. Phys. B **43**, 155004 (2010).

[Has89]   H. Hasegawa, M. Robnik, and G. Wunner, *Classical and quantal chaos in the diamagnetic Kepler problem*, Progr. Theor. Exp. Phys. **98**, 198 (1989).

[Has10]   M. Z. Hasan and C. L. Kane, *Topological insulators*, Rev. Mod. Phys. **82**, 3045 (2010).

[HS13]   O. A. Herrera-Sancho, N. Nemitz, M. V. Okhapkin, and E. Peik, *Energy levels of Th+ between 7.3 and 8.3 eV*, Phys. Rev. A **88**, 012512 (2013).

[Hun12]   L. R. Hunter, S. K. Peck, A. S. Greenspon, S. S. Alam, and D. DeMille, *Prospects for laser cooling TlF*, Phys. Rev. A **85**, 012511 (2012).

[Hut10]   J. M. Hutson, *Ultracold chemistry*, Science **327**, 788 (2010).

[Ino04]   S. Inouye, J. Goldwin, M. L. Olsen, C. Ticknor, J. L. Bohn, and D. S. Jin, *Observation of heteronuclear Feshbach resonances in a mixture of bosons and fermions*, Phys. Rev. Lett. **93**, 183201 (2004).

[Jak98]   D. Jaksch, C. Bruder, J. I. Cirac, C. W. Gardiner, and P. Zoller, *Cold bosonic atoms in optical lattices*, Phys. Rev. Lett. **81**, 3108 (1998).

[Jen91]   J. Jensen and A. Mackintosh, *Rare earth magnetism: Structures and excitations*, International series of monographs on physics, Clarendon Press, 1991.

[Jen92]   R. V. Jensen, *Quantum chaos*, Nature **355**, 311 (1992).

[Jia96]   H. Jiao, *Experimental and theoretical aspects of quantum chaos in Rydberg atoms in strong fields*, Ph.D. thesis, Massachusetts Institute of Technology (1996).

[Jin90]   W. G. Jin, T. Horiguchi, M. Wakasugi, and Y. Yoshizawa, *Hyperfine structure and isotope shift in Er I by the atomic-beam laser spectroscopy*, J. Phys. Soc. Jpn. **59**, 3148 (1990).

[Joc04]   S. Jochim, *Bose-Einstein condensation of molecules*, Ph.D. thesis, Faculty of Mathematics, Computer Science and Physics of the University of Innsbruck (2004).

[Jud61]   B. R. Judd and I. Lindgren, *Theory of Zeeman effect in the ground multiplets of rare-earth atoms*, Phys. Rev. **122**, 1802 (1961).

[Kat99]   H. Katori, T. Ido, Y. Isoya, and M. Kuwata-Gonokami, *Magneto-optical trapping and cooling of strontium atoms down to the photon recoil temperature*, Phys. Rev. Lett. **82**, 1116 (1999).

[Kat04]   Y. K. Kato, R. C. Myers, A. C. Gossard, and D. D. Awschalom, *Observation of the spin Hall effect in semiconductors*, Science **306**, 1910 (2004).

[Ket96]   W. Ketterle and N. Van Druten, *Evaporative cooling of trapped atoms*, Adv. At. Mol. Opt. Phys. **37**, 181 (1996).

[Ket99]   W. Ketterle, D. S. Durfee, and D. M. Stamper-Kurn, *Making, probing and understanding Bose-Einstein condensates*, ArXiv cond-mat/9904034 (1999).

[Ket08]   W. Ketterle and M. W. Zwierlein, *Making, probing and understanding ultracold Fermi gases*, ArXiv 0801.2500 (2008).

[Kit08]   M. Kitagawa, K. Enomoto, K. Kasa, Y. Takahashi, R. Ciuryło, P. Naidon, and P. S. Julienne, *Two-color photoassociation spectroscopy of ytterbium atoms and the precise determinations of s-wave scattering lengths*, Phys. Rev. A **77**, 012719 (2008).

[Köh06]   T. Köhler, K. Góral, and P. S. Julienne, *Production of cold molecules via magnetically tunable feshbach resonances*, Rev. Mod. Phys. **78**, 1311 (2006).

[Kol10]   C. Kollath, G. Roux, G. Biroli, and A. M. Läuchli, *Statistical properties of the spectrum of the extended Bose-Hubbard model*, J. Stat. Mech. **2010**, P08011 (2010).

[Kot]   S. Kotochigova, private communication.

[Kot97]   S. Kotochigova, H. Levine, and I. Tupitsyn, *Correlated relativistic calculation of the giant resonance in the Gd3+ absorption spectrum*, Int. J. Quant. Chem. **65**, 575 (1997).

[Kot11]   S. Kotochigova and A. Petrov, *Anisotropy in the interaction of ultracold dysprosium*, Phys. Chem. Chem. Phys. **13**, 19165 (2011).

[Kot14]   S. Kotochigova, *Controlling interactions between highly magnetic atoms with Feshbach resonances*, Rep. Prog. Phys. **77**, 093901 (2014).

[Kra06]   T. Kraemer, M. Mark, P. Waldburger, J. G. Danzl, C. Chin, B. Engeser, A. D. Lange, K. Pilch, A. Jaakkola, H.-C. Nägerl, and R. Grimm, *Evidence for Efimov quantum states in an ultracold gas of caesium atoms*, Nature **440**, 315 (2006).

[Kra09]   S. Kraft, F. Vogt, O. Appel, F. Riehle, and U. Sterr, *Bose-Einstein condensation of alkaline earth atoms: ^{40}Ca*, Phys. Rev. Lett. **103**, 130401 (2009).

[Kro02]   S. Kroboth, *Laserkühlung von Ytterbiumatomen*, Master's thesis, 5. Physikalisches Institut, University of Stuttgart (2002).

[Kuw99]   T. Kuwamoto, K. Honda, Y. Takahashi, and T. Yabuzaki, *Magneto-optical trapping of Yb atoms using an intercombination transition*, Phys. Rev. A **60**, R745 (1999).

[Lah08]   T. Lahaye, J. Metz, B. Fröhlich, T. Koch, M. Meister, A. Griesmaier, T. Pfau, H. Saito, Y. Kawaguchi, and M. Ueda, *d-Wave collapse and explosion of a dipolar Bose-Einstein condensate*, Phys. Rev. Lett. **101**, 080401 (2008).

[Lah09]   T. Lahaye, C. Menotti, L. Santos, M. Lewenstein, and T. Pfau, *The physics of dipolar bosonic quantum gases*, Rep. Prog. Phys. **72**, 126401 (2009).

[Lal99]   L. Laloux, P. Cizeau, J.-P. Bouchaud, and M. Potters, *Noise dressing of financial correlation matrices*, Phys. Rev. Lett. **83**, 1467 (1999).

[Lan77]   L. Landau and E. Lifshits, *Quantum mechanics: Non-relativistic theory*, Butterworth-Heinemann, 1977.

[Lan08]   F. Lang, K. Winkler, C. Strauss, R. Grimm, and J. H. Denschlag, *Ultracold triplet molecules in the rovibrational ground state*, Phys. Rev. Lett. **101**, 133005 (2008).

[Law81]   J. E. Lawler, A. Siegel, B. Couillaud, and T. W. Hänsch, *A hollow cathode for Doppler-free spectroscopy*, J. Appl. Phys. **52**, 4375 (1981).

[Law10]   J. E. Lawler, J.-F. Wyart, and E. A. D. Hartog, *Atomic transition probabilities of Er I*, J. Phys. B **43**, 235001 (2010).

[Lee05]   S. H. Lee, S. Sasaki, I. Vasserman, and D. R. Walters, *Magnetic properties of undulator vacuum chamber materials for the LINAC coherent light source*, Proceedings of the 27th International Free Electron Laser Conference, 383 (2005).

[Let89]   P. D. Lett, W. D. Phillips, S. L. Rolston, C. E. Tanner, R. N. Watts, and C. I. Westbrook, *Optical molasses*, J. Opt. Soc. Am. B **6**, 2084 (1989).

[Lev05]   R. Levine, *Molecular reaction dynamics*, Cambridge University Press, 2005.

[Lid10]   D. Lide, *CRC handbook of chemistry and physics, 90th edition*, CRC Handbook of Chemistry and Physics, 90th Ed, p. 14, Taylor & Francis, 2010.

[Lin11]   Y.-J. Lin, K. Jimenez-Garcia, and I. B. Spielman, *Spin-orbit-coupled Bose-Einstein condensates*, Nature **471**, 83 (2011).

[Lis99]   F. Lison, P. Schuh, D. Haubrich, and D. Meschede, *High-brilliance Zeeman-slowed cesium atomic beam*, Phys. Rev. A **61**, 013405 (1999).

[Lof04]   T. H. Loftus, T. Ido, M. M. Boyd, A. D. Ludlow, and J. Ye, *Narrow line cooling and momentum-space crystals*, Phys. Rev. A **70**, 063413 (2004).

[Lu10]   M. Lu, S. H. Youn, and B. L. Lev, *Trapping ultracold dysprosium: A highly magnetic gas for dipolar physics*, Phys. Rev. Lett. **104**, 063001 (2010).

[Lu11]   M. Lu, N. Q. Burdick, S. H. Youn, and B. L. Lev, *Strongly dipolar Bose-Einstein condensate of dysprosium*, Phys. Rev. Lett. **107**, 190401 (2011).

[Lu12]   M. Lu, N. Q. Burdick, and B. L. Lev, *Quantum degenerate dipolar Fermi gas*, Phys. Rev. Lett. **108**, 215301 (2012).

[Mai14]   T. Maier, H. Kadau, M. Schmitt, A. Griesmaier, and T. Pfau, *Narrow-line magneto-optical trap for dysprosium atoms*, Opt. Lett. **39**, 3138 (2014).

[Mar78]   W. C. Martin, *Atomic energy levels: The rare earth elements (the spectra of lanthanum, cerium, praseodymium, neodymium, promethium, samarium, europium, gadolinium, terbium, dysprosium, holmium, ebrium, thulium, ytterbium, and lutetium)*, Tech. report, National Standard Reference Data System, 1978.

[Mar80]   J. Marek and H. Stahnke, *Radiative lifetimes of optical levels of neutral erbium, gadolinium and neodymium*, Zeitschrift für Physik A Atoms and Nuclei **298**, 81 (1980).

[Mar98]   M. Marinescu and L. You, *Controlling atom-atom interaction at ultralow temperatures by dc electric fields*, Phys. Rev. Lett. **81**, 4596 (1998).

[Mar10]   K. Marvel and U. Agvaanluvsan, *Random matrix theory models of electric grid topology*, Physica A **389**, 5838 (2010).

[May12]   M. Mayle, B. P. Ruzic, and J. L. Bohn, *Statistical aspects of ultracold resonant scattering*, Phys. Rev. A **85**, 062712 (2012).

[May13]   M. Mayle, G. Quéméner, B. P. Ruzic, and J. L. Bohn, *Scattering of ultracold molecules in the highly resonant regime*, Phys. Rev. A **87**, 012709 (2013).

[McC06a] J. J. McClelland, *Natural linewidth of the 401-nm laser-cooling transition in Er I*, Phys. Rev. A **73**, 064502 (2006).

[McC06b] J. J. McClelland and J. L. Hanssen, *Laser cooling without repumping: A magneto-optical trap for erbium atoms*, Phys. Rev. Lett. **96**, 143005 (2006).

[McC08]   D. J. McCarron, S. A. King, and S. L. Cornish, *Modulation transfer spectroscopy in atomic rubidium*, Meas. Sci. Technol. **19**, 105601 (2008).

[Meh63]   M. L. Mehta and F. J. Dyson, *Statistical theory of the energy levels of complex systems. V*, J. Math. Phys. **4**, 713 (1963).

[Mia14]   J. Miao, J. Hostetter, G. Stratis, and M. Saffman, *Magneto-optical trapping of holmium atoms*, Phys. Rev. A **89**, 041401 (2014).

[Mie00]   F. H. Mies and M. Raoult, *Analysis of threshold effects in ultracold atomic collisions*, Phys. Rev. A **62**, 012708 (2000).

[Mit10]   G. E. Mitchell, A. Richter, and H. A. Weidenmüller, *Random matrices and chaos in nuclear physics: Nuclear reactions*, Rev. Mod. Phys. **82**, 2845 (2010).

[Miy08]   T. Miyakawa, T. Sogo, and H. Pu, *Phase-space deformation of a trapped dipolar Fermi gas*, Phys. Rev. A **77**, 061603 (2008).

[Mod01]   G. Modugno, G. Ferrari, G. Roati, R. J. Brecha, A. Simoni, and M. Inguscio, *Bose-Einstein condensation of potassium atoms by sympathetic cooling*, Science **294**, 1320 (2001).

[Mon93]   C. R. Monroe, E. A. Cornell, C. A. Sackett, C. J. Myatt, and C. E. Wieman, *Measurement of Cs-Cs elastic scattering at $T = 30\,\mu\text{K}$*, Phys. Rev. Lett. **70**, 414 (1993).

[Mor11]   I. O. Morales, E. Landa, P. Stránský, and A. Frank, *Improved unfolding by detrending of statistical fluctuations in quantum spectra*, Phys. Rev. E **84**, 016203 (2011).

[Mos43]   G. Mosander, *Philosophical magazine*, p. 241, Taylor & Francis., 1843.

[Mül72]   J. Müller, B. Singh, and N. A. Surplice, *The gettering action of evaporated films of titanium and erbium*, J. Phys. D: Appl. Phys. **5**, 1177 (1972).

[Mül04]   S. Müller, S. Heusler, P. Braun, F. Haake, and A. Altland, *Semiclassical foundation of universality in quantum chaos*, Phys. Rev. Lett. **93**, 014103 (2004).

[Mul11]   D. Mulhall, *Maximum likelihood method to correct for missed levels based on the $\Delta_3(L)$ statistic*, Phys. Rev. C **83**, 054321 (2011).

[Mül13]   R. R. Müller, G. Alfano, B. M. Zaidel, and R. de Miguel, *Applications of large random matrices in communications engineering*, ArXiv e-prints 1310.5479 (2013).

[Mus62]   T. Musha, *Cathode sputtering in hollow cathode discharges*, J. Phys. Soc. Jpn. **17**, 1440 (1962).

[Nas13]   S. Nascimbène, *Realizing one-dimensional topological superfluids with ultracold atomic gases*, J. Phys. B **46**, 134005 (2013).

[Ni08]   K.-K. Ni, S. Ospelkaus, M. H. G. de Miranda, A. Peér, B. Neyenhuis, J. J. Zirbel, S. Kotochigova, P. S. Julienne, D. S. Jin, and J. Ye, *A high phase-space-density gas of polar molecules*, Science **322**, 231 (2008).

[Oga07]   V. Oganesyan and D. A. Huse, *Localization of interacting fermions at high temperature*, Phys. Rev. B **75**, 155111 (2007).

[Orl02]   H. Orland and A. Zee, *RNA folding and large N matrix theory*, Nucl. Phys. B **620**, 456 (2002).

[Osp10]   S. Ospelkaus, K.-K. Ni, D. Wang, M. H. G. de Miranda, B. Neyenhuis, G. Quéméner, P. S. Julienne, J. L. Bohn, D. S. Jin, and J. Ye, *Quantum-state controlled chemical reactions of ultracold potassium-rubidium molecules*, Science **327**, 853 (2010).

[Pas11]   B. Pasquiou, G. Bismut, E. Maréchal, P. Pedri, L. Vernac, O. Gorceix, and B. Laburthe-Tolra, *Spin relaxation and band excitation of a dipolar Bose-Einstein condensate in 2D optical lattices*, Phys. Rev. Lett. **106**, 015301 (2011).

[Pec84]   P. Pechukas, *Remarks on "quantum chaos"*, J. Phys. Chem. A **88**, 4823 (1984).

[Pet02]   C. Pethick and H. Smith, *Bose-Einstein condensation in dilute gases*, Cambridge University Press, 2002.

[Pet12]   A. Petrov, E. Tiesinga, and S. Kotochigova, *Anisotropy-induced Feshbach resonances in a quantum dipolar gas of highly magnetic atoms*, Phys. Rev. Lett. **109**, 103002 (2012).

[Pfa]   T. Pfau, private communication.

[Pil09]   K. Pilch, A. D. Lange, A. Prantner, G. Kerner, F. Ferlaino, H.-C. Nägerl, and R. Grimm, *Observation of interspecies Feshbach resonances in an ultracold Rb-Cs mixture*, Phys. Rev. A **79**, 042718 (2009).

[Plu13]   Z. Pluhař and H. A. Weidenmüller, *Universal chaotic scattering on quantum graphs*, Phys. Rev. Lett. **110**, 034101 (2013).

[Plu14]   Z. Pluhař and H. A. Weidenmüller, *Universal quantum graphs*, Phys. Rev. Lett. **112**, 144102 (2014).

[Pol09]   S. E. Pollack, D. Dries, M. Junker, Y. P. Chen, T. A. Corcovilos, and R. G. Hulet, *Extreme tunability of interactions in a ^7Li Bose-Einstein condensate*, Phys. Rev. Lett. **102**, 090402 (2009).

[Por56]   C. E. Porter and R. G. Thomas, *Fluctuations of nuclear reaction widths*, Phys. Rev. **104**, 483 (1956).

[Qi11]   X.-L. Qi and S.-C. Zhang, *Topological insulators and superconductors*, Rev. Mod. Phys. **83**, 1057 (2011).

[Raj06]   K. Rajan and L. F. Abbott, *Eigenvalue spectra of random matrices for neural networks*, Phys. Rev. Lett. **97**, 188104 (2006).

[Ral11]   Y. Ralchenko, A. Kramida, J. Reader, and NIST ASD Team, *NIST atomic spectra database*.

[Ram05]   N. Ramsey, *Molecular beams*, Oxford classics series, Oxford University Press, 2005.

[Rel02]   A. Relaño, J. M. G. Gómez, R. A. Molina, J. Retamosa, and E. Faleiro, *Quantum chaos and $1/f$ noise*, Phys. Rev. Lett. **89**, 244102 (2002).

[Ric14]   F. Richter, D. Becker, C. Bény, T. A. Schulze, S. Ospelkaus, and T. J. Osborne, *Ultracold chemistry and its reaction kinetics*, ArXiv quant-ph/1405.6811 (2014).

[Rie12]   A. Rietzler, *Narrow-line cooling light for a magneto-optical trap of erbium atoms*, Master's thesis, Faculty of Mathematics, Computer Science and Physics of the University of Innsbruck (2012).

[Rob01]   A. Robert, O. Sirjean, A. Browaeys, J. Poupard, S. Nowak, D. Boiron, C. I. Westbrook, and A. Aspect, *A Bose-Einstein condensate of metastable atoms*, Science **292**, 461 (2001).

[Ros60]   N. Rosenzweig and C. E. Porter, *"Repulsion of energy levels" in complex atomic spectra*, Phys. Rev. **120**, 1698 (1960).

[Sad00]   H. R. Sadeghpour, J. L. Bohn, M. J. Cavagnero, B. D. Esry, I. I. Fabrikant, J. H. Macek, and A. R. P. Rau, *Collisions near threshold in atomic and molecular physics*, J. Phys. B **33**, R93 (2000).

[San00]   L. Santos, G. V. Shlyapnikov, P. Zoller, and M. Lewenstein, *Bose-Einstein condensation in trapped dipolar gases*, Phys. Rev. Lett. **85**, 1791 (2000).

[San03a] L. Santos, G. V. Shlyapnikov, and M. Lewenstein, *Roton-maxon spectrum and stability of trapped dipolar Bose-Einstein condensates*, Phys. Rev. Lett. **90**, 250403 (2003).

[San03b] R. Santra and C. H. Greene, *Tensorial analysis of the long-range interaction between metastable alkaline-earth-metal atoms*, Phys. Rev. A **67**, 062713 (2003).

[Sau10]   J. D. Sau, R. M. Lutchyn, S. Tewari, and S. Das Sarma, *Generic new platform for topological quantum computation using semiconductor heterostructures*, Phys. Rev. Lett. **104**, 040502 (2010).

[Sch03]   P. O. Schmidt, *Scattering properties of ultra-cold chromium atoms*, Ph.D. thesis, 5. Physikalisches Institut, University of Stuttgart (2003).

[Sch11]   J. Schindler, *Characterization of an erbium atomic beam*, Master's thesis, Faculty of Mathematics, Computer Science and Physics; University of Innsbruck (2011).

[Sha72]   R. Shakeshaft, *Low energy scattering by the r^{-3} potential*, J. Phys. B **5**, L115 (1972).

[Shi82]   J. H. Shirley, *Modulation transfer processes in optical heterodyne saturation spectroscopy*, Opt. Lett. **7**, 537 (1982).

[Sie01]   M. Sieber and K. Richter, *Correlations between periodic orbits and their rôle in spectral statistics*, Physica Scripta **T90**, 128 (2001).

[Smi65]   K. F. Smith and P. J. Unsworth, *The hyperfine structure of 167 Er and magnetic moments of 143, 145 Nd and 167 Er by atomic beam triple magnetic resonance*, Proceedings of the Physical Society **86**, 1249 (1965).

[Ste09]   S. Stellmer, M. K. Tey, B. Huang, R. Grimm, and F. Schreck, *Bose-Einstein condensation of strontium*, Phys. Rev. Lett. **103**, 200401 (2009).

[Ste13]   S. Stellmer, *Degenerate quantum gases of strontium*, Ph.D. thesis, Faculty of Mathematics, Computer Science and Physics of the University of Innsbruck (2013).

[Suk10]   D. Sukachev, A. Sokolov, K. Chebakov, A. Akimov, S. Kanorsky, N. Kolachevsky, and V. Sorokin, *Magneto-optical trap for thulium atoms*, Phys. Rev. A **82**, 011405 (2010).

[Tak03]   Y. Takasu, K. Maki, K. Komori, T. Takano, K. Honda, M. Kumakura, T. Yabuzaki, and Y. Takahashi, *Spin-singlet Bose-Einstein condensation of two-electron atoms*, Phys. Rev. Lett. **91**, 040404 (2003).

[Tak14]   T. Takekoshi, L. Reichsöllner, A. Schindewolf, J. M. Hutson, C. R. Le Sueur, O. Dulieu, F. Ferlaino, R. Grimm, and H.-C. Nägerl, *Ultracold dense samples of dipolar RbCs molecules in the rovibrational and hyperfine ground state*, ArXiv 1405.6037 (2014).

[Tar12]   L. Tarruell, D. Greif, T. Uehlinger, G. Jotzu, and T. Esslinger, *Creating, moving and merging Dirac points with a Fermi gas in a tunable honeycomb lattice*, Nature **483**, 302 (2012).

[Tay97]   J. Taylor, *An introduction to error analysis: The study of uncertainties in physical measurements*, University Science Books, 1997.

[Tho05]   S. T. Thompson, E. Hodby, and C. E. Wieman, *Ultracold molecule production via a resonant oscillating magnetic field*, Phys. Rev. Lett. **95**, 190404 (2005).

[Tic08]   C. Ticknor, *Collisional control of ground state polar molecules and universal dipolar scattering*, Phys. Rev. Lett. **100**, 133202 (2008).

[Tim06]   T. Timberlake, *Random numbers and random matrices: Quantum chaos meets number theory*, Am. J. Phys. **74**, 547 (2006).

[Tul04]   A. M. Tulino and S. Verdú, *Random matrix theory and wireless communications*, Foundations and Trends in Communications and Information Theory **1**, 1 (2004).

[Web03]   T. Weber, J. Herbig, M. Mark, H.-C. Nägerl, and R. Grimm, *Bose-Einstein condensation of cesium*, Science **299**, 232 (2003).

[Wei09]   H. A. Weidenmüller and G. E. Mitchell, *Random matrices and chaos in nuclear physics: Nuclear structure*, Rev. Mod. Phys. **81**, 539 (2009).

[Wer05]   J. Werner, A. Griesmaier, S. Hensler, J. Stuhler, T. Pfau, A. Simoni, and E. Tiesinga, *Observation of Feshbach resonances in an ultracold gas of ^{52}Cr*, Phys. Rev. Lett. **94**, 183201 (2005).

[Wig51a] E. P. Wigner, *On a class of analytic functions from the quantum theory of collisions*, Ann. Math. **53**, 36 (1951).

[Wig51b] E. P. Wigner, *On the statistical distribution of the widths and spacings of nuclear resonance levels*, Mathematical Proceedings of the Cambridge Philosophical Society **47**, 790 (1951).

[Wig57a] E. P. Wigner, *Characteristics vectors of bordered matrices with infinite dimensions II*, Annals of Mathematics **65**, pp. 203–207 (1957).

[Wig57b] E. P. Wigner, *Results and theory of resonance absorption*, Conference on neutron physics by time-of-flight, Oak Ridge National Laboratory Report No. 2309, 1957, p. 59.

[Wig58] E. P. Wigner, *On the distribution of the roots of certain symmetric matrices*, Ann. Math. **67**, pp. 325–327 (1958).

[Wil09] E. Wille, *Preparation of an optically trapped Fermi-Fermi mixture of ^6Li and ^{40}K atoms and characterization of the interspecies interactions by Feshbach spectroscopy*, Ph.D. thesis, Faculty of Mathematics, Computer Science and Physics of the University of Innsbruck (2009).

[WL11] W. Wen-Li and X. Xin-Ye, *Modulation transfer spectroscopy of ytterbium atoms in a hollow cathode lamp*, Chinese Physics Letters **28**, 033202 (2011).

[Wor78] E. F. Worden, R. W. Solarz, J. A. Paisner, and J. G. Conway, *First ionization potentials of lanthanides by laser spectroscopy*, J. Opt. Soc. Am. **68**, 52 (1978).

[Wyb07] B. Wybourne and L. Smentek, *Optical spectroscopy of lanthanides: Magnetic and hyperfine interactions*, Taylor & Francis, 2007.

[Xu02] X. Xu, T. H. Loftus, M. J. Smith, J. L. Hall, A. Gallagher, and J. Ye, *Dynamics in a two-level atom magneto-optical trap*, Phys. Rev. A **66**, 011401 (2002).

[Ye] J. Ye, private communication.

[Yin13] C. Yin, M. Rancic, G. G. de Boo, N. Stavrias, J. C. McCallum, M. J. Sellars, and S. Rogge, *Optical addressing of an individual erbium ion in silicon*, Nature **497**, 91 (2013).

Acknowledgments

The design, construction, and operation of the erbium experiment has been a vast undertaking. From the beginning it required hard work but we were soon rewarded with beautiful results. The experiment held several surprises, luckily most of them were positive in nature, which made the last five years an enjoyable adventure. Setting up such a huge experiment makes one dependent on the help of a tremendous amount of people. Only if all of them work together flawlessly a project of this scale can succeed. And succeed it did. Therefor, I would like to utilize the last pages in concluding my thesis for thanking everybody who contributed in one way or the other to my work on the erbium experiment.

First and most of all, I would like to thank my supervisor Francesca Ferlaino for giving me the great opportunity and trust to set up the erbium machine. Her understanding and intuition for some of the most interesting topics in ultracold atomic physics and her ability to put together a perfectly working team is unsurpassed. Specifically, I would like to thank Francesca for her endless drive in exploring new physics, for making time for discussions, as well as for carefully reading and correcting my thesis. Many little things, like organizing pizza when we achieved the first BEC in the middle of the night and our somewhat regular 'B&B-meetings', which included a full-sized breakfast, made the daily work in the lab very pleasant and became fond memories for me. Because of this, I wish her all the best for her scientific future as well as for her charming family with Pello and their two kids Michele and Cora.

I'd also like to thank Rudi Grimm who founded the ultracold-atoms research group in Innsbruck many years ago. He generously offered his laboratory space after my former master thesis advisor Johannes Hecker-Denschlag went to Ulm and left behind an empty lab. Rudi's exceptional experience and deep understanding of nearly everything relating to atomic physics has been a key element in the development of the erbium experiment. Having erbium as the third element to be Bose-Einstein-condensed in Innsbruck for the first time, after cesium and strontium, made him especially proud as a 'grandfather' to the experiment.

The rest of the erbium team deserves huge thanks as they are the ones who made the time spent in the lab worthwhile. This includes Kiyotaka Aikawa and Michael Mark, two post-docs, Simon Baier, another PhD student, Johannes Schindler, Alexander Rietzler, Daniel Petter, and Michael Springer, all of whom master's students, and Eric Zupanič, a long-term visitor. Having two experienced post-docs in the team was tremendously helpful. Working with Kiyo in the lab was a once in a lifetime experience. I could learn so many things from him and enjoyed his subtle sense of humor a lot. Good luck with you future scientific career! Especially to Simon I give my best wishes, since he is going to continue with the experiment and will lead it to new frontiers. May working with the erbium machine be even more fun

for him than it was for me. Recently, Tadas Pyragius started to work on the new erbium experiment and I wish him all the best with that.

Some people in our research group played a very special and important role during the design and setup of the erbium experiment. These include Florian Schreck, with his invaluable efforts in setting up a versatile experimental control system, Simon Stellmer, who discussed the narrow-line cooling approach and the experimental setup with us, Manfred Mark together with Gerhard Hendl, with their comprehensive understanding of electronics and the development of most of our homebuilt electronic devices, and Anton Schönherr and Matthias Szabados, who helped with designing and manufacturing the main chamber and many other mechanical parts. Each one of you has been of great help and was a source of inspiration for me!

The following list contains all coworkers of the many other experiments which were conducted simultaneously during my PhD studies. I would like to thank each one of them for their individual contributions, which added up to a unique working environment. This includes the people from the LevT experiment: Alessandro Zenesini, Martin Berninger, and Bo Huang; from the RbCs: Tetsu Takekoshi, with whom I shared my office for many years, Lukas Reichsöllner, Andreas Schindewolf, Silva Mezinska, Markus Debatin, Michael Kugler, Bastian Schuster, and Almar Lercher; from the CsIII: Manfred Mark, Katharina Lauber, Florian Meinert, Johann Danzl, Elmar Haller, and Russell Hart; from the KCs: Emil Kirilov, Philipp Weinmann, and Michael Gröbner; from the DyK: Slava Tzanova and Cornelis Ravensbergen; from the FeLiKx: Marco Cetina, Rianne Lous, Michael Jag, Matteo Zaccanti, Devang Naik, Christoph Kohstall, Andreas Trenkwalder, and Frederik Spiegelhalder; from the Li: Meng Khoon Tey, Leonid Sidorenkov, and Edmundo Sanchez; and from the Sr: Benjamin Pasquiou, Simon Stellmer, and Alex Bayerle.

The mechanical workshop consisting of Armin Sailer, Anton Schönherr, Helmut Jordan, and Christoph Wegscheider as well as the electronic workshop with Gerhard Hendl, Wolfgang Kratz, Michael Hofer, and Wolfgang Kuen were most important for setting up an experiment. I really enjoyed the open atmosphere when working with these people and their offer to use most of their available equipment. The secretaries Nicole Jorda, Carla Fantini, Christine Götsch-Obmascher, Karin Köhle, Michaela Palz, Patricia Moser, and Renate Rupprechter are real masters of administrative work. Thanks to all of you for doing a great job!

I would also like to thank some master's students from the ultracold group, including David Baier, Walter Harm, Andreas Klinger, and Stefan Besler. I enjoyed the company of every single one of you. At the beginning of my PhD work I had some overlap with the guys from the BaRbI experiment, who later moved to the university of Ulm, namely Stefan Schmid and Arne Härter. I knew them since writing my master's thesis, which dealt with that experiment. Working with them in the lab was always great fun. I am grateful to Christoph Kohstall, Michael Niedermayer, and Birgit Brandstätter for always being around for interesting side projects involving more applied physics.

Some of my best friends Richard Schwarz, Markus Piff, Robert Spindler, Richard Spindler, and Christoph Sengthaler as well as some people from the 'Innsbrucker hackerspace' were there for me whenever I needed a different point of view on scientific problems or just

some timeout from physics. I've always very much appreciated their willingness for lengthy discussions about any topic whatsoever.

My biggest thanks is to my family, especially to my parents Pia and Günter, for their strong initial support and for offering me the possibility to study physics in the first place. My uncle Walter introduced me to the fascinating field of electronics when I was just five years old, which I still remember vividly. I am very lucky to have my two sisters Birgit and Veronika standing by my side. They will always have a special place in my heart. But my heart truly belongs to my beloved Sabine: I have the utmost gratitude for your love and support in every condition of life.